



**HAL**  
open science

# Comment coule une pâte granulaire? Etudes des composantes primaire et secondaire et des fluctuations de l'écoulement

Octavian Blaj

► **To cite this version:**

Octavian Blaj. Comment coule une pâte granulaire? Etudes des composantes primaire et secondaire et des fluctuations de l'écoulement. Fluid Dynamics [physics.flu-dyn]. Université Sciences et Technologies - Bordeaux I, 2012. English. NNT: . tel-00750737

**HAL Id: tel-00750737**

**<https://theses.hal.science/tel-00750737>**

Submitted on 12 Nov 2012

**HAL** is a multi-disciplinary open access archive for the deposit and dissemination of scientific research documents, whether they are published or not. The documents may come from teaching and research institutions in France or abroad, or from public or private research centers.

L'archive ouverte pluridisciplinaire **HAL**, est destinée au dépôt et à la diffusion de documents scientifiques de niveau recherche, publiés ou non, émanant des établissements d'enseignement et de recherche français ou étrangers, des laboratoires publics ou privés.



# THÈSE

PRÉSENTÉE A

**L'UNIVERSITÉ BORDEAUX 1**

ÉCOLE DOCTORALE DES SCIENCES PHYSIQUES ET DE L'INGENIEUR

Par

**OCTAVIAN BLAJ**

POUR OBTENIR LE GRADE DE

DOCTEUR

SPÉCIALITÉ : Lasers et Matière et Nanoscience (LMN)

## **Comment coule une pâte granulaire? Etudes des composantes primaire et secondaire et des fluctuations de l'écoulement**

Directeurs de recherche : Bernard POULIGNY et Patrick SNABRE

Soutenue le : 10 Octobre 2012

Devant la commission d'examen formée de :

M. Guillaume OVARLEZ	Chargé de Recherche, CNRS	Rapporteur
M. François PETERS	Maître de Conférences, HDR	Rapporteur
M. Bernard POULIGNY	Directeur de Recherche, CNRS	Directeur de thèse
M. Patrick SNABRE	Directeur de Recherche, CNRS	Directeur de thèse
Mme. Annie COLIN	Professeur, Université Bordeaux 1	Examineur
M. Christophe ANCEY	Professeur, Ecole Polytechnique Fédérale de Lausanne	Examineur



# Contents

Acknowledgements .....	6
Glossary.....	9
<b>Chapter A - Introduction.....</b>	<b>11</b>
Introduction (Française) .....	11
Introduction (English) .....	16
<b>Chapter B – Materials and Couette shear cell.....</b>	<b>20</b>
B.1: PMMA spheres .....	20
B.2: Immersion fluids; index- and density – matching .....	20
B.3: Fluorescent tracers and fluorescent immersion fluids .....	23
B.4: Two-motor transparent Couette cell .....	25
B.5: The assumption of rotation invariance .....	28
<b>Chapter C – Dynamics of concentrated suspensions in Couette flow .....</b>	<b>29</b>
C.1: Multiple particle videotrajectory method .....	29
C.1.a: General principle .....	29
C.1.b: Uniform translation of disks .....	36
C.1.c: Random position fluctuations of translating disks.....	41
C.1.d: Circular motion of disks with random angular fluctuations .....	47
C.2: Experimental setup and dynamic analysis of suspension flows .....	50
C.3: Dynamics of density – matched suspensions .....	56
C.4: Dynamics of non density – matched suspensions .....	64
C.4.a: Non isodense suspension, with extra fluid .....	64
C.4.b: Non isodense suspension, without extra fluid .....	73
<b>Chapter D – Concentration Field .....</b>	<b>75</b>
D.1: Experimental technique.....	76
D.1.1: Optical setup.....	78
D.1.2: Detection .....	80
D.1.3: Calibration.....	81
D.1.4: Accuracy, reproducibility.....	83
D.2: Concentration fields .....	84
D.2.1: Density – matched suspension .....	84
D.2.2: Non density – matched suspension .....	89
D.3: Summary .....	97

Appendix D-A: Laser beam and sheet characteristics .....	98
Appendix D-B: Optically measured concentration field in Couette geometry. Compensation for laser sheet non uniformity and attenuation.....	101
Appendix D-C: Rotation invariance.....	106
<b>Chapter E – Normal force balance model: viscous resuspension in a large – gap Couette flow.....</b>	<b>109</b>
E.1: Force balance equations.....	109
E.2: Viscometric function .....	111
E.3: Density matched suspension.....	112
E.3.a: Concentration field.....	112
E.3.b: Orthoradial velocity field.....	114
E.4: Non density – matched suspension.....	115
E.4.a: Concentration field.....	115
E.4.b: Orthoradial velocity field.....	117
E.4.c: Coherence of equations.....	118
E.5: Model and experiments for a density matched suspension .....	120
E.5.a: Power law viscometric functions .....	120
E.5.b: Morris and Boulay viscometric functions.....	126
E.6: Model and experiments for a non density – matched suspension .....	128
E.7: Summary and conclusion.....	136
<b>Chapter F – Single Particle Tracking (SPT).....</b>	<b>138</b>
F.1: Experimental techniques .....	139
F.1.1: “Passive” mode .....	140
F.1.2: Automated tracking system.....	141
F.1.2.a: Experimental setup (active SPT).....	142
F.1.2.b: Servo system performance .....	145
F.1.2.c: A neutrally buoyant tracer in a Newtonian fluid.....	147
F.2: (r, z) trajectories of a “host like” tracer.....	152
F.2.1: in the density – matched system (active mode) .....	152
F.2.2: in a non density – matched system .....	155
F.2.2.1: Passive mode.....	155
F.2.2.2: Active mode .....	158
F.3: Size effects (non density – matched system) .....	162
F.4: Discussion .....	164
F.4.1: Shear – induced particles diffusion.....	164
F.4.2: Loops.....	166
F.4.3: Size effect.....	168

F.5: Summary and conclusions .....	169
Appendix F-A: Servo system .....	171
Appendix F-B: Tracer migration in Newtonian fluid.....	173
<b>Chapter G- Conclusion and prospects .....</b>	<b>174</b>
<b>Chapitre G- Conclusion et perspectives .....</b>	<b>178</b>
<b>Bibliography .....</b>	<b>182</b>



## Acknowledgements

*It is curious that typically the only person who doubts the results of an experimentalist is the experimentalist himself and the only one who believes the results of a theorist is the theorist himself.*

Albert Einstein

*During my PhD work, I had to learn new techniques and methods, make nice investigations and try to contribute to a better understanding of world of granular materials. There were a lot of new thinks for me to conclude, but the most important one is that I could never have done any of this without the support and encouragement from many people.*

*I would like to say a great “thank you” to **Philippe Richetti**, Director of our research laboratory (Centre de Recherché Paul Pascal) for welcoming me and giving opportunity to work in such a wonderful collective. Also thanks to **Corinne Amengual** who helps me with all the paper work concerning my residence in France. I would like to thank **Nadine Laffargue** for her kindness and efficient help for my bibliographic work.*

*I thank **Dr. Guillaume Ovarlez** and **Dr. François Peters** for reviewing this thesis; **Prof. Christophe Ancey** and **Prof. Annie Colin** for agreeing to participate in the thesis committee. Thank you all for dedicating your time to assess my manuscript.*

*I am deeply grateful to my supervisors, **Dr. Bernard POULIGNY** and **Dr. Patrick SNABRE**, for having introduced me into an interesting research field of granular materials. **Bernard**, I appreciate you humour and manner of teaching me a lot of experimental tricks. I will remember all my life that means “what I’m doing now is forbidden, you should not repeat this”. The way as you can teach and innovative ideas help me during these 3 years. **Patrick**, thank you for helping me and remarks that you made during my work. A lot of what I done is of your major support. Your pluggins and software saved my time, and our discussions were of great impact upon my vision on granular materials. I thank them for the guidance, and encouragement, which they provided through their work.*

*I would like to mention members of our team. Thanks to **Besira** for supporting me and give some guidance upon my work and basic knowledge of Matlab. Thanks to **Damien** and **Andie** being kind with me, improving my French. A special mention is to my office colleagues, **Parantap**, who always find a good joke for my results, **Jullien**, our King of the office who can be a great French teacher and for his help with all the French documents and e-mails. I will like to thanks to **Alexandra**, our “petite Nimoise” for encouragements and funny stories that makes me more relaxed during last weeks before the defense.*

*I express thanks to all people from CRPP. I thanks to **Lionel Buisson**, **Pascal Merzeau**, **J.C. Loudet**, **Ahmed Bentaleb** and all CRPP services: “service informatique, mission, gestion, accueil et bâtiment, cellule chimie et instrumentation, atelier mécanique”. Your help makes our ideas come true. Special thanks to **Pascal**, who made my SPT setup fully automated and for “stealing” me opportunity to operate it with the joy stick. Great “Merci” to **Phillipe Barboteau**, **Jean-Yves Juanico** and **Emmanuel Texeir** from mechanic shop who design and always helps me with my Couette cell and other needs. Thanks to **Eric Laurichesse** for support and help me with rheological measurements. Special thanks to **Renaud Vallee**, for showing me how to plan my experiments in such a way to make more than one think. Thank you for introducing in Belgian beer land, showing what sky Nordic is at least more consumptive than Alpine. Thank you for supporting me on fluorescent measurements.*

*The influence of those with whom I worked before coming to CRPP is also important. The supervisors of my master thesis, **Igor Evtodiev and Mihail Caraman**, who has a great impact of choosing me the scientific direction. Also thank to all professors who teach me and colleagues, specially to **Sergiu Anghel**.*

*This work would not have been possible without the support of my Moldavian friends. My deepest gratitude to **Rodica and Igor Ababei**. She was the person who guided me in the unknown world of “thousands” of documents and administrative centres that we should pass before becoming a PhD student and during my study here. Thanks **Igor** for always supporting me, offering ideas and suggestions. I will remember your barbeque here in Bordeaux and your ability to help people. Thanks to **Simona Ungureanu** (Moldavian from Romania), who was my office mate for the last period, most important. Your kindness and delicious cakes makes my life more charming. Thanks deeply to **Diana and Igor Siretanu** who always help me. Thanks to **Igor** for proposing me to come here in Bordeaux to make my PhD. Without you I could not find here such interesting persons. Also I will remember moments when we watched football and played tennis. Thanks to **Diana** for being around me when I need, helps upon French and papers. I appreciate your culinary art and planning abilities. Thanks to **Oleg and Tatiana Palamarciuc, Dmitri and Liuba Mitcov, Sergiu Calancea, Mihail Secu, Alexandru Vreme and Maryna Kuzminska**. You were always around me during my nice or bad moments in Bordeaux. I could always count on you, when I needed help in my research or simple moral support, but also for spending great time together. This, I believe, is the key to getting through a PhD program – having good friends to have fun with and complain to. Special thanks to **Maryna** who supports me a lot, especially when I was stressed writing my manuscript. And thank you for telling to left sometime job and escape in the city, making photo and enjoy the beauty of Bordeaux.*

*Finally, my heartiest thanks are dedicated to my family. I thank to my loving, supportive, encouraging, and patient sister **Olivia** and my parents **Timofei and Lidia**. During PhD I was far away from them and being busy sometime I forget to call. Anyway they always find me even in the lab and encourage continuing started job. Without their eternal support and love I would never made it through this process or any of the hard time in my life.*

***Thank you – Merci à tous – Mulțumesc - Cnacубo***

Octavian BLAJ  
Pessac, 11 July 2012

## Glossary

$\dot{\gamma}$	<i>Shear rate</i>
$\bar{\phi}$	<i>Averaged volume fraction at a fixed altitude over radial gap</i>
$\bar{\phi}$	<i>Averaged volume fraction over all Couette space</i>
$\Delta\vec{r}$	<i>Displacement vector</i>
$a$	<i>Particle radius</i>
$A(u)$	<i>Attenuation of laser light through a distance <math>u</math> inside the granular paste</i>
<b>As</b>	<i>Astigmatic optics</i>
<b>BNE</b>	<i>Brazil nut effect</i>
<b>C(r,z)</b>	<i>Collection efficiency of the imaging optics</i>
<b>C16</b>	<i>n-hexadecane 99.9% (Sigma Aldrich)</i>
<b>CCD</b>	<i>Charged-coupled device</i>
<b>CL</b>	<i>Cylindrical lens</i>
$d$	<i>Couette cell gap (between cylinders)</i>
$d'$	<i>Plate-plate gap</i>
$f$	<i>Fluorescence efficiency of the immersion fluid</i>
$f(\phi)$	<i>Ratio between normal and shear viscosity</i>
$g$	<i>Gravity</i>
$G(x)$	<i>Function based on the viscometric function <math>f_{MB}(\phi)</math></i>
$H$	<i>Height of the Couette cell</i>
$h_0$	<i>Height of the granular sediment in Couette cell</i>
$I$	<i>Intensity of transmitted light</i>
$I_0$	<i>Intensity of incident light</i>
$k$	<i>Ration between outer and inner radii</i>
<b>LP</b>	<i>Long pass filter</i>
<b>MMH</b>	<i>Mobile microscope head</i>
<b>MRI</b>	<i>Magnetic resonance imaging</i>
$n$	<i>Refractive index</i>
$N$	<i>Number of events</i>
<b>OF</b>	<i>Optical fiber</i>
<b>OI</b>	<i>Olearium</i>
$p$	<i>Fluorescence efficiency of the particles' material (PMMA)</i>
$P$	<i>Power</i>
<b>PMMA</b>	<i>Poly(methyl methacrylate)</i>
$r$	<i>Radius from central axis of rotation</i>
$R_{in}$	<i>Inner cylinder radius</i>
$R_{out}$	<i>Outer cylinder radius</i>
$r_c$	<i>Critical radius</i>
$Re$	<i>Reynolds number</i>
<b>RM</b>	<i>Rotating mirror</i>
<b>ROI</b>	<i>Region of interest</i>
$S$	<i>Signal</i>
<b>S150</b>	<i>Immersion oil (Sigma Aldrich)</i>
<b>SPT</b>	<i>Single particle tracking</i>
$t$	<i>Time</i>
<b>T (C)</b>	<i>Temperature</i>
$Ta$	<i>Taylor number</i>
$V_{ac}$	<i>Sinusoidal voltage</i>
$w_0$	<i>Beam-waist</i>
$x$	<i>Distance (direction)</i>
$z$	<i>Altitude</i>
$\delta P$	<i>Power fluctuation</i>
$\delta T$	<i>Temperature fluctuations</i>
$\Delta\rho$	<i>Density difference</i>
$\eta$	<i>Dynamic viscosity</i>
$\eta_0$	<i>Dynamic viscosity of the interstitial fluid</i>

$\eta_n$	<i>Normal viscosity</i>
$\eta_r$	<i>Relative viscosity (<math>\eta/\eta_0</math>)</i>
$\eta_s$	<i>Shear viscosity</i>
$\theta$	<i>Angle in radians</i>
$\lambda$	<i>Wavelength</i>
$\lambda_i$	<i>Viscometric coefficients</i>
$\nu$	<i>Kinematic fluid viscosity</i>
$\Pi_{\text{ref}}$	<i>Reference plan</i>
$\rho$	<i>Density</i>
$\Sigma_{zz}$	<i>Vertical component of stress tensor</i>
$\tau_{\text{mig}}$	<i>Migration time</i>
$v_\theta$	<i>Azimuthal velocity</i>
$\Phi$	<i>Volume fraction</i>
$\varphi$	<i>Ratio between <math>\Phi/\Phi_m</math></i>
$\Phi(\mathbf{r})$	<i>Concentration profile</i>
$\varphi_c$	<i>Critical reduced volume fraction</i>
$\phi_m$	<i>Maxim volume fraction</i>
$\phi_{\text{RCP}}$	<i>Random close packing</i>
$\phi_{\text{RLP}}$	<i>Random loose packing</i>
$\omega$	<i>Angular velocity</i>
$\Omega_{\text{off}}$	<i>Offset</i>
$\Omega_{\text{in}}$	<i>Angular velocity of inner cylinder</i>
$\Omega_{\text{out}}$	<i>Angular velocity of outer cylinder</i>

## Chapter A - Introduction

### Introduction (Française)

Dans cette thèse, nous étudions l'écoulement et les structures de matériaux constitués de grains solides en très forte concentration dans un fluide visqueux. Les grains sont assez gros (100 micromètres, typiquement) pour n'être pas browniens (c'est-à-dire assez gros pour n'être pas agités par la température). Suivant le cas, on parle de suspensions non-colloïdales denses, de matériaux granulaires mouillés, ou de « pâtes granulaires », voire de « boues ».

Un exemple très ordinaire de ce genre de matériau est le sable gavé d'eau sur lequel nous marchons en bordure de plage. Dans les matériaux de construction, l'exemple type de pâte granulaire est le béton frais, qui contient une multitude de grains de toutes tailles. Ces grains doivent être mélangés en proportions convenables, ce qui implique une étape de malaxage. Sur chantier, le béton frais auto-compactant est transporté dans des tuyaux, et déposé dans des coffrages. Bien entendu, il est important que la composition reste homogène, jusqu'à l'étape finale du processus.

En principe, cette exigence ne peut pas être satisfaite complètement, car l'écoulement lui-même agit directement sur la répartition des grains dans l'espace, créant des zones de fortes et basses concentrations. L'écoulement dans un tuyau crée un cisaillement, réparti de façon plus ou moins compliquée dans l'espace. Lorsque le matériau contient des grains différents, par exemple des gros et des petits, il arrive que le cisaillement sépare partiellement les différentes espèces. Ce phénomène très général en physique des granulaires est appelé « *ségrégation induite par le cisaillement* ». Dans l'application courante, par exemple dans le béton, l'effet de ségrégation est faible et sans grande conséquence, mis à part à proximité des torons en acier; mais le défaut d'homogénéité peut être très gênant pour des matériaux de très haute performance. On rencontre des problèmes similaires dans le cas des propergols solides, qui au départ sont aussi des pâtes granulaires, et pour lesquels l'exigence d'homogénéité est très sévère.

La ségrégation est un aspect particulier d'un problème qu'on peut énoncer de façon plus générale. Calculer l'écoulement d'une pâte granulaire implique de répondre à deux questions : typiquement, quels débits peut-on obtenir et comment la composition du matériau évolue-t-elle en conséquence de l'écoulement ? Dans la pratique, on aimerait disposer d'une théorie universelle constituant une « *mécanique des pâtes granulaires* », qui permettrait de calculer les écoulements et les répartitions des différentes espèces de grains dans toutes les conditions expérimentales.

A l'heure actuelle, les connaissances dont nous disposons sont loin de répondre à cet objectif. On sait grossièrement décrire certains écoulements simples, pour des systèmes monodisperses, c'est-à-dire contenant des particules sphériques de même taille, dans un fluide Newtonien. On fait l'hypothèse d'un fluide effectif, qui consiste à ignorer la nature particulaire de la structure, et on formule un problème à deux champs couplés : une fraction volumique de particules  $\Phi(\mathbf{r}, t)$  et un unique champ de vitesse  $v(\mathbf{r}, t)$ , dépendant de l'espace  $\mathbf{r}$  et du temps  $t$  [Nott and Brady 1994, Morris and Boulay 1999, Lenoble *et al.* 2005, Boyer *et al.* 2011]. On parle de « *migration* » pour désigner le fait que le couplage vitesse-concentration aboutit à ce que les particules (et donc  $\Phi$ ) se répartissent de manière non uniforme dans le fluide. Les propriétés rhéologiques du fluide sont représentées par le système de forces, tangentielle et normales, développée par le système de particules en réponse à un cisaillement ( $\dot{\gamma}$ ). Dans le régime visqueux, ces forces sont proportionnelles à  $\dot{\gamma}$ , et les préfacteurs -ou coefficients viscométriques- associés sont des fonctions de  $\Phi$  [Lemaitre *et al.* 2009]. On résout le problème de l'écoulement en réalisant l'équilibre des forces visqueuses avec les contraintes appliquées. Cette représentation très simplifiée est efficace en ce qu'elle permet de reproduire certaines des observations expérimentales, mais les résultats des calculs dépendent fortement des formes adoptées pour les fonctions viscométriques. A l'heure actuelle, il existe des conflits d'interprétation entre les différents types d'expérience, et l'unanimité n'est pas faite sur les formes de ces fonctions. Une formulation alternative est basée sur le mécanisme de diffusion induite par le cisaillement [Leighton and Acrivos 1987]. A cause des multiples chocs échangés avec leurs voisines, les particules ne suivent pas les lignes de l'écoulement moyen. L'effet de ces collisions accumulées ressemble au mouvement brownien des molécules dans un fluide à température finie. Dans ce cadre, on décrit le champ de concentration dans l'écoulement par un équilibre de flux, qui représentent la diffusion des particules en réponse aux gradients de concentration et de cisaillement [Phillips *et al.* 1992, Mills et Snabre 1995]. En ajoutant une dépendance à la courbure des lignes de courant, on arrive à une formulation analogue de celle du modèle d'équilibre des forces. Ici aussi, les résultats des calculs dépendent fortement des ingrédients adoptés pour les différents termes de flux. En particulier, les données manquent quant à la diffusion d'une particule en régime de forte concentration [Meunier et Bossis 2008].

Dans la grande majorité de ces travaux, on ajoute à l'hypothèse de monodispersité celle d'une gravité nulle. Cette condition est assurée dans les expériences en choisissant un fluide d'immersion dont la densité coïncide avec celle des particules. Les systèmes réels, évidemment, ne sont ni isodenses, ni monodisperses. En conséquence, les particules ont tendance à sédimenter. Le cisaillement a pour effet de re-suspendre partiellement les

particules, de les répartir différemment (migration) et de façon différenciée (ségrégation). Seulement quelques tentatives ont été faites pour généraliser les concepts évoqués plus haut pour décrire la ségrégation, basées essentiellement sur la différence des coefficients de diffusion de grosses et petites particules dans un mélange [Mehri thesis 2001, Shauly *et al.* 1998, Krishan *et al.* 1996]. Aucune n'inclut le rôle de la gravité, à notre connaissance.

Les travaux que nous présentons dans ce mémoire sont une – modeste – contribution à quelques unes des questions que nous venons d'énoncer. Nous aborderons quelques points sur les suspensions isodenses monodisperses, d'autres sur les systèmes polydisperses et sensibles à la gravité. Ces travaux s'appuient fortement sur les recherches entreprises par le groupe du CRPP sur la ségrégation depuis le début des années 2000. Historiquement, ces travaux ont commencé dans le cadre d'une collaboration avec la Société Nationale des Poudres et Explosifs (SNPE) et avec le Centre National d'Etudes Spatiales (CNES) sur le thème des propergols solides. Ces propergols sont en fait une catégorie particulière de matériaux granulaires polydisperses, susceptibles de ségréger sous cisaillement. Un matériau de laboratoire, transparent optiquement, a été élaboré pour représenter les propriétés essentielles (au sens de la rhéologie) de la pâte propergolique. Les expériences sur ce matériau ont permis de bien mettre en évidence la ségrégation entre grosses et petites particules et de mesurer des paramètres importants dans les conditions académiques du laboratoire, dans des géométries standard de cisaillement (disques parallèles et cellule de Couette). Des connaissances de principe ont pu être acquises sur les écoulements du matériau modèle et comment la ségrégation « s'appuie » sur le phénomène de localisation de l'écoulement [Barentin *et al.* 2004, Lenoble *et al.* 2005, Plantard *et al.* 2006].

La pâte modèle de ces expériences est faite de particules sphériques de polyméthacrylate (PMMA) dans une huile d'indice de réfraction adapté à celui du PMMA ( $n= 1.48$ ), ce qui assure la transparence et permet de sonder le système sous écoulement par des moyens purement optiques. Des formulations existent pour le fluide d'immersion, qui peut-être isodense du PMMA ( $1.18 \text{ g/cm}^3$ ), ou de densité inférieure ( $0.78 \text{ g/cm}^3$ ), auquel cas le système est sensible à la gravité. Nous présentons dans la suite de ce mémoire plusieurs travaux expérimentaux sur des mélanges dans ces deux versions. Toutes ces expériences utilisent un même modèle de cellule de Couette, elle-même transparente et à cylindres contra-rotatifs. Les données techniques de base, sur les suspensions et les dispositifs de cisaillement, sont présentées dans le chapitre B.

Dans les chapitres C, D, et E, nous aborderons une série de questions directement en relation avec le modèle de fluide effectif, dans la version « simple » où on réduit la description de l'écoulement à sa seule *composante primaire*, c'est-à-dire, dans la cellule de

Couette, à la vitesse orthoradiale. Nous verrons que les expériences apportent des informations précises et nouvelles sur l'hydrodynamique à l'échelle des particules mais aussi à l'échelle de la cellule en relation avec les fonctions viscométriques, pour le système monodisperse. Pour obtenir ces données, nous avons développé deux méthodes de mesure nouvelles, l'une concernant les déplacements spatiotemporels des particules (video-trajectographie) et l'autre le champ de concentration, par photométrie de fluorescence. Les aspects techniques de ces méthodes sont détaillés respectivement dans les chapitres C et D. L'exploitation des données est l'affaire du chapitre E : nous nous basons sur l'équilibre des forces normales de Morris et Boulay [Morris et Boulay 1999], dont nous rappelons les équations de base, et présentons la méthode de résolution que nous avons adoptée, en particulier pour le système non isodense. A notre connaissance, les résultats numériques que nous présentons sur la re-suspension visqueuse en écoulement de Couette à large gap, sont nouveaux.

Nous verrons que les expériences présentées dans le chapitre C apportent des informations sur d'autres points, en particulier la diffusion des particules en fonction de la concentration locale, jusque très près de la fraction de blocage. La méthode permet également d'examiner les vitesses des différentes sortes de particules dans un système non monodisperse, et donc de tester l'hypothèse de champ de vitesse unique inhérente au modèle de fluide effectif, par opposition aux modèles qui distinguent les écoulements des particules et du fluide d'immersion [Jackson 2000, Ouriemi *et al.* 2009, Lhuillier 2012].

On trouve dans la littérature plusieurs travaux décrivant des phénomènes de migration dans un tambour tournant, c'est-à-dire un cylindre d'axe horizontal, partiellement rempli avec une suspension non colloïdale. Dans ce cas, l'écoulement primaire a lieu perpendiculairement à l'axe du tambour. Ces travaux montrent des effets spectaculaires de migration, et démontrent l'existence de *courants secondaires* ou différentiels associés [Timberlake et Morris 2002, Jin et Acrivos 2004, Govindarajan *et al.* 2001, Lipson et Seiden 2002, Lenoble chapitre 2]. Marie Lenoble a, de son côté, cherché à mettre en évidence des courants secondaires en géométrie Couette, avec le système monodisperse non isodense. Elle a utilisé pour cela un dispositif de poursuite de particule construit au laboratoire. Le principe est de suivre un traceur unique, à la manière d'une « filature », et de restituer sa trajectoire, sur plusieurs heures. La poursuite est réalisée de la façon suivante : un microscope muni d'une caméra est pointé vers la particule ; celle-ci est maintenue dans le champ du microscope et dans le plan de mise au point en pilotant deux translations et les vitesses des deux cylindres de la cellule de Couette. Les corrections appliquées sont enregistrées, ce qui permet de reconstituer la trajectoire du traceur. Cette version du montage n'était qu'un démonstrateur,

qu'il fallait piloter à la main. L'exercice était très difficile, limitant la poursuite à quelques minutes ordinairement (20 mn, au mieux). Malgré tout, M. Lenoble a pu enregistrer des portions de trajectoires, montrant des amorces de recirculation radiale. L'équipe du CRPP a par la suite fait évoluer le montage, pour l'automatiser, et j'ai participé à la mise au point de la version finale, que j'ai ensuite exploitée. Ce travail est présenté dans le chapitre F. Le chapitre comporte une large part technique, pour décrire le dispositif et les tests effectués. Nous présentons ensuite les résultats de nos enregistrements, qui révèlent les trajectoires tridimensionnelles de traceurs dans la cellule de Couette, pour les systèmes isodense et non isodense, et, dans ce deuxième cas, pour des tailles différentes de traceurs.

Les résultats essentiels de la thèse sont résumés dans le dernier chapitre (G), qui présente également quelques pistes pour la suite.

Le corps du document est rédigé en Anglais, qui a été ma langue de travail tout au long de cette thèse. Le mémoire utilise largement les textes des articles publiés ou en cours de rédaction, avec quelques compléments techniques sous forme d'appendices aux différents chapitres.

## Introduction (English)

This Dissertation is about flows and structures of so-called “dense non colloid suspensions”. Other names used in the literature are “wet granular materials”, “granular pastes”, or “slurries”. These names are not strictly equivalent, but in general they all deal with materials composed of particles large enough to be non-Brownian, immersed inside a viscous fluid, most often at high concentration. Wet sand at the beach and fresh concrete are very common examples of granular pastes. Solid propellants, involved in space and military technologies, initially are prepared as granular pastes. Self compacting concrete and solid propellants are polydisperse pastes, meaning that they contain grains of different sizes. Of course the overall solid concentration ( $\Phi$ ) and those of the different categories of grains ( $\Phi_i$ ) must be in appropriate proportions for the material to perform well. Processing these materials in general involves shear, at the initial step (mixing) and later when the paste is transported through pipes and poured into a reservoir. In demanding applications, where preserving the composition of the material is critical, a problem may arise due to the fact that shear in general modifies the spatial repartition of grains. As a consequence, the composition of the material becomes non homogeneous. The modification of  $\Phi$  is called “shear-induced migration”, while differential migration is called “shear-induced segregation”. In simple words, if we start with e.g. a homogeneous mixture of  $i$  and  $j$  categories of grains, say with  $\Phi_i = \Phi_j$  everywhere, we may end with  $\Phi_i > \Phi_j$  somewhere, and reversely in another region.

Predicting the amounts of such phenomena in given conditions demands calculating coupled characteristics of flows and concentrations. The solution of this problem should rely on a general hydrodynamics theory of granular pastes, which is far from available yet. However a simplified form of the problem has been addressed by several research teams, in the case of monodisperse suspensions. The particles are spherical and of same size, and the material is considered as an effective fluid, meaning that the grainy structure is spatially averaged. Local space and time characteristics of the material then amount to a couple of continuous fields, the concentration  $\Phi(r,t)$  and a unique velocity  $\mathbf{v}(r,t)$  [Nott and Brady 1994, Morris and Boulay 1999, Lenoble *et al.* 2005, Boyer *et al.* 2011]. Rheological properties of the suspension are represented by a set of forces, namely shear and normal stresses. In the viscous limit, the forces are proportional to the local shear rate  $\dot{\gamma}$ , with prefactors, the viscometric functions, that only depend on  $\Phi$  [Lemaitre *et al.* 2009]. In the stationary regime, all forces, including external stresses, balance each other, a condition which provides equations that can be solved for  $\Phi$  and  $\mathbf{v}$ .

The force balance model, in different versions, has been successful in reproducing experimental observations [Morris and Boulay 1999, Lenoble *et al.* 2005, Boyer *et al.* 2011], but computed characteristics of the flows depend much on properties of the chosen viscometric functions. As a matter of concern, conflicting forms have been proposed based on different kinds of experimental observables.

An alternate description of migration is based on the so-called « shear-induced diffusion » mechanism [Leighton and Acrivos 1987a]. Because of many collisions with neighbours, particles' trajectories do not coincide with average flow streamlines. Cumulating collisions make a particle undergo a random motion, much like the Brownian motion in thermal systems. In this context, the concentration field in a flowing suspension can be found from a balance of diffusion fluxes, due to gradients in concentration and shear rate [Phillips *et al.* 1992, Mills and Snabre 1995]. Adding a dependence on the local curvature of streamlines yields results analogous to those of the force balance model. Again calculated concentration fields depend on the choices made for the prefactors of the fluxes. A difficulty arises with high concentrations, because diffusion laws are not well known in this limit [Meunier and Bossis 2008].

Most experimental and theoretical works only deal with isodense suspensions, i.e. situations where the densities of the immersion fluid and of the solid particles are equal ( $\Delta\rho = 0$ ). Thus the action of gravity may be ignored, an appreciable simplification. Real systems obviously are not isodense and not monodisperse either. Consequently “heavy” particles ( $\Delta\rho > 0$ ) tend to sediment. Sedimentation is counter acted by shear, which tends to re-suspend the particles. Resuspension includes migration and, in a polydisperse system, generates segregation. Only a few attempts have been made at generalizing the above mentioned models to such situations [Mehri thesis 2001, Shauly *et al.* 1998, Krishan *et al.* 1996]. The role of gravity has not yet been addressed, to our knowledge.

In the following, we address a few points among the above problems through a series of mainly experimental works. Some of them are about monodisperse isodense suspensions, and some about non isodense ones, with a part dedicated to polydispersity. These works are sequels of an earlier research program led by the CRPP group about segregation. The root of this program was a research contract with Société Nationale des Poudres et Explosifs (SNPE) and Centre National d'Etudes Spatiales (CNES) about segregation effects in solid propellants. Experiments carried out in CRPP used model suspensions that were supposed to represent the main mechanical characteristics of the propellant pastes. The suspensions were made of acrylate (PMMA) spheres inside a fluid (different kinds of oil) whose refractive index was

matched to that of particles. Thus the samples were transparent, and optical means could be used to investigate their behaviors under shear. However, densities were not matched, meaning that the systems were sensitive to gravity. Samples were sheared in standard geometries, between parallel disks and between coaxial cylinders (Couette cell). Very intense segregation effects were evidenced with non isodense bi-modal samples, containing small and big particles. Based on the observations, the researchers drew the conclusion that segregation was closely related to shear localisation, which was about the same in monodisperse and bi-disperse systems [Barentin *et al.* 2004, Lenoble *et al.* 2005, Plantard *et al.* 2006]. In her thesis, Marie Lenoble [Lenoble thesis 2005] also explored cases of nearly isodense ( $\Delta\rho \cong 0$ ) suspensions, and even investigated the case of creaming particles ( $\Delta\rho < 0$ ).

Our own experiments, reported in the chapters hereafter, have been carried out with suspensions of same compositions as in [Lenoble thesis 2005], in the isodense and non-isodense versions; and we used a unique kind of shear cell, namely a large-gap Couette cell with contra-rotating cylinders. Basic characteristics of the suspensions and of the shear devices are given in chapter B.

Chapters C, D, E are mainly about *primary flows*, meaning that only the orthoradial (or azimuthal) component of the velocity field ( $v_\theta$ ) within the Couette cell is measured and considered in the data analyses. Chapter C specifically deals with primary flow velocimetry (average  $v_\theta$  and angular fluctuations in the velocity direction), while chapter D is about the concentration field ( $\Phi$ ), i.e. shear-induced migration in the steady state regime. The  $v_\theta$ , diffusion coefficient  $D_{\theta\theta}$  in the flow direction and  $\Phi$  data were obtained by means of measurements techniques that we specially developed for the purpose of this work, namely *multiparticle video-trajectory* (MPVT) and *concentration photometry* (CP). Both techniques are described in details in chapters C, D, respectively. While the main body of chapter C is about monodisperse suspensions, we also report experiments involving particles of different sizes. These experiments were aimed at evidencing size dependent velocities and thus may be viewed as tests of the effective fluid picture (conversely to two-phase schemes [Jackson 2000, Ouriemi *et al.* 2009, Lhuillier 2012]).

The data about  $v_\theta$  and  $\Phi$  are jointly analysed in Chapter E, in the frame of the force balance model. As we will see, the experimental data yield novel information about viscometric functions, for the monodisperse system, and the model satisfactorily accounts for resuspension profiles in the large-gap Couette cell.

Works have been reported in the literature about migration in rotating drums, i. e. horizontal circular cylinders rotating around their symmetry axis. In a typical experiment, the

cylinder is partially filled with a suspension, and rotation results in regions of high concentration in particles coexisting with nearly pure fluid zones. In such geometries, the primary flow occurs in vertical planes, perpendicular to the axis. Interestingly, observations have revealed that migration occurred concomitantly with secondary flows, i.e. with non zero axial velocities, or differential flows (distinctly different particle and immersion fluid velocities) [Lenoble thesis chapter 2, Timberlake and Morris 2002, Jin and Acrivos 2004, Govindarajan *et al.* 2001, Lipson and Seiden 2002]). Secondary flows, -otherwise called re-circulations- in a Couette shear cell consist in meridian motions (within  $(r, z)$  plane, in cylindrical coordinates). Lenoble reported observations of such motions with the PMMA suspension [Lenoble thesis 2005]. However data were limited to rather short portions of the meridian trajectories, not enough to provide clear information about the shape of the re-circulations. To observe meridian motions, Lenoble used a special version of the Couette cell setup that allowed her to track a fluorescent tracer in 3 dimensions. Essentially a video-microscope is aimed at the tracer, towards the Couette cell axis. The principle of the experiment is to keep the image of the moving tracer near the centre of the video frame and in focus. Meeting this condition was made possible by permanently driving the position of the microscope radially and vertically, and simultaneously driving the repartition of angular velocities between the contra-rotating cylinders. Driving the 3 degrees of freedom was performed “by hand”, by means of two joysticks. Lenoble was successful in operating the setup, but typical runs were limited to a few minutes before the tracer was lost. The setup was later improved and transformed into a fully automated version (ASPT, for “*automated single particle tracking*”). Experiments which I carried out with ASPT are the matter of chapter F. The chapter starts with a detailed description of the setup, and reports results of tests done to validate the technique. We afterwards turn to suspensions, and show records of secondary motions in the isodense and non-isodense systems. A part of the work is dedicated to size effects, i.e. secondary motions of large and small intruders.

Essential results of these works are gathered in chapter G, together with a few suggestions for future investigations.

Note: large parts of the dissertation are taken from articles, either published or to be published. Complementary information on technical points is given as appendices, at the end of the chapters.

## Chapter B – Materials and Couette shear cell

In this chapter, we give characteristics of the materials, procedures and devices that were common to all experiments carried out in the thesis. What is specific to each experiment is described in the corresponding chapters.

### B.1: PMMA spheres

As in the previous experiments of the group [Barentin *et al.* 2004, Lenoble *et al.* 2005, Plantard *et al.* 2006] we use polymethylmethacrylate (PMMA) spherical particles, with diameters  $2a$  ranging from 20 to 600  $\mu\text{m}$ . Most of the experiments involve diameters between 180 and 200  $\mu\text{m}$  (Fig. B.1). Density and refractive index of PMMA are  $\rho = 1.18 \text{ g/cm}^3$  [<sup>1</sup>] and  $n = 1.4947$  at 532 nm [<sup>1</sup>], respectively. The above range of particle size was obtained by sieving from a batch provided by Atoglas. Sieving was performed “by hand”, preferably to automatic sieving, which was observed to generate electrostatic interaction between particles. A problem may arise from a high degree of humidity, which makes particles sticky. Consequently, particles were heated in a climatic chamber at a temperature of 40°C and relative humidity of 10% during few days. It was observed that heating particles provides a better sieving, resulting in lower polydispersity. We made estimates of the distribution of particle sizes using two methods: usual optical microscopy and scanning electron microscopy. Results obtained from a collection of 160 particles are displayed in Fig. B.1. We noticed that some particles were clearly not spherical, but these are very few, say less than 1 among 1000 particles.

### B.2: Immersion fluids; index- and density – matching

To obtain a transparent granular medium, particles are immersed in a liquid which has the same index of refraction as PMMA.

In most of our experiments we used a mixture of two liquids: Immersion Oil (Sigma Aldrich S150) and n-Hexadecane 99.9% (Sigma Aldrich C16), mixed in a mass proportion of 73% (S150) and 27% (C16). These values were found to give a refractive index very close to that of PMMA spheres at room temperature for green light, corresponding to the 532 nm or 514 nm laser lines. Note that **this liquid mixture does not provide density matching**: the

---

<sup>1</sup> [http://en.wikipedia.org/wiki/Poly\(methyl\\_methacrylate\)](http://en.wikipedia.org/wiki/Poly(methyl_methacrylate))

difference between solid and liquid densities is positive ( $\Delta\rho=0.3 \text{ g/cm}^3$ ), meaning that the particles accumulate into a dense sediment in absence of shear.

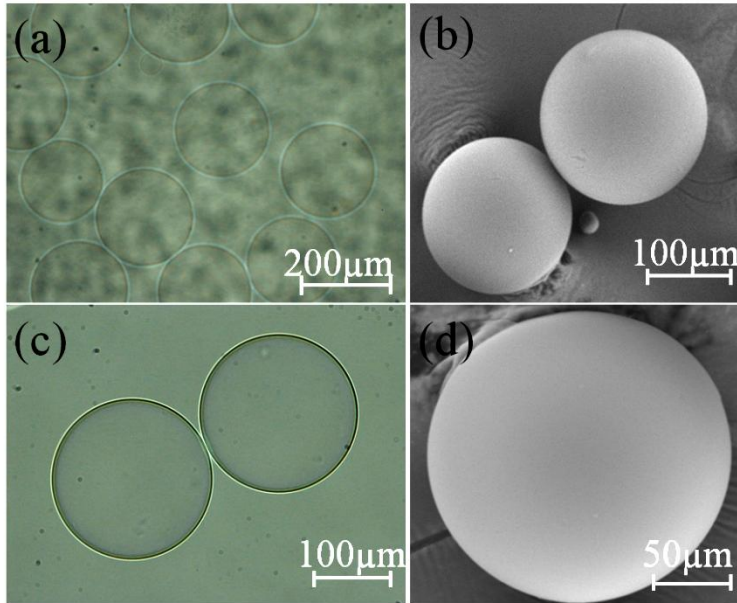


**Fig.B.1** *Examples of granular materials used. PMMA 180-200 $\mu\text{m}$  particles observed in (a,c) optical microscopy and (b,d) Scanning Electron Microscopy*

Transparency of the granular paste can be achieved through at least 1 cm, provided that temperature fluctuations are limited to  $\pm 1^\circ\text{C}$ ; see Fig. B.3.

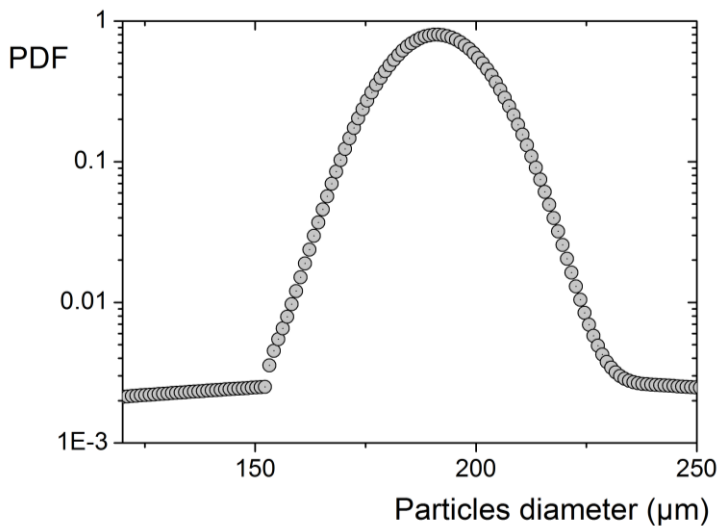


**Fig.B.2** *Result of sieving between 180 and 200  $\mu\text{m}$ . PMMA particle size distribution (in semi-log representation). Average diameter  $\approx 198 \mu\text{m}$*

As a criterion for quality of index matching, we prepare a 1 cm thick sample of the granular paste, with a solid fraction about 50 %, inside a Petri dish. We observe a text written with a 14 font size through the sample. Index matching is deemed “excellent” when we can read the text while the paper is at about 20 cm below the sample.

The C16-S150 liquid was tested in rheometry with an AR1000 (TA Instruments) instrument, under shear rates ranging from 0.03 to 2800 s<sup>-1</sup>, and was found Newtonian, with a viscosity of  $\eta_0 = 20$  cP at room temperature.

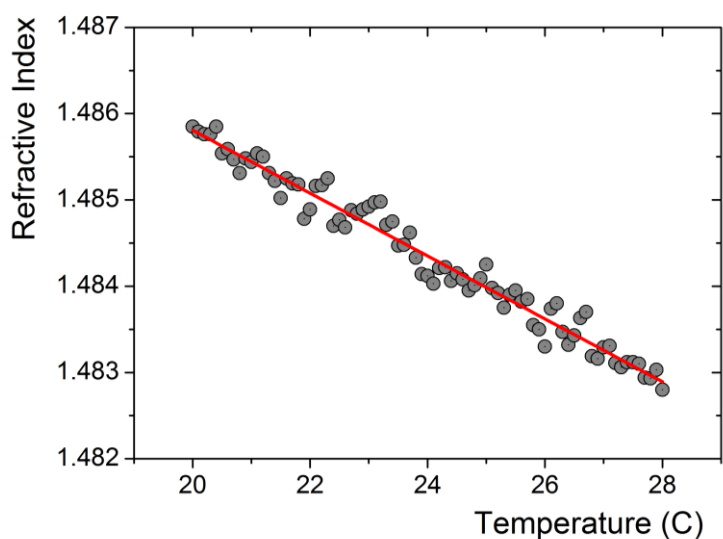


**Fig.B.3** Temperature variation of the refractive index of the C16-S150 mixture, measured at 656 nm with an ARAGO refractometer (Cordouan Technologies).

A few experiments were carried out with a mixture that provides **both density and refractive index matching** (for a review of this problem, see [Wiederseiner et al. 2011](#)). This was achieved using three special liquids from Cargille Laboratories, which we denote A, B, C. Corresponding indices and densities are given in the table below, for the D sodium line wavelength (589.29 nm) and at 25 °C.

	A	B	C
$n_D$	1.403	1.518	1.574
$\rho$ (g.cm <sup>-3</sup> )	1.901	0.919	1.006
Volume fractions (%)	27.3	72.7	
Volume fractions (%)	51.3		48.7

**Table B.1** Cargille liquids characteristics, at 25 °C.

In our procedure, we start with binary mixtures, AB and AC, with the volume fractions indicated in Table 1. Both are approximately index-matched with the particles, but one is “a bit light” ( $\rho_{AB} < \rho_{PMMA}$ ) and one is “heavy” ( $\rho_{AC} > \rho_{PMMA}$ ). Ultimately we add a small amount of AC to AB, to reach a state by which particles float within the liquid with no marked tendency to either sediment or cream. Limiting the observation to about 30 mn, we estimate

that density matching is achieved within  $\Delta\rho=2\cdot 10^{-3}$  g/cm<sup>3</sup> (corresponding to 2 $\mu$ m/s to for the particle settling velocity). Temperature must be kept constant to within one degree.

### B.3: Fluorescent tracers and fluorescent immersion fluids

Fluorescent tracers are made from the PMMA particles, using the procedure described by Lenoble [Lenoble thesis 2005], with diameters ranging from 20 to 600  $\mu$ m. Basically, the particles are dyed with a laser fluorophore, either sulforhodamine B (SRB) or rhodamine 6G. In this work, we used rhodamine 6G perchlorate laser grade 99% produced by Acros Organics. When excited by laser green light, at 532 nm (YAG) or 514 nm (Argon ion), the dye emits an orange light that can be collected through a long pass filter. A cheap and convenient filter that we most often use in the experiments is made from a plastic panel used for protection from laser light. Such panels completely block the green light and have large transparency for orange and red wavelengths.

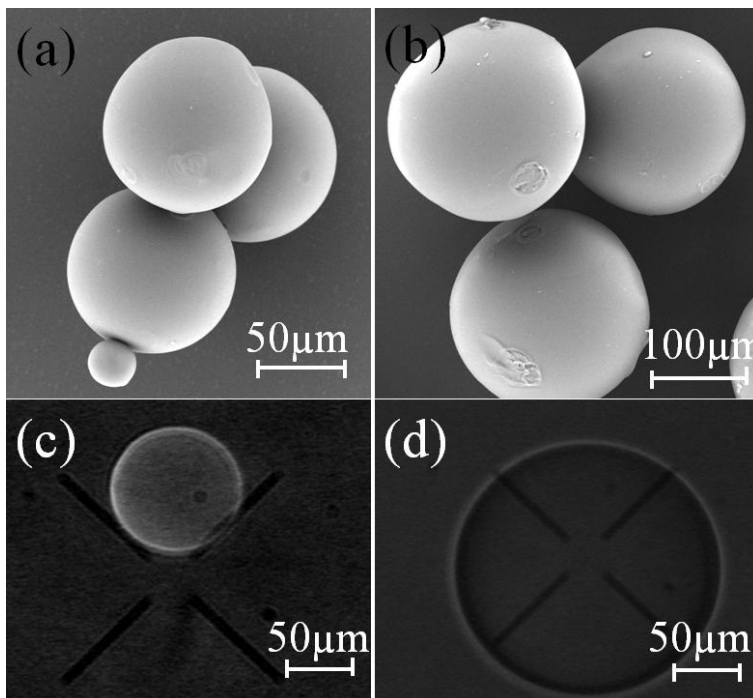


**Fig.B.4** *Fluorescent tracers of different sizes seen in electron microscopy (a, b) and through an optical fluorescence microscope (c,d). Note the damages on some of the particles*

*Preparation procedure:* We first dissolve 0.07g of rhodamine 6G in 200 mL of pure ethanol. The solution is vigorously stirred at 35<sup>o</sup>C for 45 minutes. Next we add 3-4g of particles (the future tracers) and continue mixing for about 15 minutes, with moderate stirring. This time interval was found to be sufficient for the dye to impregnate the particles. It is not advisable to greatly increase impregnation, as this may seriously damage the particle surfaces,

inducing cracks and possibly making the tracers sticky. Particles are separated from the solution thru a paper filter, and rinsed with water (Millipore MilliQ water). Ultimately the stack of dyed particles is placed into a climatic chamber at 40-45°C for a few days, for complete drying. Fig. B.4 shows tracers of different sizes prepared using this procedure. In general, the dried particles slightly adhere to each other, making an aggregate that we gently break using a spatula. When immersed into the C16-S150 or Cargille mixture, and illuminated by a green laser beam, the tracers show a nice fluorescence, and no discernible tendency to stick to each other. However, the amount of fluorescence is far from constant among particles. This dispersion of fluorescence intensity is not a big problem, as long as the tracers are used to visualize motions in the granular sample. Conversely, there is a severe problem if the tracers are used to evaluate concentrations fields: the dispersion causes a statistical error that becomes unacceptably large when high spatial resolution (say within a millimeter) is looked for.

An important requirement in the use of fluorescent tracers is that *the fluorophore must remain with the particles*, meaning that it should not get dissolved into the immersion fluid. This requirement is met by rhodamine in our systems: we checked that the fluid around the tracers never got red-fluorescent, even after months of storage. However note that the immersion fluid in general has a weak direct (with no dye) fluorescence, but it is in general negligible compared to that of the tracers.

In experiments dedicated to measuring *concentration fields* (chapter D), we use a *fluorescing immersion fluid*. Here the requirement is opposite to that for tracers: we want the fluorophore to be dissolved in the fluid, and impregnation through the particles' surfaces is forbidden. We made tests with different dyes: two of them are illustrated in Fig. B.5. below. The panel at left shows what happens with quantum dots (Evidentech Q540) in C16-S150, seen through a fluorescence microscope. The dye gives a nice fluorescence but a bright layer is clearly visible on the particle periphery, indicating that the dye indeed accumulates on or through the particle surface. Quite differently, the panel at right shows what we obtained with FLUORESCENT YELLOW 131SC provided by Keystone Europe Ltd, an oil soluble fluorophore provided by Sigma-Aldrich, still in C16-S150. In this case, the characteristic side peaks of panel (a) are absent, indicating that the dye does not interact with PMMA. The behavior is similar with the Cargille fluid mixture. We selected this dye for the concentration measurements. We used it in some of the videotrajectory experiments as well, since velocities can be measured either from tracers or using the immersion fluid fluorescence (chapter C).

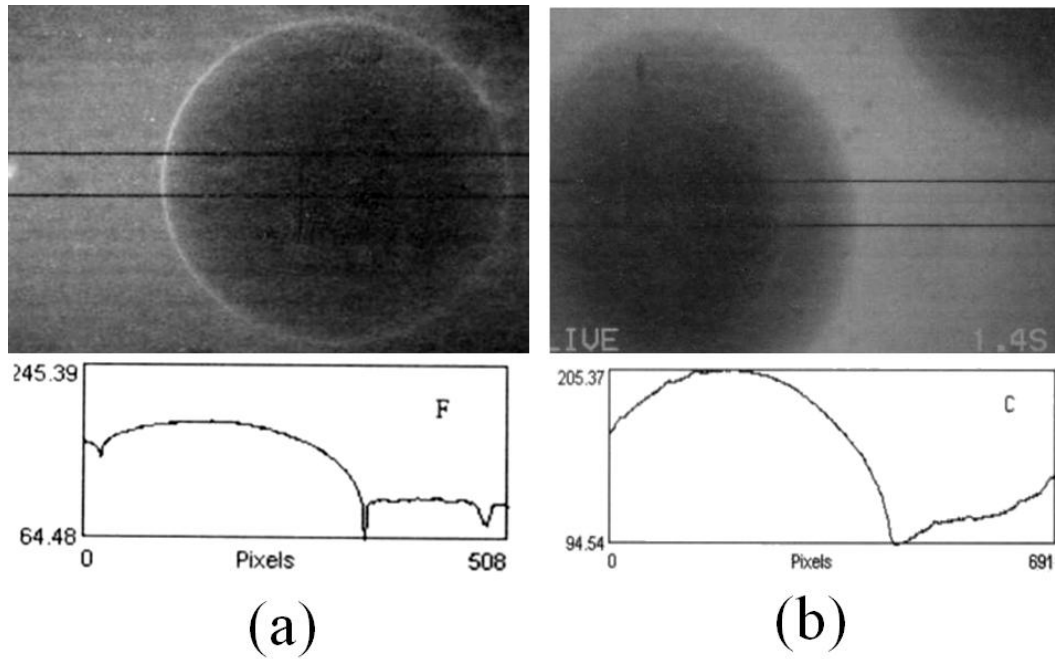


**Fig.B.5** Making the immersion fluid (C16-S150) fluorescent. (a): with quantum dots (Evidentech Q540); excitation at 436 nm. (b): with FLUORESCENT YELLOW 131SC; excitation at 546 nm. The quantum dots are soluble in the oil, but accumulate on the surfaces of the particles. This can be seen directly on the fluorescence image, and is confirmed by the grey level profile, at bottom. Conversely, the FLUORESCENT YELLOW 131SC dye does not accumulate on particle surfaces. The grey level profile corresponds to what is expected for a transparent non fluorescent spherical particle.

#### B.4: Two-motor transparent Couette cell

We used two identical 2-motor Couette cells, one for concentration fields and videotrajectory (chapters C, D), and one for single particle tracking (chapter F).

Each cell is composed of an inner cylinder ( $R_{in}$  in radius) and an outer cylinder ( $R_{out}$  in radius).  $R_{out}$  is fixed ( $= 20$  mm), while different inner cylinders can be inserted ( $5\text{mm} < R_{in} < 17.5$  mm). All experiments reported in this thesis have been performed with  $R_{in}=15$  mm; thus the Couette gap was  $d = 5$  mm. Both cylinders are made from polymetacrylate (PMMA) and have the same index of refraction as our particles and immersion fluids. We noticed that highly concentrated granular samples were poorly entrained by smooth surfaces, resulting in large slip rates along both cylinder surfaces. We found that wall-slip was significantly decreased (but not eliminated) by making surfaces rough on the scale of typical particle sizes [Lenoble thesis 2005]. This was achieved by hand

using a simple wood file, to scratch the surfaces in an approximately random fashion [Lenoble thesis 2005]. The inner cylinder penetrates into the coaxial cavity of the outer cylinder, as shown in Fig. B.6. The outer surface of the outer cylinder, being cylindrical, is not appropriate for optical imaging, due to strong astigmatism. For this reason, the cell is inserted inside a parallelepiped transparent auxiliary cavity (named “olearium”). The space between the outer cylinder and the olearium is filled with a few  $\text{cm}^3$  of the C16-S150 mixture, to avoid parasitic optical reflections.

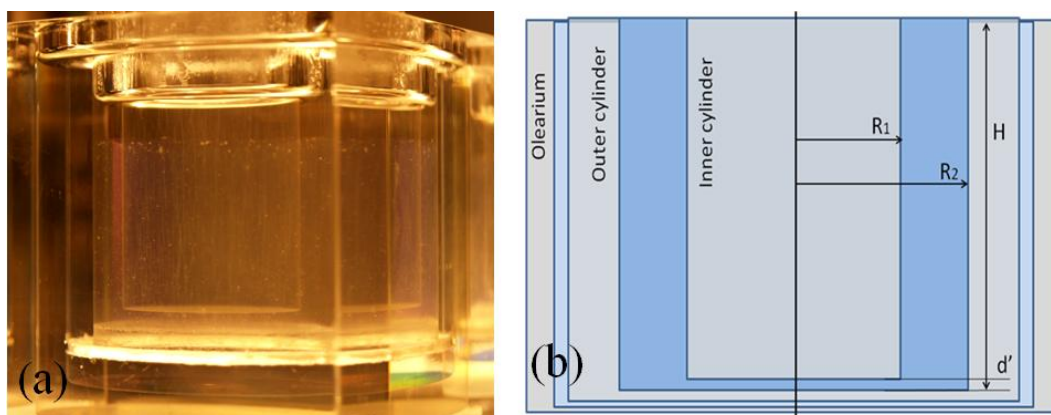


**Fig.B.6** (a) Photo of the transparent Couette cell. The granular paste is weakly visible due to its slight opalescence. Particles, which are heavier than the immersion fluid, culminate at finite distance below the oil-air meniscus. (b) Sketch of Couette cell.

The cylinders are connected to a couple of coaxial ball bearing pulleys and driven in rotation by independent motors. Positions of the cylinders relatively to the pulley axes can be finely tuned through a system of screws that provide 5 degrees of freedom (Fig. B.7). Coincidence of the rotation axes and of the cylinder axes can thus be satisfied to within  $\pm 25\mu\text{m}$  (outer cylinder) and  $\pm 20\mu\text{m}$  (inner cylinder) everywhere inside the Couette gap. Final check is performed from video sequences of the rotating cylinders, which help evidencing off-centering defaults. The lower part of the apparatus, bounded by the flat ends of both cylinders, defines a kind of parallel-disk geometry, of thickness  $d'$ . In all our experiments,  $d'$  was fixed = 1.5 mm.

The temperature of the Couette cell is monitored with a simple thermometer and roughly controlled by means of the air conditioning system that serves for the whole lab room. In routine operation, we noticed that fluctuations were limited to within about  $1^\circ\text{C}$  for a few hours in day time, which turned out sufficient for most of the experiments. We tested a

dedicated system based on water circulation through a radiator close to the cell, but this version did not perform better and was abandoned.

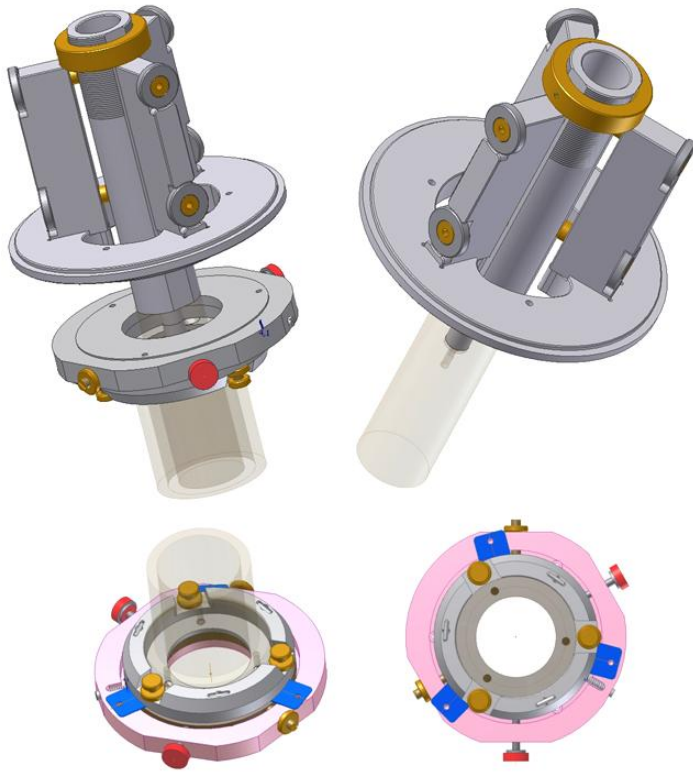


**Fig.B.7** *Couette cell components part with system of screw used for tunings. Position of the yellow ring tune the bottom gap.*

The inner and outer cylinders are driven by two identical direct current motors (Faulhaber 3863H), through belt transmissions in contra rotating mode. Each motor includes a digital tachometer and is fed by a tension driven servo-amplifier (MATTKE MTRF25...61/5-15) including a power unit.

The average shear applied to the sample is defined through a difference in velocity  $\Omega = \Omega_{in} - \Omega_{out}$  between cylinders ( $\Omega_{in,out}$  are the angular velocities of the inner and outer cylinder, respectively). Increasing both velocities by a same *offset* value ( $\Omega_{in} \rightarrow \Omega_{in} + \Omega_{off}$ ,  $\Omega_{out} \rightarrow \Omega_{out} + \Omega_{off}$ ) does not change the average shear, and simply amounts to rotating the whole Couette cell in the laboratory frame at angular velocity  $\Omega_{off}$ . In a purely azimuthal flow, this property provides a simple way to compensate for the flow velocity  $v_{\theta}$  at any distance  $r$  from the Couette axis. In other words, particles in a granular system or tracers in a fluid at distance  $r$  and altitude  $z$  can be made about immobile in the lab frame by tuning the offset  $\Omega_{off}$  to a value  $\Omega_{off}(r, z)$  located between  $-\Omega_{in}$  and  $-\Omega_{out}$ . Measuring the value of

$\Omega_{off}(r, z)$  that achieves immobilization of the particle(s) thus provides a simple mean to deduce the azimuthal velocity  $v_\theta(r, z)$  at any distance and altitude [Barentin *et al.* 2004].

Interestingly, both cylinders can be made to rotate at the same velocity,  $\Omega_{in} = \Omega_{out}$ . In this way, the sample is not sheared and rotates as a solid block, hence the name “block mode”. Operating the Couette cell in block mode is valuable in experiments using a vertical laser sheet (chapter D), as it allows us to spatially average measurement over different planar cuts.

### **B.5: The assumption of rotation invariance**

It should be noted that the above reasoning with the offset only holds in the limit of negligible inertial forces, since rotating the whole cell in general modifies the flow. We may try to guess whether inertia is important by estimating typical values of Reynolds numbers ( $Re$ ) in our experiments. Let us define the Reynolds number as  $Re = \rho\omega R d / \eta$ , where  $\rho$  and  $\eta$  are the granular paste density and shear viscosity, respectively, and  $R$  can be taken  $= R_{in}$  or  $R_{out}$ . The angular velocity  $\Omega$  is at most a few rad/s in our experiments. Taking  $\rho \approx 1 \text{ g}\cdot\text{cm}^{-3}$  and  $\eta \approx 6 \text{ Poise}$  (for a 50% volume fraction, see [Lenoble thesis 2005]), we find  $Re$  always  $< 1$  in our conditions. We may thus hope that  $\Omega_{off}$  does not significantly modify the flow profile, and conclude that our operating principle is justified. However we cannot rule out all subtle inertial effects that may arise. After all, these may accumulate in time and ultimately have visible consequences on the flow. Instead of relying on such vague reasoning, we made experimental tests whenever it was possible in the context of a given experiment. These tests are described in each chapter (C, D, F). As we will see, all of them were positive, meaning that contra-rotation does modify the flow, compared to the standard situation where only the inner cylinder is rotating.

## Chapter C – Dynamics of concentrated suspensions in Couette flow

Knowledge of velocity profiles and diffusion coefficients is highly desirable for understanding the microhydrodynamics and migration phenomena in concentrated suspensions. The first part of the chapter concerns an optical flow method to visualize the orientation of particles in continuous space-time images and estimate accurately the average azimuthal velocity of colliding particles in a Couette flow. The main originality of such a global approach comes from the extension to the measurement of the rms displacement of particles to estimate the diffusion coefficient in the velocity direction. We first introduce numerical simulations of the uniform vertical motion of 2D disk within a plane to present the videotrajectory method and then we precise the influence of particle number, random disk fluctuations, aliasing effects, out of plane motion and uniform circular trajectories upon the oriented patterns in the spatiotemporal image. Finally, we derive expressions of the average velocity and the rms fluctuation in the flow direction from grey level properties of the autocorrelation image in a spatiotemporal domain properly chosen. The second and third part of the chapter use the multiparticle videotrajectory method to investigate the flow features of either a density or a non density-matched suspension in a Couette geometry as a function of the radial distance, the altitude and the differential angular velocity between inner and outer cylinders.

### C.1: Multiple particle videotrajectory method

#### C.1.a: General principle

This paragraph presents the general principle of an original optical flow technique dedicated to the measurement of the mean velocity and the position fluctuations of particles in the flow direction [Snabre *et al.* 2011].

Classical flow visualization is based on direct observation of the 2D motion of tracer particles [Adrian 1991, Raffel *et al.* 2000]. Conventionally, PIV images are recorded on photographic film, and the two dimensional displacement field is obtained via the analysis of subsequent images and the computation of the spatial autocorrelation into small search regions [Hesselink 1988]. An alternative approach, referred to as Digital Particle Image Velocimetry (DPIV), uses a CCD camera. The digital technique allows a fast computation of cross correlation for pairs of images and removes the ambiguity of the sign of the displacement [Willert and Gharib 2000]. Cross correlation-based DPIV determines the average motion of small groups of particles contained within small regions known as interrogation regions.

Essentially, two subsequent frames are divided into interrogation regions, and the cross correlation function is computed sequentially over all regions providing one displacement vector per region. The location of the cross-correlation peak provides the mean displacement of particles, and the relative amplitude indicates the accuracy of the estimation [Prasad 2000].

The maximum displacement that can be measured by a cross correlation technique accelerated by fast Fourier transform (FFT) is half of the interrogation region dimension  $h$  (Nyquist criterion). One of the main drawbacks of DPIV is the inability to accurately resolve flow regions. PIV measurements indeed contain errors arising from several sources [Huang *et al.* 1993, Merzkirch and Gui 1996, Scarano and Reithmuller 2000, McKenna and McGillis 2002]: (1) a *random error* due to noise in the recorded images; (2) a *bias error* arising from the process of computing the correlation peak location to sub-pixel accuracy; (3) *gradient errors* resulting from velocity gradients within an interrogation region leading to loss of correlation; (4) an *acceleration error* caused by random particle displacements. Particle streamlines in flowing concentrated suspensions are not straight and particle displacement is overestimated when the Eulerian velocity is approximated using Lagrangian particle displacements. Out-of-plane motions make some particles exit from the laser sheet and then decreases the number of particles pairs between two frames. This problem is a source of false displacement vectors. Usually, one has to reduce the time interval  $\delta t$  between frames resulting in a smaller particle displacements. In reality, loss of particle pairs significantly reduces the signal-to-noise ratio for particle displacements exceeding about  $h/4$  [Raffel *et al.* 2000]. The dynamics of sub-pixel DPIV methods thus ranges from 0.1 pixel up to  $h/4$  pixels [Raffel *et al.* 2000], corresponding to two-decades dynamics for a typical interrogation region of maximum size  $h = 100$  pixels.

The optical flow methods offer a new approach for analysing an image sequence with a largely improved spatial accuracy and reduced number of false displacement vectors [Horn and Schunck 1981, Barron *et al.* 1994, Alavarez *et al.* 2000]. Optical-flow approaches consist in extracting a dense velocity field (i.e. one vector per pixel) from the observed motion of photometric patterns in an image sequence. Despite the obvious disadvantages of DPIV methods, the mainstream of research in fluid mechanics only gradually evolves towards motion estimation in space-time windows [Corpetti *et al.* 2002, Heitz *et al.* 2009]. Yet, the term "optical flow" was first used by the psychologist James Jerome Gibson in the 1940s as part of a theory of human vision [Gibson 1950]. Low level processing in visual cortex extracts information about motion from a continuous stream of visual stimuli [Hubel and Wiesel 1962, Anderson and Burr 1985, Adelson 1991] and research in biological vision now interprets the perception of motions in the space-time domain.

The optical flow methods can track not only tracer motions but also texture motions to capture clouds, sea ice or pollutant displacements from sequences of meteorological satellite images [Corpetti *et al.* 2002, Heitz *et al.* 2009]. These methods are also widely used in video compression [Barron *et al.* 1994], in computer vision and in robotics to build a representation of the environment of a moving robot [Lee and Song 2004]. In this context, a number of methods have been proposed to measure dense displacement fields. Barron *et al.* [Barron *et al.* 1994] classify optical flow methods into four categories: regularization methods based on the optimization of an objective functional [McKenna and McGillis 2002] (1981), correlation-based or block matching methods [Wahl and Simpson 1990] (1990), spatiotemporal filtering methods [Adelson and Bergen 1985] (1985) and filtered differential methods [Weber and Malik 1995] (1995). Not all of these methods are well suited for particle image velocimetry.

In order to establish the optical flow constraint equation, let us consider a sequence of  $n$  images represented by a grey level intensity  $I(x, y, t)$ . The assumption common to most optical flow algorithms in measuring structures motion is that  $I(x, y, t)$  remains approximately constant in time, at least for a short duration. The constant brightness assumption thus provides the following equation:

$$\frac{d}{dt} I(x, y, t) = \frac{\partial I}{\partial t} + \mathbf{V} \cdot \nabla I = 0 \quad (\text{C.1})$$

where the optical flow vector  $\mathbf{V}(u, v)$  denotes the instantaneous velocity of the structure. Equation (C.1) involves two unknowns (amplitude and direction of  $\mathbf{V}$ ) and cannot be solved as such. This is known as the *aperture problem*. Also note that only the velocity component along the spatial intensity gradient can be estimated. Additional conditions are necessary to estimate the optical flow. The regularization method introduced by Horn and Schunck in 1981 [Horn and Schunck 1981] consists in enforcing the smoothness of the flow and looking for a solution at a given time as a minimum of the following functional:

$$\int_S (\partial I / \partial t + \mathbf{V} \cdot \nabla I)^2 + b (|\nabla u|^2 + |\nabla v|^2) dx dy \quad (\text{C.2})$$

where  $b$  is a constant over the domain of interest  $S$ .

In the following, the additional condition concerns the known direction of particle motion and we use a spatiotemporal filtering method that exploits the fact that detecting motion is equivalent to extracting an orientation inside a correlation image. Let us consider a  $n$ -frame sequence  $(x, y, t)$  with a circular disk (diameter  $2a$  pixels) moving to the bottom of the image with a constant velocity  $v = -2$  pixels/frame. A region of interest (ROI of height  $h$  and thickness  $e = 2a$ ) parallel to the object motion includes the falling disk, as shown in Fig. C.1.a. The time projection of the grey levels within the ROI perpendicularly to the motion produces

an oriented texture in the spatiotemporal window  $T(y,t)$  (Fig. C.1.b). The tilt angle  $\Psi$  of the oblique line with respect to  $x$  axis is related to the disk velocity through the relation:

$$v = \frac{f_t}{f_S} \tan \psi \quad (\text{C.3})$$

where  $f_t$  and  $f_S$  are the temporal and the spatial sampling frequencies, respectively (with  $f_t=1$  pixel/frame and  $f_S=1$  pixel). As proposed initially by Adelson and Bergen [Adelson and Bergen 1985], a spectral analysis of the time-space window  $T(y,t)$  in the Fourier space gives a Dirac ridge whose support is orthogonal to the velocity vector. A powerful way to characterize oriented structures with low sensitivity to noise is the autocorrelation image  $A[T(y,t)]$ . This function directly indicates similarities between  $T(y,t)$  and its shifted version. The graph of  $A[T(y,t)]$  features a centred sharp pattern (or ridge line) with the same orientation  $\psi$  as the disk trajectory (Fig. C.1.c)<sup>2</sup>. Let us perform a radial integration of  $A[T(y,t)]$  inside a circular ROI (radius  $p$ ) centred on the origin. We obtain the angular distribution  $P(\theta)$  shown in Fig. C.2.a, with a maximum whose position directly indicates the value of  $\Psi$ . The finite length  $l$  of the disk trajectory in the spatiotemporal window  $T(y,t)$  causes a linear decrease of the normalized grey level intensity  $g_\psi^*(c)$  along the ridge line in the autocorrelation image (Fig. C.1.c and Fig. C.2.b):

$$g_\psi^*(c,l) = 1 - c/l \quad (\text{C.4})$$

where  $c$  is the distance along the ridge line.

One may note that the discrete signal  $g_\psi^*(c)$  shows short scale undulations (red symbols in Fig. C.2.b). In fact these details are caused by sampling artifacts and time aliasing (Fig. C.2.b). One may get rid of the undulations and obtain a smooth signal by an appropriate choice of the sampling rate and by using interpolation methods (see next paragraph C.1.b).

---

<sup>2</sup> The discrete 2D autocorrelation is usually computed through the inverse Fourier transform  $F^{-1}[F(T) F^*(T)]$  where  $F(T)$  denotes the Fourier transform of the image  $T$  and  $*$  the complex conjugate (Wiener Kinchin theorem). Here, we use a discrete fast Hartley transform (DFHT) instead of a discrete Fast Fourier transform (DFFT) to reduce the computer memory required and to decrease the number of arithmetic operations [Weber and Malik 1995, Bracewell et al. 1986]. Prior to any discrete transform in the Hartley space, the boundaries of the spatio temporal window of size  $(h,n)$  are extended up to a size  $(H,N)$  such that  $H = 2^i$  and  $N = 2^j$ . Extra pixels in the  $(N,H)$  image are padded with the averaged grey level of the spatio temporal  $(n,h)$  window. This procedure helps reducing high frequency noise.

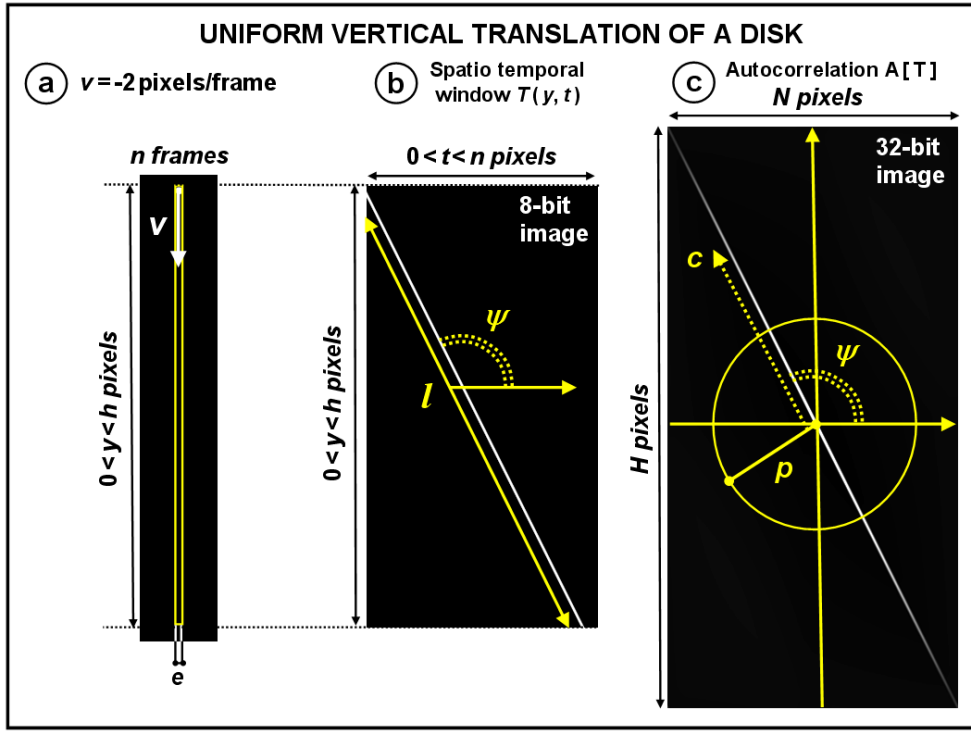


**Fig. C.1** (a) Uniform vertical translation of a disk ( diameter  $2a=9$  pixels,  $v = -2$  pixels/frame) within a rectangular region of interest (height  $h=550$  pixels and width  $e = 2a$ ). (b) Tilt angle  $\psi$  of the disk trajectory with length  $l$  in the spatiotemporal window  $T(y,t)$ . (c) Autocorrelation image  $A[T(y,t)]$  and sharp ridge line in the  $\Psi$  direction,  $n = 290$  frames.

We now introduce random Gaussian-like fluctuations of the disk position along the direction of motion. Let  $\langle \delta y^2 \rangle^{1/2}$  be the mean square vertical displacement between two consecutive frames (Fig. C.3.a). Random fluctuations in the velocity direction give a twisty trajectory in the spatiotemporal window (Fig. C.3.b) with a steep and non linear decay of the discrete signal  $G_{\psi}(c)$  along the ridge line (Fig. C.3.c and Fig.C.4.b)<sup>3</sup>. However, note that the average orientation of the ridge line is about unaffected by the large rms fluctuations ( $\langle \delta y^2 \rangle^{1/2} = 2$  pixels), and that the orientation angle  $\psi$  of the ridge line still allows to accurately determine the disk velocity (Fig. C.4.a).

<sup>3</sup> The notation  $g_{\psi}^*$  is dedicated to the grey level variation along the ridge line for the uniform motion of a single disk while the function  $\bar{G}_{\psi}$  refers to disk motion with random displacements.

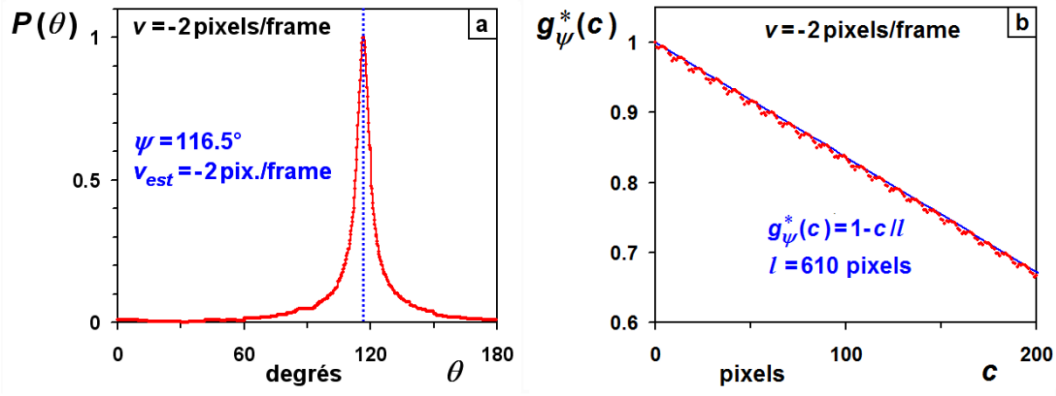


**Fig. C.2** (a) Normalized grey level angular distribution  $P(\theta)$  within a circular ROI centred on the autocorrelation image  $A[T]$  and estimation of the tilt angle  $\psi$  of the ridge line ( $p = 60$  pixels,  $\psi = 116.5^\circ$ ,  $v_{est} \approx -2$  pixels/frame) for a uniform translation motion ( $v = -2$  pixels/frame). (b) Normalized discrete function  $g_\psi^*(c)$  versus the number  $c$  of pixels along the ridge line (red symbols) and linear expression  $g_\psi^*(c, l) = 1 - c/l$  with  $l = 610$  pixels (blue solid curve).  $2a = 9$  pixels,  $h = 550$  pixels and  $n = 290$  pixels.

The optical method is sensitive to a few pixels displacements of a slowly moving disk during a  $n$  image sequence and to a  $h/4$  displacement for a more rapid disk motion between two consecutive images. As a consequence, the treatment of a  $n$  image sequence can detect an averaged velocity ranging from  $2/n$  pixels/frame up to  $h/4$  pixels/frames, corresponding to five decades dynamics for  $n = 1000$  frames and a ROI height  $h = 1000$  pixels!

Displacements that can be detected by this method range from a few pixels, corresponding to a very slowly moving disk, to about  $h/4$ , the higher limit corresponding to high velocity. Supposing an  $n$ -image sequence, the detection range goes from  $2/n$  pixels/frame up to  $h/4$  pixels/frames. With  $h = 1000$  pixels, a common value, the detection dynamics spans 5 decades!

Unlike usual DPIV methods, which cross correlate two consecutive interrogation regions, the optical flow methods analyze a continuous space time window (and not a discrete displacement) which offers a higher accuracy to determine the average velocity of the disk.

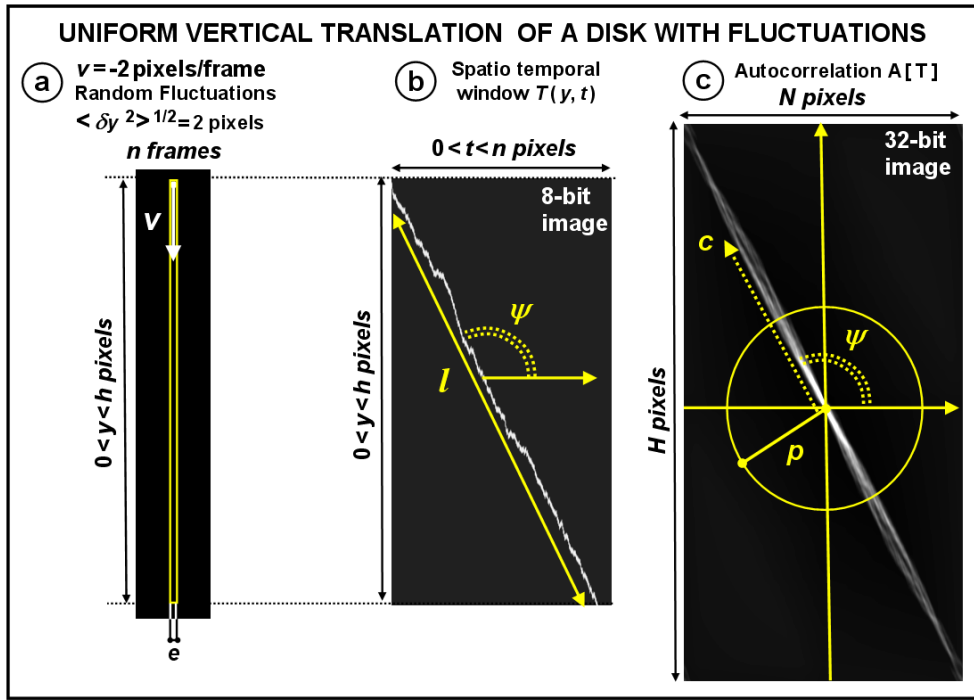


**Fig. C.3** (a) Uniform vertical translation of a disk with longitudinal random fluctuations (diameter  $2a=9$  pixels,  $v=-2$  pixels/frame,  $\langle \delta y^2 \rangle^{1/2}=2$  pixels) within a rectangular ROI ( $h = 550$  pixels and  $e = 2a$ ). (b) Tilt angle  $\psi$  of the disk trajectory with length  $l$  in the spatiotemporal window  $T(y,t)$ . (c) Autocorrelation image  $A[T(y,t)]$  and ridge line in  $\Psi$  direction.  $n = 290$  frames.

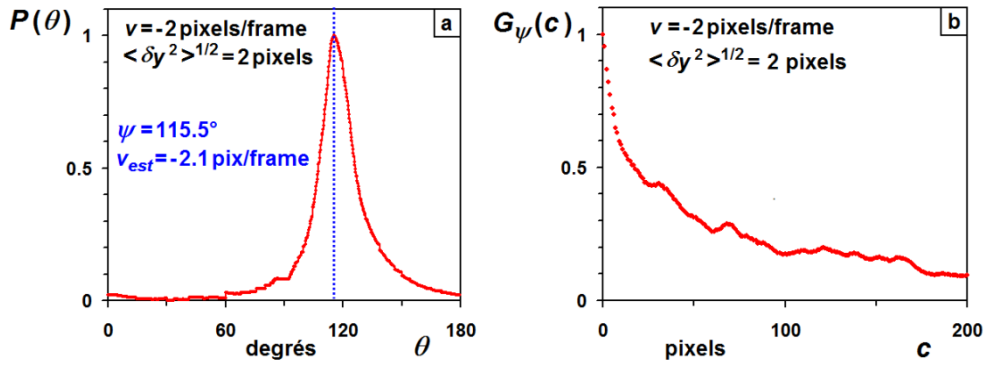


**Fig. C.4** (a) Normalized grey level angular distribution  $P(\theta)$  within a circular roi centered on the autocorrelation image  $A[T]$  and estimation of the tilt angle  $\psi$  of the ridge line ( $p=60$  pixels,  $\psi = 116.5^\circ$ ,  $v_{est} \approx -2.1$  pixels/frame) for a uniform translation motion with vertical random fluctuations ( $v=-2$  pixels/frame,  $\langle \delta y^2 \rangle^{1/2}=2$  pixels). (b) Normalized discrete data  $G_\psi(c)$  along the ridge line (red symbols).  $2a = 9$  pixels,  $h = 550$  pixels and  $n = 290$  pixels.

The method yet relies on the assumption of almost constant brightness of the moving objects along the visual trajectories. Moreover we only consider situations where average streamlines are uniform within the selected ROI. Interestingly, the brightness decay along the ridge line of the autocorrelation image may be exploited to estimate the rms position fluctuations in the flow direction<sup>4</sup>. A larger number of objects moving along close streamlines with a similar velocity can greatly improve the statistics and the accuracy of the estimations in the spatiotemporal window. The next paragraphs concerns a higher surface density of disks and functional forms of the grey level variation along the ridge line.

### C.1.b: Uniform translation of disks

The accuracy of the velocity measurement was investigated using particle image sequences generated with a 2D numerical simulation (Monte Carlo simulations). The first image of the sequence is randomly filled with non interpenetrating disks of diameter  $2a$  occupying a surface fraction  $\Phi_s$ . Grey levels of the disks are supposed constant in time, but have random values. We suppose a Gaussian-like distribution with an average level  $\langle I \rangle$  and a finite rms fluctuation  $\langle \delta I^2 \rangle^{1/2}$  (Fig. C. 5.a).

A uniform motion of disks with the same velocity results in a textured spatiotemporal window  $T(y,t)$  consisting of a large number of constant brightness and similarly oriented trajectories (Fig. C.5.b,  $v = -0.2$  pixel/frame), the autocorrelation image  $A[T(y,t)]$  displays a centered ridge line with parallel surrounding patterns (Fig. C.5.c). The normalized angular distribution  $P(\theta)$  is computed inside a centered circular ROI, radius  $p = 60$  pixels, and discretized into 720 angular sectors (angular resolution 0.25 degree). From the fit of a Lorentzian function to  $P(\theta)$ , we obtain the tilt angle  $\psi$  of the bright ridge line (Fig. C.6.a). Using Eq. C.3, we deduce the velocity of the disks (Fig. C.6.b).

As mentioned above, the discrete grey level intensity  $g_\psi(c)$  along the ridge line is corrupted as a result of sampling artifacts (red symbols in Fig. C.6.b). A sampling rate  $s(\psi)$  synchronized with the distance  $s$  between integral pixel values along the ridge line (Fig. C.7) and a nearest neighbor bicubic interpolation efficiently remove the artifactual pixels and considerably smooth the discrete function  $g_\psi(c)$  (black symbols in Fig. C.6.b):

---

<sup>4</sup> We will see later that transverse fluctuations remain quite small and hardly influence the function  $G_\psi(c)$ .

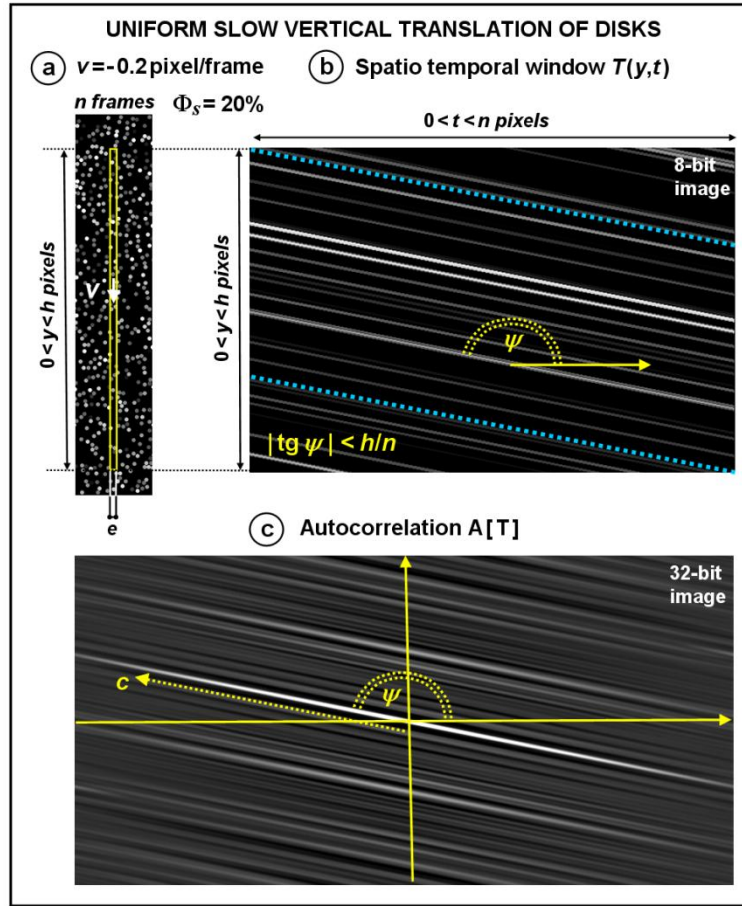


**Fig. C.5** (a) Uniform slow vertical translation of disks (diameter  $2a=5$  pixels,  $v = -0.2$  pixel/frame, surface density  $\Phi_s = 20\%$ ) within a rectangular ROI (height  $h=400$  pixels and width  $e=8$  pixels). (b) Tilt angle  $\psi$  of disk trajectories in the spatiotemporal window  $T(y,t)$ . (c) Autocorrelation image  $A[T(y,t)]$  and bright ridge line along the  $\Psi$  direction.  $n = 600$  frames.  $\langle I \rangle = 125$  and  $\langle \delta I^2 \rangle^{1/2} = 50$ .

$$\begin{aligned}
 s(\psi) &\approx \sqrt{2} + \text{tg } \psi - 1 && \text{for } \tan \psi < 1 \\
 s(\psi) &\approx \sqrt{2} + 1/\text{tg } \psi - 1 && \text{for } \tan \psi > 1
 \end{aligned}
 \tag{C.5}$$

The spatiotemporal window includes trajectories of variable length  $l$ . The length dispersion influences the decay of the signal  $g_\psi(c)$  in the autocorrelation image  $A[T(y,t)]$ . For slowly moving disks ( $|\tan \psi| < h/n$ ), a fraction  $1 - n|\tan \psi|/h$  of the trajectories has a constant length  $L = n/|\cos \psi|$  (paths bounded by the blue dotted lines in Fig. C.5.b) while complementary trajectories display a linear path length distribution on the interval  $0 < l < L$ .

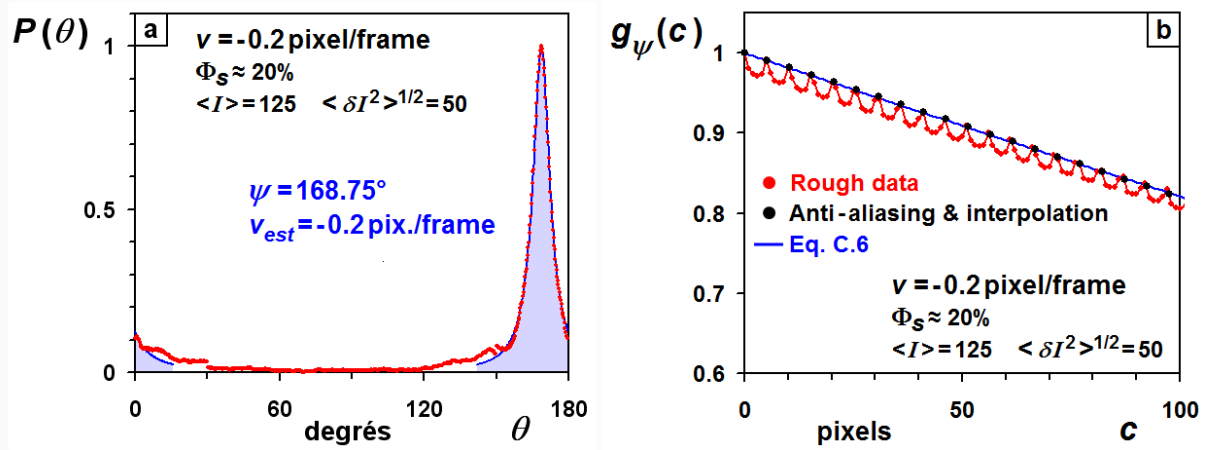


**Fig. C.6** (a) Normalized grey level angular distribution  $P(\theta)$  within a circular ROI centred on the autocorrelation image  $A[T]$  and estimation of the tilt angle  $\psi$  of the ridge line ( $p = 60$  pixels,  $\psi = 168.75^\circ$ ,  $v_{est} \approx -0.2$  pixel/frame) from a Lorentzian fit (blue solid curve) for a uniform slow translation motion of ( $v = -0.2$  pixels/frame). (b) Normalized discrete function  $g_\psi(c)$  versus the number  $c$  of pixels along the  $\psi$  direction of the ridge line (red symbols). Black symbols show discrete data after removal of artefactual pixels while the blue solid line is derived from Eq. C.6 with  $h = 400$  pixels,  $n = 600$  pixel and  $\psi = 168.75^\circ$ .

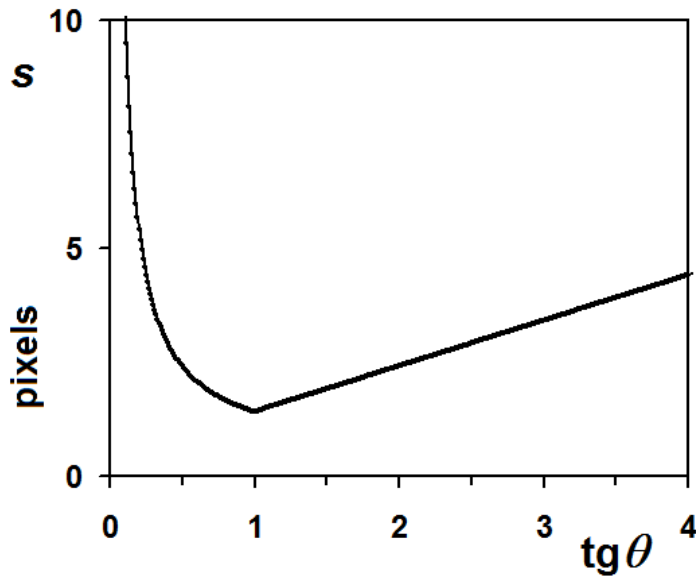


**Fig. C.7** Resampling rate  $s(\psi)$  of pixels along the  $\psi$  direction of a tilted line to remove artefactual pixels and aliasing effects (Eq. C.5).

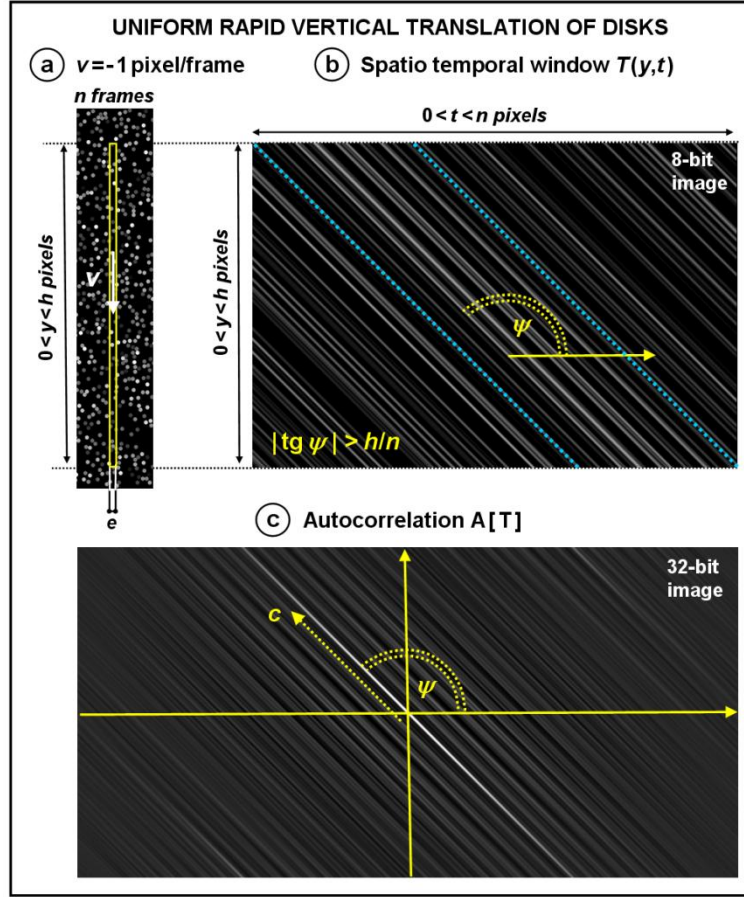


**Fig. C.8** (a) Uniform rapid vertical translation of disks (diameter  $2a=5$  pixels,  $v = -1$  pixel/frame, surface density  $\Phi_s = 20\%$ ) within a rectangular ROI (height  $h=400$  pixels and width  $e = 8$  pixels). (b) Tilt angle  $\psi$  of disk trajectories in the spatiotemporal window  $T(y,t)$ . (c) Autocorrelation image  $A[T(y,t)]$  and bright ridge line along the  $\Psi$  direction.  $n = 600$  frames,  $\langle I \rangle = 125$  and  $\langle \delta I^2 \rangle^{1/2} = 50$ .

The signal  $g_\psi(c,n,h)$  can be expressed as an integral of Eq. (C.4) over the set of variable path lengths:

$$g_\psi(c,n,h) = \left(1 - \frac{n|\tan\psi|}{h}\right) g_\psi^*(c,L) + \frac{n|\tan\psi|}{h} \frac{\int_c^L 1 g_\psi^*(c,l) dl}{\int_0^L 1 dl} \quad \text{for } |\tan\psi| < h/n$$

which finally gives:

$$g_\psi(c,n,h) = \left(1 - n|\tan\psi|/h\right) \left(1 - c|\cos\psi|/n\right) + \left(n|\tan\psi|/h\right) \left(1 - c|\cos\psi|/n\right)^2 \quad (\text{C.6})$$

The above relation well accounts for the decay of the grey level intensity along the re-sampled pixels of the ridge line when uniformly translating disks move slowly (blue solid line in Fig. C.8.b).

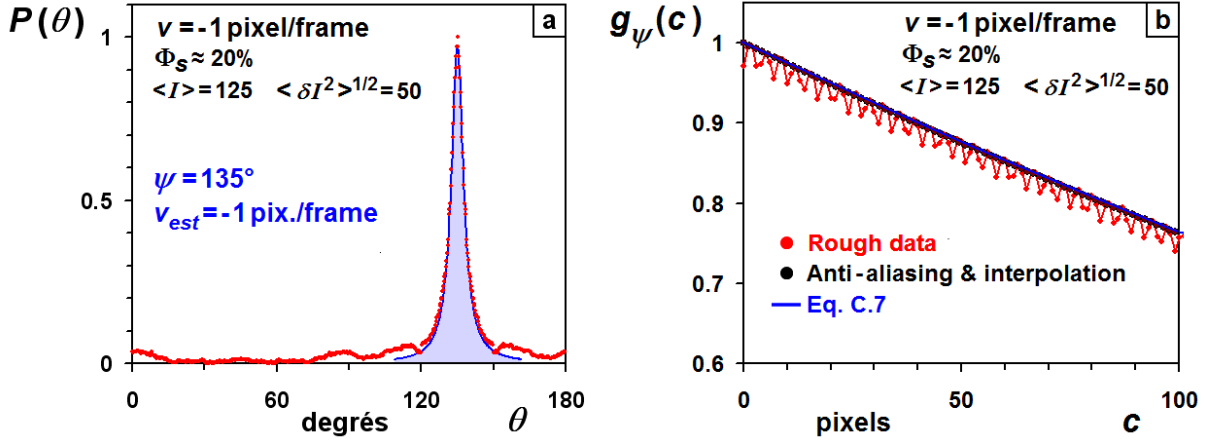


**Fig. C.9** (a) Normalized grey level angular distribution  $P(\theta)$  within a circular ROI centred on the autocorrelation image  $A[T]$  and estimation of the tilt angle  $\psi$  of the ridge line ( $p=60$  pixels,  $\psi=135^\circ$ ,  $v_{est} \approx -1$  pixel/frame) from a Lorentzian fit (blue solid curve) for a uniform slow translation motion ( $v=-1$  pixel/frame). (b) Normalized discrete function  $g_\psi(c)$  along the  $\psi$  direction of the ridge line (red symbols). Black symbols show data after removal of artefactual pixels while the blue solid line is derived from Eq. C.7 with  $h=400$  pixels,  $n=600$  pixel and  $\psi=135^\circ$ .

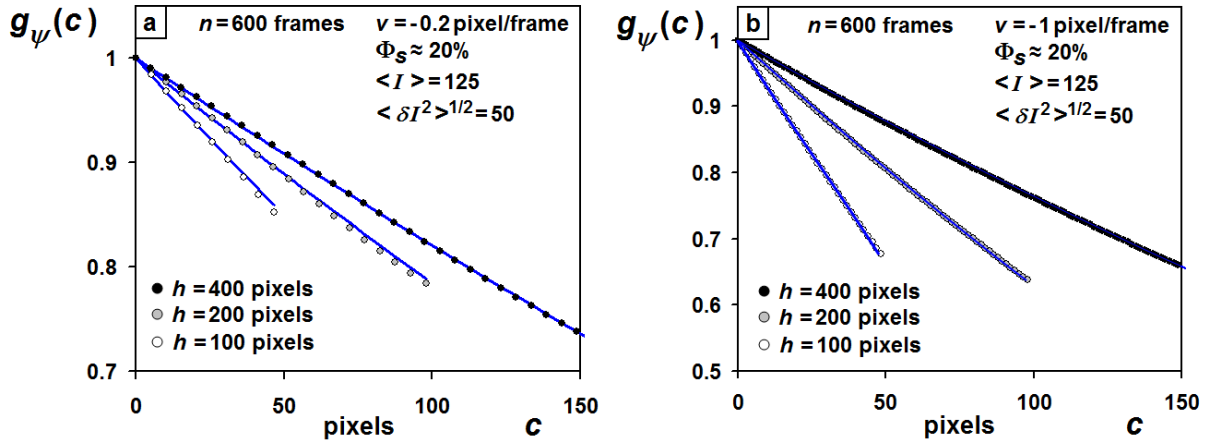


**Fig. C.10** Normalized discrete function  $g_\psi(c)$  along the  $\psi$  direction of the ridge line in the autocorrelation image for variable height  $h$  of the spatiotemporal window. (a)  $v=-0.2$  pixel/frame, (b)  $v=-1$  pixel/frame. Theoretical predictions according to Eq. C6 (a) or Eq. C.7 (b) appear as blue solid lines.  $n=600$  frames,  $\Phi_s=20\%$ ,  $\langle I \rangle = 125$  and  $\langle \delta I^2 \rangle^{1/2} = 50$ .

For a rapid motion ( $|\tan\psi| > h/n$ , Fig. C.8), a lesser proportion  $1-h/n|\tan\psi|$  of trajectories has a constant length  $L = h/|\sin\psi|$  (paths bounded by the blue dotted lines in Fig. C.8.b) and  $g_\psi(c, n, h)$  now takes on the functional form:

$$g_\psi(c, n, h) = \left(1 - \frac{h}{n|\tan\psi|}\right) g_\psi^*(c, L) + \left(\frac{h}{n|\tan\psi|}\right) \frac{\int_c^L 1 g_\psi^*(c, l) dl}{\int_0^L 1 dl} \quad \text{for } |\tan\psi| > h/n$$

$$g_\psi(c, n, h) = (1 - h/n|\tan\psi|)(1 - c|\sin\psi|/n) + (h/n|\tan\psi|)(1 - c|\sin\psi|/n)^2 \quad (\text{C.7})$$

Equations C.6 and C.7 nicely describe the decrease of  $g_\psi(c, n, h)$  whatever the size ( $h, n$ ) of the spatiotemporal window, as shown by the treatment of particle image sequences (Fig. C.10). The next section introduces non linear effects such as random particle fluctuations or out of plane motion that may degrade the accuracy of the optical flow method and influence the sharpness of the tilted ridge line.

### C.1.c: Random position fluctuations of translating disks

Now we relax the assumption of a rigid collection of moving disks, and introduce fluctuations of the disks' positions along the direction of motion. For illustration, let us suppose vertical fluctuations  $\langle \delta y^2 \rangle^{1/2}$  of same order as the vertical displacement between two frames (e.g.  $v = -2$  pixel / frame and  $\langle \delta y^2 \rangle^{1/2} = 2$  pixels, Fig. C.11.a and b). Let us denote  $G_\psi(c)$  the autocorrelation function along the ridge line, now including position noise. Compared to  $g_\psi(c)$  the main effect of the fluctuations is to produce a steeper decorrelation of  $G_\psi(c)$ , as shown in figure C.11.d. Though  $\langle \delta y^2 \rangle^{1/2}$  is large in the chosen example, the optical flow method still correctly estimates the velocity (Fig. C.11.c). This is made possible by the large number of disks, which helps statistics. Note that disks may interpenetrate in the course of motion, and that this only has little influence on the tilt angle  $\psi$  of the ridge line and on the shape of  $G_\psi(c)$  (Fig.C.11.c and C.11.d).

We now want to infer a functional form of the signal  $G_\psi(c)$ , which we will later exploit in the analysis of experimental signals to deduce the amplitude of position fluctuations. As a helpful analogy, we consider the problem of the intensity fluctuations in fluorescence

spectroscopy correlation methods (FCS). The central idea of FCS is the analysis of intensity fluctuations from fluorescent molecules (radius  $a$ ) inside a finite volume. The molecules are excited by a focused laser beam, and the fluorescence intensity  $I(t)$  is measured inside the diffraction limited focal region ( $\approx 1\mu\text{m}^3$ ) of the laser beam. At thermal equilibrium, the signal  $I(t)$  fluctuates about a mean value  $\langle I \rangle$  as a result of random changes in the number of molecules moving through the focal region. From the autocorrelation of intensity fluctuations, it is possible to extract diffusion coefficients and identify the macromolecular units inside living cells [Taylor 1953, Breedveld *et al.* 2002]. For a stationary ergodic sample (time averaging and thermodynamic ensemble averaging are identical), the normalized autocorrelation function  $G(\tau)$  can be expressed as [Graham *et al.* 1991]:

$$G(\tau) = \frac{\langle \delta I(t) \delta I(t+\tau) \rangle}{\langle I^2 \rangle} = \left(1 + \frac{\tau}{\tau_D}\right)^{-3/2} \quad \text{with} \quad \tau_D = \frac{a^2}{6D} \quad (\text{C.8})$$

where  $\delta I(t) = I(t) - \langle I \rangle$ ,  $\tau_D$  is a characteristic decorrelation time and  $D$  the diffusion coefficient of fluorescing species.

Equivalently, position fluctuations of disks (of radius  $a$ ) contribute as random changes in the number of points located along ideal straight lines (similarly to the focal volume in FCS). The autocorrelation function  $G_\psi(c)$  in the diffusive regime then takes on the form:

$$G_\psi(c) = g_\psi(c) \left(1 + \frac{c |\cos \psi|}{t_D}\right)^{-1/2} \quad \text{with} \quad t_D = \frac{a^2}{2 \langle \delta y^2 \rangle} = \frac{a^2}{2 \langle \delta y^2 \rangle}, \quad (\text{C.9})$$

where the exponent 1/2 results from the 1D geometry of non noisy trajectories (with  $g_\psi(c)$  obeying Eq. C.6 or C.7),  $t = c |\cos \psi|$  is the frame number (the time in the video sequence) related to a number  $c$  of pixels along the ridge line, and  $t_D$  a characteristic frame number associated with a mean square displacement  $a^2 = 2 \langle \delta y^2 \rangle t_D$  that shifts the disk out of the ideal straight path in the spatiotemporal window.

$$\text{Finally:} \quad G_\psi(c) = g_\psi(c) \left(1 + \frac{2 \langle \delta y^2 \rangle c |\cos \psi|}{a^2}\right)^{-1/2} \quad (\text{C.10})$$

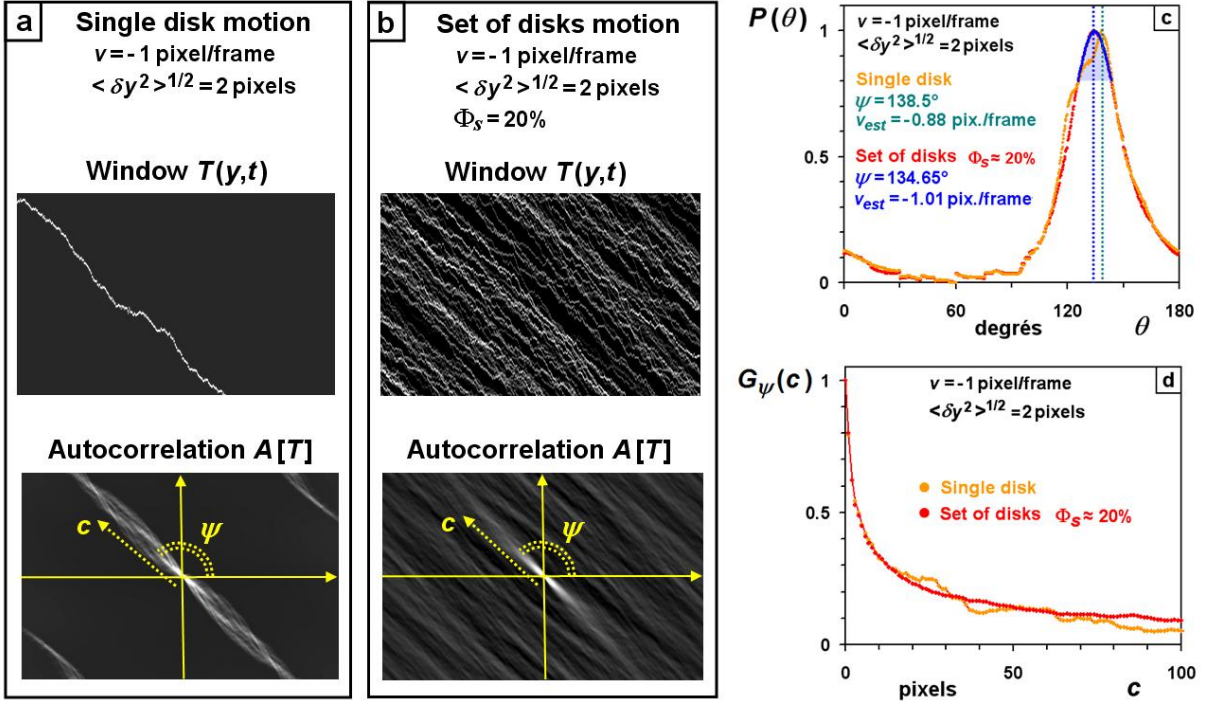


**Fig. C.11** Spatiotemporal window  $T(y,t)$  and autocorrelation image  $A[T]$  for the uniform vertical translation with random fluctuations of either a single disk (a) or a set of disks (b) ( $v = -1$  pixel/frame,  $\langle \delta y^2 \rangle^{1/2} = 2$  pixels, diameter  $2a = 5$  pixels,  $\Phi_s = 20\%$ , ROI height  $h = 400$  pixels and ROI width  $e = 8$  pixels). (c) Normalized grey level angular distribution  $P(\theta)$  and estimation of the tilt angle  $\psi$  of the ridge line from a Lorentzian fit (blue solid curve). (d) Normalized discrete function  $G_\psi(c)$  along the  $\psi$  direction of the ridge line (orange symbols for a single disk and red symbols for a set of disks).  $\langle I \rangle = 125$  and  $\langle \delta I^2 \rangle^{1/2} = 50$ .

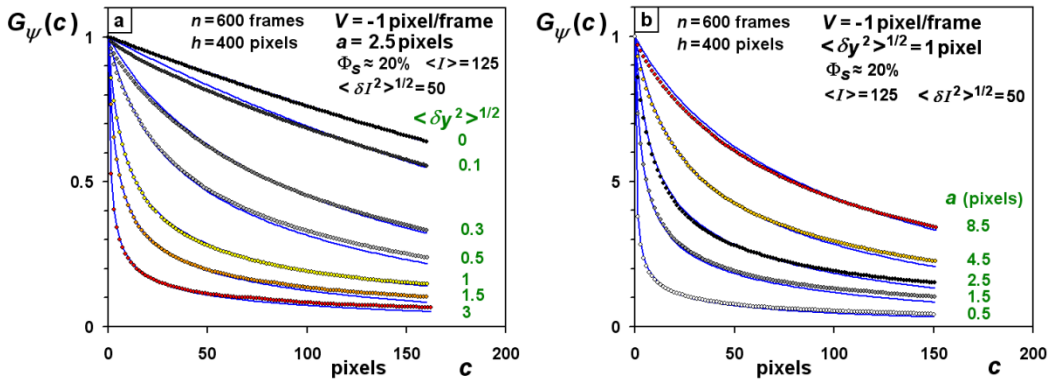


**Fig. C.12** Normalized discrete function  $G_\psi(c)$  along the  $\psi$  direction of the ridge line in the autocorrelation image as a function of either rms fluctuation  $\langle \delta y^2 \rangle^{1/2}$  (a) or disk radius (b). Theoretical predictions according to Equations C6, C7 and C10 appear as blue solid lines.  $v = -1$  pixel/frame,  $\Phi_s = 20\%$ ,  $n = 600$  frames,  $n = 400$  pixels,  $\langle I \rangle = 125$  and  $\langle \delta I^2 \rangle^{1/2} = 50$ .

Below, in Fig. C.12, we show tests of Eq. (C.10) based on simulations. The value of  $\psi$  is estimated from the autocorrelation image, following the same procedure as before. Note that the above relation correctly accounts for the non linear decay of  $G_\psi(c)$  along the ridge line, for all tested values of  $\langle \delta y^2 \rangle^{1/2}$  (Fig. C12.a) or of the disk radius (Fig. C.12.b).

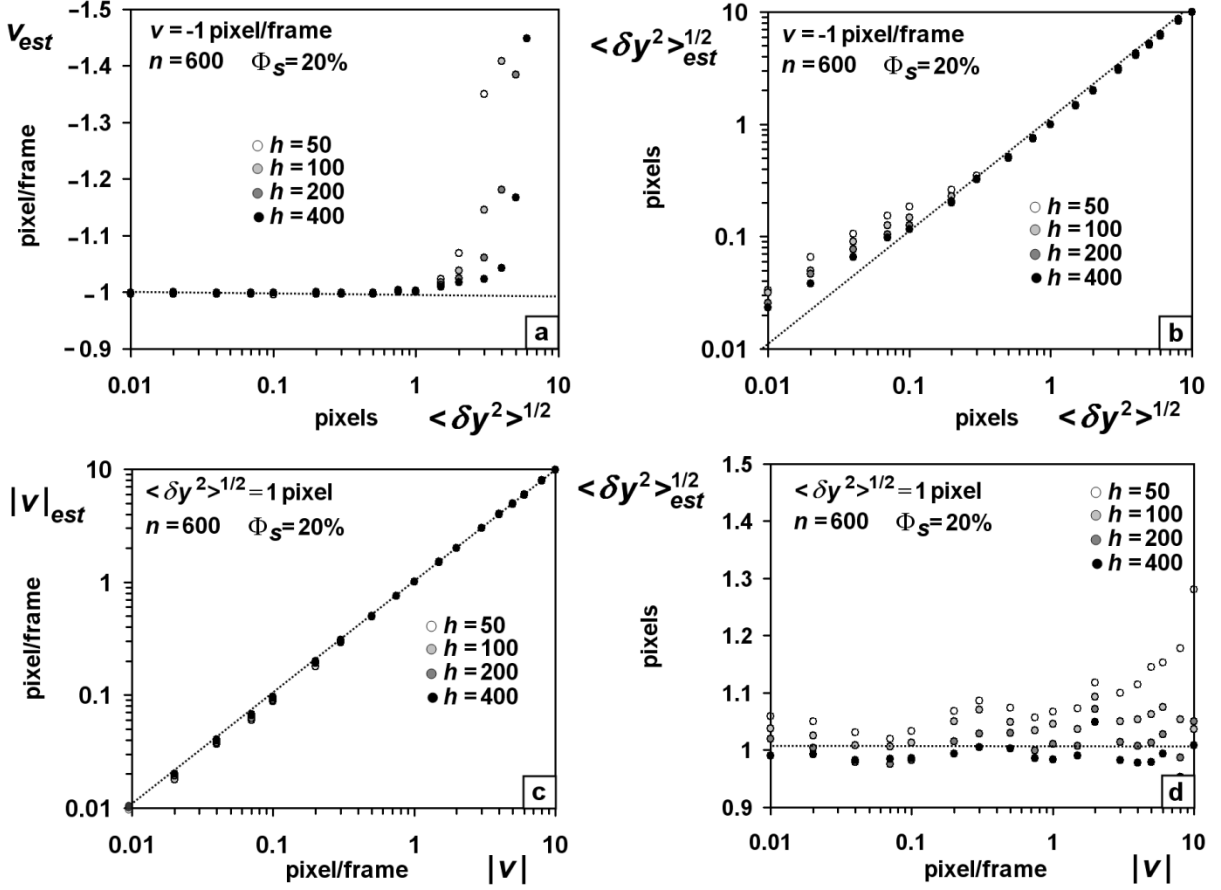


**Fig. C.13** Estimated velocity  $v_{est}$  and estimated rms fluctuation  $\langle \delta y^2 \rangle_{est}^{1/2}$  of disks moving either with a vertical velocity  $v = -1$  pixel/frame and variable rms fluctuation (a,b) or fixed rms fluctuation  $\langle \delta y^2 \rangle^{1/2} = 1$  pixel and variable vertical velocity (c,d). Least squares fits of Eqs. C.3 and C10 with  $n=600$  frames,  $h=400$  pixels and  $2a=5$  pixels.  $\Phi_s=20\%$  and  $\langle \delta I^2 \rangle^{1/2}=50$ .

Fig. C.13 displays a set of estimated data from the treatment of image sequences and illustrates the performance of the method. The rms vertical fluctuation is derived from Eq. (C.10) and from a second order polynomial fit to discrete data  $1/G_\psi^2(c)$ . Not surprisingly, the accuracy of estimations increases with the path length of trajectories and the height  $h$  of the ROI (Fig. C.13). The variance  $\alpha$  of the estimated velocity remains less than 2% and the variance  $\beta$  of the estimated rms fluctuation less than 10% for  $h=400$  pixels:

- **Estimated velocity:**  $\alpha < 2\%$  for  $0.01 \text{ pixel/frame} < |v| < 3 \langle \delta y^2 \rangle^{1/2} / \text{frame}$
- **Estimated rms fluctuation:**  $\beta < 10\%$  for  $0.1 \text{ pixel} < \langle \delta y^2 \rangle^{1/2} < 10 |v| * \text{frame}$

One may note that large rms fluctuation  $\langle \delta y^2 \rangle^{1/2} > 3$  pixels remain precisely measurable (Fig. C.13.b) despite much lower accuracy in the estimate of the disk velocity (Fig. C.13.a).

We have also performed Monte Carlo simulations to test the robustness of the method with respect to the disk density, the brightness distribution of disks and possible out of plane motion (Fig. C.14). A high surface density  $\Phi_s = 30\%$  of variable or of uniform brightness disks ( $\langle \delta I^2 \rangle^{1/2} = 50$  in Fig.C.14.a or  $\langle \delta I^2 \rangle^{1/2} = 0$  in Fig. C.14.b) hardly influences the shape of  $G_\psi(c)$  and the estimated rms fluctuation  $\langle \delta y^2 \rangle^{1/2}$  (Fig. C.15.a and b).

In experimental conditions, a particle that is free to move out of the observation plane cannot keep a constant brightness over time. To illustrate the incidence of brightness fluctuations, we suppose that disks have finite lifetimes, and introduce a Gaussian distribution of disk lifetime around the average value  $\mu$ . Random numbers are drawn at each time step of the image sequence to test the survival of each moving disk. A finite lifetime reduces the path length in the spatiotemporal window (Fig. C14.c) and causes a faster decay of  $G_\psi(c)$  (Fig. C.15.c). In this model, birth and death of the disks along the flow are statistically independent. In this context, we expect the brightness fluctuations to simply contribute as a multiplicative exponential term in the expression of the function  $G_\psi(c)$ :

$$G_\psi(c) \cong g_\psi(c) \left( 1 + \frac{2 \langle \delta y^2 \rangle c |\cos \psi|}{a^2} \right)^{-1/2} e^{-\frac{c |\cos \psi|}{\mu}} \quad (\text{C.11})$$

where  $t = c |\cos \psi|$  is the frame number related to a number  $c$  of pixels along the ridge line. In first approximation, the above equation describes the faster decay of the function  $G_\psi(c)$  (Fig. C.15.b). Consequently, out-of-plane motion spoil the estimation of rms disk fluctuations when considering time scales  $c |\cos \psi|$  larger than the average life time  $\mu$  of moving particles.

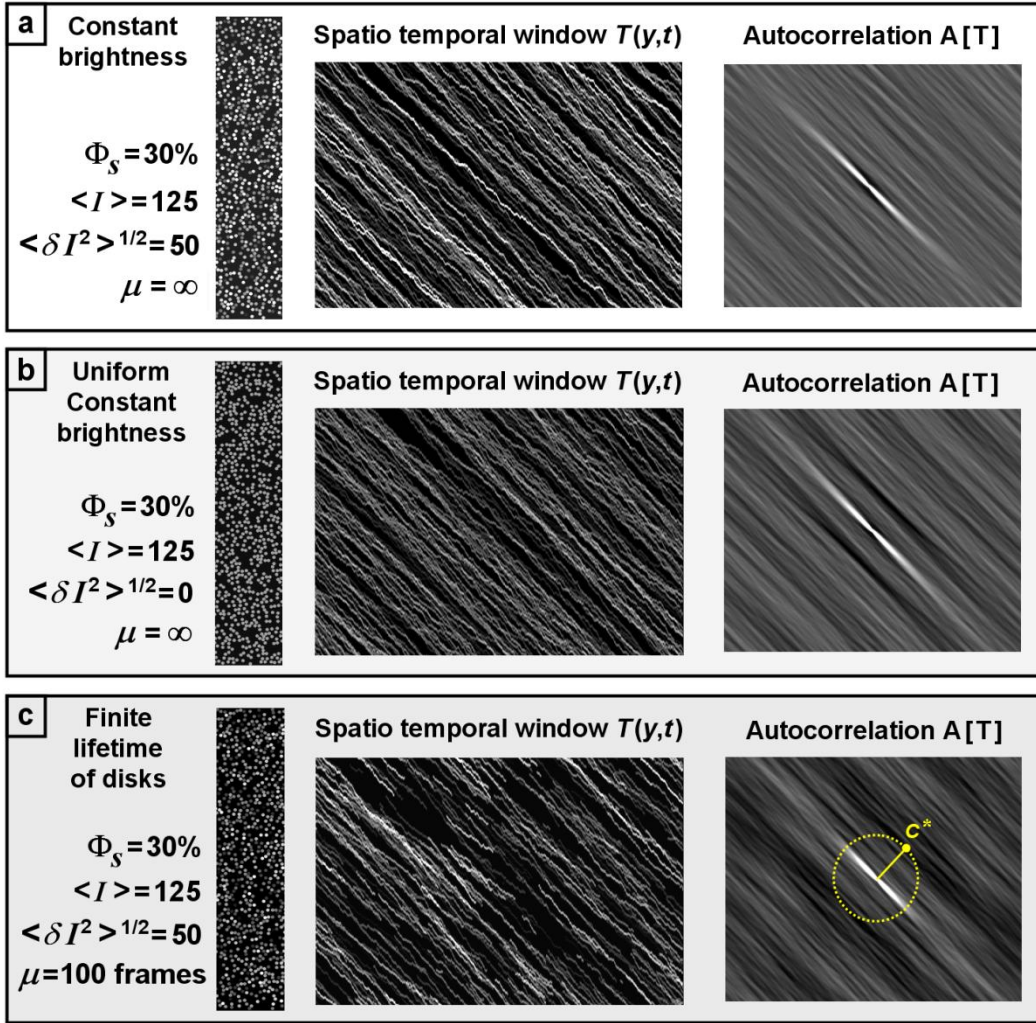


**Fig. C.14** Spatiotemporal window  $T(y,t)$  and autocorrelation image  $A[T]$  for the uniform vertical translation of disks with random fluctuations ( $v = -1$  pixel/frame,  $\langle \delta y^2 \rangle^{1/2} = 1$  pixel,  $n = 600$  frames,  $h = 400$  pixels and  $\Phi_s = 30\%$ ). (a) Gaussian distribution of constant disk brightness with  $\langle I \rangle = 125$  and  $\langle \delta I^2 \rangle^{1/2} = 50$ . (b) Uniform and constant disk brightness with  $\langle I \rangle = 125$  and  $\langle \delta I^2 \rangle^{1/2} = 0$ . (c) Disk motion with average lifetime  $\mu = 100$  frames.

For this reason, we will consider later discrete  $G_\psi(c)$  data over a finite domain  $c < c^*$ , covering only a few tens of pixels, to estimate  $\langle \delta y^2 \rangle^{1/2}$  without artefacts due to out-of-plane motion (Fig. C.14.c). However, the maximum time scale  $c^*$  should be long enough to analyse long-time displacements of disks in the diffusive regime.

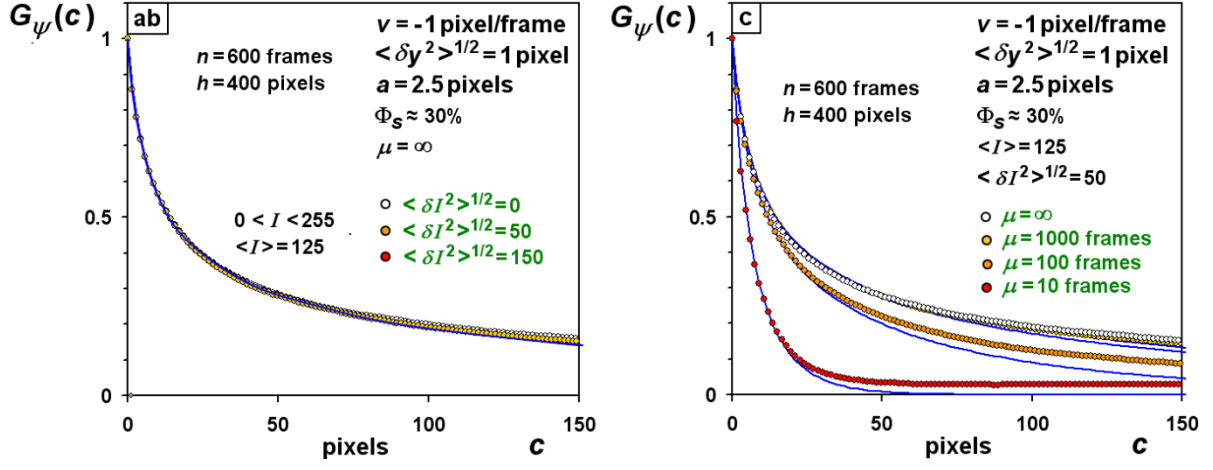


**Fig. C.15** Normalized discrete function  $G_\psi(c)$  along the  $\psi$  direction of the ridge line in the autocorrelation image as a function of the rms fluctuation  $\langle \delta I^2 \rangle^{1/2}$  of disk brightness (ab) or the average disk lifetime  $\mu$  in the spatiotemporal window (c). Theoretical predictions according to Eqs C6, C7 and C11 appear as blue solid lines.  $v = -1$  pixel/frame,  $\langle \delta y^2 \rangle^{1/2} = 1$  pixel,  $n = 600$  frames,  $h = 400$  pixels,  $\Phi_s \approx 30\%$ , and  $\langle I \rangle = 125$ .

#### C.1.d: Circular motion of disks with random angular fluctuations

In the framework of suspension flows in Couette geometry, particles are moving along circular paths, at least for a short period. Particle trajectories should then be analyzed in a polar coordinate system. For this purpose, we define a curved region of interest aligned in the flow direction as a portion of circular crown of radius  $r$ , thickness  $e = 2a$  and length  $h = r \Delta\theta$ , where  $\Delta\theta$  is the central angle which subtends the arc (Fig. C.16.a). The projection of grey levels within the curved ROI in a direction perpendicular to the flow motion gives a spatiotemporal window  $T(\theta r, t)$ . This construction, based on transforming discrete polar coordinates  $[\theta(t), r(t)]$  into discrete Cartesian coordinates  $(\theta r, t)$ <sup>5</sup>, still yields straight trajectories, in the simple case of a uniform circular motion of the disks (Fig. C.16.b). Using equations (C.3) and (C.10), the mean angular velocity  $\omega(r) = v_\theta / r$  of disks and the rms

<sup>5</sup> A bicubic interpolation of grey levels pixels is further necessary to reduce distortion effects associated to the reference change from discrete polar coordinates  $[\theta(t), r(t)]$  to discrete Cartesian coordinates  $(\theta r, t)$ .

angular fluctuation  $\langle \delta\theta^2 \rangle^{1/2}$  in the flow direction can be estimated from the tilt angle  $\psi(r)$  and from the decay of the  $G_\psi(c, r)$  along the ridge line<sup>6</sup>:

$$\omega(r) = \frac{f_t}{f_s r} \tan \psi(r) \quad \text{and} \quad G_\psi(c, r) = g_\psi(c) \left( 1 + \frac{2 r^2 \langle \delta\theta^2 \rangle c |\cos \psi|}{a^2} \right)^{-1/2} \quad (\text{C.12})$$

with  $g_\psi(c)$  obeying either Eq. (C.6) or Eq. (C.7) according to the value of  $n|\tan \psi|/h$  with respect to unity.

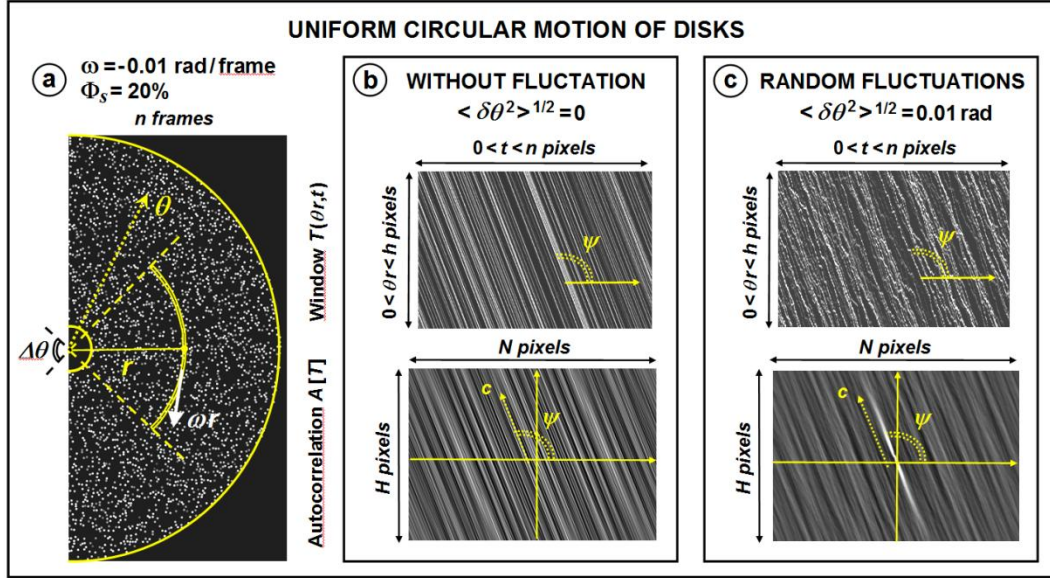


**Fig. C.16** Monte Carlo simulation of the uniform circular motion of disks with constant angular velocity  $\omega(r) = 0.01$  rad/frame (a) either without fluctuation (b) or with random angular fluctuations of rms amplitude  $\langle \delta\theta^2 \rangle^{1/2} = 0.01$  rad (c). Spatiotemporal window  $T(\theta r, t)$  and autocorrelation image  $A[T]$ . Simulation parameters :  $n = 600$  frames,  $h = 400$  pixels,  $50 \text{ pixels} < r < 480 \text{ pixels}$ ,  $\Phi_s = 20\%$ ,  $\langle I \rangle = 125$  and  $\langle \delta I^2 \rangle^{1/2} = 50$ .

Figure C.17 displays the results from an image sequence of disks (surface density  $\Phi_s = 20\%$ ) with a circular motion of constant angular velocity  $\omega = 0.01$  rad/s and subject to angular fluctuations with a rms amplitude  $\langle \delta\theta^2 \rangle^{1/2} = 0.01$  rad between two consecutive frames. For  $h = 600$  pixels and  $50 < r < 500$  pixels, Eq. (C.12) together with Eqs. (C.6) and (C.7) allow us

<sup>6</sup> One may also extract information about rms fluctuation  $\langle \delta r^2 \rangle^{1/2}$  of disks in the radial direction from projection of grey levels in the velocity direction to obtain a spatio temporal window  $T(r, t)$ . However, such an optical flow analysis requires a statistical treatment over a large number of circular ROIs that contain only a few disks (crown shaped ROIs of radius  $r$  with a small angular aperture  $\Delta\theta$  and a radial thickness  $e$  of approximately a few disk diameter).

to retrieve the values of  $\omega(r)$  and of  $\langle \delta\theta^2 \rangle^{1/2}$  within less than 6% uncertainty ( $0.5 \text{ pixel/frame} < v_\theta < 5 \text{ pixels/frame}$  and  $0.5 \text{ pixel} < r < \delta\theta^2 >^{1/2} < 5 \text{ pixels}$ ).

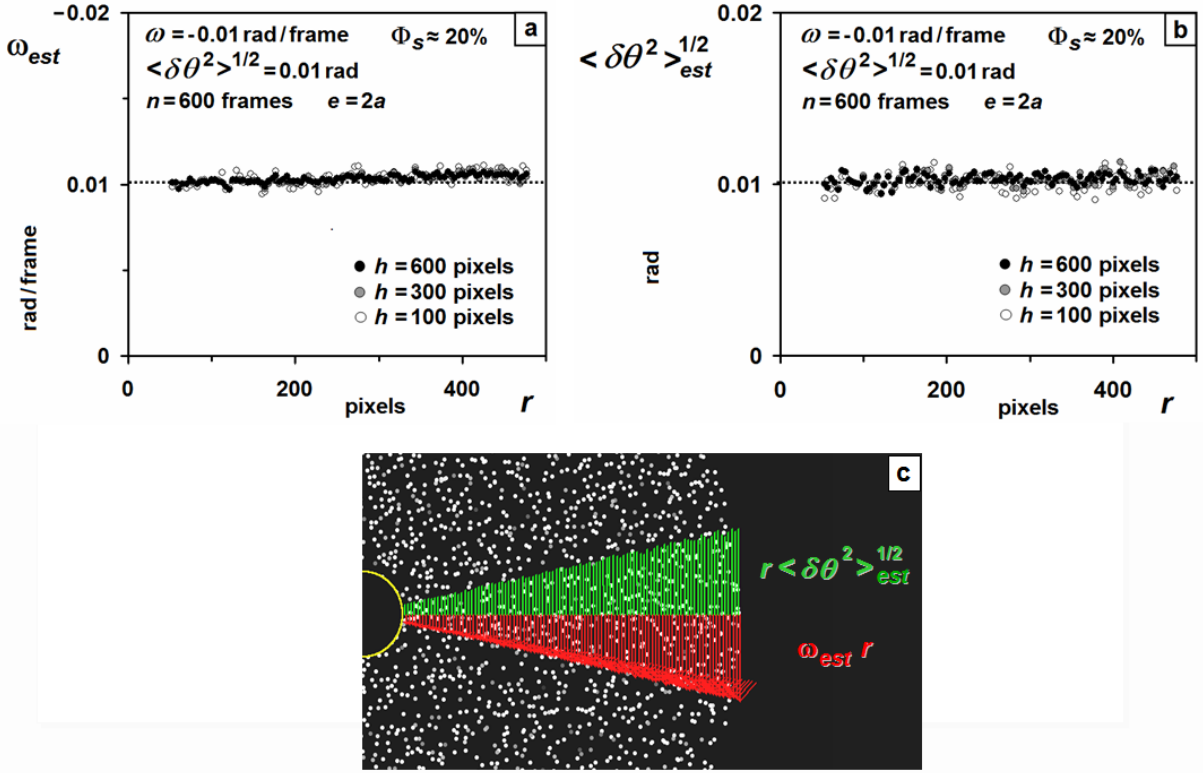


**Fig. C.17** Estimated angular velocity  $\omega_{est}(r)$  (a) and rms angular fluctuation  $\langle \delta\theta^2 \rangle_{est}^{1/2}$  (b) of disks with circular motion as a function of radius  $50 \text{ pixels} < r < 480 \text{ pixels}$ . (c) Estimated velocity profile  $\omega_{est} r$  (red arrows) and rms angular fluctuation profile  $r \langle \delta\theta^2 \rangle_{est}^{1/2}$  (green arrows). Least squares fits of Eqs. C.12. Simulation parameters :  $\omega(r) = 0.01 \text{ rad/frame}$ ,  $\langle \delta\theta^2 \rangle^{1/2} = 0.01 \text{ rad}$ ,  $n = 600 \text{ frames}$ ,  $h = 400 \text{ pixels}$  and  $2a = 5 \text{ pixels}$ .  $\Phi_s = 20\%$ ,  $\langle I \rangle = 125$  and  $\langle \delta I^2 \rangle^{1/2} = 50$ .

In the above simulations and analyses, we supposed that the particles only moved along the azimuthal coordinate. The picture turns out more complex if particles also move radially, due to shear-induced cross-streamline motion. This effect results in an augmented apparent  $\langle \delta\theta^2 \rangle^{1/2}$ , a phenomenon known as ‘‘Taylor dispersion’’ [Taylor 1953].

In this study we use a ROI whose width is about a particle diameter ( $e \cong 2a$ ). In such conditions we expect the optical flow method to be hardly sensitive to Taylor dispersion. We tested this prediction by simulation, with disks that made random excursions both in  $\theta$  and  $r$ . Results, shown in Fig. C.18, indeed confirm that the statement was correct, in so far as radial

fluctuations are smaller than those in azimuth:  $\langle \delta r^2 \rangle^{1/2} \leq r \langle \delta \theta^2 \rangle^{1/2}$ . However, larger radial motions lead to over-estimating the azimuthal fluctuations.

For concentrated particulate systems, the diffusion in the velocity direction is almost one order of magnitude larger than the other components of the diffusion tensor [Breedveld *et al.* 2002]. Consequently, one may use the optical method to analyze long-time displacements of particles in a suspension and estimate the rms fluctuation in the velocity direction despite local velocity gradients.

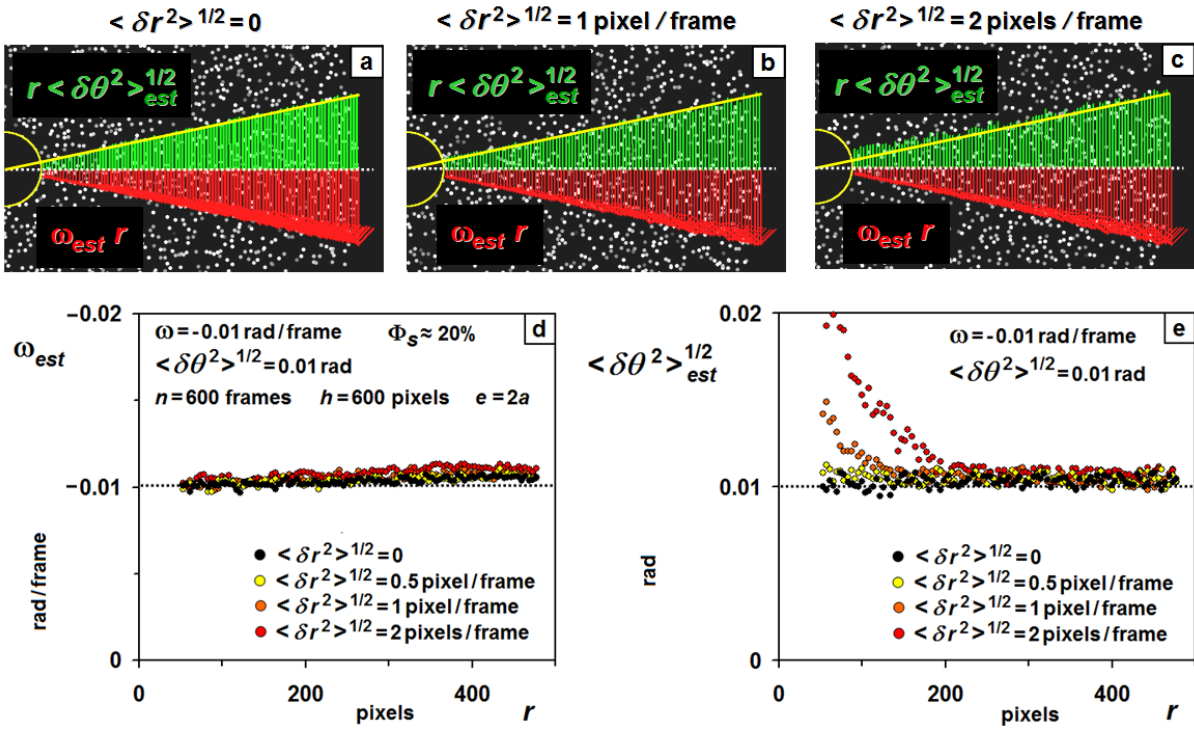


**Fig. C.18** (a,b,c) Uniform circular motion of disks with both angular fluctuations  $\langle \delta \theta^2 \rangle^{1/2} = 0.01$  rad and radial fluctuations  $\langle \delta r^2 \rangle^{1/2}$ . Estimated angular velocity  $\omega_{est}(r)$  (d) and estimated rms angular fluctuation  $\langle \delta \theta^2 \rangle_{est}^{1/2}$  (e) versus radius  $50 \text{ pixels} < r < 480 \text{ pixels}$ . Least squares fits of Eqs. C.12. Simulation parameters :  $\omega(r) = 0.01$  rad/frame,  $\langle \delta \theta^2 \rangle^{1/2} = 0.01$  rad,  $n = 600$  frames,  $h = 400$  pixels and  $2a = 5$  pixels.  $\Phi_s = 20\%$ ,  $\langle I \rangle = 125$  and  $\langle \delta I^2 \rangle^{1/2} = 50$ .

## C.2: Experimental setup and dynamic analysis of suspension flows

A Couette cell is certainly amongst the most convenient devices for analyzing the steady flow behaviour of complex materials. Proton Magnetizing Resonance Imaging (MRI) has been used to measure averaged velocity profiles in optically opaque suspensions through cross

correlation of MRI images of either the solid or liquid phase [Graham *et al.* 1991, Chow *et al.* 1994, Mueth *et al.* 2000, Ovarlez *et al.* 2006, Moucheron *et al.* 2010]. The MRI method images the flow field on intermediate length scales because of a limited capability to visualize and track individual particles. For optically transparent systems, the motion of individual particles can be imaged and tracked using laser sheet imaging to measure the pair distribution function [Leighton and Rampall 1993, Blanc *et al.* 2011], the averaged velocity [Lenoble *et al.* 2005, Weiderseiner thesis 2010, Weiderseiner *et al.* 2011], and the self-diffusion coefficient of particles in Couette flow [Breedveld *et al.* 2002, Orpe and Kudrulli 2007, Lorincz and Schall 2010]. Laser Doppler velocimetry (LDV), also applied to a refractive index-matched suspension, is a best suited technique for accurate spatial and temporal measurements of the mean and fluctuating parts of the velocity [Koh *et al.* 1994, Averbakh *et al.* 1997, Lyon and Leal 1998, Sharpey *et al.* 2002]. However, particle rotation and LDV system noise can alter the measurement of particle velocity fluctuations [Averbakh *et al.* 1997].

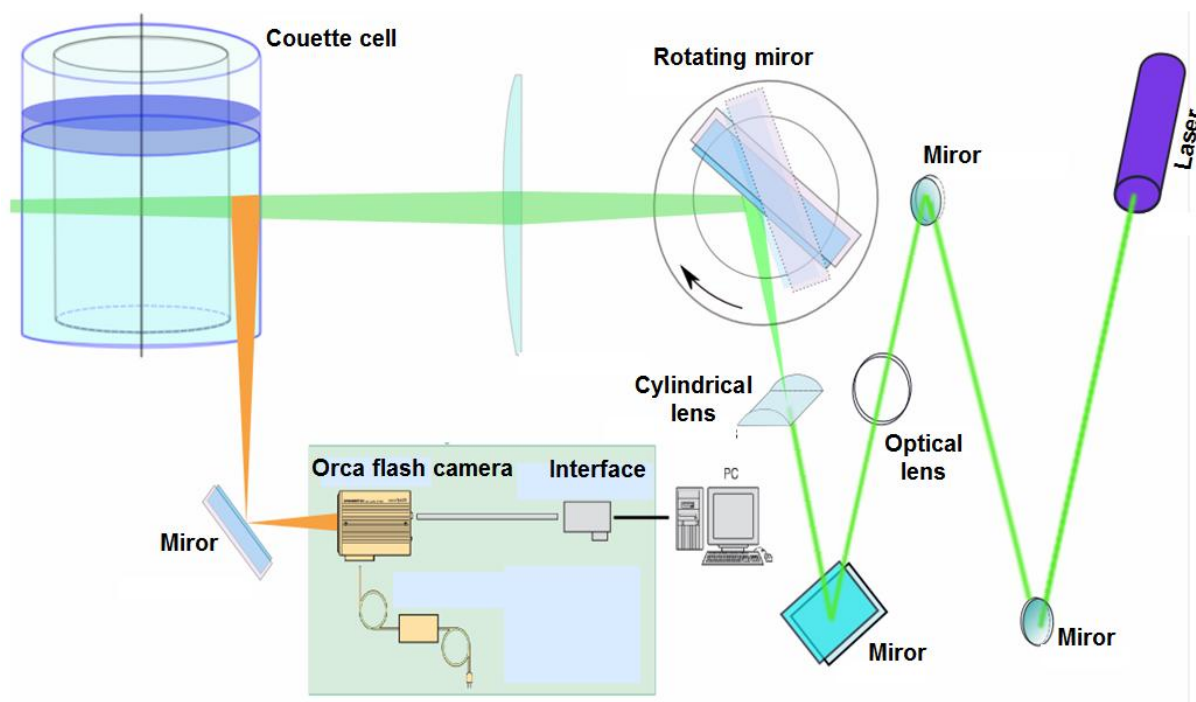


**Fig. C.19** *Experimental setup for the observation of fluorescent moving patterns excited with a thin horizontal laser sheet crossing the Couette cell.*

Here, video image sequences of our model suspensions in a Couette flow geometry are analysed with the previously described optical flow method to obtain both the local mean azimuthal velocity and the rms angular fluctuation of grey level patterns. For this purpose, a homemade videotrajctography plugin was developed in java for use with ImageJ image processing software [Schneider *et al.* 2012].

The Optical setup is largely identical to that implemented for concentration measurements (chapter D), except the use of two lenses to convert the laser beam into a horizontal laser sheet with a rotating mirror (Fig. C.19). Fluorescence is excited within the laser sheet (wavelength: 514 nm). Optical observation is performed from below through the bottom of the Couette cell, by means of a mirror that directs the fluorescence light to a camera (Hamamatsu Orca flash CMOS camera, with HImage Hamamatsu commercial software). The camera is positioned to observe only a part of the Couette cell over an angular sector of about 40 degrees ( $\approx 0.7$  radian). Fluorescence is collected through an orange filter, which is opaque to green light. An auxiliary camera allows us to observe the Couette cell from the side, and to measure the altitude  $z$  of the laser sheet, with  $z = 0$  taken at the bottom of the cell (the lower boundary of the suspension).  $z$  was varied between 3 and 20 mm, as for concentration measurements.

The suspension consists of 200 $\mu$ m PMMA spheres immersed in a viscous fluid C16-S150 matching the refractive index  $\approx 1.49$  of the particles. A mixture of Cargille fluids can also provide both a precise refractive index matching and density-matching (see Chapter B).

Initially the suspension is filled into the coaxial cavity (radius  $R_{out} = 20$ mm) and the inner cylinder (radius  $R = 15$ mm) is brought down so that the distance between the lower plane of the inner cylinder and the bottom plane of the outer cylinder spans a few millimeters (1.5mm). Before each shear experiment, a reproducible initial state is prepared by pre-shearing very gently the suspension during two days at an angular velocity  $\Omega = 0.005$  rad/s before increasing step by step the differential angular velocity between cylinders in the range from 0.11 rad/s up to 0.57 rad/s. After a waiting time of a few tens of minutes enough to reach a stationary regime, image sequences of 1000 frames (width  $\approx 1000$  pixels and height  $\approx 1500$  pixels) are collected with a frame rate  $f_t$  between 30Hz and 45Hz and recorded in a 8-bit uncompressed Tif format.

We can observe motions of tracers, i.e. the particles made fluorescent by impregnation of an organic dye (R6G). An alternate or complementary method is to use the fluorescence from the immersion fluid. In this case, we observe the motions of the small volumes of liquid between neighbouring particles. The liquid, either C16-S150 or the Cargille mixture, is very weakly fluorescent under illumination by the green laser; however this is not enough to provide a clear image with a large signal-to-noise ratio. We thus add a little amount of YELLOW 131SC dye, to increase the fluorescence (the same as for concentration experiments, see chapter D for more details) up to an acceptable level.

The fluorescence of both dyes can be excited simultaneously by the laser sheet. Fig. C.20.a shows an image obtained with the non density-matched suspension. The image contains

a multitude of grey spots, corresponding to the interstitial fluid, and a few much brighter spots: these were tracers ( $200\mu\text{m}$  in diameter) which were added to the suspension.

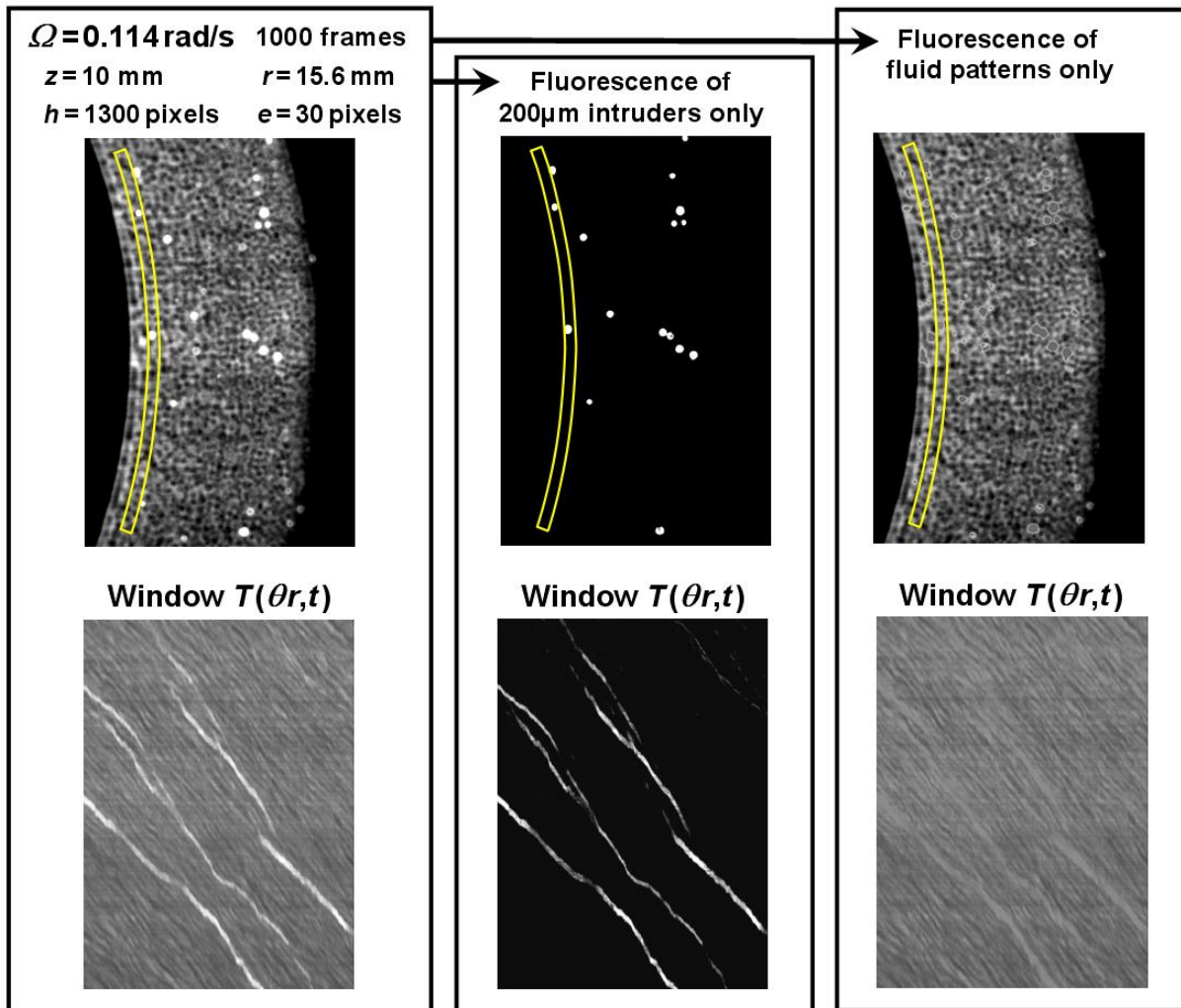


**Fig.C.20** Image sequences of a non-density matched flowing suspension of non fluorescent  $200\mu\text{m}$  diameter spheres (angular velocity of the inner cylinder  $\Omega = 0.114 \text{ rad/s}$ , altitude  $z = 10\text{mm}$ ) and spatiotemporal window  $T(\theta, t)$  at a radial distance  $r = 15.6\text{mm}$  ( $n = 1000$  frames,  $h = 1300$  pixels,  $e = 30$  pixels, frame rate  $33\text{Hz}$ ) in the non density-matched suspension. Fluorescence image and spatiotemporal window  $T(\theta, t)$  for both the fluorescent fluid and a few fluorescent  $200\mu\text{m}$  intruders (a). Grey level processing of the original image sequence and extraction of either the fluorescence of intruders only (b) or the fluorescence of the fluid (c).

An image sequence was recorded for an angular velocity  $\Omega = 0.114 \text{ rad/s}$  of the inner cylinder, at altitude  $z = 10\text{mm}$  (the height of the suspension was about  $27 \text{ mm}$ ). A grey level processing of the image sequence allows us to extract either the fluorescent intruders only (Fig. C.20.b) or the fluorescent fluid patterns only (Fig. C.20.c). Fig. C.20 shows different versions of the spatiotemporal image  $T(\theta, t)$  at radial distance  $r = 15.6\text{mm}$  (about three

particle diameters from the inner cylinder), to reveal trajectories corresponding to the fluid and those of the tracers (Fig. C.20.a).

Interestingly, the optical flow treatment of either the original or the processed image sequences gives the same tilt angle  $\psi \approx 129^\circ$  (Eq. C.12 yields  $\omega \approx 0.0186 \text{ rad/s}$  and  $v_\theta = \omega r \approx 290 \mu\text{m/s}$  with a temporal sampling frequency  $f_t = 33 \text{ pixels/s}$  and a spatial sampling frequency  $f_S = 0.14 \text{ pixel}/\mu\text{m}$ , Fig. C.21.a) and a very similar decay  $G_\psi(c)$  of the ridge line in the autocorrelation image (Fig. C.21.b).

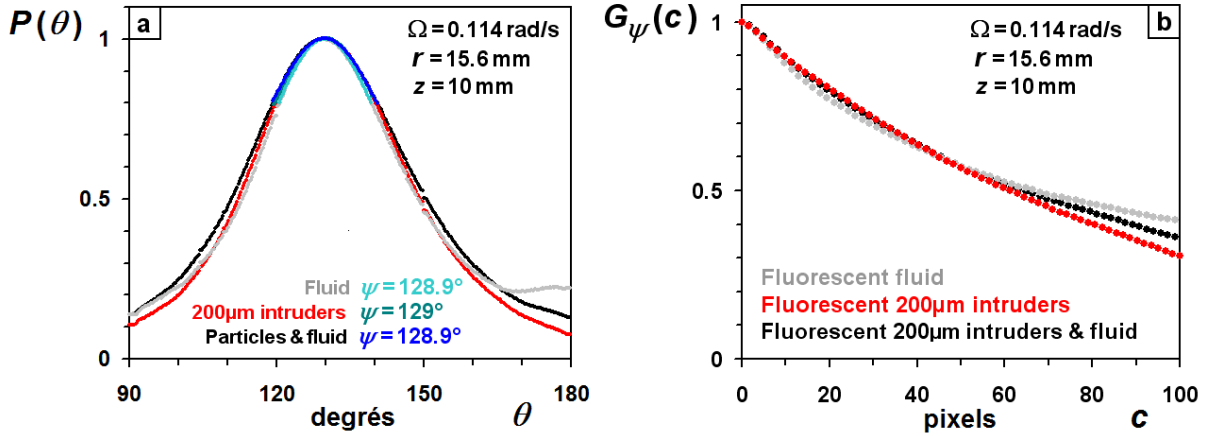


**Fig.C.21** Optical flow analysis of the original image sequence (black symbols) and after extraction of fluorescent fluid only (grey symbols) or fluorescent 200µm diameter intruders only (red symbols) in the non density-matched suspension. (a) Normalized grey level angular distribution  $P(\theta)$  and estimation of the tilt angle  $\psi$  of the ridge line from a Lorentzian fit (blue solid curves). (b) Normalized discrete function  $G_\psi(c)$  along the  $\psi$  direction of the ridge line. Angular velocity of the inner cylinder  $\Omega = 0.114 \text{ rad/s}$ , altitude  $z = 10 \text{ mm}$ ,  $n = 1000$  frames,  $h = 1300$  pixels,  $e = 30$  pixels and frame rate  $33 \text{ Hz}$ .

The motion of the fluorescent fluid patterns around the spherical particles (recall that these are not fluorescent, and then not directly visible) is indeed representative of particle dynamics, since the autocorrelation operation is invariant under an inversion of grey levels in the spatiotemporal window. One may use this property and analyze the displacement of fluorescent intruders introduced in the suspension to detect hypothetical differential motions between spheres of different sizes. For this purpose, we have recorded the motion of a few fluorescent intruders of diameter  $2a_i$  ( $2a_i = 6 \mu\text{m}$ ,  $32 \mu\text{m}$ ,  $100 \mu\text{m}$ ,  $200 \mu\text{m}$  or  $600 \mu\text{m}$  respectively) in a non density-matched suspension of  $200 \mu\text{m}$  spheres. We use a crown shaped ROI of radius  $r$  and constant thickness of about  $200 \mu\text{m}$ . Operating the same filtering as above; we extract the spatiotemporal windows  $T(\theta r, t)$  of the fluorescent intruders and of the fluorescent fluid (Fig. C.22). From the spatiotemporal windows, we deduce the mean angular

velocity  $\omega_i(r)$  of intruders only and the mean angular velocity  $\omega(r)$  of the fluorescent fluid patterns.

We find that small intruders move faster than the  $200\mu\text{m}$  host spheres near the inner cylinder while the motion of large intruders is slower near the wall (Fig. C.23). Velocity differences remain significant over a radial distance of about a few particle diameters. At large distance from the inner cylinder ( $r - R > 10a$ ), there is no more significant difference between the motion of intruders and that of the host particles (Fig. C.23).

Despite the roughness of the inner cylinder, gravity forces in non density-matched suspensions are responsible for slip phenomena (particularly in the deep layers of the suspension, see paragraph C.4). Wall slip is a possible cause for the slower motion of large intruders near the rotating inner cylinder since small particles can dodge among bigger ones.

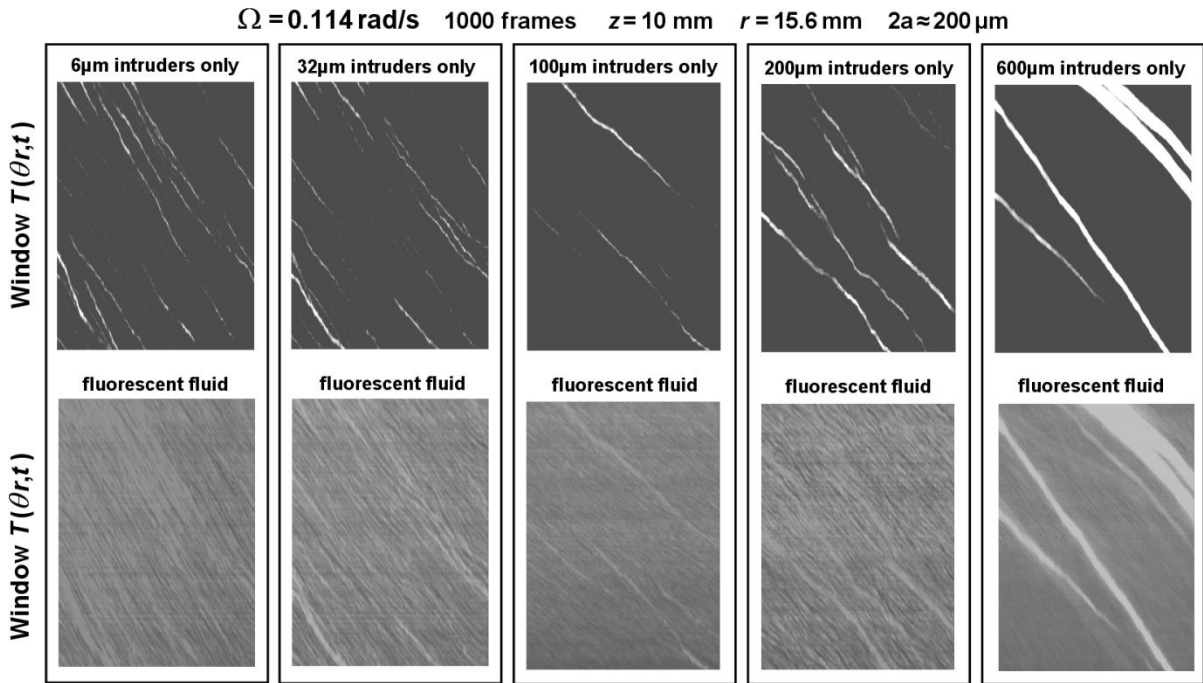


**Fig. C.22** Spatiotemporal windows  $T(\theta, t)$  of either fluorescent intruders only (top images) or the fluorescent fluid (bottom images) in the non density-matched suspension of non fluorescent spheres (diameter  $2a \approx 200\mu\text{m}$ ). Angular velocity of the inner cylinder  $\Omega = 0.114 \text{ rad/s}$ , altitude  $z = 10\text{mm}$ ,  $r = 15.6\text{mm}$ ,  $n = 1000$  frames,  $h = 1300$  pixels,  $e = 30$  pixels, frame rate  $33H$  and spatial frequency sampling  $f_S \approx 0.135 \text{ pixel}/\mu\text{m}$ .

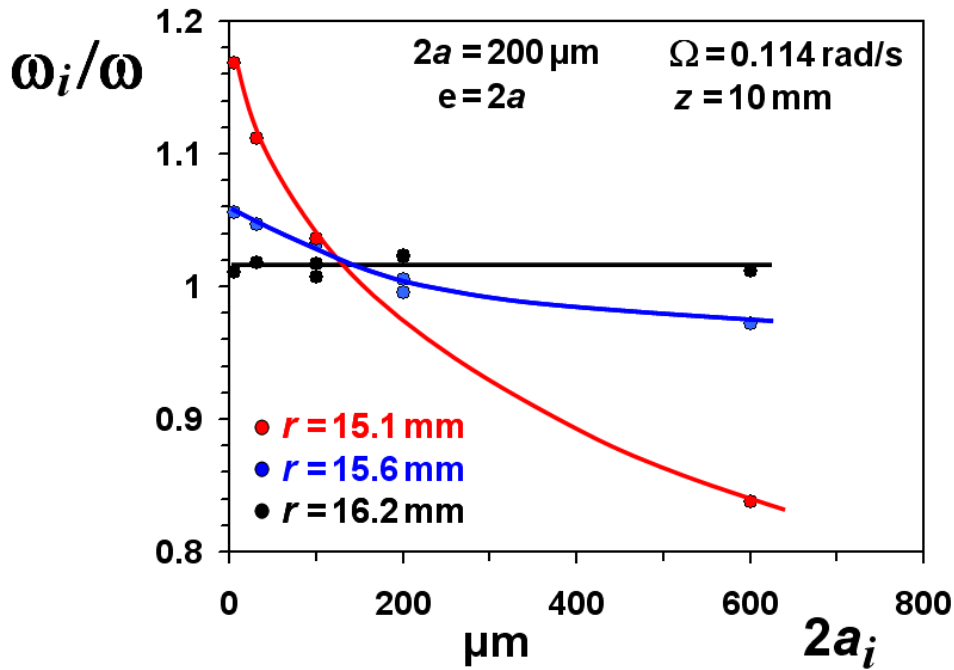


**Fig. C.23** Dimensionless angular velocity  $\omega_i(r)/\omega(r)$  of fluorescent intruders in the non density-matched suspension of non fluorescent spheres (diameter  $2a = 200\mu\text{m}$  and angular velocity  $\omega(r)$ ) versus the intruder diameter  $2a_i$  for different radial position  $r$  of the ROI (length  $h = 1300$  pixels, width  $e = 30$  pixels). Angular velocity of the inner cylinder  $\Omega = 0.114$  rad/s, altitude  $z = 10$  mm,  $n = 1000$  frames, frame rate 33Hz and spatial frequency sampling  $f_S = 0.135$  pixel/ $\mu\text{m}$ .

### C.3: Dynamics of density – matched suspensions

We now consider particles immersed in a fluorescent density-matched fluid (mixture of Cargille fluids, see Chapter B). No particle sedimentation or creaming can be observed after a time delay of about a few hours. Careful index matching of the fluid enables particle imaging deep in the suspension (altitude  $z < 25$  mm). The optimal matching temperature was determined by minimizing the scattering of a laser beam through the suspension, and found to be about  $22^\circ\text{C}$ . Experiments were performed at this temperature, within  $\pm 0.5^\circ\text{C}$ . Note that a temperature variation of  $1^\circ\text{C}$  is enough to alter the refractive index-matching. Unlike classical DPIV techniques, the optical flow method is sensitive to the motion of grey levels patterns and therefore remains very robust in cases of degraded optical contrast due to refractive index mismatch. A neutrally buoyant and transparent suspension of  $200\mu\text{m}$  diameter PMMA spheres was prepared with a mean volume fraction  $\tilde{\Phi} \approx 55\%$  and filled into the Couette cell (suspension height  $H \approx 30$  mm). Furthermore, great care was taken for the adjustment of the

coaxiality of cylinders since a weak mechanical mistuning distorts the particle trajectories, especially near the rotating cylinders.

Figure C.24 shows the spatiotemporal windows  $T(\theta, r, t)$  at altitude  $z = 10$  mm from the bottom plane for three different radial positions. Only the inner cylinder was rotating, at  $\Omega = 0.114$  rad/s. The mean tilt angle  $\pi - \psi(r)$  of trajectories decreases with the distance  $r - R$  from the inner cylinder (Fig. C.24). The local angular velocity  $\omega(r) = (f_t / f_S r) \tan \psi(r)$  of particles is estimated from a Lorentzian fit to the angular grey level distribution  $P(\theta)$  (Fig. C.25.a). However a complication arises because of a diffuse bright horizontal line in the autocorrelation images, see Fig. C.24.b. This line is due to defects in the PMMA parts of the Couette cell, which generate static parasitic patterns across the image sequence. Fortunately enough, this only has a very little influence on  $P(\theta)$  if the radius  $p$  of the integration circle is made small enough (the software allows the user to adjust the value of  $p$ ).

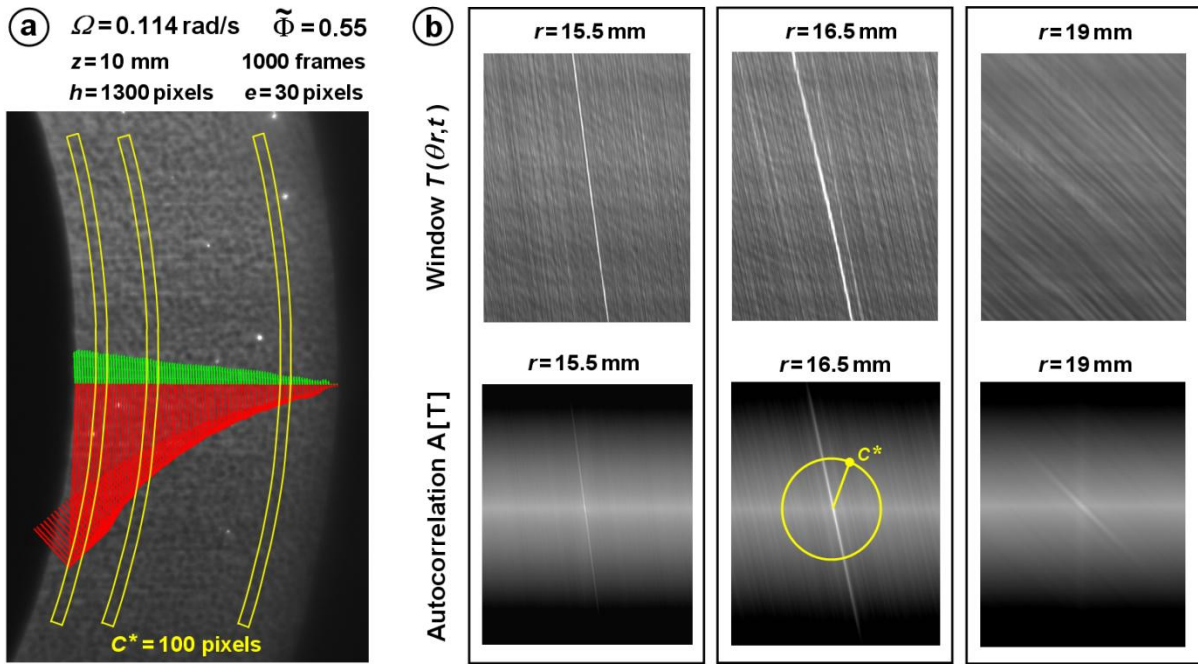


**Fig. C.24** Optical flow analysis of the 55% density-matched suspension at radial distance  $r = 15.5$  mm,  $16.5$  mm and  $19$  mm (angular velocity of the inner cylinder  $\Omega = 0.114$  rad/s, altitude  $z = 10$  mm and  $H \approx 30$  mm). (a) Angular velocity profile  $\omega(r)$  (red arrows) and rms angular fluctuation (green arrows) for  $c^* = 100$  pixels. (b) Spatiotemporal windows  $T(\theta, r, t)$  and autocorrelation image  $A[T]$  for several radial position  $r$  of the crown shaped ROI.  $f_t = 33$  Hz and  $f_S = 0.135$  pixel/ $\mu$ m.

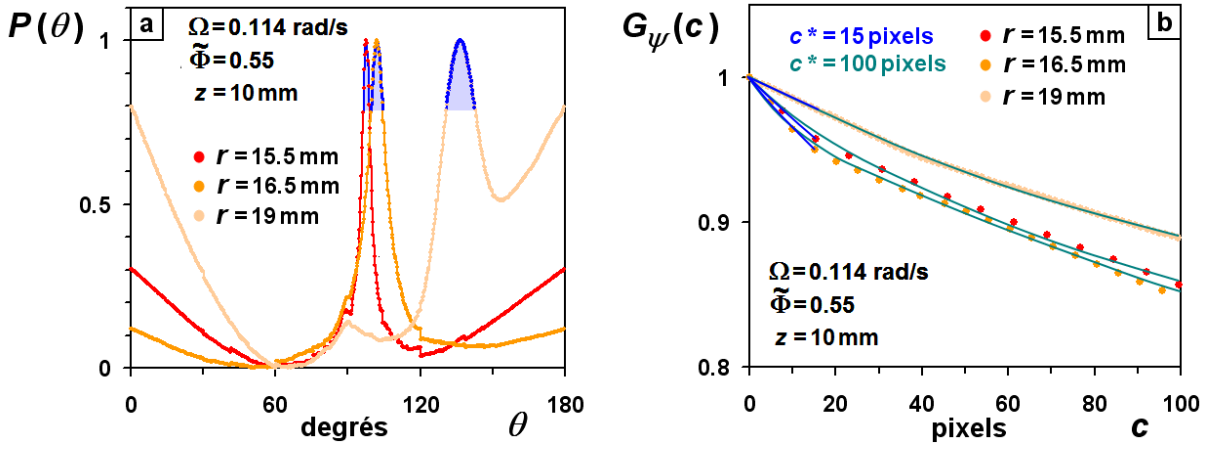


**Fig. C.25** Optical flow analysis of the 55% density-matched suspension at radial distance  $r = 15.5\text{mm}$ ,  $16.5\text{mm}$  and  $19\text{mm}$  (angular velocity of the inner cylinder  $\Omega = 0.114\text{rad/s}$ , altitude  $z = 10\text{mm}$ , and  $H \approx 30\text{mm}$ ). (a) Normalized grey level angular distribution  $P(\theta)$  and estimation of the tilt angle  $\psi(r)$  of the ridge line from a Lorentzian fit (blue solid curves). (b) Normalized discrete function  $G_\psi(c)$  along the  $\psi$  direction of the ridge line and second order polynomial fit of discrete data  $1/G_\psi^2(c)$  over the finite domain  $c < c^* = 15$  pixels or  $c < c^* = 100$  pixels.  $n = 1000$  frames,  $h = 1300$  pixels,  $e = 30$  pixels,  $f_t = 33\text{Hz}$  and  $f_s = 0.135$  pixel/ $\mu\text{m}$ .

The decay of the discrete grey level signal  $G_\psi(c)$  along the ridge line further gives information about particle fluctuations in the velocity direction (Fig. C.25.b). The rms angular fluctuation  $\langle \delta\theta^2 \rangle^{1/2}$  is derived using Eq. (C.12), through a second order polynomial fit to discrete data  $1/G_\psi^2(c)$ . Fitting is performed over a finite domain  $c < c^*$ , to be insensitive to out-of-plane particle motion (Fig. C.24.b). We find that  $c^*$  may be chosen between 15 and 100 pixels, with no definite differences on the estimated rms fluctuation (Fig. C.25.b). For observation time  $c |\cos\psi| / f_t$  greater than the inverse  $1/|\dot{\gamma}|$  of the local shear rate, the graph contains enough statistics about the diffusion of particles in the flow direction and the diffusion coefficient  $D_{\theta\theta}$  can be obtained from  $G_\psi(c, r)$  through the relation:

$$G_\psi(c, r) = g_\psi(c) \left( 1 + \frac{2 D_{\theta\theta} c |\cos\psi|}{f_t a^2} \right)^{-1/2} \quad \text{with} \quad D_{\theta\theta} = r^2 \langle \delta\theta^2 \rangle f_t \quad (\text{C.13})$$

The image sequence is analyzed sequentially with the videotrajectory plugin over 100 ROIs (height  $h = 1300$  pixels and width  $e = 2a$ ) to obtain the angular velocity profile  $\omega(r)$  and the diffusion coefficient  $D_{\theta\theta}(r)/a^2$  from Eq. C.13 (Fig. C.24.a). The computing

time of an image sequence ( $n = 1000$  frames and 100 ROIs) with a personal computer is about 15 minutes, much shorter than the time necessary to extract time resolved velocities by cross correlating consecutive images with a DPVI method.

The measured profile is shown in dimensionless form,  $\omega(r)/\Omega$ , in Fig. C.26.a. We find that the suspension flows over the whole gap, with about a 2-decade decrease of the velocity from inner to outer cylinder (Fig. C.26.a). The high spatial resolution and accuracy of the optical flow method allows us to estimate the dimensionless local shear rate from the relation  $|\dot{\gamma}(r)|/\Omega = (r/\Omega)|\partial\omega(r)/\partial r|$  (Fig. C.26.b). The local shear rate  $|\dot{\gamma}(r)|$  seems to decrease exponentially with the radial distance  $r$ , starting from  $1\text{s}^{-1}$  close to the inner cylinder, down to  $0.2\text{s}^{-1}$  in the peripheral region.

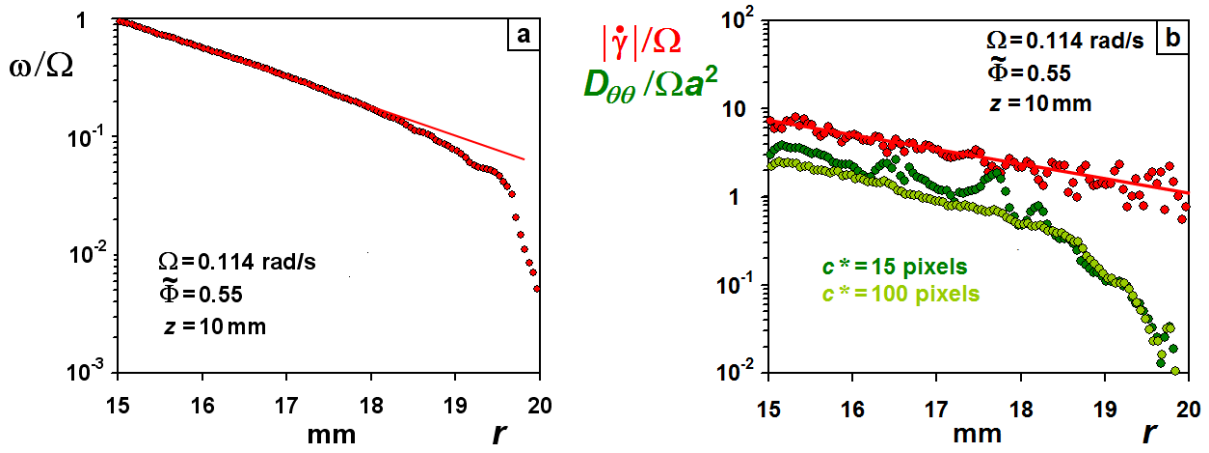


**Fig. C.26** (a) Semi-log plot of the dimensionless angular velocity profile  $\omega(r)/\Omega$  of the 55% density-matched suspension (angular velocity of the inner cylinder  $\Omega = 0.114\text{rad/s}$ , altitude  $z = 10\text{mm}$  and  $H \approx 30\text{mm}$ ). (b) Semi-log of the dimensionless shear rate profile  $|\dot{\gamma}(r)|/\Omega = (r/\Omega)\partial\omega(r)/\partial r$  and dimensionless diffusion coefficient  $D_{\theta\theta}(r)/\Omega a^2$  ( $c^* = 15\text{pixels}$  or  $c^* = 100\text{pixels}$ ).

Figure C.26.b shows the dimensionless diffusion coefficient  $D_{\theta\theta}(r)/\Omega a^2$ . The latter also decreases exponentially with  $r$ , but only up to  $r \cong 18.5\text{mm}$ , and drops more abruptly close to the outer cylinder. The reduced observation time  $c^*|\cos\psi||\dot{\gamma}|/f_t$  represents the strain and is of order 1 for  $c^* = 100$ , large enough to consider a diffusive regime [Taylor 1953, Lorincz and Schall 2010, Pine *et al.* 2005].

The weak dependence of the estimated diffusion coefficient  $D_{\theta\theta}(r)$  with respect to the  $c^*$  value (Fig. C.26.b) further confirms that the observation time scale  $c^*|\cos\psi|/f_t$  is long

enough to capture diffusive processes. The accuracy of the diffusion coefficient estimation increases with the observation time  $c^*|\cos\psi|/f_t$  but out-of-plane motion can occur. For this reason, we now consider an intermediate value  $c^* = 50$  to characterize the diffusive processes.

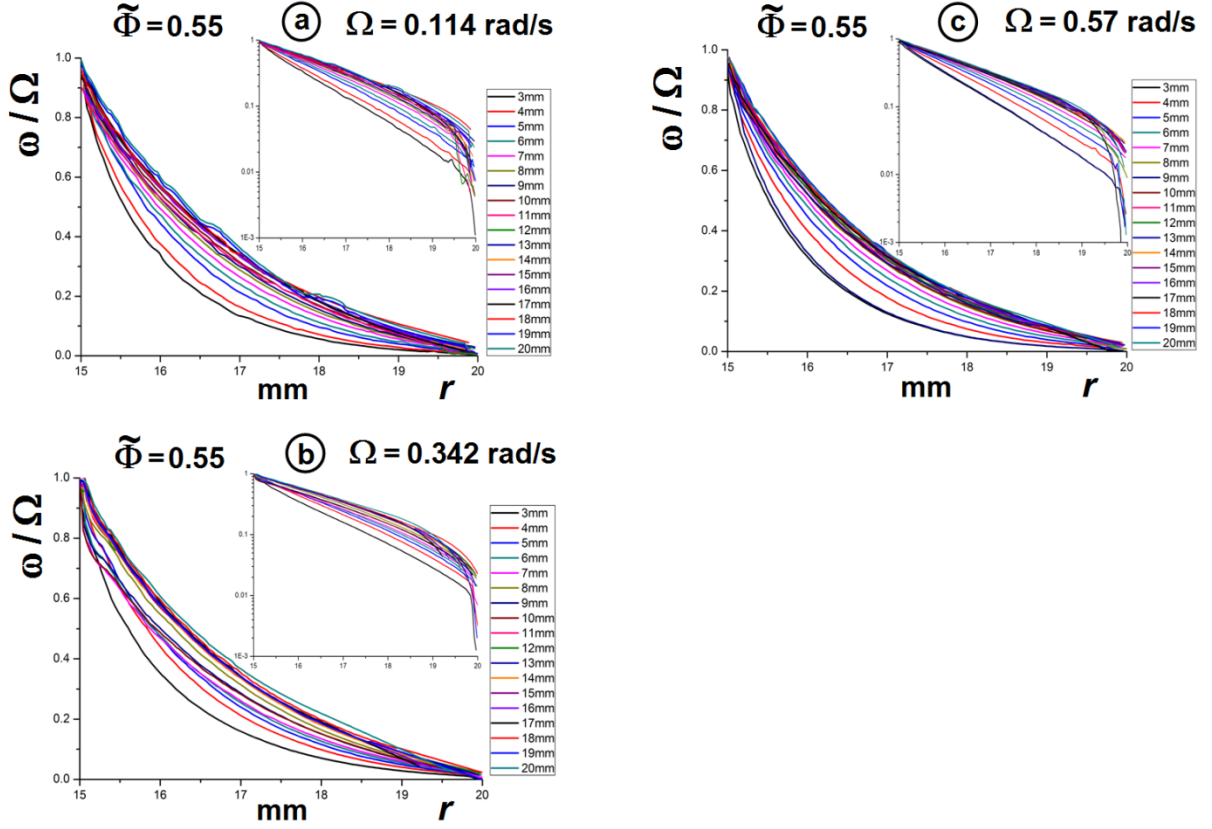


**Fig. C.27** Dimensionless angular velocity profile  $\omega(r, z)/\Omega$  of the 55% density-matched suspension for inner cylinder angular velocity  $\Omega = 0.114 \text{ rad/s}$  (a),  $\Omega = 0.342 \text{ rad/s}$  (b) and  $\Omega = 0.57 \text{ rad/s}$  (c). Altitudes  $3 \text{ mm} < z < 20 \text{ mm}$  and  $H \approx 30 \text{ mm}$ .

We have performed experiments for increasing values of  $\Omega$ , from 0.114 to 0.57 rad/s (Fig. C.27). We verified that angular velocity profiles  $\omega(r, z)$  obtained after a few days of shearing remained the same within experimental error and then, were representative of stationary regime. Furthermore, increasing or decreasing  $\Omega$  has no significant influence upon the velocity profiles.  $\omega(R, z)$  is close to  $\Omega$  (Fig. C.27), which means that wall-slip is negligible in the density matched suspension. We find that velocity profiles  $\omega(r, z)$  in the stationary regime are weakly dependent upon  $\Omega$  and roughly  $z$ -invariant (for  $10 \text{ mm} < z < 20 \text{ mm}$  in our experiment). This conclusion is in line with observations by Ovarlez [Ovarlez *et al.* 2006] for the flow of another kind of density-matched suspension, in a slightly larger Couette geometry. Conversely, profiles in the bottom part of the Couette cell ( $z < 10 \text{ mm}$ ) are not  $z$ - and  $-\Omega$  invariant. The reason for that is most probably the proximity of the bottom

part, which imposes zero velocity along the  $z = 0$  plane. The transition to  $z$ - and  $-\Omega$  invariance thus occurs for  $z$  larger than about twice the gap ( $R_{out} - R$ ) between cylinders (Fig. C.27). A similar crossover was observed for concentration profiles  $\Phi(z)$  in the bottom region of the sheared density matched suspension (Chapter D, paragraph D.2).

Semi-log inserts in Fig. C.27 indicates a roughly exponential decay of  $\omega(r, z)$ , starting from the inner cylinder through almost the whole gap. One may define an experimental decay length  $r^* - R$  such that the reduced angular velocity  $\omega(r^*, \Omega) / \omega(R, \Omega)$  takes the value  $1/e$  ( $e=2,718..$  is the Neper constant). The reduced decay length  $\xi_{exp}(z, \Omega) = (r^* - R) / (R_{out} - R)$  displays a rather constant value  $0.38 < \xi_{exp} < 0.40$  independent of  $\Omega$  and  $z$  in the suspension, except in the bottom region of the Couette cell (Fig. C.28). The lower values  $0.2 < \xi_{exp}(z, \Omega) < 0.35$  at low altitudes ( $z < 10\text{mm}$ ) correlate with slightly higher particle concentrations in this region ( $\bar{\Phi}(r, z = 3\text{mm}) - \bar{\Phi}(r, z = 15\text{mm}) \approx 0.2\%$  for  $17\text{mm} < r < 19\text{mm}$ , see Chapter D, paragraph D.2) and more pronounced migration effects in the steady state regime.

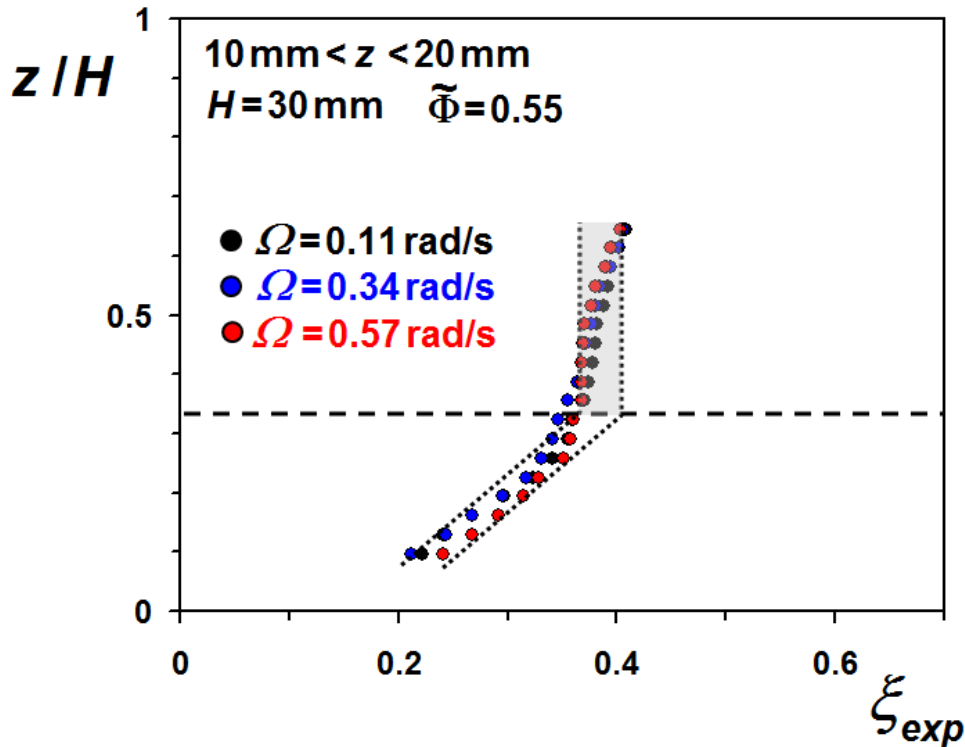


**Fig. C.28** Dimensionless decay length  $\xi_{exp}(z, \Omega) = (r^* - R) / (R_{out} - R)$  versus the reduced altitude  $z/H$  in the 55% density-matched suspension for  $\Omega = 0.114, 0.342$  and  $0.57\text{rad/s}$ .

The shear rate  $\dot{\gamma}(r, \Omega) = r \partial \omega(r, \Omega) / \partial r$  derived from the experimental angular velocity profile  $\omega(r, \Omega)$  was averaged over six different altitudes between 10mm and 15mm. Except within the first particle layer in contact to the inner cylinder ( $R < r < R + 2a$ ), the  $z$ -averaged shear rate  $\left| \langle \dot{\gamma}(r, \Omega) \rangle_z \right|$  seems to decrease exponentially with  $r$  through the whole gap (Fig. C.29). The non linear velocity gradient in the first layer may be related to structuration of the sheared suspension in this region (see the concentration profiles, chapter D).

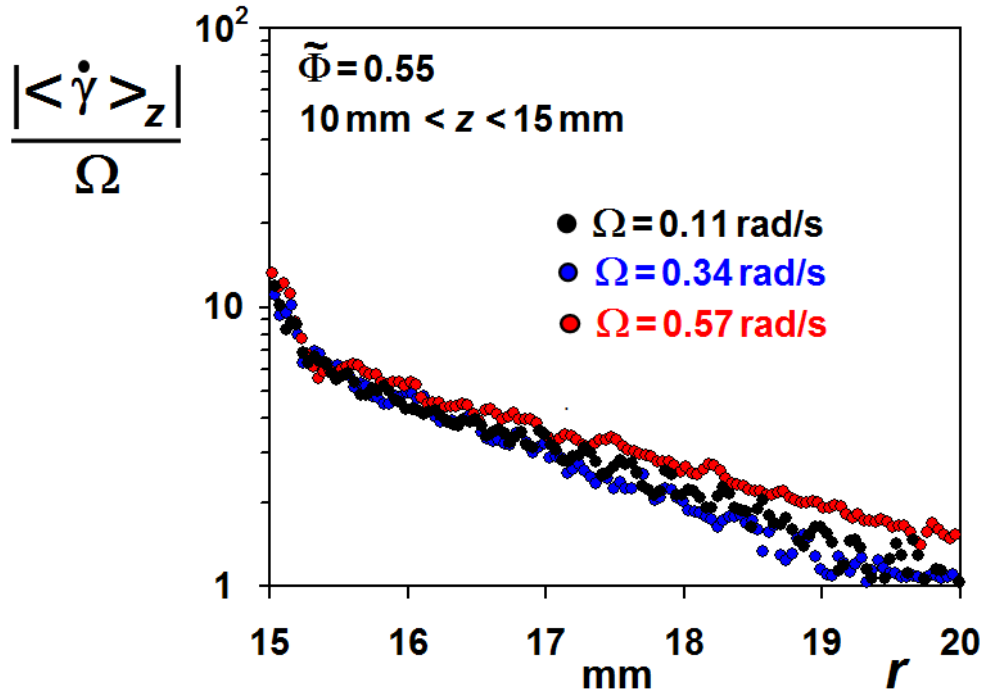


**Fig. C.29** Dimensionless  $z$  averaged shear rate profile  $\left| \langle \dot{\gamma}(r, \Omega) \rangle_z \right| / \Omega$  in the 55% density-matched suspension for  $\Omega = 0.114$ ,  $0.342$  and  $0.57 \text{ rad/s}$ . Altitudes  $10 \text{ mm} < z < 15 \text{ mm}$  and  $H \approx 30 \text{ mm}$ .

Shear induced self diffusion of particles in a suspension results from excluded volume effects since hard spheres are displaced when passing each other, and give rise to macroscopic particle migration in non homogeneous flows [Breedveld *et al.* 2002, Leighton and Acrivos 1987, Mills and Snabre 1995]. For long-time displacements of particles ( $c|\dot{\gamma}|/f_t > 1$ ) and diffusive processes, dimensional analysis shows that the components of the self diffusion tensor scale as  $q(\Phi)\dot{\gamma}a^2$  with a prefactor  $q(\Phi)$  depending upon the local volume fraction. To date,

experimental results have been reported on diffusion coefficients  $D_{rr}$  and  $D_{zz}$  [Leighton and Acrivos 1987a, Leighton and Acrivos 1987b, Acrivos *et al.* 1992] for buoyant spheres in a viscous fluid and particle volume fraction  $\Phi < 0.5$ . Only a few experimental works concern the more delicate measurement of the diffusion coefficient  $D_{\theta\theta}$  in the velocity direction. Breedveld *et al.* [Breedveld *et al.* 2002] tracked particles in a narrow gap counter-rotating Couette cell and found  $D_{\theta\theta} \approx 0.6 \dot{\gamma} a^2$ , larger than  $D_{rr}$  and  $D_{zz}$  by about one order of magnitude, in line with the numerical results of the Stokesian dynamics method [Sierou and Brady 2004].

The video records in our experiments with the 55% suspension indeed show that particles can hardly pass each other. The picture is reminiscent of the formation of transient clusters as in traffic jams on highways. Jamming effects give rise to large velocity changes in the flow direction, while transitions to a nearby layer are rather rare events. This naïve description may explain the higher values of  $D_{\theta\theta}$  compared to more constrained diffusion in transverse directions.

Figure C.30.a gathers the measurements of the  $z$ -averaged dimensionless diffusion coefficient  $D_{\theta\theta}(r, \Omega) / a^2 |\dot{\gamma}(r, \Omega)|$  in the velocity direction as a function of the radial distance  $r$  for several values of the angular velocity  $\Omega$  of the inner cylinder (for each  $\Omega$ , experimental data are averaged over six different altitudes between 10mm and 15mm). The data are further combined with the experimental measurements of particle volume fraction  $\Phi(r, \Omega)$  for altitudes  $10\text{mm} \leq z \leq 15\text{mm}$  (Fig. C.30.b), see chapter D.2. Remarkably,  $D_{\theta\theta} / a^2 |\dot{\gamma}|$  remains rather constant, between 0.4 and 0.5, for  $0.53 < \Phi < 0.55$ , and decreases roughly linearly above a critical volume fraction, located between 55% and 56% (Fig. C.30.b). Note that the crossover occurs around the so-called “random-loose packing” concentration ( $\Phi_{RLP} \cong 0.555$  for hard spheres), following the terminology proposed by Onoda and Liniger [Onoda and Liniger 1990].

The value of  $D_{\theta\theta} / a^2 |\dot{\gamma}| \approx 0.4 \div 0.5$  well agrees with experimental data from Breedveld [Breedveld *et al.* 2002] for particle concentration  $0.2 < \Phi < 0.5$  [Breedveld *et al.* 2002]. The lower amplitude of  $D_{\theta\theta}$  at  $\Phi > \Phi_{RLP}$  indicates a dramatic decay in velocity changes along the flow direction. Yet, one may debate about the significance of the measured diffusion coefficient in a highly concentrated suspension because of the non diffusive behavior over a too short observation time scale. Nevertheless, the decrease of the rms angular fluctuation above 55% indeed corresponds to the occurrence of collective phenomena (finite sized transient clusters) and jamming effects. As a suggestion for future studies, one may use counter-rotation of the cylinders to keep particles at given  $r$  within the spatio-temporal

window. This would help analyzing particle fluctuations in highly concentrated suspensions over an extended range of time scales.

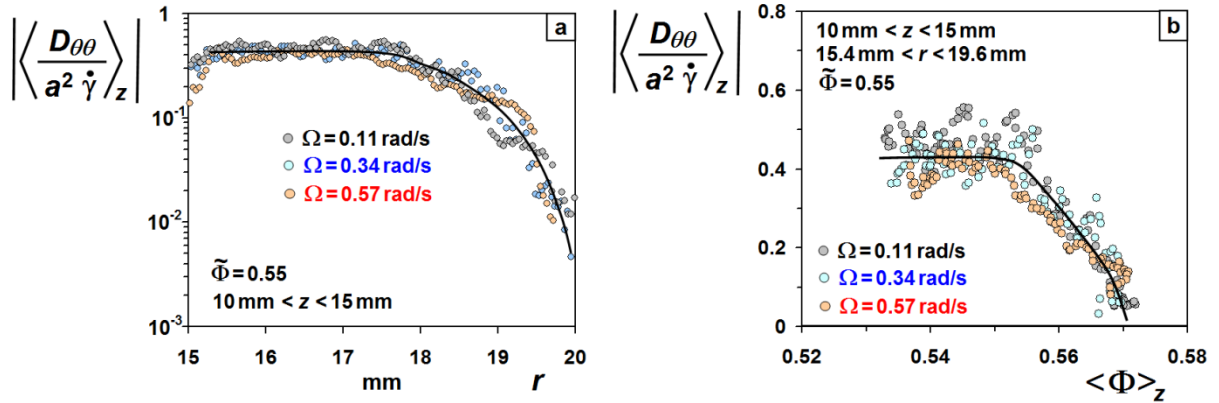


**Fig. C.30** Dimensionless  $z$ -averaged diffusion coefficient  $\left\langle D_{\theta\theta}(r, \Omega) / a^2 \dot{\gamma} \right\rangle_z$  in the 55% density-matched suspension versus the radial distance  $r$  (a-panel) or the  $z$  averaged particle concentration  $\langle \Phi \rangle_z$  (b-panel) for  $\Omega = 0.114, 0.342$  and  $0.57$  rad/s. Altitudes  $10 \text{ mm} < z < 15 \text{ mm}$  and  $H \approx 30 \text{ mm}$ .

## C.4: Dynamics of non density – matched suspensions

### C.4.a: Non isodense suspension, with extra fluid

This section concerns the flow of an index matched suspension of  $200 \mu\text{m}$  spheres (density  $\approx 1.19 \text{ g/cm}^3$ ) heavier than the suspending fluid (density  $\approx 0.89 \text{ g/cm}^3$ ). After filling the Couette cell with the non density-matched suspension, the air liquid interface is located at an altitude  $H \approx 30 \text{ mm}$ . If no shear is applied, particles settle down within about 10 minutes. The process leaves a pure fluid layer, a few millimeters in thickness, between the air-liquid interface and the pile of sedimented particles. The system is afterwards sheared for a few hours, enough to reach a steady state regime.

We first present the experimental results for a low angular velocity  $\Omega = 0.114 \text{ rad/s}$  of the inner cylinder and an altitude  $z = 10 \text{ mm}$  (Fig. C.31). Unlike neutrally buoyant particles (Fig. C.24), the flow of non density-matched suspensions is much more non linear in the low shear regime. The non linearity is flagrant as the inclination  $\psi(r)$  of grey level patterns in the spatiotemporal window  $T(\theta r, t)$  changes more rapidly with the radial position  $r$  of the ROI. For  $r > 17.7 \text{ mm}$ , the patterns become horizontal and particles remain static on a time scale

of at least a few seconds (Fig. C.31.b). We thus observe a localization of the flow, whereby a shear zone coexists with an almost arrested state. One may note that the diffuse bright horizontal line in the autocorrelation images is much less pronounced than in Fig. C.25 for neutrally buoyant particles because of the better refractive index matching (here with the C16S150 fluid).

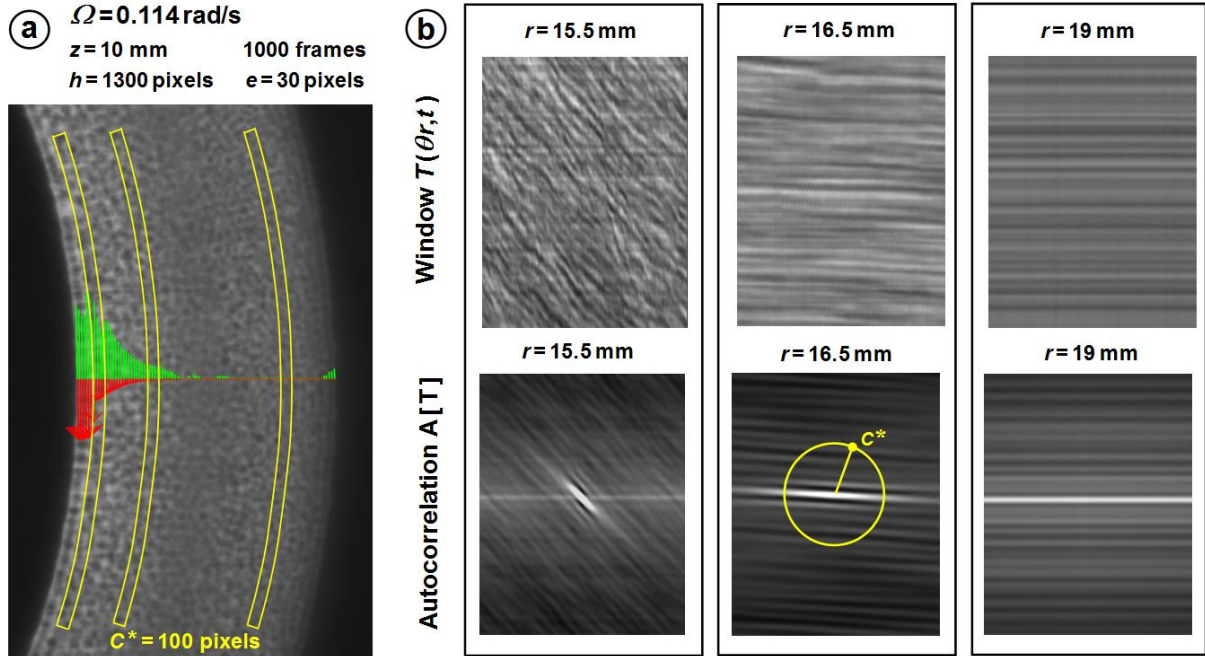


**Fig. C.31** Optical flow analysis of the non density-matched suspension at radial distance  $r = 15.5, 16.5$  and  $19 \text{ mm}$  (angular velocity of the inner cylinder  $\Omega = 0.114 \text{ rad/s}$ , altitude  $z = 10 \text{ mm}$  and  $H \approx 30 \text{ mm}$ ). (a) Angular velocity profile  $\omega(r)$  (red arrows) and rms angular fluctuation (green arrows) for  $c^* = 100 \text{ pixels}$ . (b) Spatiotemporal windows  $T(\theta, t)$  and autocorrelation image  $A[T]$  for several radial position  $r$  of the crown shaped ROI.  $f_t = 33 \text{ Hz}$  and  $f_s = 0.135 \text{ pixel}/\mu\text{m}$ .

Once again, the local angular velocity  $\omega(r) = (f_t / f_s r) \tan \psi(r)$  of particles is estimated from the tilt angle  $\psi(r)$  of the ridge line in the autocorrelation function after a Lorentzian fit of the angular grey level distribution  $P(\theta)$  (Fig. C.32.a). Interestingly, Fig. C.32.b indicates a fast decay of  $G_\psi(c)$ : this feature reveals rms fluctuations in the flow direction which are larger than those in the density-matched suspension. The diffusion coefficient  $D_{\theta\theta}$  in the velocity direction is estimated from Eq. (C.13) and a second order polynomial fit to discrete data  $1/G_\psi^2(c)$  over the domain  $c < c^*$  (Fig. C.32.b). The value of  $c^*$  may be varied between 15 and 100 pixels without notably changing the estimated diffusion coefficient in the shear zone (Fig. C.32.b). This insensitivity may be viewed as a

signature of a diffusive regime. However, the observation time  $c^*|\cos\psi|/f_t \approx c^*/f_t$ , not more than a few seconds, is much shorter than the inverse of the local shear rate  $1/|\dot{\gamma}| > 10^2 \text{s}$  in nearly arrested regions ( $r > 16 \text{mm}$ , Fig. C.33.a). Consequently the diffusive behaviour of particles in the velocity direction far from the inner cylinder is questionable.

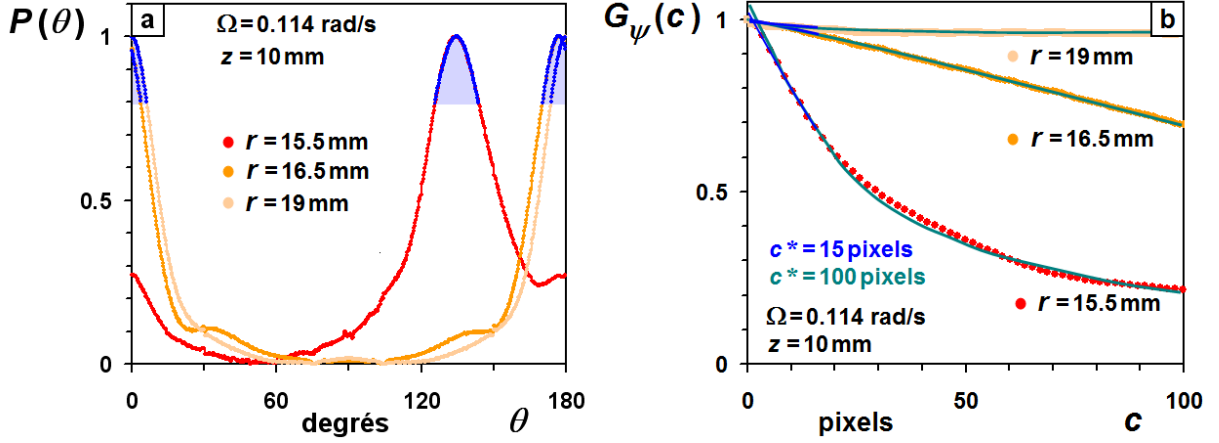


**Fig. C.32** Optical flow analysis of the non density-matched suspension at radial distance  $r = 15.5, 16.5$  and  $19 \text{mm}$  (angular velocity of the inner cylinder  $\Omega = 0.114 \text{rad/s}$ , altitude  $z = 10 \text{mm}$  and  $H \approx 30 \text{mm}$ ). (a) Normalized grey level angular distribution  $P(\theta)$  and estimation of the tilt angle  $\psi(r)$  of the ridge line from a Lorentzian fit (blue solid curves). (b) Normalized discrete function  $G_\psi(c)$  along the  $\psi$  direction of the ridge line and second order polynomial fit of discrete data  $1/G_\psi^2(c)$  over the finite domain  $c < c^* = 15$  pixels or  $c < c^* = 100$  pixels.  $n = 1000$  frames,  $h = 1300$  pixels,  $e = 30$  pixels,  $f_t = 33 \text{Hz}$  and  $f_S = 0.135 \text{pixel}/\mu\text{m}$ .

The image sequence was analyzed sequentially over 100 ROIs (height  $h = 1300$  pixels and width  $e = 2a$ ) to obtain both the angular velocity profile  $\omega(r)$  and the diffusion coefficient profile  $D_{\theta\theta}(r)/a^2$  from Eq. (C.13) (Fig. C.33).

The optical flow method nicely resolves slip phenomena near the inner cylinder (Fig. C.33.a). In line with early observations by Mueth [Mueth *et al.* 2000] for spherical mustard seeds in oil, the shape of the angular velocity profile  $\omega(r)$  across the shear band can be understood as arising from two main contributions: the slip contribution of an ordered layer close to the inner cylinder ( $\omega(r)/\Omega \approx 0.42$  for  $0 < r - R < 2a$ ), and a second slip contribution associated to the sliding of a second much disordered layer on the first layer ( $\omega(r)/\Omega \approx 0.15$  for  $2a < r - R < 3a$ , insert in Fig. C.33.a). The first ordered layer plays a role similar to a layer of spheres more or less glued to the inner cylinder through viscous lubrication forces (in

reference [Mueth *et al.* 2000], seeds were glued on both cylinders which cancels out any slip of the first particle layer).

The local shear rate  $|\dot{\gamma}(r)|/\Omega = (r/\Omega)|\partial\omega(r)/\partial r|$  decreases about exponentially with the radial distance  $r$  in the non slipping region  $r > 3a$  from about  $1\text{s}^{-1}$  down to  $10^{-3}\text{s}^{-1}$  at the outer limit of the shear band (Fig. C.33.b).

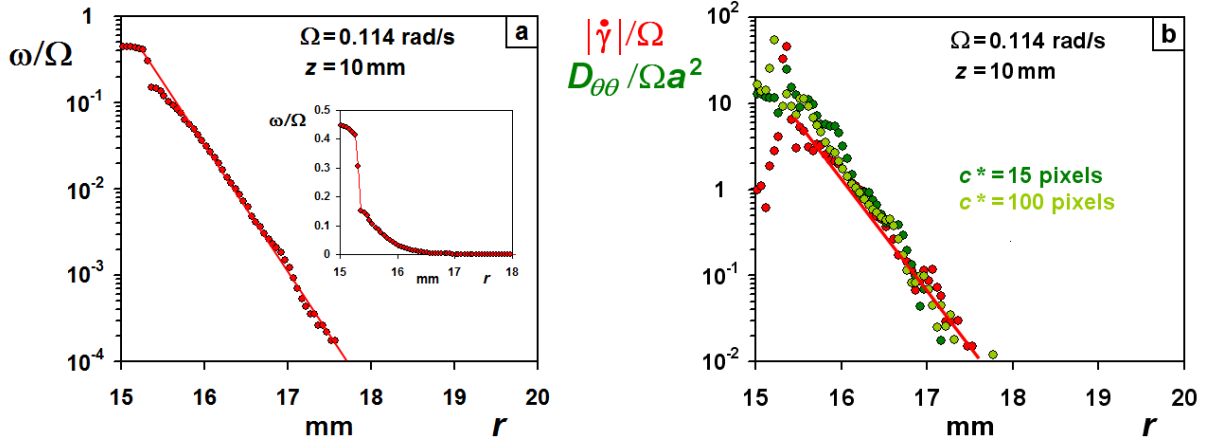
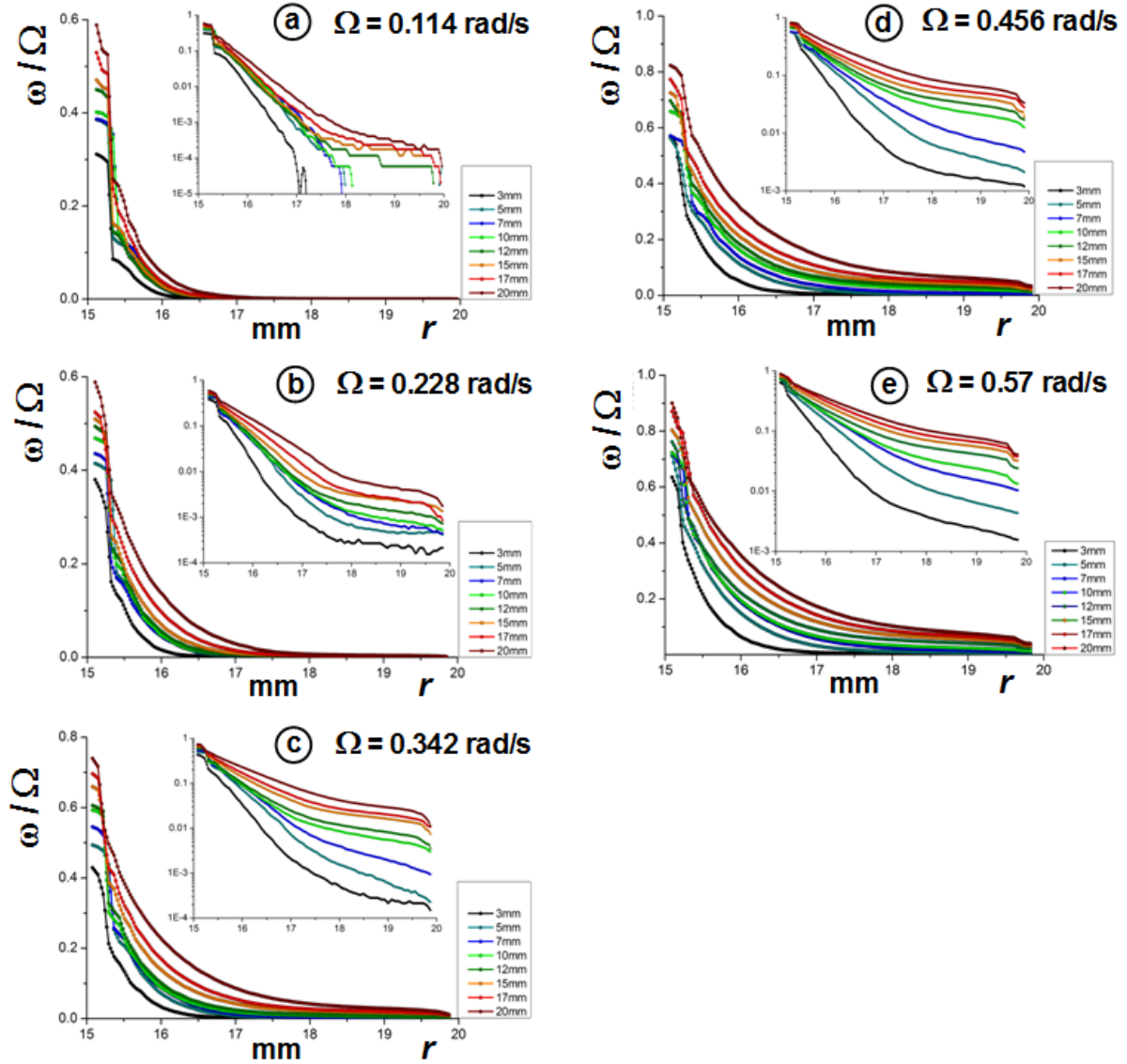


**Fig. C.33** (a) Semi-log plot of the dimensionless angular velocity profile  $\omega(r)/\Omega$  of the non density-matched suspension (angular velocity of the inner cylinder  $\Omega=0.114\text{rad/s}$ , altitude  $z=10\text{mm}$  and  $H \approx 30\text{mm}$ ). The insert shows a linear plot. (b) Semi-log plot of the dimensionless shear rate profile  $|\dot{\gamma}(r)|/\Omega = (r/\Omega)\partial\omega(r)/\partial r$  and dimensionless diffusion coefficient  $D_{\theta\theta}(r)/\Omega a^2$  ( $c^*=15$  pixels or  $c^*=100$  pixels).  $f_t=33\text{Hz}$  and  $f_S=0.135$  pixel/ $\mu\text{m}$ .

The dimensionless diffusion coefficient  $D_{\theta\theta}(r)/\Omega a^2$  also features an exponential decrease with  $r$  inside the shear band ( $15\text{mm} < r < 18.5\text{mm}$ , Fig. C.33.b). The non zero value of the diffusive coefficient in the first particle layer indicates significant relative angular displacements of spheres despite lubrication interactions with the inner wall. In the following, we choose an intermediate value  $c^*=50$  to obtain  $D_{\theta\theta}$ . This choice is a trade off between accuracy and insensitivity to out-of-plane motion of particles in the determination of  $D_{\theta\theta}$ .

Experiments were performed for increasing values of  $\Omega$ , from  $0.114\text{ rad/s}$  up to  $0.57\text{ rad/s}$  (Fig. C.34).  $\omega(r, z)$  profiles obtained after a few hours of shearing represent stationary regimes. Conversely to the isodense suspension, the flow characteristics of the non density-matched suspension greatly depend on  $\Omega$  and  $z$ . Slip phenomena and localization of the flow within a shear band are much more pronounced in the deep layers of the suspension, most strikingly at low  $\Omega$  (Fig. C.34).

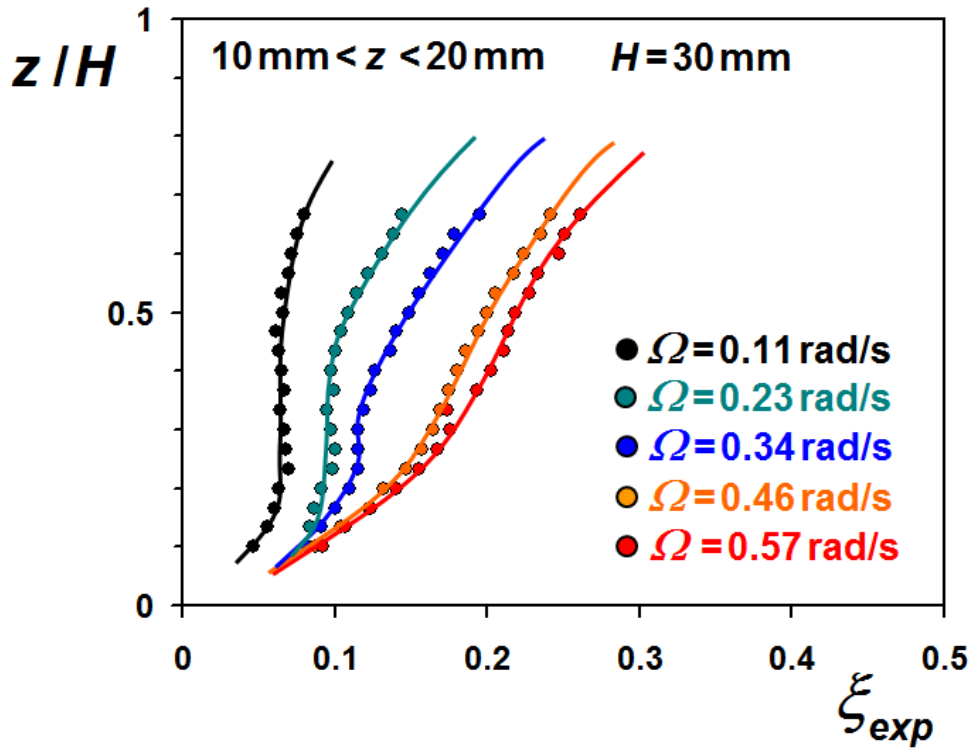
Moreover, the shear-induced dilation of the suspension reduces slip phenomena in the shear band. However, slip phenomena in the top region  $z > 20$  mm of the suspension only appears when shearing more vigorously the paste ( $\Omega > 0.3$  rad/s, Fig. C.34). Slip phenomena both depend on the shear rate  $\dot{\gamma}(R, z)$  and the particle concentration  $\Phi(R)$  close to the inner cylinder. In the high shear regime, the lower concentrations in the top layers of the shear-induced diluted suspension somewhat promote particle exclusion near the inner cylinder and then increase slip phenomena.



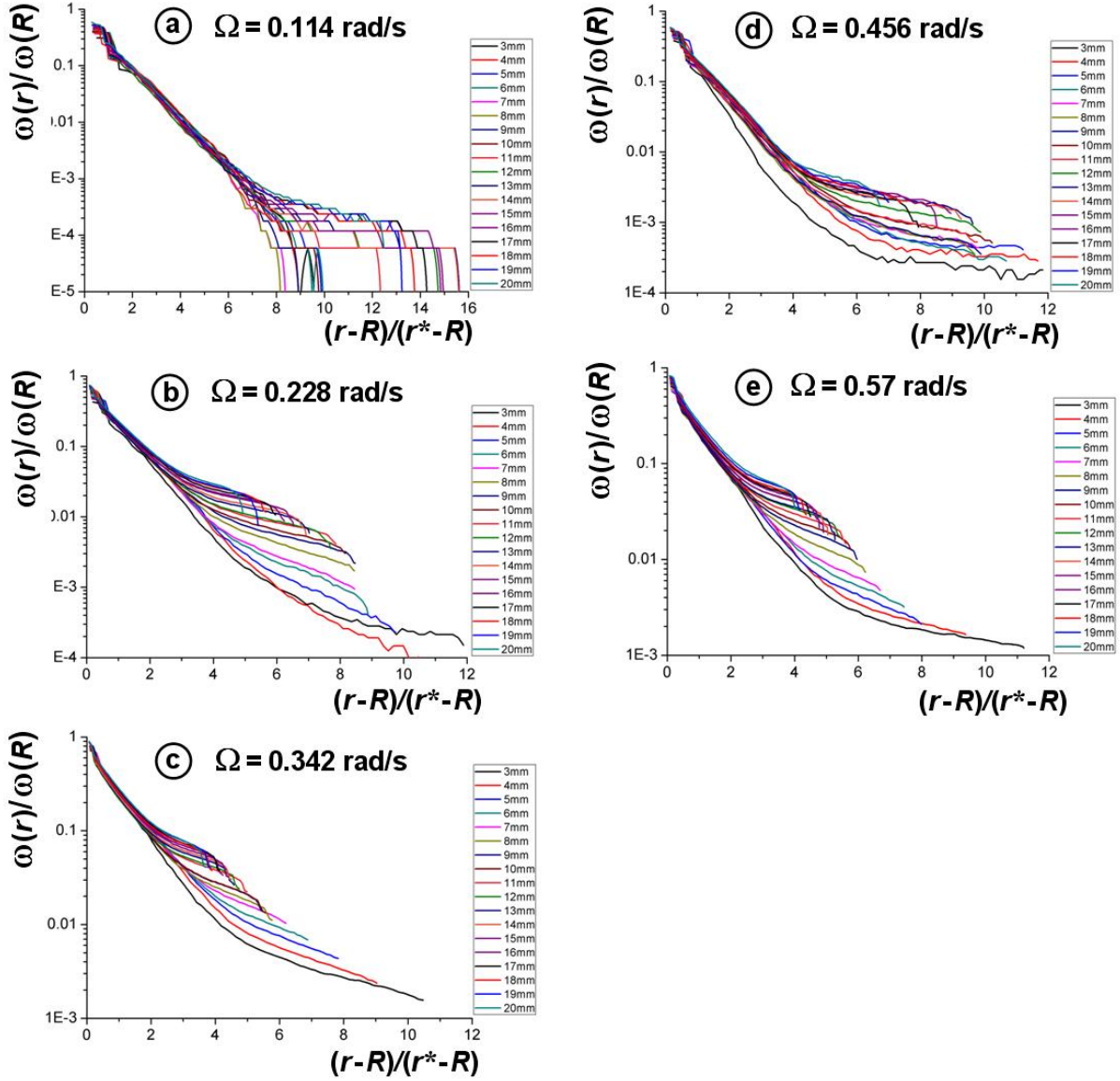
**Fig. C.34** Dimensionless angular velocity profile  $\omega(r, z)/\Omega$  of the non density-matched suspension for inner cylinder angular velocity  $\Omega=0.114$  rad/s (a),  $\Omega=0.228$  rad/s (b),  $\Omega=0.342$  rad/s (c),  $\Omega=0.456$  rad/s (d), and  $\Omega=0.57$  rad/s (e). Altitudes  $3 \text{ mm} < z < 20 \text{ mm}$  and  $H \approx 30 \text{ mm}$ .

Semi-log inserts in Fig. C.34 indicates a roughly exponential decay of  $\omega(r, z)$  in the shear band, down to plateau-like values in the nearly arrested region. As before, we extract a characteristic decay length  $r^* - R$  from the exponential profile.

As expected from previous remarks,  $\xi_{exp}(z, \Omega) = (r^* - R)/(R_{out} - R)$  increases with  $z$  and  $\Omega$  due to the shear-induced re-suspension of particles. When plotting the reduced angular velocity profiles  $\omega(r, \Omega)/\omega(R, \Omega)$  as a function of the dimensionless radial coordinate  $(r - R)/(r^* - R)$ , experimental data collapse onto a single curve for  $\omega(r)/\omega(R) > 0.1$  and  $r - R > 3a$  (Fig. C.36). Huang [Huang *et al.* 2005] drew a similar conclusion in the frictional regime when a reduced velocity is plotted as a function of a rescaled length involving the thickness of the shear band. Recall that this scaling only holds in the shear band, not in the nearly arrested region (Fig. C.36).



**Fig.C.35** Dimensionless decay length  $\xi_{exp}(z, \Omega) = (r^* - R)/(R_{out} - R)$  versus the reduced altitude  $z/H$  in the non density-matched suspension for  $\Omega = 0.114$  up to  $\Omega = 0.57 \text{ rad/s}$ . Altitudes  $10 < z < 20 \text{ mm}$  and  $H \approx 30 \text{ mm}$ .



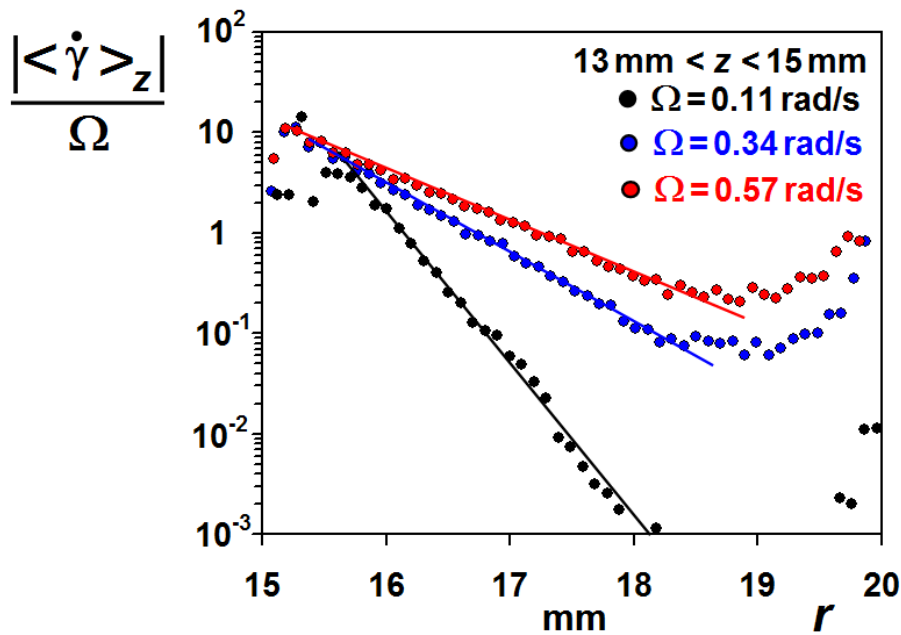
**Fig. C.36** Dimensionless angular velocity profile  $\omega(r,z)/\omega(R,z)$  of the non density-matched suspension versus rescaled distance  $(r-R)/(r^*-R)$  for  $\Omega=0.114$  rad/s (a),  $\Omega=0.228$  rad/s (b),  $\Omega=0.342$  rad/s (c),  $\Omega=0.456$  rad/s (d), and  $\Omega=0.57$  rad/s (e). Altitudes  $3 < z < 20$  mm and  $H \approx 30$ mm.

Figure C.37 shows the radial variation of the shear rate  $\dot{\gamma}(r,\Omega) = r \partial\omega(r,\Omega)/\partial r$  derived from experimental data  $\omega(r,\Omega)$  and averaged over three neighboring altitudes between 13mm and 15mm. The  $z$ -averaged shear rate  $\langle \dot{\gamma}(r,\Omega) \rangle_z$  also seems to decrease exponentially with the distance from the inner wall over the shear band, at least for  $R-r > 3a$ .

Figure C.38.a gathers the measurements of the  $z$ -averaged dimensionless diffusion coefficient  $D_{\theta\theta}(r,\Omega)/a^2|\dot{\gamma}(r,\Omega)|$  in the velocity direction as a function of  $r$  for variable  $\Omega$  (as

in Fig. C.36, experimental data are averaged over three neighboring altitudes between 13 and 15mm). The graphs leave the impression of a complex dependence of  $D_{\theta\theta}$  on  $r$ , but the picture fortunately simplifies if we plot  $D_{\theta\theta}/a^2|\dot{\gamma}|$  as a function of the  $z$ -averaged concentration  $\langle\Phi(r,\Omega)\rangle_z$  obtained in Chapter D for altitudes  $13\text{mm}\leq z\leq 15\text{mm}$  (Fig. C.30.b).  $D_{\theta\theta}/a^2|\dot{\gamma}|$  keeps a rather constant value in the range  $1.5\div 2.5$  for  $0.51<\Phi<0.57$  and decreases roughly linearly above a crossover volume fraction, around  $0.57\div 0.58$ . Diffusion becomes vanishingly small when  $\Phi\rightarrow 0.6$  (Fig.C.30.b), close to the maximal packing fraction [Onoda and Liniger 1990].

Remarkably, diffusion in the non iso-dense suspension turns out qualitatively similar to that obtained for neutrally buoyant particles. However the amplitude  $D_{\theta\theta}/a^2|\dot{\gamma}|\approx 2$  is much larger than for the isodense case ( $0.4\div 0.5$ ). We also find a difference for the crossover fraction, which is slightly larger in the non isodense system ( $0.57\div 0.58$ ) than in the isodense one ( $\approx 0.55$ ). Why gravity effects increase velocity changes in the flow direction and make such differences and is an intriguing question, which we leave as an open problem.



**Fig. C.37** Dimensionless  $z$  averaged shear rate profile  $|\langle\dot{\gamma}(r,\Omega)\rangle_z|/\Omega$  in the non density-matched suspension for inner cylinder angular velocity  $\Omega=0.114\text{rad/s}$ ,  $\Omega=0.342\text{rad/s}$  and  $\Omega=0.57\text{rad/s}$ . Altitudes  $13\text{ mm} < z < 15\text{ mm}$  and  $H \approx 30\text{mm}$ .

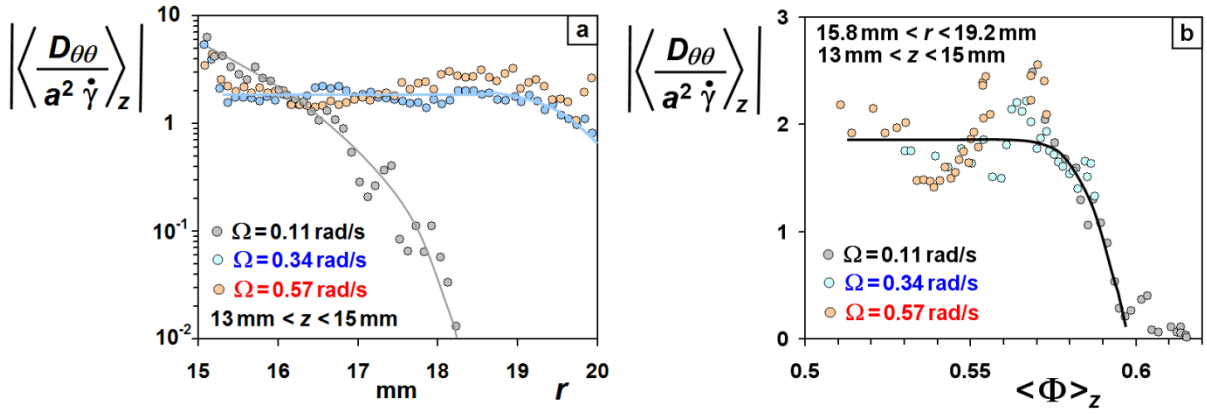


**Fig. C.38** Dimensionless  $z$  averaged diffusion coefficient  $\left\langle \frac{D_{\theta\theta}(r, \Omega)}{a^2 \dot{\gamma}} \right\rangle_z$  in the non density-matched suspension versus the radial distance  $r$  (a) or the  $z$  averaged particle concentration  $\langle \Phi \rangle_z$  (b) for inner cylinder angular velocity  $\Omega = 0.114 \text{ rad/s}$ ,  $\Omega = 0.342 \text{ rad/s}$  and  $\Omega = 0.57 \text{ rad/s}$ . Altitudes  $13 \text{ mm} < z < 15 \text{ mm}$  and  $H \approx 30 \text{ mm}$ .

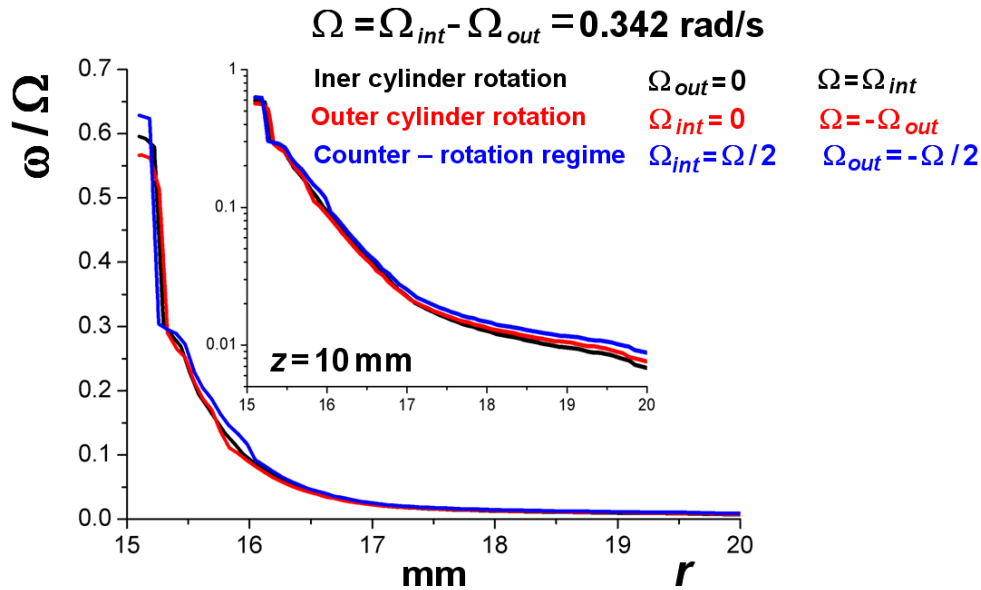


**Fig. C.39** Steady state angular velocity profiles  $\omega(r)/\Omega$  of the non density-matched suspension for a constant differential angular velocity  $\Omega = \Omega_{int} - \Omega_{out} = 0.342 \text{ rad/s}$  between inner and outer cylinders : rotation of the inner cylinder only (black solid curves), rotation of the outer cylinder only (red solid curves) or counter-rotation mode (blue solid curves). The insert shows a semi-log plot. Altitude  $z = 10 \text{ mm}$  and  $H \approx 30 \text{ mm}$ .

Another important result is about what we called “rotation invariance” (chapter B), i.e. the similarity of velocity profiles in the stationary regime when only the inner or the outer

cylinder rotates or both cylinders are operated in counter-rotation mode ( $\Omega_{out} = -\Omega_{int}$ ), provided that the differential angular velocity  $\Omega = \Omega_{int} - \Omega_{out}$  remains the same (Fig. C.39). Such an observation seems trivial but demonstrates that inertial effects are negligible and that shear-induced particle collision is the dominant mechanism of momentum and energy transport in the suspension.

#### **C.4.b: Non isodense suspension, without extra fluid**

In this paragraph, we examine what happens if the layer of pure immersion fluid, on top of the suspension, is not present. In this case, shear-induced dilation is much more constrained than when the layer is present, and this may cause visible differences on the flow characteristics. We have carefully pumped out the top fluid at rest on a height of about 3 millimeters ( $H \approx 27\text{mm}$ ), so that the average particle concentration in the fully fluidized suspension is about  $\tilde{\Phi} = 0.58 \div 0.59$  compared to  $\tilde{\Phi} \approx 0.55$  for  $H \approx 30\text{mm}$ . Remarkably, the velocity profiles with or without extra fluid remain very similar (Fig. C.40). One only observes a slightly more pronounced slip phenomenon and a shear band of reduced thickness in the high shear regime ( $0.4 < \Omega < 0.6$  rad/s, Fig. C.40.d, e). The increase of the average concentration  $\tilde{\Phi}$  close to the maximum packing fraction  $\Phi_m \approx 0.6$  is not enough to produce strong flow localization, as one might have expected. Such a surprising result will be discussed in chapter E dedicated to a numerical resolution of the force balance model equations from Morris and Boulay.

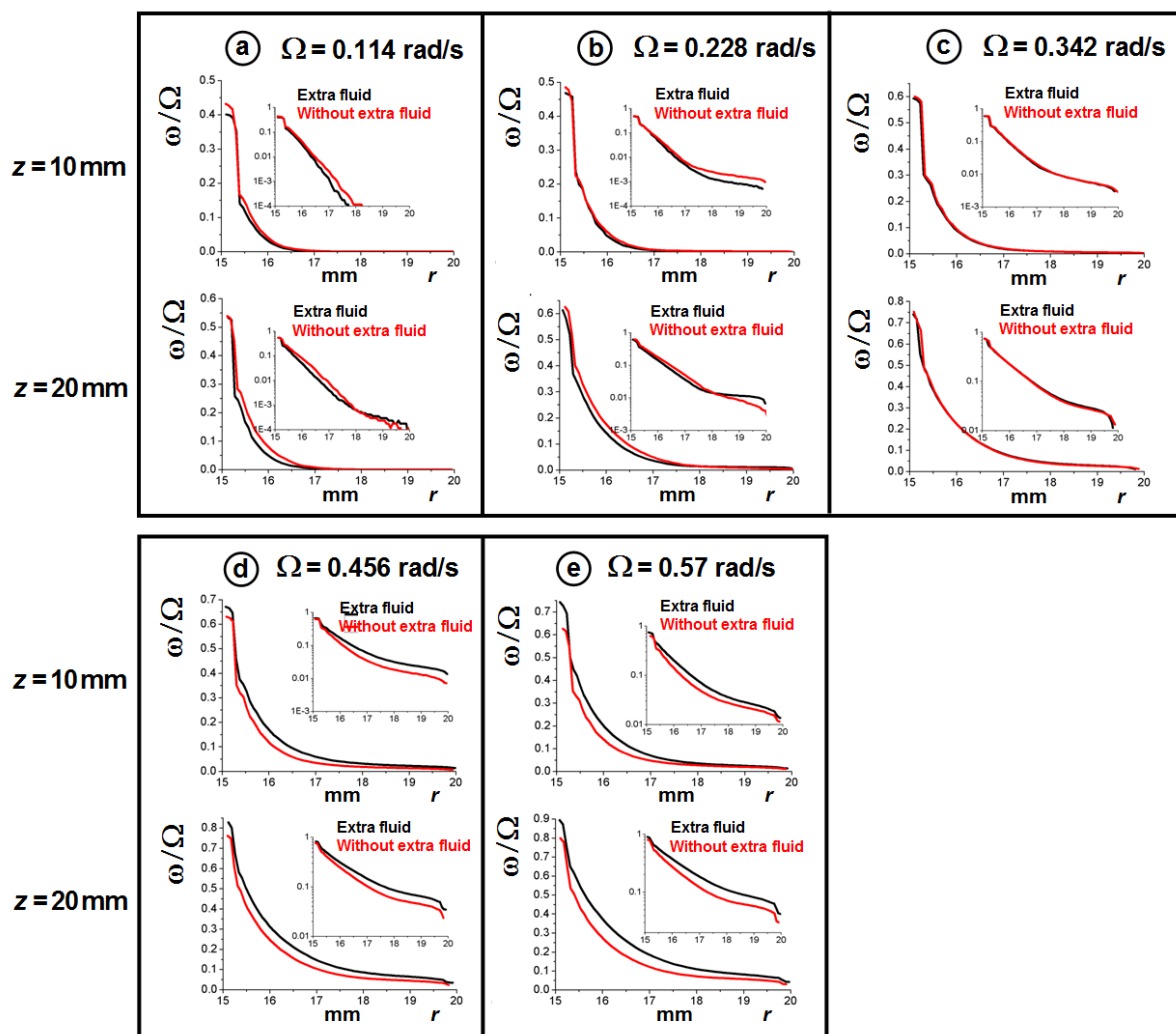


**Fig. C.40** Steady state angular velocity profiles  $\omega(r)/\Omega$  of the non density-matched suspension with extra fluid (red solid curves,  $\tilde{\Phi} \approx 0.55$  and  $H \approx 30\text{mm}$ ) or without extra fluid (black solid curves,  $\tilde{\Phi} = 0.58 \div 0.59$  and  $H \approx 27\text{mm}$ . Altitudes  $z = 10\text{ mm}$  or  $z = 20\text{ mm}$ .

## Chapter D – Concentration Field

The flow of a granular paste may be regarded as a two-field problem, involving both velocity and concentration. In simple words, shearing the material makes it flow; resulting in some shear profile across the gap of the Couette cell, and this shear modifies the concentration. The concentration profile produced by shear is not flat: in general particles accumulate near the outer cylinder, a phenomenon called “shear-induced migration” [Galada-Maria and Acrivos 1980, Leighton and Acrivos 1987, Abbott *et al.* 1991, Mills and Snabre 1995]. Because the viscometric coefficients depend on the concentration [Krieger and Dougherty 1959, Frankel and Acrivos 1967], the migration itself has consequences on the flow profile. Concentration and shear are coupled. Having characterized the flow in Chapter C, we now come to the concentration profile  $\Phi(r)$ . This chapter deals with the measurement of  $\Phi(r)$  by optical means.

In recent years magnetic resonance imaging (MRI) has become a standard technique to measure concentration in flowing granular materials [Ovarlez *et al.* 2006, Huang *et al.* 2005, Jamy *et al.* 2005, Bonn *et al.* 2008, Taberlet *et al.* 2006, Sieden and Thomas 2011, Gray 2001]. The MRI technique has the advantage of being compatible with optically opaque materials, and is able to yield both velocity and concentration profiles. However it involves a very heavy and costly instrumentation, with limited accessibility in time. Here we offer the alternative of an optical method, which has the advantage of low cost and which can be operated permanently (over days) “at home”. The technique is based on measuring the fluorescence from the immersion fluid, illuminated by a laser planar sheet. The method is simple, but necessitates precaution, as we will explain. To our knowledge, it has not been used prior to us to investigate the flow of a granular suspension.

Coupled flow localization and migration has been studied with MRI [Ovarlez *et al.* 2006] in density-matched suspensions, in a large-gap Couette cell similar to ours. Relating local shear rates  $\dot{\gamma}(r)$  to local concentrations  $\Phi(r)$ , these authors were able to determine the way in which the shear viscosity  $\eta$  depends on  $\Phi$ . They also found that the amount of migration, i.e. the  $\Phi(r)$  profile, was about independent of the inner cylinder velocity (the outer cylinder was static). This finding is at odd with simple intuition, which tells that the effect (migration) should increase when the cause ( $\omega$ ) increases.

In this chapter, we look for the same information, now with the non density matched suspension ( $\Delta\rho > 0$ ). We also investigate the  $\Delta\rho = 0$  case, to cross our findings with those obtained by MRI. As far as we know, the influence of gravity on migration in large-gap

Couette flow has not been investigated yet. The problem that we tackle is then a generalization of the works that have been done up to now, which were only concerned with situations where gravity does not play a direct role. Stated differently, we investigate the problem of viscous resuspension in a large-gap Couette cell.

The chapter is organized as follows: The following section (D.1) is dedicated to the optical technique for concentration measurements. Results in terms of concentration maps are reported in Section D.2. Concentration and velocimetry data are gathered in Section D.3, whose objective is to offer a complete description of the resuspension, showing the coupling between concentration and shear. Section D.4 summarizes the results. This chapter is complemented by 3 appendices: D-A is about the characterization of the laser sheet (D-A), and (D-B) about the calibration procedure. Appendix D-C deals with the problem of rotation invariance that we mentioned in chapter B. Essentially we find that concentration profiles are the same, within experimental uncertainty, when the Couette cell is operated with only one cylinder (inner or outer) or with both cylinders rotating. Proofs of this statement are provided in D-C, through a few examples. Note that this chapter does not deal with modelisation of resuspension, a task which we postpone to chapter E.

## D.1: Experimental technique

The general principle of the measuring technique is illustrated below in Fig. D.1.

A laser planar sheet,  $2w$  in thickness, illuminates the sample. The granular system is supposed statistically invariant along  $y$  direction, meaning that the flow and particle concentration are constant along  $y$ , in average (in the sense of “ensemble” average, in statistical physics). The immersion fluid has been made fluorescent by addition of a dye, as explained in chapter B. The laser light propagates along  $x$  direction; illumination is constant along  $\hat{\mathbf{z}} = \hat{\mathbf{x}} \times \hat{\mathbf{y}}$ . Fluorescence (orange in Fig. D.1) is excited everywhere inside the laser sheet. Spheres are supposed non fluorescent; consequently the fluorescence light comes entirely from the fluid. The fluorescence signal is collected through an imaging lens onto the sensor of a camera (CCD or CMOS). The lens simply builds an image of the illuminated section: the particles appear dark in the bright fluid. We thus obtain a kind of planar cut across the sample, corresponding to the particular position of the laser sheet, say  $y_i$ . Let us denote  $I_i(x, z)$  the intensity in the image. In the experiment, we accumulate a series of  $N$  such images corresponding to different positions of the laser sheet,  $0 \leq y_i \leq L$ , where  $L$  is the dimension of the sample along  $y$ . Summing up all images and dividing by  $N$ , we obtain

$\bar{I}(x, z) = N^{-1} \sum_{i=1}^N I_i(x, z)$ , the spatially averaged image of the planar cuts. If  $N$  is large enough, particles are no more discernible in the average image, and  $\bar{I}(x, z)$  is simply proportional to  $1 - \bar{\Phi}(x, z)$ , the spatially averaged volume fraction of fluid. If  $L$  is large enough, we may suppose that spatial and ensemble averages are the same (ergodism); we thus end up with  $\langle \Phi(x, z) \rangle$ , the average particle concentration field within the laser sheet.

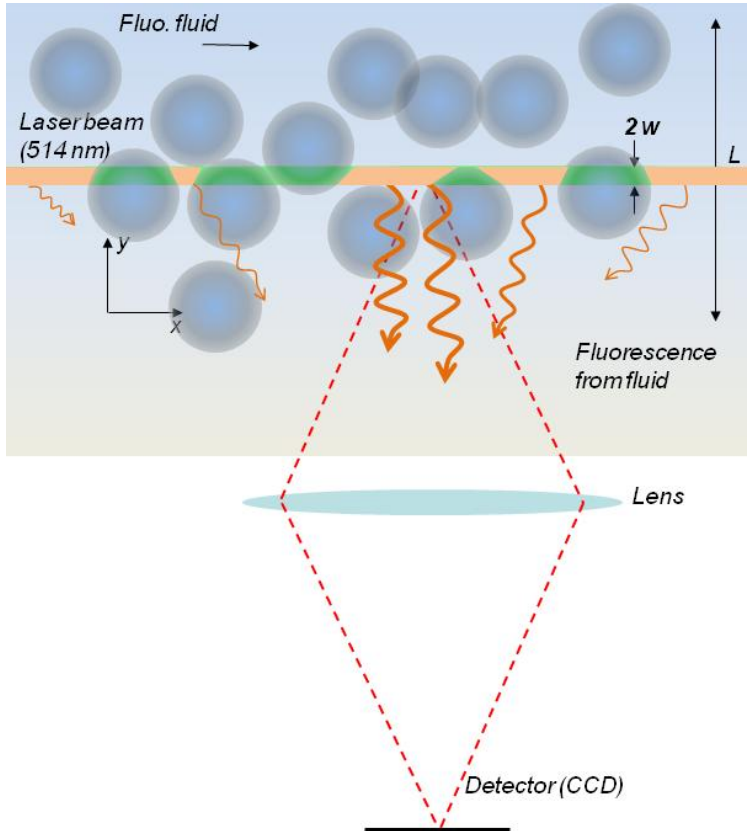


**Fig.D.1** Principle of concentration measurement.

Note that the thickness of the sheet,  $2w$ , does not play a crucial role in the above reasoning. It is not profitable to have  $2w \ll 2a$ , since accumulating positions of the sheet within a particle diameter does not explore much of the system configurational space. Conversely, a too large thickness,  $2w \gg 2a$ , will degrade spatial resolution. Consequently, it is advisable to have  $w$  on the order of the particle size.

In practical conditions, with the Couette cell, the system features statistical invariance along the azimuthal coordinate  $\theta$ . Averaging is obtained by rotating the system, a condition which is automatically satisfied whenever both cylinders are rotating. If the experiment has been started for instance with only the inner cylinder rotating ( $\Omega_{in} = \Omega$ ,  $\Omega_{out} = 0$ ), it suffices

to add a finite amount of offset ( $\Omega_{in} = \Omega + \Omega_{off}$ ,  $\Omega_{out} = \Omega_{off}$ ), following the principle explained in chapter B.

### D.1.1: Optical setup

The setup is sketched in Fig. D.2 below. The source is the same as in the trajectography experiments, i.e. a Coherent Innova 300 argon ion laser, operated on the  $\lambda = 514$  nm line. After reflections by  $M_1$ ,  $M_2$ , and focusing by a low power objective (OL), the beam is scanned vertically by a rotating mirror (Lincoln Laser, Laser Scanner Polygon EX-1188), denoted RM in Fig. D.2. The rotation speed is very high (up to 20000 rpm). As a result, the system generates a series of rays that is felt as a vertical sheet of light, through time averaging, either by naked eye or by the camera. These rays approximately originate from a point source located close to RM rotation axis. CL is a cylindrical lens whose front focal plane is located near RM. The purpose of CL is to collimate laser light coming from RM. We thus obtain a vertical laser sheet composed of approximately horizontal rays. The intensity along vertical ( $z$ ) is constant within 2 %, from bottom to top of the sheet. Note that such uniformity is not possible using only cylindrical lenses, unless at the expense of considerable losses in power. Having a uniform laser sheet is very important in this experiment, in essence photometry, contrary to velocimetry (where illumination homogeneity is not critical).

The laser sheet goes across the full Couette cell through the rotation axis, see Figs D.2, 4. We thus obtain a two-side view (Fig. D.4), with “in” (the laser propagates towards the axis, right part in Fig. D.4.a) and “out” (the laser propagates out of the axis, left part in Fig. D.4.a) sides. Ideally, both sides should be mirror images of each other. This is so if the beam width is constant through the cell and if attenuation of the beam intensity is negligible. In reality, there is a little absorption by the fluorescent dye and because of light scattering due to imperfect index matching. The beam width cannot be constant because of diffraction. Let be  $x$  the direction of propagation of the sheet and  $y$  the direction transverse to the sheet. The sheet has a Gaussian intensity profile given by:

$$I(y) = I_0 \exp\left(-\frac{2y^2}{w^2}\right) \quad (\text{B.1})$$

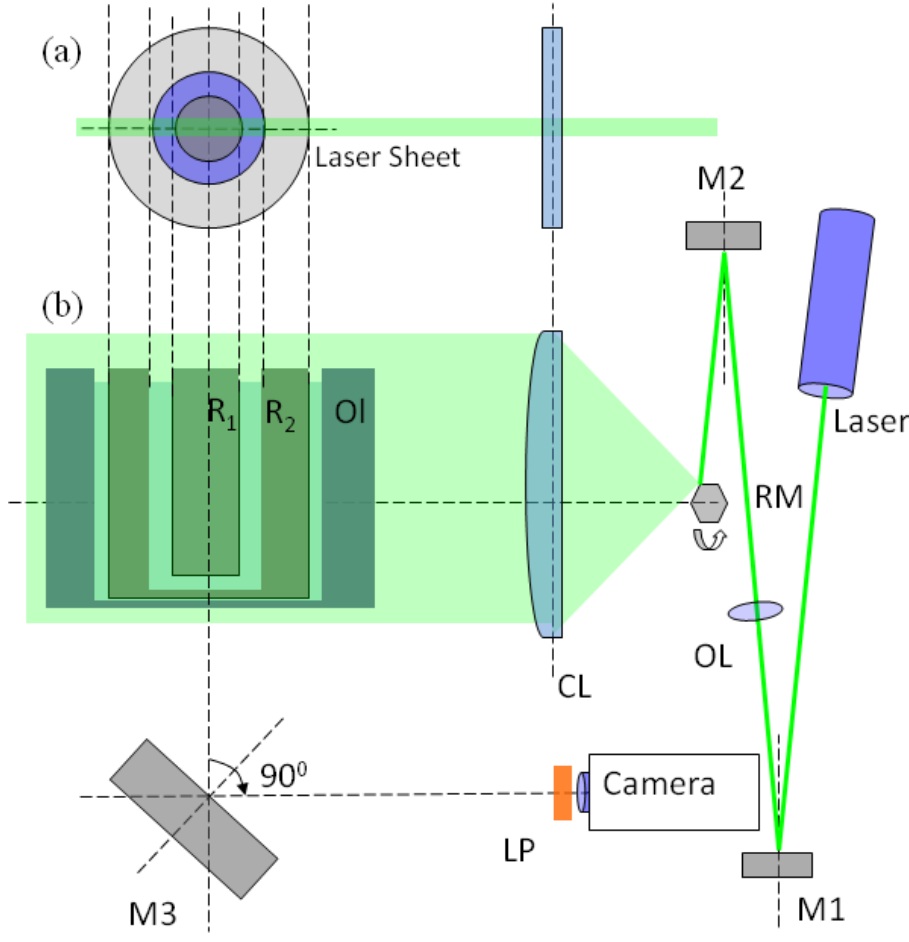


**Fig.D.2** Top (a) and side view (b) of experimental setup and components.  $M1$ ,  $M2$ ,  $M3$  : mirrors;  $RM$  : rotating mirror;  $CL$ : cylindrical lens (focal length: 240 mm);  $OI$  : olearium;  $OL$ : spherical lens ( $f=800\text{mm}$ );  $LP$ : long pass filter;  $R_1, R_2$  : inner and outer cylinder radii.

$I_0$  is the on-axis intensity. The width  $w$  has a minimum, the beam-waist  $w_0$ , inside a vertical plane which is located close to  $CL$ . At a distance  $x$  from the beam-waist plane, the sheet width increases according to the classical diffraction formula for Gaussian beams [Saleb *et al.* 1991]:

$$w(x) = w_0 \left[ 1 + \left( \frac{\lambda x}{\pi w_0^2} \right)^2 \right]^{1/2} \quad (\text{B.2})$$

We measured the beam parameters following the procedure explained in Appendix D-A. We thus found:  $w_0 = 0.136$  mm, and  $w_{in} \cong 0.264$  mm and  $w_{out} \cong 0.290$  mm for the in and out sides of the Couette cell, respectively. Thus the beam width does not vary much from one side to the other and is about 3 times a particle size. We might have chosen to focus the beam more tightly, but diffraction would have been more intense. The above values are a trade-off, which we found satisfactory. The granular suspension is made fluorescent by addition of special dye (FLUORESCENT YELLOW 131SC provided by Keystone Europe Ltd). As we explained in

chapter B, this dye gets dissolved in the immersion fluid, not in PMMA. Thus the fluorescence light comes essentially from the fluid, as desired. Under illumination by the green laser light, PMMA however emits a faint fluorescence, independently of the dye. Adding much dye may make this parasitic contribution negligible compared to that from the fluid. Unfortunately, adding too much dye makes the solution absorbing, with the consequence that the laser beam gets attenuated on its way through the Couette cell. As absorption may greatly complicate data analysis (see below and Appendix D-B), the dye concentration should be as small as possible. We thus have opposite requirements for the dye content, which imposes us to find a trade off. We empirically found a procedure that turned out about satisfactory: in short we impose that the signal picked up by the camera (see below) be near saturation when the laser is operated at 2 Watt (about 70% of its maximum power). To reach this level, we first prepared a highly diluted version of the mother solution of the dye into 1 ml of the immersion fluid, and added a few drops of this solution into the Couette cell. In such conditions, the absorption turns out very small, as far as we can tell from the “in” and “out” images (Fig. D.4). Both images have nearly equal intensities, and the intensity profiles in horizontal cross sections are close to mirror images of each other.

### D.1.2: Detection

The fluorescence light is collected through an optical lens (50 mm lens) and a long pass filter by the same digital camera as in the trajectography experiments (Hamamatsu ORCA Flash 2.8, CMOS 12 bits). The gray levels thus range from 0 to 4096. The CMOS sensor has 1920x1440 pixels, corresponding to about 0.03 mm in resolution in the video image. In general we operate the camera with a 0.55 s exposure time and gain set at 0, giving  $S \approx 3000$  for the signal intensity, in grey level (see Fig. D.4.b). The signal is partly contributed by the dark noise of the camera,  $S_{dark} \approx 50$  units in grey level. Note that the exposure time does not have a crucial importance, since we only study stationary patterns. For each experiment, corresponding to a given angular velocity  $\Omega$ , we perform  $\theta$ -averaging by recording about 1000 images, along the procedure explained in the introduction. The video sequence is saved in TIFF format and later analyzed with Image J software<sup>7</sup>. The measurement procedure implies that the video signal, in grey level, be proportional to the intensity of fluorescence light, which in turn has to be proportional to the laser power  $P$ . This point was tested by varying  $P$ , see the graph below. Linearity is well satisfied. The straight

---

<sup>7</sup> ImageJ , <http://rsbweb.nih.gov/ij/docs/user-guide.pdf>

line intercepts the ordinate axis at about 50 in grey level, the above mentioned dark signal ( $S_{dark}$ ).

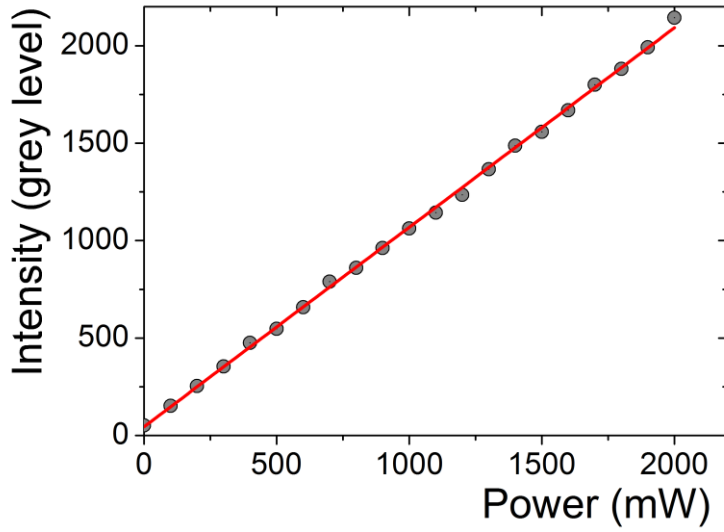


**Fig.D.3** Test of linearity between laser power and grey level.

### D.1.3: Calibration

Intensity maps in the video images do not directly represent the physical quantity that we are looking for, i.e.  $1 - \langle \Phi(x, z) \rangle$ . Complications arise due to different causes:

- (a) the laser sheet is not perfectly constant along  $z$  ;
- (b) the laser intensity is not constant along  $x$  , due to absorption and light scattering;
- (c) PMMA contributes a small but not null fluorescence signal;
- (d) a uniform image source in general does not appear uniform in the video image. This is due to non uniformity of the collection efficiency and possibly non uniform sensitivities and gain among the pixels;
- (e) the sensor dark signal  $S_{dark}$  .

The last contribution may be easily eliminated, computing the difference  $S - S_{dark}$  . (a), (b), (c), (d) impose a calibration procedure. To make a calibration image we replace the granular sample with an identical volume of immersion liquid (with no particles inside). The liquid must be made fluorescent, along the same criteria as for the suspension. We record a  $\theta$ -averaged image of the system,  $S_{cal}$  (see Fig. D.4 below and Fig.D-B.2). The corrected image,  $S_{cal} - S_{dark}$  , is the basis for calibration. Essentially, calibration amounts to dividing  $S - S_{dark}$

by  $S_{cal} - S_{dark}$ . A general calibration procedure, including correction for absorption and PMMA fluorescence is detailed in Appendix D-B. The results reported below were obtained from a simplified analysis, where only (a), (d), (e) have been taken into account. We made a few tests with the complete procedure. The results from these tests turned out close to those from the simplified analysis, indicating that absorption and PMMA fluorescence do not cause serious errors. Note that both sides in Fig. D.4 are close to right-left symmetry, as they should be if absorption is very weak.

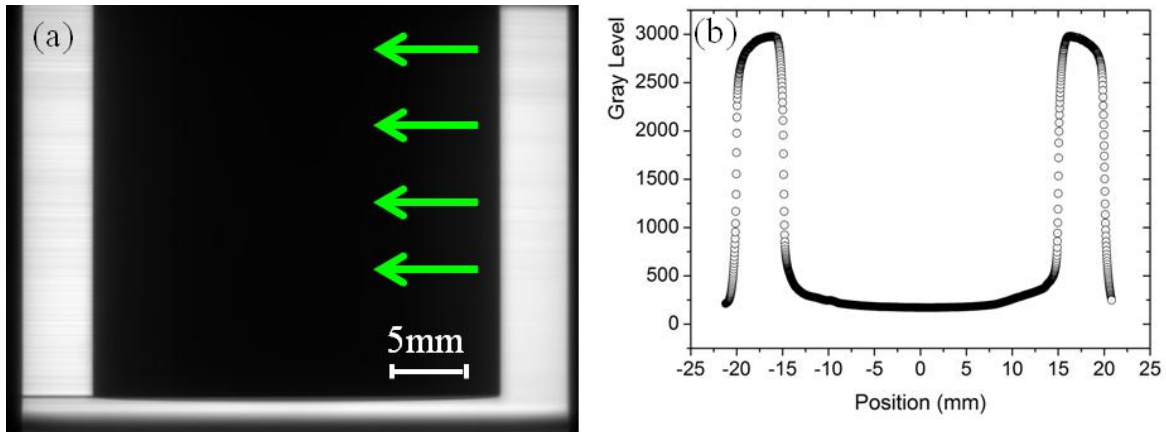


**Fig. D.4** Calibration signal. (a) shows the fluorescence from the Couette cell filled with dyed immersion fluid only (here C16-S150), and (b) intensity distribution for a altitude of 15mm. Laser light comes from the right side, as indicated by the green arrows.

In principle, the calibration signal should fall abruptly down to  $S_{dark}$  when  $r$  goes across either  $R_{in}$  or  $R_{out}$ , since there is no fluorescent fluid outside of the Couette gap. We might take into account the slight fluorescent from bulk PMMA, but this does not change the picture much. Rather unexpectedly the signal definitely rounds off within a distance  $e \approx 1$  mm of each boundary (Figs D.4 and D-B.2). Note that the finite width of the laser sheet would give  $e \approx 0.01$  mm, a negligible contribution. Another possible cause of blunting is the mechanical imperfection of the Couette cell, essentially non concentricity between rotation axes of the cylinders and the rotation stages. But this should not contribute more than 0.1 mm in typical conditions. The very large blunt may rather indicate a poor focusing of the camera lens. Indeed the amount of blunt was not constant between different experiments, most probably because we were not able to achieve optimal focusing every time. Because of this problem, we estimate that the calibration procedure may be seriously biased within the boundary zones, say the “ $e$ -layers”. In other words, quantitative data for the concentration

may be relied on only between 16 and 19 mm. However the information within both  $e$ -layers still has some value, at least qualitatively. As we will see, characteristic oscillations are clearly observed with the granular systems within both  $e$ -layers (see Fig.D.5, Fig.D.6, Fig.D.9 and Fig.D.10 below). These oscillations, which are due to wall-induced layering, are real, though their amplitudes may have been distorted by the unreliable calibration in this region.

#### **D.1.4: Accuracy, reproducibility**

There are different sources of experimental uncertainty:

- Concentration profiles have intrinsic noise (see e.g. Fig. D.6), due to the granular nature of the system and to the fact that the laser sheet only probes a small volume (corresponding to about 100 particles per  $\text{mm}^2$  in the image). Indeed the fluorescence map from a single cut across the Couette cell shows large spatial fluctuations ( $\sim 20\%$ ), but this noise is considerably reduced by azimuthal averaging. The latter is performed by operating the shear cell in contra-rotation mode, a procedure which allows us to sum the fluorescence maps over  $360^\circ$  in  $\theta$ .
- Fluctuations ( $\delta P$ ) of the laser power ( $P$ ), which affect the fluorescence intensity both in the calibration step and in measurements with the granular sample.  $\delta P/P$  is about 1%, resulting in 2% for the concentration.
- Temperature fluctuations ( $\delta T$ ): a shift in temperature causes a mismatch in refractive index. A shift  $\delta T \sim 1^\circ\text{C}$  from optimum index-matching has a visible impact, as the transparency of the sample across the Couette cell definitely decreases. The degradation is due to light scattering by the particles' surfaces. We did not perform a quantitative analysis of how much refractive index mismatch affects concentration measurements. We just suspect that scattering results in spreading the laser sheet and induces losses of the fluorescence light towards the detector. The resulting systematic error is probably not uniform inside the image, and thus may distort the fluorescence map. In practical conditions, using the air conditioning inside the lab, we were able to maintain the temperature around the Couette cell around optimum ( $\approx 22^\circ\text{C}$ ), within  $\pm 0.2^\circ\text{C}$  for about an hour, well enough to perform concentration measurements at a given value of  $\omega$ .

Under such conditions, our measurements were found reproducible within about  $\pm 0.015$  in concentration. This estimate holds outside of the “ $e$ -layers”, as we explained above.

We also made a few tests (with the density matched system only) to detect possible hysteretic effects, by comparing measurements taken at increasing and decreasing values of  $\omega$ . We in fact found no hysteresis, within experimental uncertainty.

## D.2: Concentration fields

### D.2.1: Density – matched suspension

The granular suspension was prepared with the Cargille fluid mixture, as explained in chapter B. The composition of the system was (in mass): PMMA particles (17.00 g); fluid (13.70 g). The corresponding average volume fraction of solid is  $\bar{\Phi} \cong 55\%$ . Similarly to the procedure for velocimetry experiments, we prepare the sample in the “open” Couette cell, i.e. inside the cup made by the hollow outer cylinder, while the inner cylinder has been removed (see Fig. B.6). The latter is afterwards brought back into the cell, by pushing through the suspension, and fixed. Preparation of the Couette cell ends with a fine tuning sequence to ensure coaxiality of both cylinders.

We then add a few drops of the fluorescent 131SC dye through the openings on top of the inner cylinder (Fig. B.6). At this stage, the fluorescence from the sample is not homogeneous, as can be checked from profiles along different  $\theta$ -cuts. To reach cylindrical symmetry ( $\theta$  invariance), we pre-shear the suspension at high angular velocity (5 rad/s) for several hours, then stop the motors and let the system relax for about 30 mn. This time is essentially limited by the imperfect density-matching, which makes the particles sediment or cream if we wait several hours. We thus start with a pre-sheared suspension, which we refer to as “at rest”.

The results displayed in Figs. D.5, 6, 7 correspond to **stationary states**. Experimentally, “stationarity” means that the concentration profiles did not significantly evolve over time, even after several hours of operation of the shear cell at the given value of  $\omega$ . We made a few attempts to study the **transient regime**, i.e. the evolution of the concentration when shear is applied, starting from rest state. The ideal procedure is then to take “snapshots” of the system at times  $t_1, t_2, \dots, t_i, \dots$ . A snapshot in our conditions takes about 20 mn, the time necessary to gather about 1000 frames, and make the system slowly rotate in contra-rotation mode to spatially average the fluorescence. Consequently two consecutive measurements must be

separated by much more than 20 mn, say an hour at least. The procedure thus cannot reveal differences between transient and stationary states. We nevertheless tried to indirectly detect a transient behaviour using the following method: we start with the system at rest (recall that it was pre-sheared), then operate shear for 1 mn, stop it and record the fluorescence as usual (the 20 mn “snapshot”), then resume shear for one more minute, stop it and record, and so on. Still with this procedure, we did not detect definite differences in concentration field over time. Overall, we are not able to resolve the time evolution of the concentration. A credible study of the transient regime would necessitate starting from an ideally uniform sample and a time resolution of the order of a minute. In our experiment, the pre-sheared sample is far from uniform, and time resolution is only about 20 mn.

**Stationary concentration fields**, corresponding to increasing values of  $\Omega$ , are displayed in Figs D.5, 6 and 7. The curves correspond to different altitudes in the Couette cell, measured starting from the bottom of the suspension (i.e; the bottom of the cup that serves as the outer cylinder). The essential result is that the radial concentration profile is about constant in altitude ( $z$ ) and is not greatly modified when  $\Omega$  increases. This finding is not surprising, in view of our results for the velocity field (chapter C), which showed the same trend.

The above statement however only holds for the “heart” of the Couette device, not close to the bottom. The bottom region may be defined as  $z$  smaller than  $z_{trans} \approx 5$  mm: in this region, the concentration profile departs from that in the heart, beyond experimental uncertainty, and depends on  $\omega$ , see Fig. 7 (altitude – 5mm). Note that  $z_{trans}$  is on the order of  $R_{out} - R_{in}$ , the Couette gap. Our data indicate that for  $z > z_{trans}$ , the flow and concentration fields are negligibly influenced by the bottom part, and hardly depend on  $\Omega$  and  $z$ .

**Summarizing**, the density-matched suspension shows a rather simple behavior, both in velocity and concentration. In the heart of the Couette cell, i.e. for  $z > z_{trans}$ , the concentration field is found about constant, both in  $z$  and  $\omega$ .

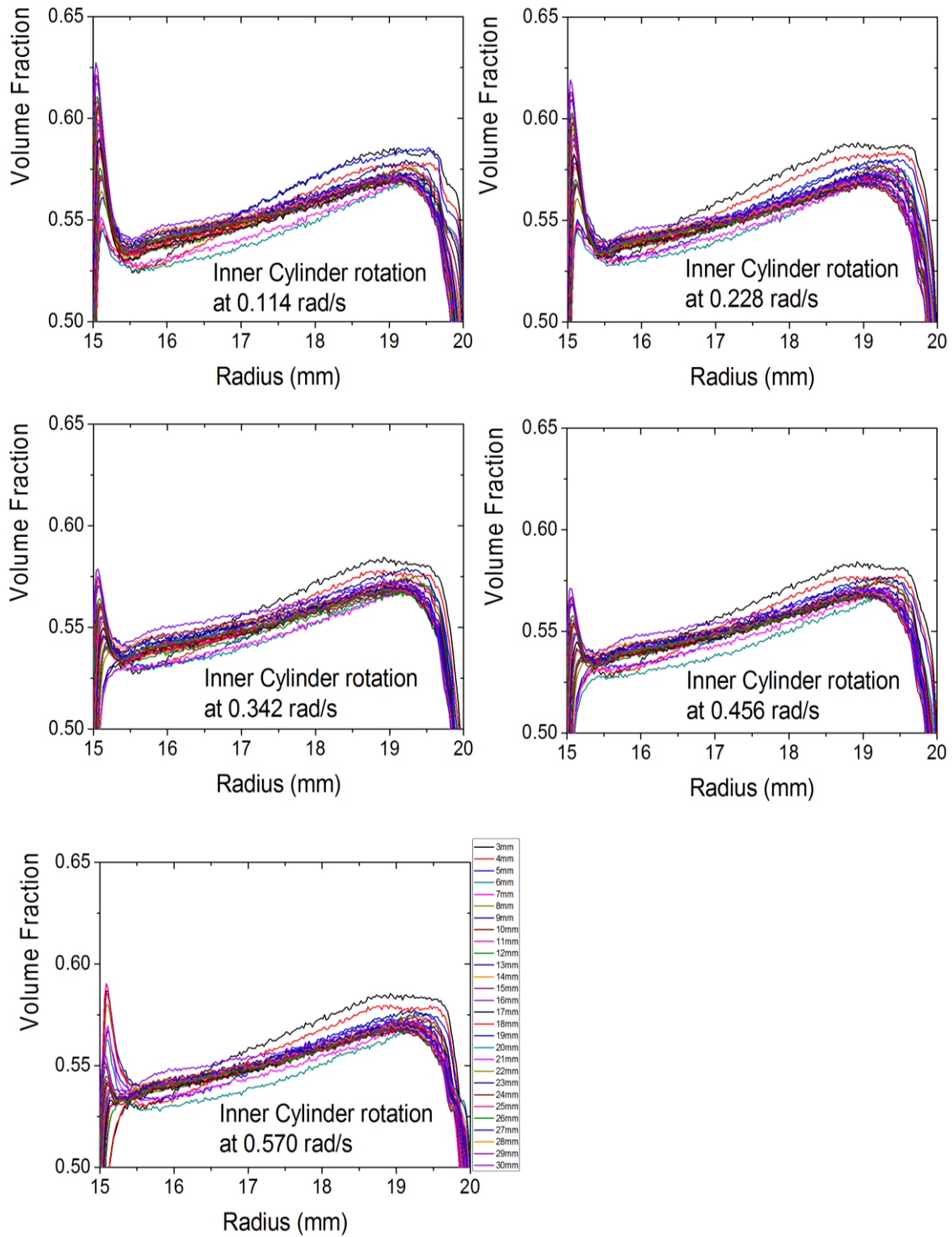


**Fig. D.5** Radial concentration profiles of the density matched suspension ( $\Delta\rho \cong 0$ ) for different altitudes in the Couette cell shear (between 3 – 30mm). Each panel corresponds to a given angular velocity,  $\Omega = \Omega_{in} - \Omega_{out}$ , whose value is indicated at bottom.

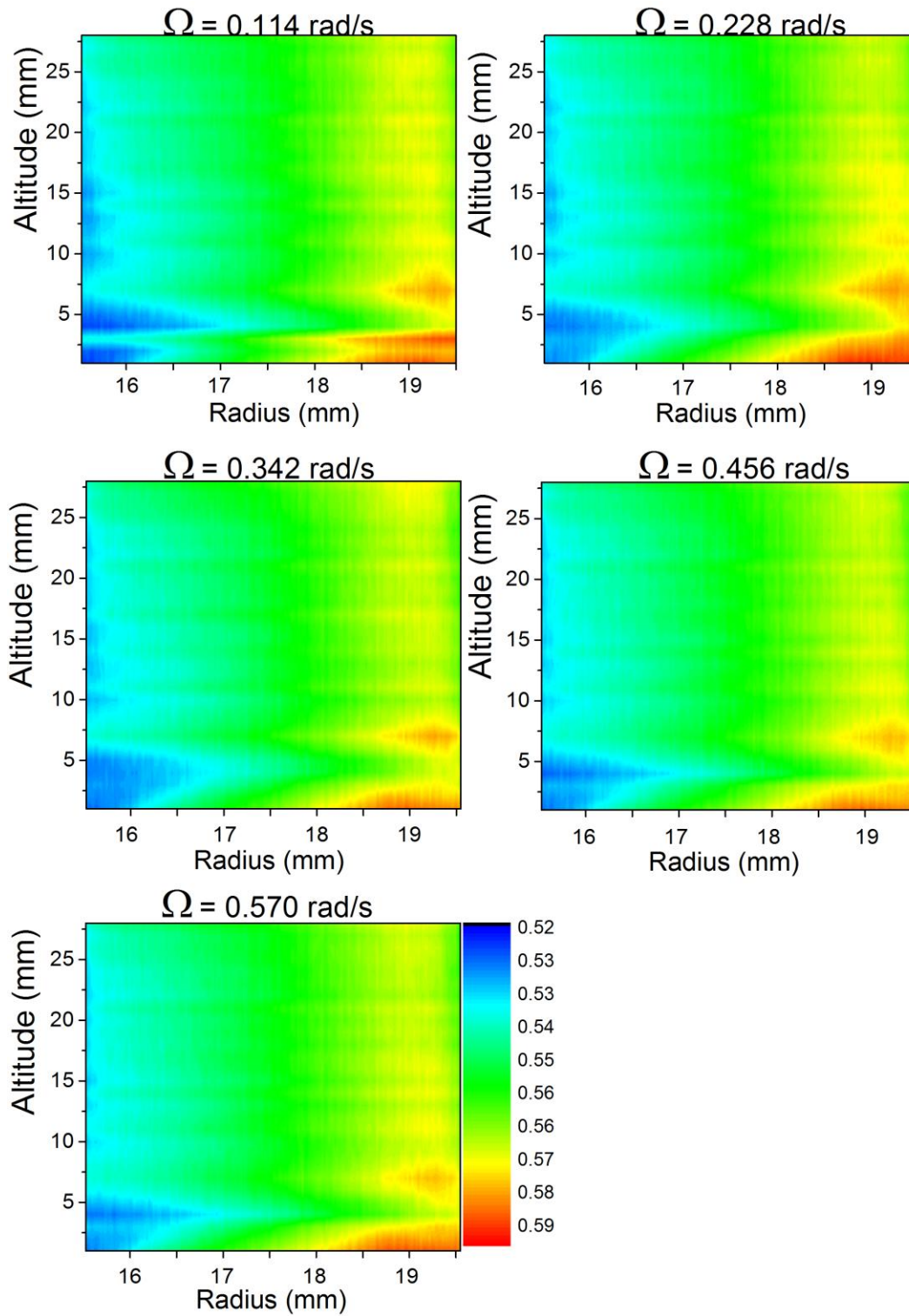


**Fig. D.6** Color coded maps of the concentration of the C16-S150 system ( $\Delta\rho \cong 0$ ). The  $\Omega$  values, indicated at top of each panel, are the same as in Fig. D.5.

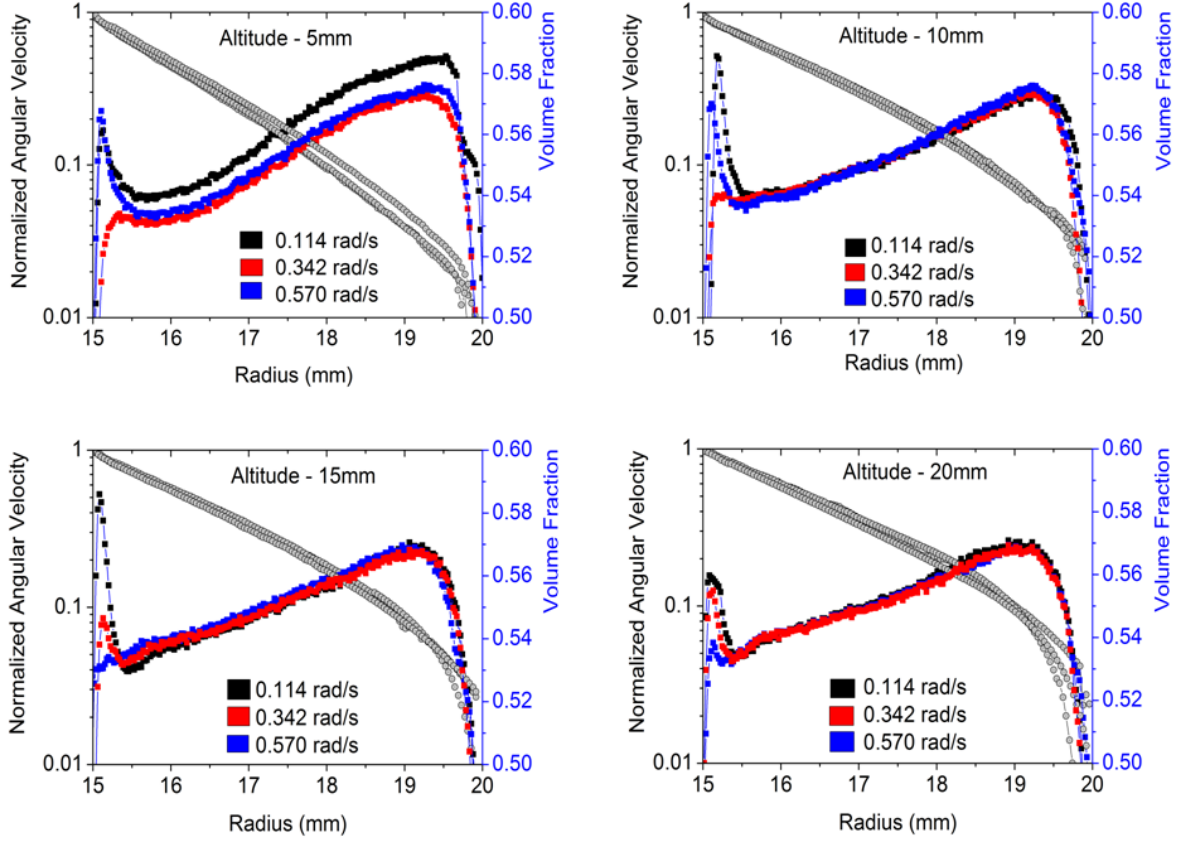


**Fig. D.7** Radial concentration and velocity profiles of the density matched suspension ( $\Delta\rho \cong 0$ ) for different angular velocities. Velocity is scaled to  $\Omega$ . Each panel corresponds to a given altitude, whose value is indicated at top.

In other words increasing the rotor velocity does not increase the amplitude of particle migration. Note that these findings only hold in the stationary regime. We also checked that the concentration fields remained the same when  $\omega$  was increased and then decreased back to the same value. Otherwise stated, we did not observe any hysteresis. The azimuthal velocity field also has a constant shape, and simply scales as  $\Omega$ . Since migration is caused by shear, we might have expected that both migration and the shape of the velocity profile would change with  $\Omega$ . The fact that they do not however is the theoretically expected behavior, as we will see in chapter E, based on force balance theory.

### D.2.2: Non density – matched suspension

The preparation procedure is the same as for the density-matched suspension. The composition of the system is (in mass): PMMA particles (15.00 g); C16-S150 fluid (10.00 g). Due to the density mismatch ( $\Delta\rho \cong 0.3 \text{ g/cm}^3$ ), the particles accumulate into a sediment, leaving a layer of pure fluid on top of the sediment. The corresponding average volume fraction of solid sediment is  $\bar{\Phi} \cong 58 \%$ . The system is pre-sheared and then left “at rest”, as for the density matched mixture.

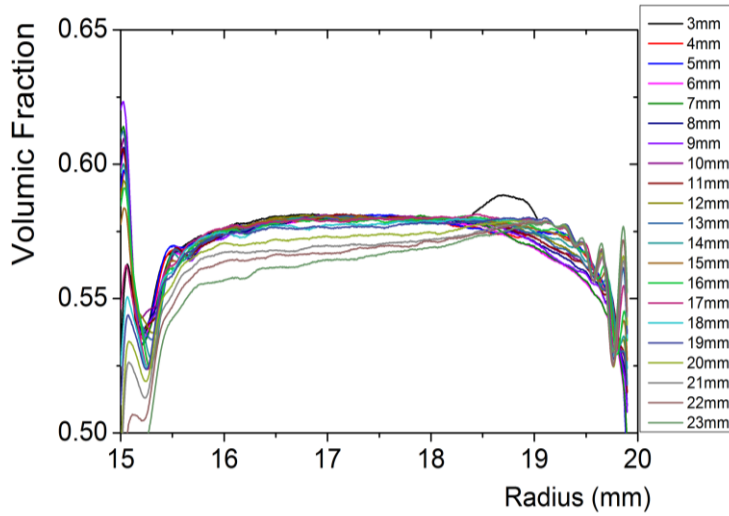


**Fig. D.8** Concentration field in the  $\Delta\rho > 0$  granular system, at rest. The system has been pre-sheared (see text).

**Pre-sheared system, at rest:** The spatially resolved volume fraction,  $\bar{\Phi}(r, z)$ , for the system “at rest”, is displayed below, Fig. D.8. Though the system is rotationally invariant, the concentration throughout the sediment is far from constant, as can be seen from the large variations both in  $r$  and  $z$ . Clearly  $\bar{\Phi}(r, z)$  increases away from the inner cylinder, certainly as a result of migration during the pre-shear period. A less intense but still visible inhomogeneity also shows up in  $z$ , with the concentration larger at bottom than on top of the sediment. The picture is then definitely different from what is obtained in “classical sedimentation”: in this case, the experiment starts with an initially homogeneous distribution of grains inside a parallelepiped vessel and results in approximately homogeneous sediment [Snabre *et al.* 2008, Snabre *et al.* 2009]. The  $\bar{\Phi}(r, z)$  profile for the system “at rest” in the Couette cell is closer to a quenched version of the granular system during pre-shear than to a classical sediment.

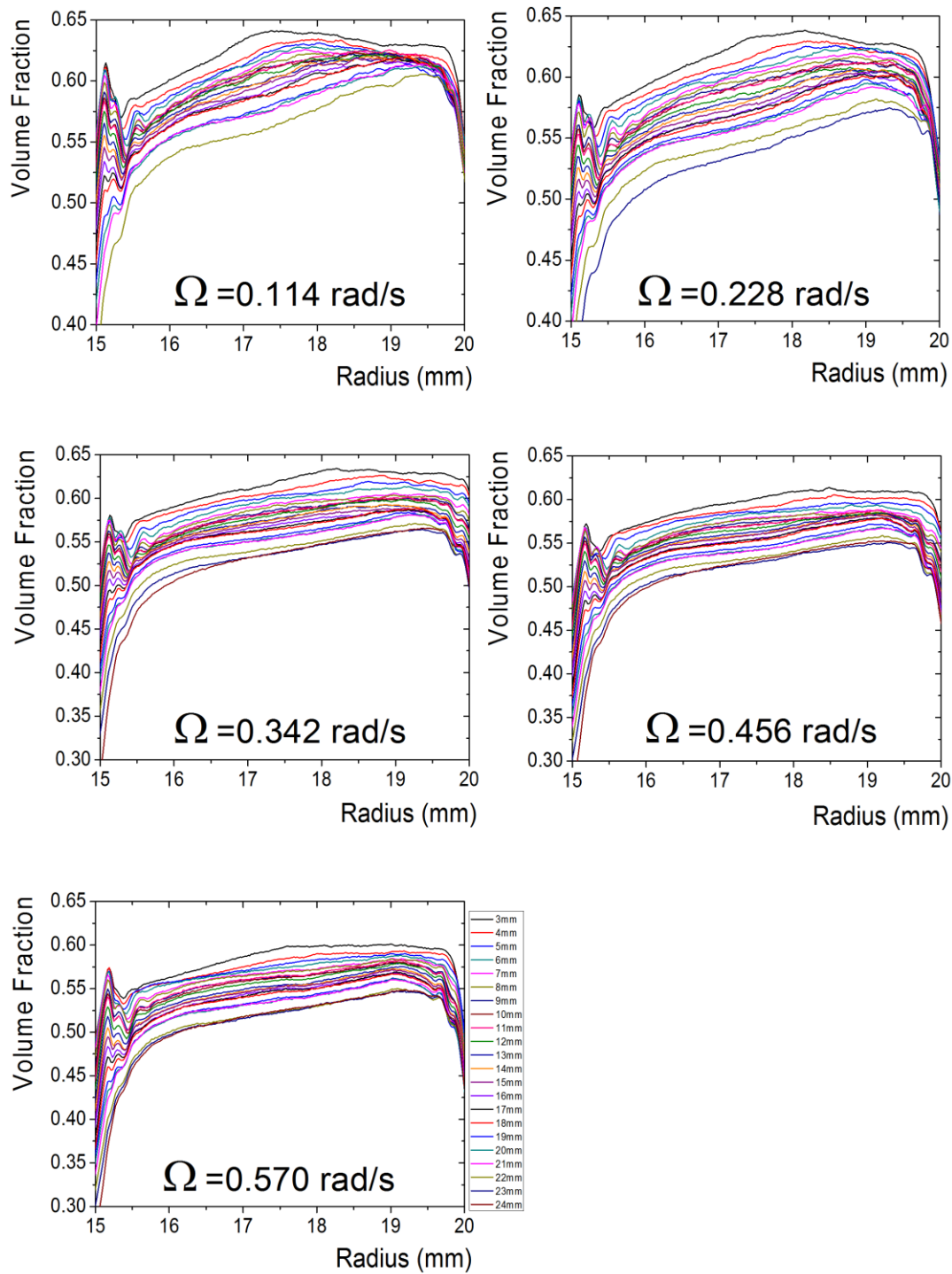


**Fig D.9** Radial concentration profiles of the C16-S150 system ( $\Delta\rho > 0$ ) for different altitudes in the Couette cell shear. The angular angular velocities,  $\Omega = \Omega_{in} - \Omega_{out}$ , are indicated in each panel. The Couette cell was operated rotating just inner cylinder.

***Shear-induced concentration field:*** We now come to the profiles while the system is under shear. We operated the Couette apparatus with  $0.1 \leq \Omega \leq 0.6$  rad/s. This range was found sufficient to evidence the main trends in the shear-induced resuspension of the particles, up to a regime where the concentration profiles were found to “saturate”, meaning that increasing the shear rate would almost not modify the profiles any more. The data displayed below correspond to stationary states, as far as we can tell from our experimental procedure: “stationarity” here simply means that the profiles have been obtained after several hours of running time, and that they did not evolve beyond experimental uncertainty when the experiment was continued for several more hours. The data in Fig. D.9 have been obtained rotating inner cylinder only.

We repeated the same measurements with different repartitions of the angular velocity, from  $\Omega = \Omega_{in}; \Omega_{out} = 0$  (only the inner cylinder is rotating) to  $\Omega_{in} = 0; \Omega_{out} = -\Omega$  (only the outer cylinder is rotating). We found that the corresponding profiles showed no definite dependence on the velocity repartition (see appendix D-C), thus confirming our hypothesis of “rotation invariance” (chapter B).

The same information is shown below (Fig. D.10) in the form of color-coded maps. The maps show that the sheared granular material is organized in a kind of 2-zone pattern: the zone in contact to the inner cylinder is characterized by a ramp of radially increasing concentration. This ramp crosses over to a plateau in the zone at left, towards the outer cylinder. Note that a maximum concentration  $\Phi_{max}(0) \cong 62\%$  is reached in the plateau zone at bottom of the Couette cell and that corresponding values  $\Phi_{max}(z)$  definitely decrease with the altitude.

Remarquably, this 2-zone pattern well correlates to what we found from the velocity profiles, i.e. the coexistence of a sheared “active” zone with a very slowly evolving zone, which we named “dead zone”. Taking  $\Phi_{max}(0) \cong 62\%$  as a lower boundary for jamming, it is clear that the dead zone everywhere at  $z > 0$  is definitely below the jamming limit. Consequently it would be wrong to state that the seemingly “dead zone” is simply a jammed state. This finding is coherent with our observation that particles inside the dead zone have fluctuating velocities, though convection is about null (chapter C).

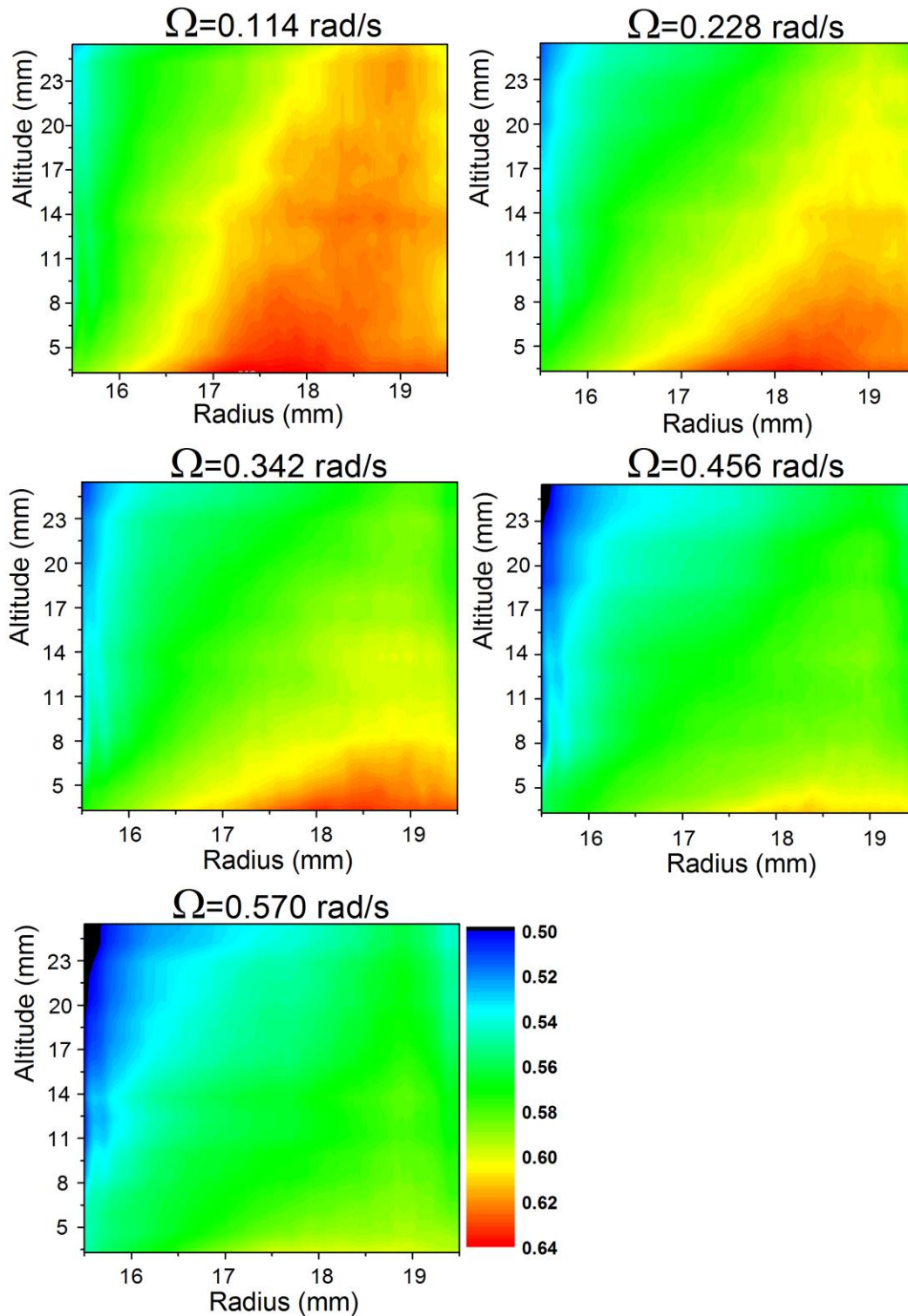


**Fig D.10** Color coded maps of the concentration of the C16-S150 system ( $\Delta\rho > 0$ ). The  $\omega$  values, indicated at bottom of each panel, are the same as in Fig. D.9

The above maps also evidence the process of shear-induced resuspension in the Couette cell. We see that increasing  $\Omega$  results in the “active” zone expanding through the gap (in line

with velocity profiles in chapter C), with a slight overall swelling of the suspension: the height occupied by the particles increases with  $\Omega$ , about 2 mm from left to right in Fig. D.11. This property was already evidenced by Lenoble, using a method based on laser speckle [Lenoble thesis 2005]. Since the Couette gap is a constant, the increase in height evidences an increase of the volume occupied by the particle, and is thus a direct illustration of Reynolds dilatancy [Reynolds 1886].

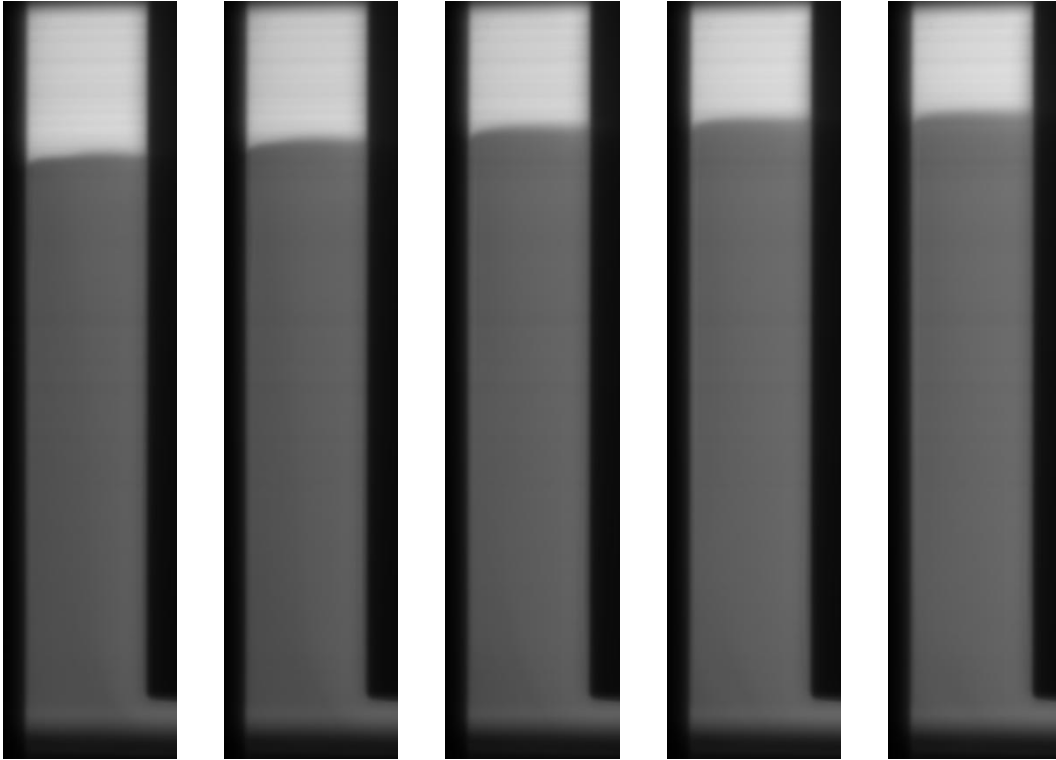


**Fig.D.11** *Granular material dilatancy under shear. Fluidization of a gravitational suspension of 58% volume fraction (at rest in sediment) under different angular velocities of inner cylinder: 0.114 rad/s; 0.228 rad/s; 0.342 rad/s; 0.465 rad/s and 0.570 rad/s (from right to left).*

**Saturation of the radial concentration profile:** shear-induced resuspension obviously increases with  $\omega$ , as can be seen from Fig. D.12. The process has an asymptotic limit, as we describe below. In the high shear limit, we expect the system to be equivalent to the density matched suspension, with no definite change in the radial concentration profile when  $\omega$  is varied. We refer to this regime as “saturation”.

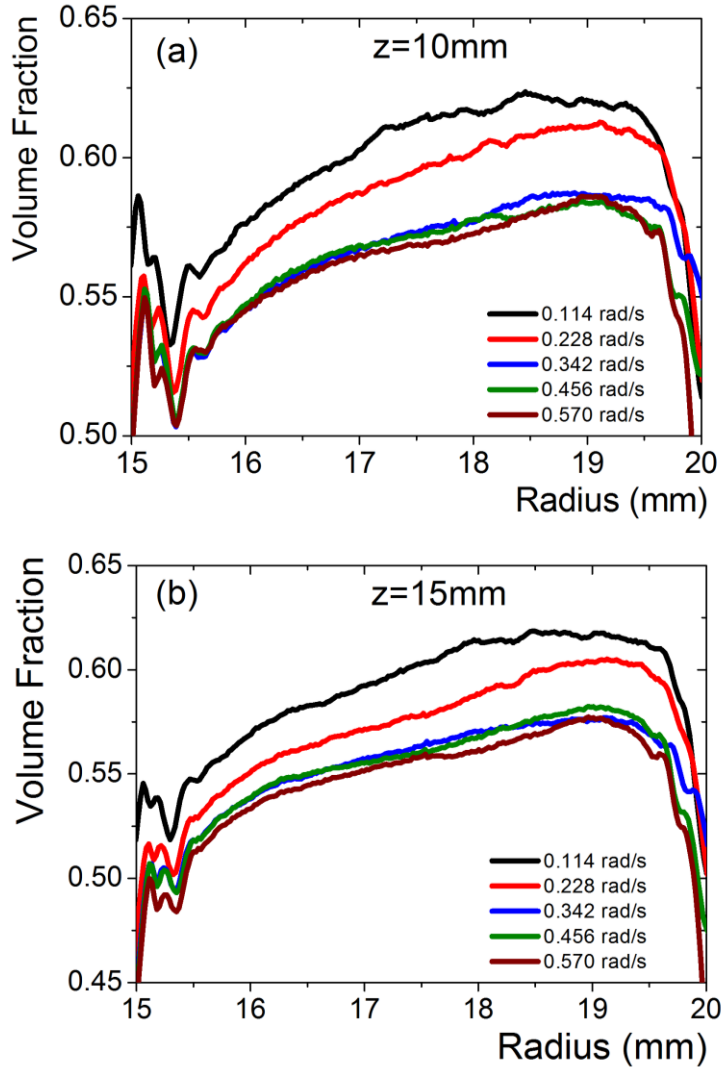


**Fig.D.12** Saturation of shear induced migration. Radial velocity profiles at (a)  $z=10\text{ mm}$  and (b)  $z=15\text{ mm}$ , for increasing inner cylinder velocities from 0.114 rad/s up to 0.570 rad/s.

The graphs in Fig.D.12 show that saturation is reached whenever  $\Omega$  is larger than  $\Omega_{sat} \cong 0.342\text{ rad/s}$ . However, note that the granular system at this rotation rate is very far from being fully resuspended, since a large layer (about 5 mm in thickness) of pure immersion fluid is still present under the meniscus. Moreover, the  $r$ -averaged concentration  $\bar{\Phi}(z)$  still definitely decreases from bottom to top. In the saturation regime, the suspension amounts to a stack of layers with different average concentrations  $\bar{\Phi}(z)$ , with each layer responding to shear similarly to a density matched suspension of same  $\bar{\Phi}$ .

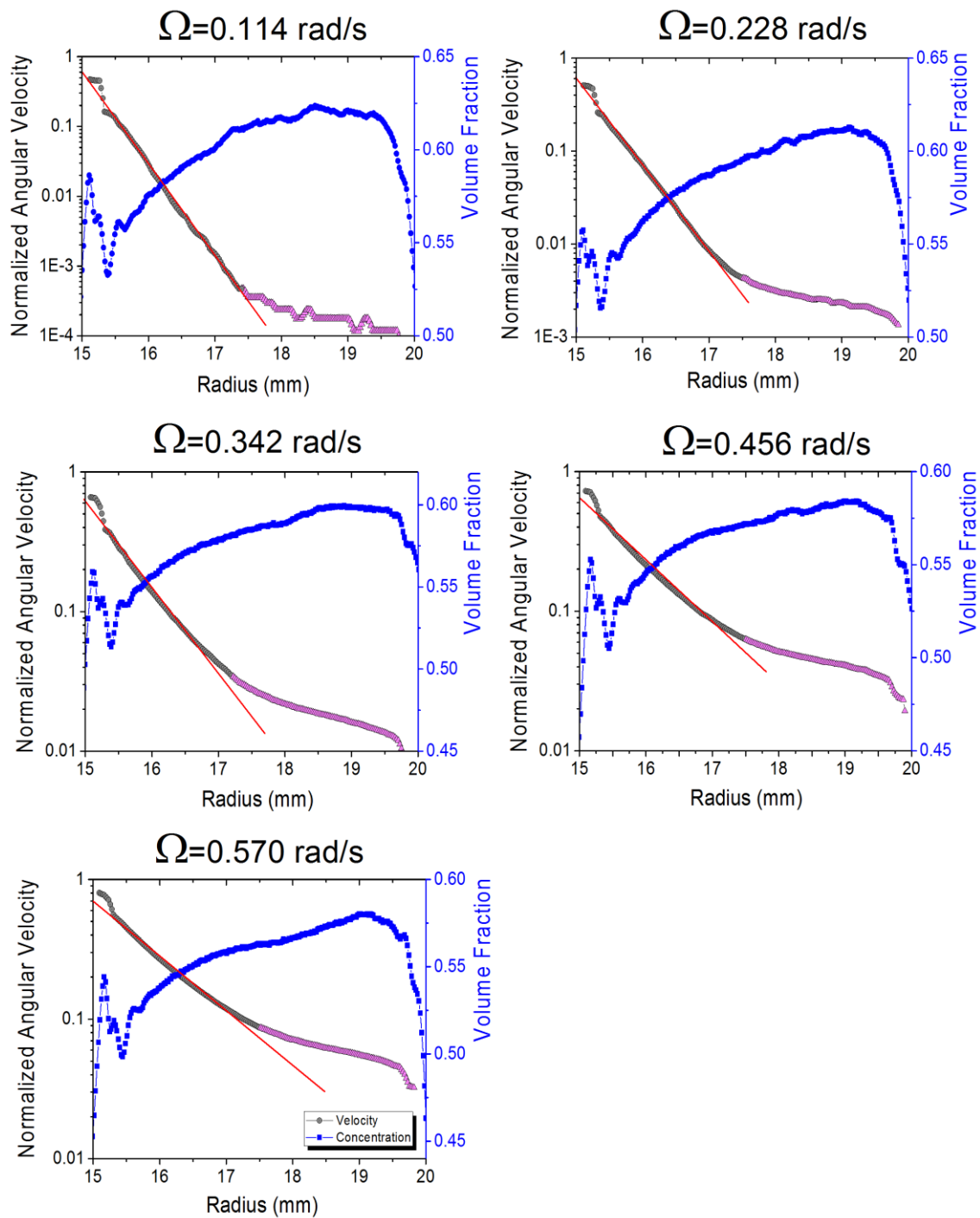


**Fig.D.13** Combining velocity and concentration data for the C16-S150 system ( $\Delta\rho > 0$ ), at  $z = 15$  mm. Velocity is plotted in semi-log scale, to show the transition between “active” (in gray) and “arrested” (in magenta) zones. Straight lines (in red) along the velocity profiles are guides to the eye.

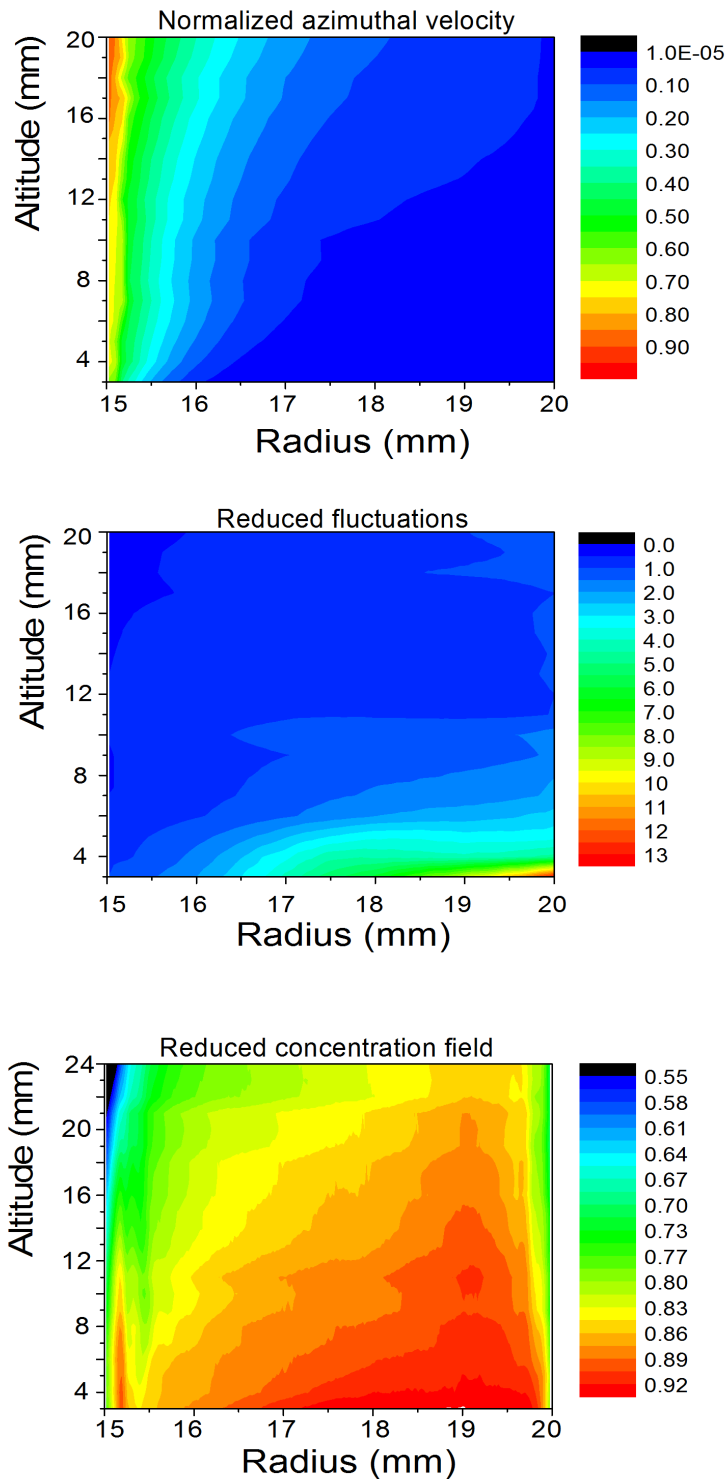


**Fig D.14** Color coded maps of normalized azimuthal velocity ( $\omega/\Omega$ ), associated reduced fluctuations ( $\Delta\omega/\omega$ ) and reduced concentration field ( $\Phi/\Phi_{RCP}$ ) for the C16-S150 system ( $\Delta\rho > 0$ ) in case of a  $\Omega = 0.570$  rad/s.  
*Note:*  
 $(\Delta\Omega = \delta\theta/\delta t)$   
 $(\Phi_{RCP} = 0.64)$

**Gathering velocity and concentration measurements:** In this paragraph we want to compare velocity and concentration maps directly. Fig. D.14, below gathers the data for average azimuthal velocity, velocity fluctuations and concentration for  $z = 15$  mm. The figure directly illustrates the coupling between migration and flow localization.

The above data clearly show how shear-induced resuspension in Couette flow organizes the granular system in two distinct zones, “active” and “dead”. Though the picture may be

viewed as a kind of localization, it is not strictly a case of two coexisting phases with a sharp interface in between. Rather than a discontinuity, we observe a crossover between both zones. The “dead” zone is not a jammed phase, as we saw, but rather a “noisy arrested” phase. To help comparison, the data for concentration, velocity and velocity fluctuations are displayed in the form of color maps below, for  $\Omega = 0.570$  rad/s (Fig. D.14). As we already mentioned, the dead zone is everywhere well below the jamming limit, and is therefore not a solid; it is in fact a very concentrated granular paste. These observations suggest that the flow of the granular paste cannot be understood without including velocity fluctuations, which are fed by the shear itself [Bocquet *et al.* 2001]. This feature is evident in the most concentrated zones of the system, corresponding to the dead zone.

### D.3: Summary

Using the fluorescence of the immersion liquid, we have been able to measure the concentration of particles under shear throughout the Couette cell. The study was carried out mainly in stationary regime, in the density-matched suspension and in the non density matched system. We thus could evidence the competition between gravity and shear, namely the shear-induced resuspension effect in a large-gap Couette cell. We found that when gravity is absent ( $\Delta\rho \cong 0$ ), the granular suspension self-organizes into remarkably constant concentration and  $\omega$ -scaled velocity profiles. These profiles presumably only depend on the average concentration of the suspension. At  $\bar{\Phi} \cong 55$  %, the azimuthal flow has a non Newtonian profile, but is not localized. Due to gravity, the non-density-matched granular suspension gets stratified, with the concentration decreasing from bottom to top. Concomitantly, the flow is strongly localized at bottom, and not localized near the suspension-pure immersion fluid on top of the shear cell. Not surprisingly, the observations also revealed the increase of the re-suspension with  $\Omega$ , but this increase was found to saturate around some finite value of  $\Omega$ .

## Appendix D-A: Laser beam and sheet characteristics

The laser source is a green ( $\lambda=514.5\text{nm}$  in air) argon ion laser Innova 300 from Coherent. The laser yields a beam of diameter 1.5 mm and divergence 0.5 mrad. In general the operational output power is between 1 and 2 W. The laser beam goes through an optical system composed of mirrors and lenses to generate a planar vertical laser sheet (Fig. D.2). The sheet has a vertical size large enough to illuminate the whole height of the Couette cell, and has an almost constant intensity, from bottom to top. This appendix deals with the measurement of the thickness ( $2w$ ) of the sheet, i.e. its horizontal dimension ( $y$ ), within the cell. We suppose that the intensity distribution is Gaussian, see Eq. (B.1).  $2w$  goes through a minimum, the so-called “beam-waist” (b.w.)  $2w_0$ , in a plane located upwards of the Couette cell. The position of the b.w. plane can be found simply by observing the spot of the beam on a white paper. A more elaborate method consists in observing the light scattered by the paper on a screen at some distance, say 20 cm, from the paper. What is seen on the screen is a speckle, whose grains are largest when the paper is in the b.w. plane. Based on this criterion, we found that the b.w. was located at  $18\pm 0.5$  cm upstream of the olearium front window (Fig. D-A1).

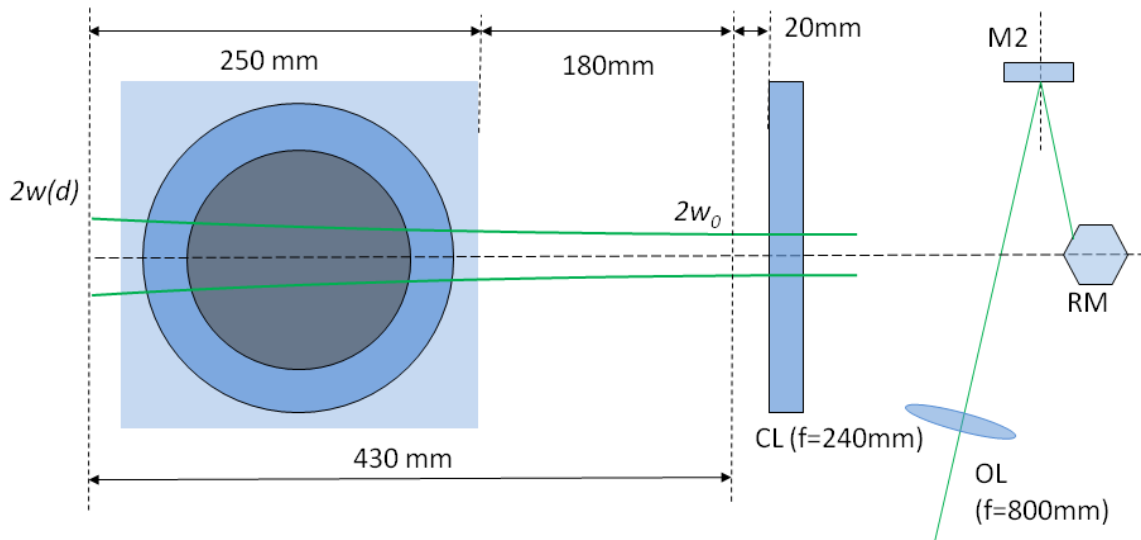


**Fig. D-A1** Laser sheet divergence scheme inside the Couette cell. OL – optical lens; M2 – mirror; RM – rotating mirror; CL – cylindrical lens

In order to characterize the transverse intensity distribution we used the so-called “knife edge technique”: the method simply amounts to partially intercept the beam with a

razor blade, and measuring the power transmitted behind the blade ( $P_{trans}$ ), with a laser powermeter. Repeating the measurement for different positions of the blade edge ( $y_{edge}$ ), we obtain:

$$P_{trans} = \int_{-\infty}^{y_{edge}} I(y) dy \quad (\text{D-A1})$$

We could not install the blade+powermeter system directly in the b.w. plane, due to space limitations. We instead performed the measurement at a distance  $d = 43$  cm from the b.w., in air, and found  $w(d) = 0.535$  mm in this plane. Deducing the value of  $w_0$  is straightforward using Eq. (B.2), with  $\lambda = 0.514$  nm. We find  $w_0 = 0.136$  mm. The corresponding diffraction length is  $l = \pi w_0^2 / \lambda \cong 115$  mm.

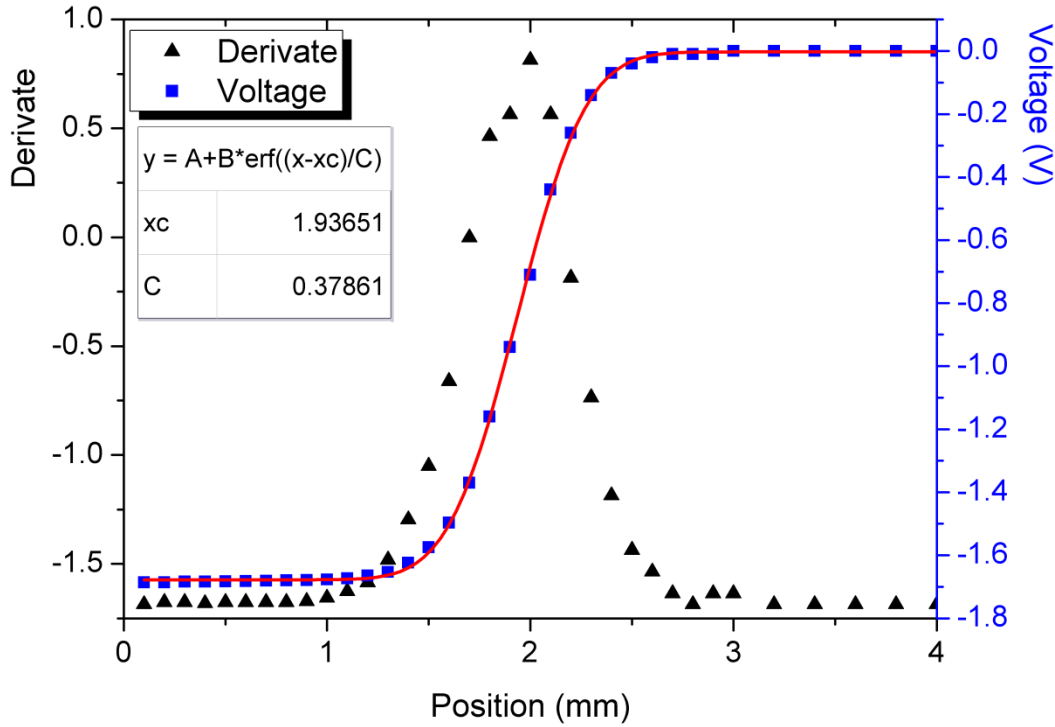


**Fig. D-A.2** Knife edge technique for determination of the laser sheet transverse intensity profile. Measurement at  $d = 43$  cm from the beam-waist. An error function very well fits to measurement points (blue squares), indicating that the profile indeed is close to Gaussian. The intensity distribution is obtained by derivation (black triangles).

We now want to calculate the laser sheet width inside the Couette cell. We take into account the refraction through the air-PMMA interface as follows (details of the reasoning can be found in G. Martinot-Lagarde PhD thesis, appendix B [[Martinot-Lagarde 1995](#)]):

- Let be  $L$  the distance of the b.w. to the olearium.  $L=180$  mm, see Fig. D-A2.
- Refraction through the PMMA interface builds a new Gaussian beam, with the *same value of the b.w.*, but whose b.w. plane has been shifted upstream, at the distance  $L' = nL \cong 266.4$  mm. Here  $n \cong 1.48$  is the refractive index of PMMA.
- The new beam propagates inside PMMA, with a diffraction length  $l' = nl \cong 170.5$  mm.

The beam enters the gap of the Couette cell at the distance  $x_{in} \cong 281.4$  mm and gets out of the gap at the distance  $x_{out} \cong 321.4$  mm, from the new b.w. plane. Applying the same diffraction law as before (Eq. B.2), now with  $l'$  as the diffraction length, we find the corresponding beam radii inside the Couette cell:  $w_{in} \cong 0.264$  mm and  $w_{out} \cong 0.290$  mm.

## Appendix D-B: Optically measured concentration field in Couette geometry. Compensation for laser sheet non uniformity and attenuation

### Definition of symbols:

$P$  : power of the laser beam (as indicated by laser remote control)

$F(z)$  : intensity distribution of the laser sheet along  $z$  (vertical)

$C(r,z)$  : collection efficiency of the imaging optics (represents the fact that a uniform scene does not give an image of uniform grey level)

$\Phi(r,z)$  : volume fraction of solid particles in the granular paste, as a function of  $r$  (distance to Couette axis) and  $z$  (vertical)

$A(u)$  : attenuation of laser light through a distance  $u$  inside the granular paste. Note:  $0 \leq u \leq d$ , where  $d$  is the gap between inner (radius  $R$ ) and outer (radius  $R+d$ ) cylinders

$f$  : fluorescence efficiency of the immersion fluid.  $f$  represents the fluorescence intensity of the fluid for  $P=1$  power unit.

$p$  : fluorescence efficiency of the particles' material (PMMA).  $p$  represents the fluorescence intensity of the fluid for  $P=1$  power unit.

$$\eta = 1 - \frac{P}{f}$$

$T$  : exposure time

$B$  : background (darkness) signal per unit exposure time

The video signal (grey level) corresponding to the **right part** (panel (b)) is given by:

$$S_{right}(r, z) = PF(z)C(r, z)A(R+d-r)f[1-\eta\phi(r, z)]T + BT \quad (1)$$

The last term in eq.(1) is the darkness signal  $S_{dark} = BT$ .

We now define the reference signal, corresponding to the pure fluid. Experimentally, this signal is measured with the Couette cell filled with the immersion fluid alone (no particles).

$$S_{right}^{ref}(r, z) = PF(z)C(r, z)fT + BT \quad (2)$$

**Both  $S_{right}^{ref}(r, z)$  and  $S_{dark}$  must be measured in calibration experiments.** On this basis we define:

$$\rho_{right}(r, z) = \frac{S_{right}(r, z) - S_{dark}}{S_{right}^{ref}(r, z) - S_{dark}} = A(R+d-r)[1-\eta\phi(r, z)] \quad (3)$$

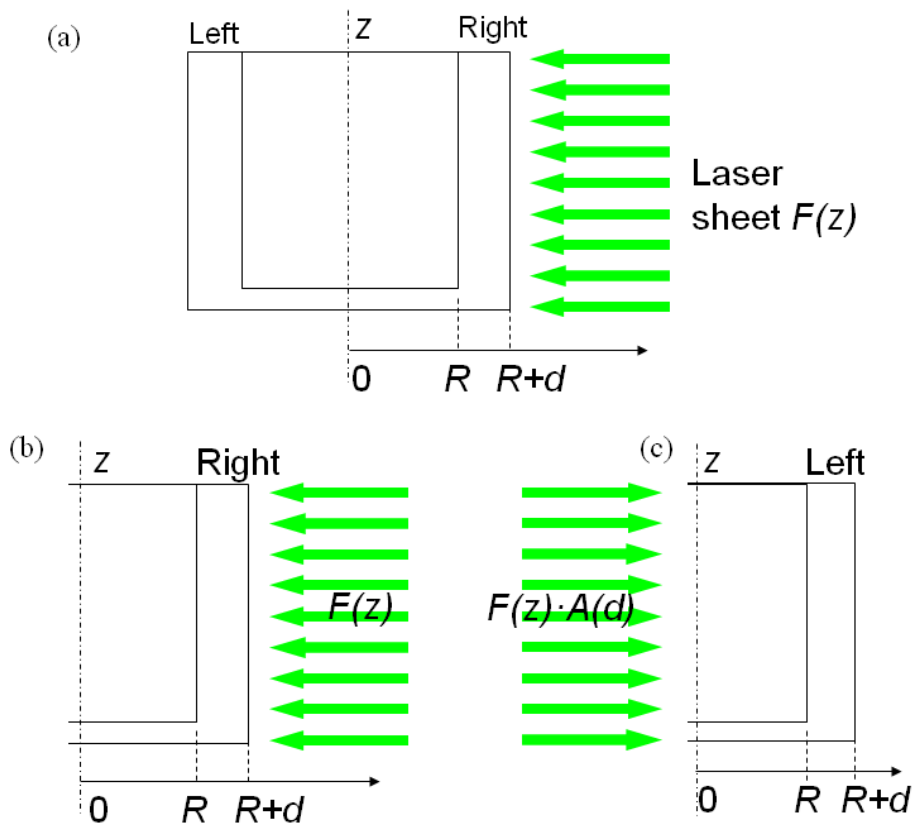


**Fig D-B.1** We suppose that the laser sheet goes through the cell axis (diametric cut). Panel (a) shows the geometry of the experiment, with the laser sheet coming from the right. The intensity is not uniform along  $z$ , hence the  $F(z)$  function. Panel (b) shows what happens in the right part of the Couette cell. The sheet intensity is maximum at  $r_{\max} = R+d$  and decreases down to  $F(z) \cdot A(d)$  at  $r_{\min} = R$ . Panel (c) shows what happens in the left part of the cell. The figure is a mirror image of the left part. In this representation, the laser light comes from the left, with intensity  $F(z) \cdot A(d)$  at  $r_{\min} = R$ . The intensity decreases down to  $F(z) \cdot [A(d)]^2$  at  $r_{\max} = R+d$ .

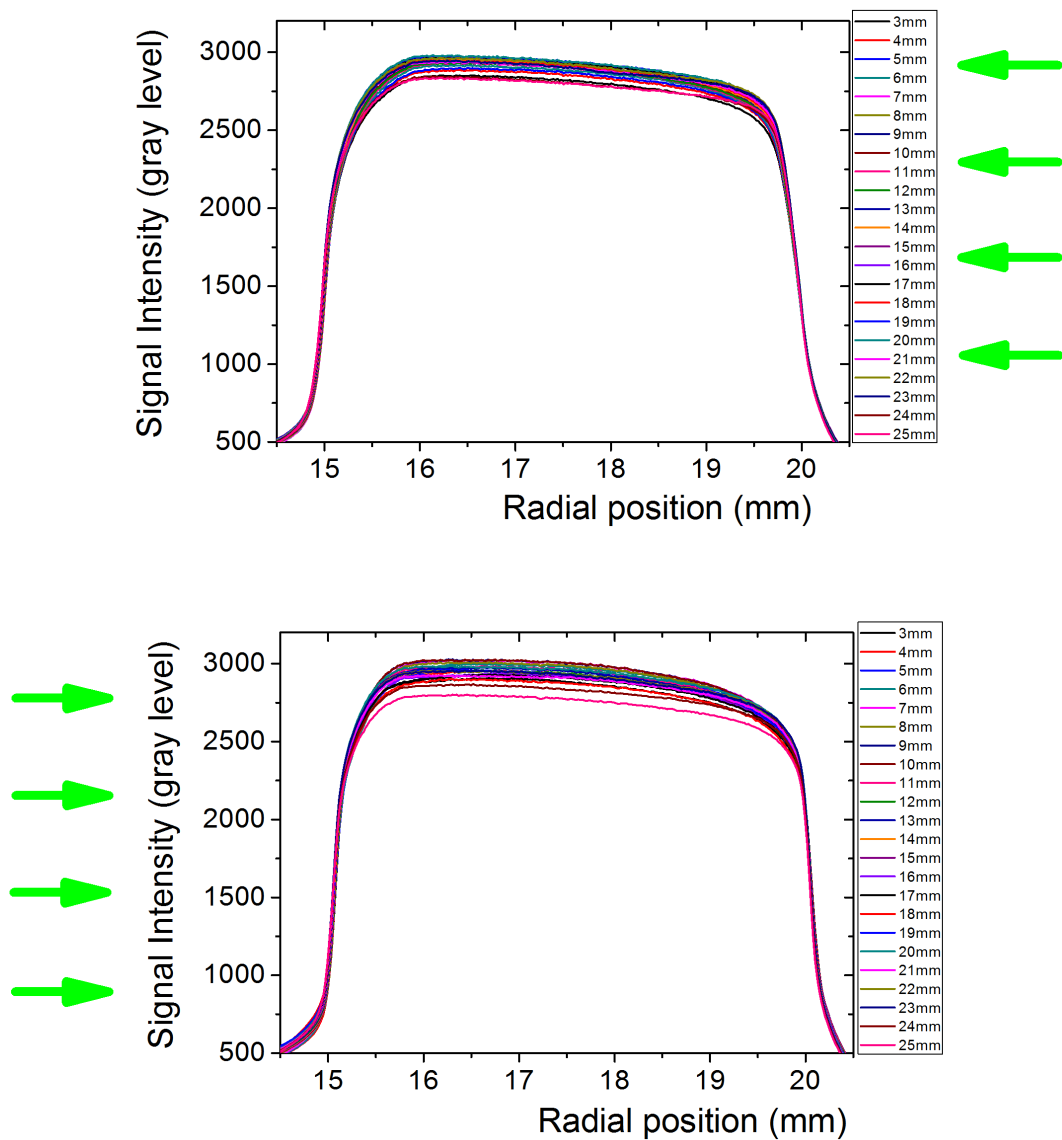


**Fig. D-B.2** Calibration signal. The graphs show the fluorescence intensity of the dyed immersion fluid for different altitudes in both sides of the Couette cell. The direction of propagation of the laser light is indicated by the arrows.

Clearly the information from the right part of the video image is not enough to find the concentration field, essentially because of the attenuation of the laser.

We now consider the video signal (grey level) corresponding to the **left part**. We apply the **mirror symmetry as defined in panel (c)**. Then:

$$S_{left}(r, z) = PF(z)C(r, z)A(d)A(r-R)f[1-\eta\phi(r, z)]T + BT \quad (4)$$

As before we define the reference signal:

$$S_{left}^{ref}(r, z) = PF(z)C(r, z)fT + BT \quad (5)$$

Similarly to eq.(3), we obtain:

$$\rho_{left}(r, z) = \frac{S_{left}(r, z) - S_{dark}}{S_{left}^{ref}(r, z) - S_{dark}} = A(d)A(r-R)[1-\eta\phi(r, z)] \quad (6)$$

Of course the information from the left part of the video image is not enough to find the concentration field, again because of the attenuation of the laser. Fortunately **it is sufficient to combine the data from both sides to isolate the relevant information, namely  $\eta\phi(r, z)$ .**

Let us define:

$$h(r) = \frac{\rho_{right}(r, z)}{\rho_{left}(r, z)} \quad (7)$$

Note that  $h(r)$  does not depend on  $z$ , and that  $h(R)=1$ . We now make the simple assumption that the attenuation is exponential, i.e.

$$A(u) \cong \exp\left(-\frac{u}{l}\right), \quad (8)$$

where  $l$  is the absorption length and  $u$  is the distance inside the medium ( $0 \leq u \leq d$ ). We are not sure that the absorption is exponential in the granular medium. Fortunately the attenuation of the laser light in our experimental conditions is weak, and thus may be approximated as linear. Eq. (8) is an acceptable approximation, in so far as  $d \ll l$ . Combining eqs. (3), (6), (7) we obtain:

$$h(r) = \exp\left(2\frac{r-R}{l}\right) \quad (9)$$

We see that  $h(r)$  monotonously increases from 1 at  $r = R$  up to

$$\left[A(d)\right]^2 = \exp(2d/l) \text{ at } r = R + d.$$

Note that this may be checked from the experimental data.

With the explicit form of  $h(r)$  given by eq. (9) and with eqs. (3) and (6), we arrive at :

$$\eta\phi(r, z) = 1 - \left[ \frac{h(r_{max})}{h(r)} \right]^{\frac{1}{2}} \rho_{right}(r, z) \quad (10a)$$

And equivalently:

$$\eta\phi(r, z) = 1 - [h(r_{\max})h(r)]^{1/2} \rho_{\text{left}}(r, z) \quad (10b)$$

When exploiting the experimental data, it will be important to check the validity of the above predictions, namely:

- Eq. (9) for  $h(r)$  ;
- The fact that eqs (10a) and (10b) indeed provide the same profiles, within experimental uncertainty.

Note that eq. (10) still contains the unknown  $\eta$  prefactor. It may be possible to determine  $\eta$  from the fluorescence levels of the immersion fluid and that of PMMA. The latter may be measured from the weak fluorescence of the PMMA constituting the Couette cell parts (this amounts supposing that the PMMA of the particles and that of the cell have the same fluorescence properties). An alternate and preferable (in my opinion) way is to numerically calculate the spatial average of  $\eta\phi$  :

$$(\eta\phi)_{av} = \frac{\iint_{\Sigma} \eta\phi(r, z) r dr dz}{\iint_{\Sigma} r dr dz} \quad (11)$$

The integration is performed throughout the area  $\Sigma$  occupied by the particles. In principle,  $(\eta\phi)_{av}$  deduced from eqs. (10) and (11) should be equal to  $\eta \cdot \bar{\phi}$ , where  $\bar{\phi}$  is the average volume fraction of grains. The value of  $\bar{\phi}$  is to be determined from the known total mass of PMMA in the sample and from the volume occupied by the grains in the shear configuration of interest. The comparison yields the value of  $\eta$ .

About light scattering : the above analysis does not include the effect of light scattering due to the imperfect index-matching between particles and immersion fluid. The issue of light scattering is certainly not as straightforward as that of simple absorption (which we dealt with). The effect of scattering is most visible in fluorescence profiles the near the boundaries of the Couette cell: the profiles are not sharp as they should be, but blunt. It may be possible to improve on this by collecting data not only in a diametric cut but through a complete set of planes at varying distances from the axis (this was suggested to us by S. Wiederseiner). This method may turn out tedious; moreover the analysis will only be possible in the frame of a model including light scattering. Such a model is still lacking.

## Appendix D-C: Rotation invariance

In this appendix we show concentration profiles obtained with the  $\Delta\rho > 0$  system (C16-S150 immersion fluid) for  $\Omega = \Omega_{in} - \Omega_{out}$  between about 0.2 and 0.6 rad/s. The test about rotation invariance amounts to recording profiles for the same  $\Omega$ , but with different repartitions of the rotation between the inner and outer cylinders:  $\Omega_{in} = \Omega$ ,  $\Omega_{out} = 0$  (only the inner cylinder is rotating);  $\Omega_{in} = 0$ ,  $\Omega_{out} = \Omega$  (only the outer cylinder is rotating); or with both cylinders in rotation, i.e.  $\Omega_{in} = \Omega + \Omega_{off}$ ,  $\Omega_{out} = \Omega_{off}$ , with a finite offset ( $\Omega_{off} \neq 0$ ). Profiles for 0.228 rad/s corresponding to different altitudes, from bottom to top of the suspension, are displayed in Fig. D-C.1.

Fig. D-C.2 has been designed to allow for direct comparison of the profiles, corresponding to a unique altitude, but for different repartitions between both cylinders and for different values of the difference in cylinders rotation rates. In general, differences between profiles are small, within statistical scatter. However some clear differences appear sometimes, but these may be related to slightly non reproducible amounts of slip along the cylinders walls, as we mentioned in chapter C. As a whole the test is positive, indicating that rotation invariance holds, at least approximately, in our experimental system.

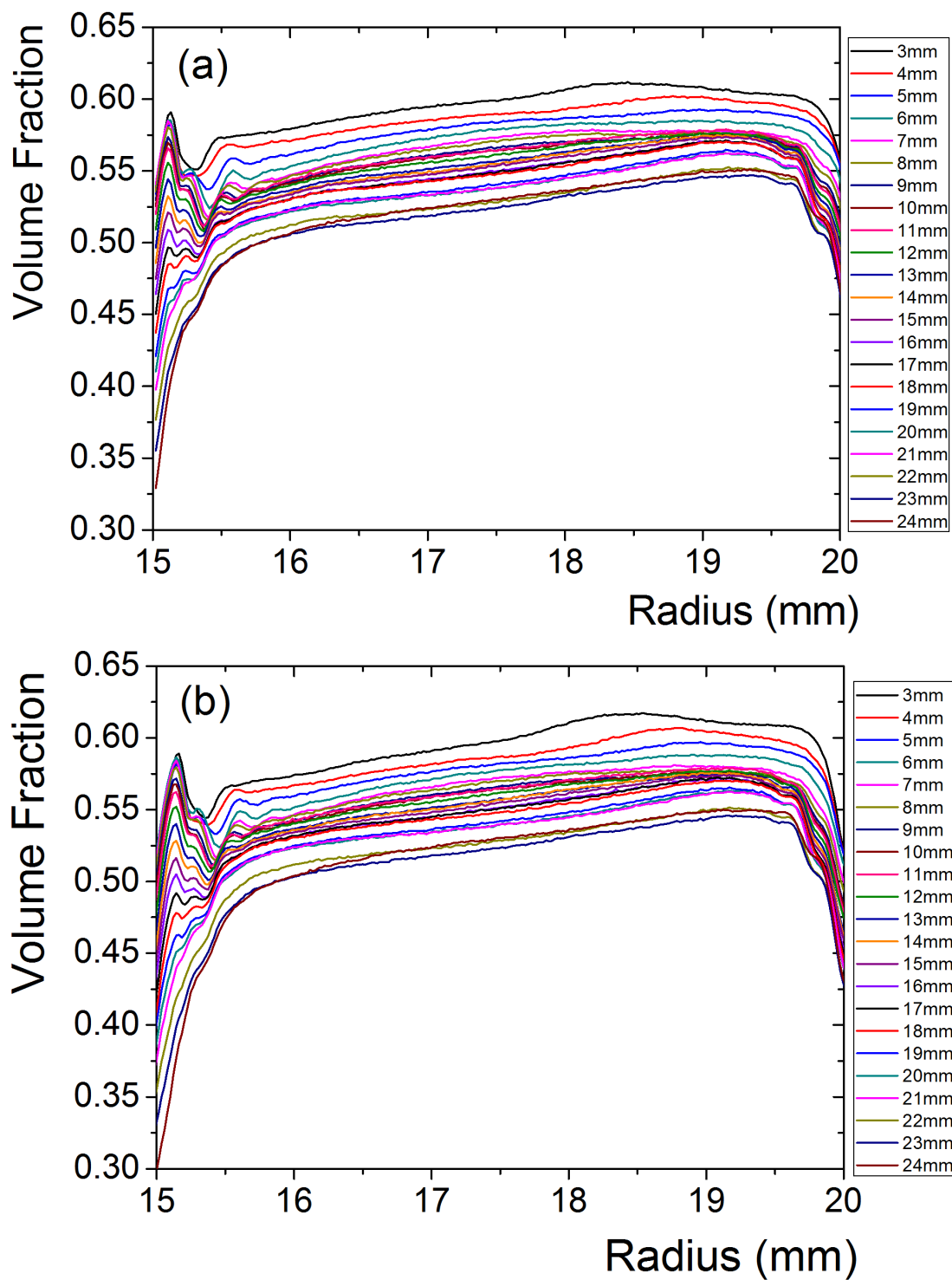


**Fig. D-C.1** Concentration fields of the  $\Delta\rho > 0$  granular suspension for different altitudes. (a):  $\Omega_{in} = 0$  rad/s,  $\Omega_{out} = 0.456$  rad/s (outer cylinder rotation). (b):  $\Omega_{in} = 0.228$  rad/s,  $\Omega_{out} = -0.228$  rad/s (contra rotation). For (b) inner and outer cylinders were rotating in opposite direction with the same angular velocity.

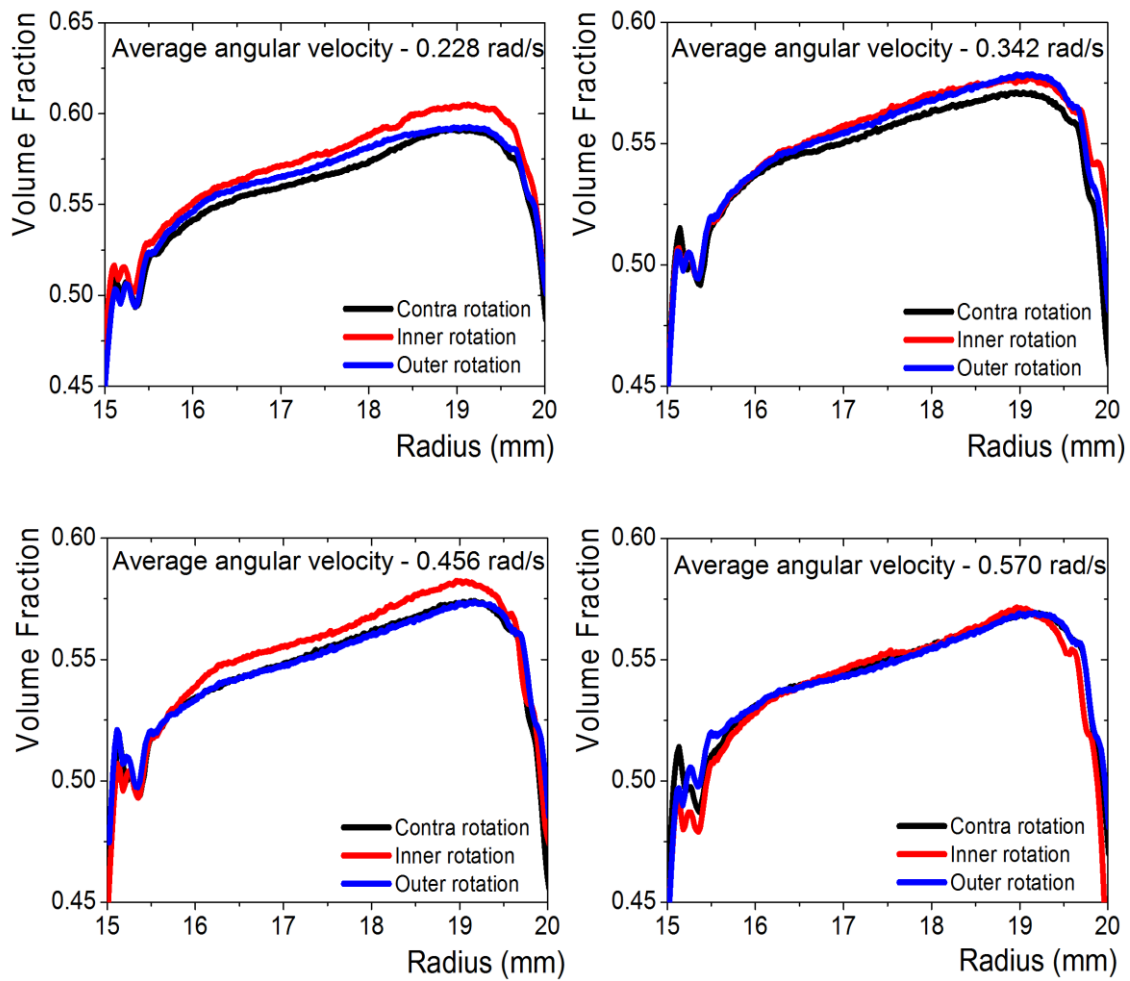


**Fig. D-C.2** Concentration fields of the  $\Delta\rho > 0$  granular suspension for different angular velocities and repartitions between both cylinders, for a given altitude (15 mm).

## Chapter E – Normal force balance model: viscous resuspension in a large – gap Couette flow

The first part of the chapter concerns the resolution of the force balance equations based on the model initially proposed by Morris and Boulay [Morris and Boulay 1999]. The physical principles of the normal force balance model are given in the original Morris and Boulay paper, and are reviewed in the recent work by Boyer *et al.* (2011). We refer the reader interested in the elaboration of the model to the cited articles. Below we adopt notations similar to those of Boyer *et al.* (2011). A numerical resolution of the force balance equations gives both concentration and velocity profiles in the sheared suspension for buoyant or non buoyant particles immersed in a viscous fluid.

The chapter is organized as follows:

After presentation of the force balance model, an analytical and numerical method provides a solution that mainly involves the function  $f(\varphi) = \hat{\eta}_n / \hat{\eta}_s$ , which is the ratio between viscometric functions of the suspension, for the normal force differences and the shear stress. The predictions of the force balance model give indication about the more appropriate viscometric function to describe the migration processes and the stationary flow of a density- matched suspension. In the case of non density-matched suspensions, the flow is no more invariant along the vertical direction and the shear induced re-suspension of particles further depends upon the amplitude of normal stress differences within the sheared suspension. The chapter ends with a discussion about non local effects and possible improvements of the force balance model to better account for the shear induced fluidization of a non density-matched suspension.

### E.1: Force balance equations

We consider the suspension as an effective viscous fluid and we suppose that the flow is simply azimuthal, i.e. the velocity  $\mathbf{v} = v\hat{\theta}$  is along the  $\hat{\theta}$  direction, in cylindrical coordinates  $r, \theta, z$ .

The shear rate is  $\dot{\gamma} = r \partial(v/r) / \partial r$ . All components of the stress tensor are supposed to scale linearly with  $\dot{\gamma}$ :

$$\tau = \eta_0 \hat{\eta}_s \dot{\gamma}, \quad (E.1)$$

is the viscous shear stress.  $\eta_0$  is the viscosity of the suspending fluid, and  $\eta_0 \hat{\eta}_s$  is the shear viscosity of the suspension, for the local volume fraction  $\Phi(r, z)$ .

$N_1, N_2$  are the first and second normal stress differences:

$$N_1 = (\lambda_2 - 1)\eta_0 \hat{\eta}_n \dot{\gamma} \quad (\text{E.2a})$$

$$N_2 = (\lambda_3 - \lambda_2)\eta_0 \hat{\eta}_n \dot{\gamma} \quad (\text{E.2b})$$

The prefactors are the normal force viscometric coefficients. The viscometric functions  $\hat{\eta}_s, \hat{\eta}_n$  increase with the volume fraction and diverge when  $\Phi \rightarrow \Phi_m$ , the maximum volume fraction. The vertical component of the particle phase stress tensor is given by

$$\Sigma_{zz} = -\lambda_3 \eta_0 \hat{\eta}_n \dot{\gamma} \quad (\text{E.3})$$

Values for the  $\lambda_i$  constant have been proposed in former works [Zarraga *et al.* 2000]:  $\lambda_2 = 0.85, \lambda_3 = 0.50$ . We now address the problem of a non neutrally buoyant suspension, made of particles that are heavier than the suspending fluid:  $\Delta\rho = \rho_p - \rho_0$  is the (positive) density difference between particles and fluid. As the experiments reveal configurations that do not evolve in time, say on a day scale, we restrict the analysis to stationary states. The corresponding equations, in cylindrical coordinates and supposing cylindrical symmetry, reduce to:

$$\frac{\partial}{\partial r} (r^2 \eta_0 \hat{\eta}_s \dot{\gamma}) = 0 \quad (\text{E.4a})$$

$$\frac{\partial}{\partial r} (-\lambda_2 \eta_0 \hat{\eta}_n \dot{\gamma}) = \frac{(\lambda_2 - 1)\eta_0 \hat{\eta}_n \dot{\gamma}}{r} \quad (\text{E.4b})$$

$$\frac{\partial}{\partial z} (\lambda_3 \eta_0 \hat{\eta}_n \dot{\gamma}) = \Delta\rho g \Phi \quad (\text{E.4c})$$

Eq. (E.4a) simply means that the torque is conserved through the gap. Eqs. (E.4b) and (E.4c) ensure radial and vertical equilibria, respectively.  $\Delta\rho g \Phi$  is the weight of the particle phase per unit altitude, which is balanced by the vertical gradient in  $\Sigma_{zz}$ .

Our task is to solve the above set of equations, with the following boundary conditions:

$$\int_0^H dz \int_R^{kR} 2\pi r dr \varphi(r, z) = \pi R^2 (k^2 - 1) \int_0^H dz \bar{\varphi}(z) = \pi R^2 (k^2 - 1) H \tilde{\varphi} \quad (\text{E.5})$$

is the condition for mass conservation. The suspension is confined between the inner cylinder (radius  $R$ ) and outer cylinder (radius  $kR$ ) of the Couette cell, of height  $H$ .  $\tilde{\varphi}$  is the volume averaged reduced concentration, and  $\bar{\varphi}(z)$  is the radially averaged concentration at altitude  $z$ . We suppose that the suspension couples with the cylinders' walls with no slip. The latter condition translates as:

$$v(R, z) = \Omega R \quad , \quad v(kR, z) = 0 \quad (\text{E.6})$$

where  $\Omega$  is the angular velocity of the rotor (inner cylinder). Here we have supposed that the outer cylinder is immobile. In a more general scheme both cylinders might be rotating. Our choice of an immobile outer cylinder however causes no loss of generality as long as inertial forces may be neglected.

## E.2: Viscometric function

Let be  $\varphi = \Phi/\Phi_m$  the reduced volume fraction and  $f(\varphi) = \hat{\eta}_n/\hat{\eta}_s$  the ratio of normal viscosity to the shear viscosity ( $\Phi_m$  represents the maximum particle packing fraction). A generally accepted view is that  $\hat{\eta}_s$  diverge as  $(1-\varphi)^{-2}$  near the  $\varphi=1^-$  limit [Mills and Snabre 2009] and that  $\hat{\eta}_n$  has the same singularity [Morris and Boulay 1999]. However, both functions are not simply proportional to each other. The following formulas have been proposed by Morris and Boulay:

$$\hat{\eta}_s(\varphi) = 1 + 2.5\Phi_m(1-\varphi)^{-1} + 0.1\varphi^2(1-\varphi)^{-2} \quad (\text{E.7a})$$

$$\hat{\eta}_n(\varphi) = 0.75\varphi^2(1-\varphi)^{-2} \quad (\text{E.7b})$$

$$f_{MB}(\varphi) = \frac{\hat{\eta}_n(\varphi)}{\hat{\eta}_s(\varphi)} = \frac{0.75\varphi^2(1-\varphi)^{-2}}{1 + 2.5\Phi_m(1-\varphi)^{-1} + 0.1\varphi^2(1-\varphi)^{-2}} \quad (\text{E.7c})$$

Recently Boyer *et al.* obtained independent information on normal force viscometric functions based on the “reverse Weissenberg effect”, i.e. the fact that the free surface of the initially sheared homogeneous suspension is slightly depressed near the rotating inner cylinder [Boyer *et al.* 2011]. They propose the alternate version:

$$f_{BPG}(\varphi) = 3.3\Phi_m(\varphi - \varphi_c) Y(\varphi - \varphi_c) \quad (\text{E.8})$$

where  $\varphi_c = 0.22/\Phi_m$  is the critical reduced volume fraction above which particle contacts induce non zero normal stresses and  $Y$  is the Heavyside function, i.e.  $f_{BPG}(\varphi) = 0$  when  $\varphi < \varphi_c$ , and  $f_{BPG}(\varphi) = 3.3\Phi_m(\varphi - \varphi_c)$  when  $\varphi > \varphi_c$ .

### E.3: Density matched suspension

#### E.3.a: Concentration field

Eq. (E.4b) yields the power law:

$$f(\varphi) \propto r^\sigma, \quad \text{with} \quad \sigma = \frac{1 + \lambda_2}{\lambda_2} \quad (\text{E.9})$$

The radial concentration profile is obtained by reversion of the  $f(\varphi)$  function (note that  $f(\varphi)$  increases monotonically with  $\varphi$ , and then has a well define reverse,  $f^{-1}$ ). At a given  $z$ ,  $\varphi(r, z)$  increases with  $\varphi$  up to the bounding value 1, which is reached at some critical “jamming” radius  $r_c$ . The radial distribution is given by:

$$\varphi(r, z) = G\left(\frac{r}{r_c}\right) \quad (\text{E.10})$$

The  $G$  function is defined as :

$$G(x) = f^{-1}\left[f(1) \cdot x^\sigma\right] \text{ for } 0 \leq x \leq 1, \text{ and } G(x) = 1 \text{ for } x \geq 1. \quad (\text{E.11})$$

The value of the jamming radius is obtained from the mass conservation condition. We find that  $R/r_c$  is the solution of the following equation:

$$\frac{1}{2} \bar{\varphi}(z) (k^2 - 1) x^2 = \int_x^{kx} u G(u) du \quad (\text{E.12})$$

with  $x = R/r_c$  as the unkown. Gathering Eqs (E.10) and (E.12), we realize that the radial concentration profile only depends on  $\bar{\varphi}(z)$ , not directly on the inner cylinder velocity. In the particular case of a density-matched suspension ( $\Delta\rho = 0$ ), the system is invariant along  $z$ , then  $\bar{\varphi}(z) = \tilde{\varphi}$  whatever  $z$ . Consequently, the above analysis predicts that the radial concentration profile remains the same, whatever  $\Omega$ . In the general case of non neutrally buoyant particles, the latter conclusion does not hold, because  $\bar{\varphi}(z)$  depends on  $z$  and  $\Omega$ .

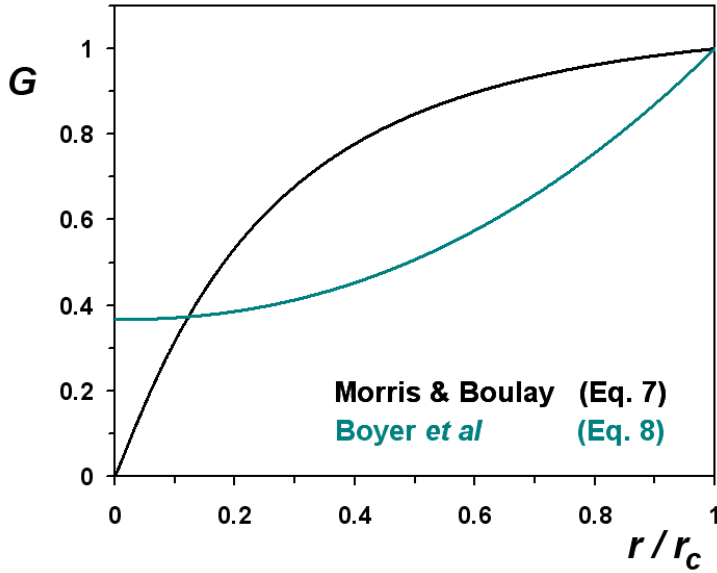


**Fig. E.1**  $G(x)$  function based on the viscometric functions  $f_{MB}(\varphi)$  from Morris & Boulay (Eq. E.7) or  $f_{BPG}(\varphi)$  from Boyer et al (Eq. E.8).

When  $r_c \geq kR$ , the system is fluidized throughout the gap at altitude  $z$ . Conversely, when  $r_c < kR$ , the jamming boundary lies within the outer cylinder radius, meaning that a sheared phase coexists with a jammed phase, which is a case of shear banding. A state diagram may thus be obtained, with  $\bar{\varphi}$  and  $k$  as control parameters, see Fig. E.2 below. In the stationary regime, the viscometric function  $f(\varphi)$  proposed by Morris and Boulay allows a full fluidization of relatively concentrated suspensions ( $\bar{\varphi} < 0.88$ , Fig. E.2.a) while the Boyer et al. expression predicts shear banding for much lower values of the radially averaged concentration  $\bar{\varphi}$  (Fig. E.2.b).

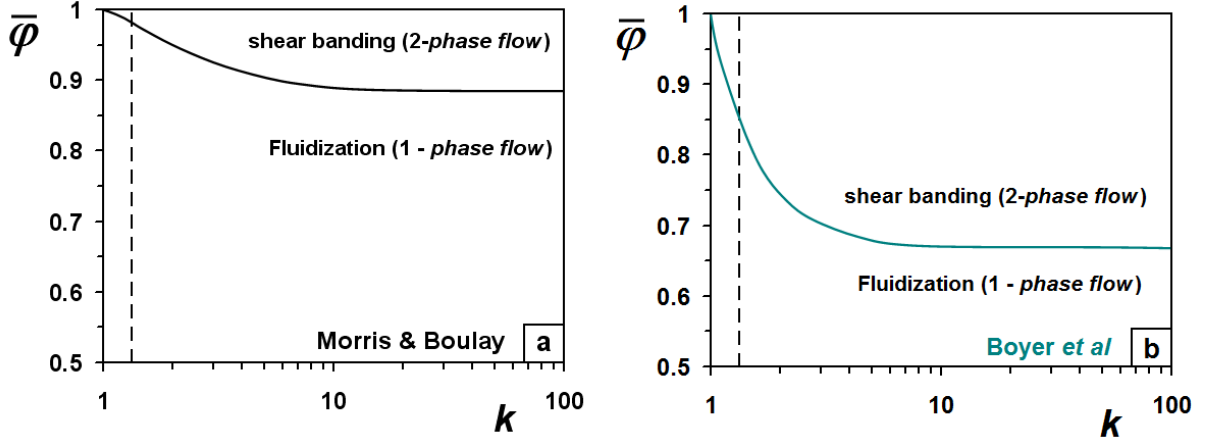


**Fig. E.2** State diagram. Boundary  $\bar{\varphi}(k)$  between full fluidisation and shear-banding in the stationary regime for Morris and Boulay  $f_{MB}(\varphi)$  (a) or Boyer et al.  $f_{BPG}(\varphi)$  (b) viscometric functions. The dashed line corresponds to  $k = R_{out} / R = 4/3$  ( $R_{out} = 20\text{mm}$  and  $R = 15\text{mm}$ ).

### E.3.b: Orthoradial velocity field

The radial distribution of the shear rate  $\dot{\gamma}(r, z)$ , and the velocity profile  $v(r, z)$ , are deduced from Eqs. (E.4a) and (E.6). We obtain:

$$\dot{\gamma}(r, z) = \Omega \cdot \frac{J\left(\frac{R}{r_c}\right)}{\left(\frac{r}{r_c}\right)^2 \hat{\eta}_s \left[ G\left(\frac{r}{r_c}\right) \right]} \quad (\text{E.13a})$$

$$v(r, z) = -r \int_{R/r_c}^X \frac{\dot{\gamma}(u, z)}{u} = -\Omega r J(R/r_c) \int_{R/r_c}^X \frac{du}{u^3 \hat{\eta}_s[G(u)]} \quad (\text{E.13b})$$

with  $X = \text{Inf}(kR/r_c, 1)$ .

The  $J(R/r_c)$  function is derived from the no slip condition  $v(R, z) = \Omega R$ :

$$\frac{1}{J(R/r_c)} = - \int_{R/r_c}^X \frac{du}{u^3 \hat{\eta}_s[G(u)]} \quad (\text{E.14})$$

Recall that  $r_c$  only depends on  $\bar{\varphi}(z)$ . Again in the case of a density matched suspension, the shear profile, and then the velocity profile, are simply proportional to  $\Omega$ , and keep constant shapes that only depend on the radially averaged reduced concentration  $\bar{\varphi}$ .

## E.4: Non density – matched suspension

### E.4.a: Concentration field

Eq. (E.4c) can be written with non-dimensional quantities as:

$$\frac{\partial \hat{\eta}_n \hat{\gamma}}{\partial \hat{z}} = \varphi \left( \frac{r}{r_c}, \hat{z} \right) \quad (\text{E.15})$$

with :

$$\hat{\gamma} = \frac{\dot{\gamma}}{\Omega}, \quad \hat{z} = \frac{z}{l}, \quad \text{and} \quad l = \Omega \frac{\eta_0 \lambda_3}{\Delta \rho g \Phi_m} \quad (\text{E.16})$$

Performing a radial integration of Eq. (E.15), and injecting the expression for the shear rate (Eq. (E.13)), we obtain:

$$\frac{1}{2} \bar{\varphi}(\hat{z}) (k^2 - 1) = \frac{\partial}{\partial \hat{z}} Q \left( \frac{R}{r_c} \right) \quad (\text{E.17a})$$

where

$$Q \left( \frac{R}{r_c} \right) = \int_{\frac{R}{r_c}}^{\frac{kR}{r_c}} \frac{J \left( \frac{R}{r_c} \right) f[G(u)]}{\left( \frac{R}{r_c} \right)^2 u} du \quad (\text{E.17b})$$

We may write Eq. (17a) under the form :

$$\frac{1}{2} \bar{\varphi}(\bar{z}) (k^2 - 1) = \frac{\partial}{\partial \bar{z}} Q(R/r_c) = \frac{\partial Q(R/r_c)}{\partial (R/r_c)} \frac{\partial (R/r_c)}{\partial \bar{\varphi}} \frac{\partial \bar{\varphi}}{\partial \bar{z}} \quad (\text{E.18})$$

From equations (E.12) and (E.17) giving  $r_c(\bar{\varphi})/R$  and  $Q(R/r_c)$ , one may compute both derivatives  $\partial Q(R/r_c)/\partial(R/r_c)$  and  $\partial(R/r_c)/\partial\bar{\varphi}$  to calculate the vertical gradient  $\partial\bar{\varphi}/\partial\hat{z}$  of the radial averaged reduced concentration.

The mass conservation equation further provides a relation between the dimensionless equilibrium height  $\hat{h}$  of the suspension, the volume averaged concentration  $\tilde{\varphi}$  and the radially averaged concentration profile  $\bar{\varphi}(\hat{z})$  :

$$\hat{H} \tilde{\varphi} = \int_0^{\hat{h}} \bar{\varphi}(\hat{z}) d\hat{z} \quad \text{with} \quad \bar{\varphi}(\hat{z}) = \bar{\varphi}(\hat{z}=0) + \int_0^{\hat{z}} \frac{\partial\bar{\varphi}}{\partial\hat{z}} d\hat{z} \quad (\text{E.19})$$

$\hat{h}$  is the height of the volume occupied by the particles. The shear induced fluidization of non density matched particles results in an increase of  $\hat{h}$  with the angular velocity  $\Omega$  of the inner cylinder. At zero shear rate particles simply pile up into a compact sediment of height  $\hat{h}_o = h_o/l$ , at maximum solid fraction ( $\varphi = 1$ ). At very large  $\Omega$ , particles are re-suspended in the whole fluid volume and then  $\hat{h} \rightarrow \hat{H} = H/l$ . Note that the shear induced re-suspension mechanism requires contact forces between particles, the source of normal force differences. Consequently the value of  $\bar{\varphi}$  on top of the suspension ( $\hat{z} = \hat{h}$ ) is the minimum concentration  $\varphi_{\text{inf}}$  at which normal forces show up. Note that  $\varphi_{\text{inf}} = 0$  in Morris and Boulay model, and  $\varphi_{\text{inf}} = \varphi_c = \Phi_c / \Phi_m = 0.22 / \Phi_m$  in Boyer *et al.* model.

Equations (E.17-E.18) together with equations (E.12, E.13) and the mass conservation (E.19) can be solved numerically to get the equilibrium suspension height  $\hat{h}(\Omega)$  as a function of  $\Omega$  and the radially averaged concentration profile  $\bar{\varphi}(\hat{z}, \Omega)$  along the vertical direction. For this purpose, a homemade java plugin was developed for use with the image processing software ImageJ [Schneider *et al.* 2012]. In the case of non isodense particles, some variables diverge near the maximum packing fraction and a great care has to be taken to accurately calculate the radially averaged concentration profile  $\bar{\varphi}(\hat{z})$  with the java plugin especially in the low shear regime.

#### E.4.b: Orthoradial velocity field

From the calculation of both the radially averaged concentration  $\bar{\varphi}(\hat{z})$  and the critical radius  $r_c(\bar{\varphi}, k)$ , equations (E.13a), (E.13b) and (E.14) give the radial distribution of the shear rate  $\dot{\gamma}(r, z)$  and the orthoradial velocity profile  $v(r, z)$ .

Combining Eq.(E.17) with Eq. (E.12) further gives :

$$\int_{\frac{R}{r_c}}^{\frac{kR}{r_c}} uG(u) du = \left(\frac{R}{r_c}\right)^2 \frac{\partial}{\partial \hat{z}} \int_{\frac{R}{r_c}}^{\frac{kR}{r_c}} \frac{J\left(\frac{R}{r_c}\right)}{\left(\frac{R}{r_c}\right)^2} \frac{f[G(u)]}{u} du \quad (\text{E.20})$$

The above expression is a differential equation for  $r_c$ , whose solution formally reads:

$$\frac{r_c(\hat{z}, k)}{R} = S(\hat{z}, k) = S\left(z \frac{\Delta\rho g \Phi_m}{\Omega \eta_o \lambda_3}, k\right) \quad (\text{E.21})$$

The equation (E.21) tells us that situations labelled as  $(\Delta\rho = 0, \Omega > 0)$  and  $(|\Delta\rho| > 0, \Omega \rightarrow \infty)$  are equivalent. This means that rotating the inner cylinder very fast gives the same configuration as with neutrally buoyant particles, in line with our intuition.

The function  $S(\hat{z}, k) = r/r_c(\hat{z}, k)$  can be obtained by numerical resolution of Eq. (E.20). The full fluidization of the suspension across the full gap of the Couette cell and the full height  $H$  of the suspension corresponds to  $S \approx k$ , and then to some value  $\hat{z}^* = H/l$  of the reduced variable  $\hat{z}$ . The value of  $\hat{z}^*$  depends on the particular  $f(\varphi)$  viscometric function and value of  $k$ . As shown in Fig. E.3 for  $k = 4/3$ ,  $\hat{z}^* \approx 3500$  for the Morris & Boulay function and  $\hat{z}^* \approx 100$  for the Boyer function.

We may make a tentative guess to estimate the angular velocity  $\Omega^* \approx \frac{\Delta\rho g \Phi_m H}{\eta_o \lambda_3 \hat{z}^*}$  of the inner cylinder at which full fluidization is realized. Taking  $\Delta\rho = 0.3 \text{ g.cm}^{-3}$ ,  $\Phi_m = 0.60$ ,  $H = 3 \text{ cm}$ ,  $\eta_o = 0.25 \text{ Poise}$ ,  $\lambda_3 = 0.50$ ,  $g = 981 \text{ cm.s}^{-2}$ , we find  $\Omega^* \approx 4000/\hat{z}^*$ . Considering the Morris and Boulay viscometric function ( $\hat{z}^* \approx 3500$ ), we may expect a full fluidization for an angular velocity  $\Omega^* \approx 1 \text{ rad/s}$ , in line with experiments. On the other hand, the resuspension of particles in the fluid volume requires much higher angular velocity  $\Omega^* > 30 \text{ rad/s}$  in the case of the Boyer function ( $\hat{z}^* \approx 100$ , Fig. E.3).

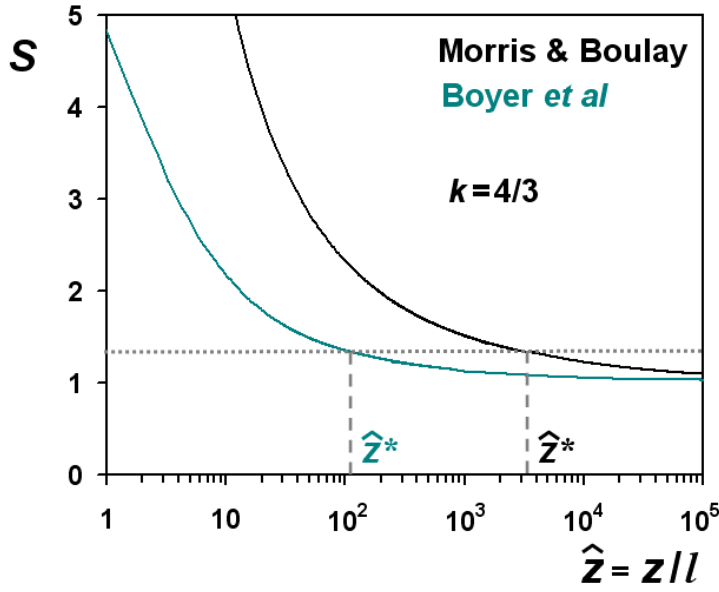


**Fig. E.3** Function  $S(\hat{z}) = r_c(\hat{z})/R$  based on Eq.(7) from Morris and Boulay (1999) or Eq.(8) from Boyer et al (2011) for  $k = 4/3$ . Intersection of curves with the dotted line ( $r_c/R = k$ ) gives the  $\hat{z}^*$  value for full fluidization of the suspension (dashed lines).

#### E.4.c: Coherence of equations

Let us come back to Eq. (E.15), and examine the dependence in  $r$  on both sides of the equation. Combining Eqs (E.13a) and (E.9), we obtain:

$$\hat{\eta}_n \hat{\gamma} = \frac{J\left(\frac{R}{r_c}\right)}{\left(\frac{r}{r_c}\right)^2} \frac{\hat{\eta}_n}{\hat{\eta}_s} = \left(\frac{r}{r_c}\right)^{-2} \cdot J\left(\frac{R}{r_c}\right) \cdot f(\varphi) = \left(\frac{r}{r_c}\right)^{\sigma-2} \cdot f(1) \cdot J\left(\frac{R}{r_c}\right) \quad (\text{E.22})$$

Consequently we have:

$$\frac{\partial \hat{\eta}_n \hat{\gamma}}{\partial \hat{z}} = r^{\sigma-2} \cdot \frac{\partial}{\partial \hat{z}} \left[ \left(\frac{1}{r_c}\right)^{\sigma-2} \cdot f(1) \cdot J\left(\frac{R}{r_c}\right) \right] \quad (\text{E.23})$$

The left-hand side of Eq. (E.23) has a simple power-law dependence on  $r$ , namely  $\frac{\partial \hat{\eta}_n \hat{\gamma}}{\partial \hat{z}} \propto r^{\sigma-2}$ . The right-hand side of Eq. (E.15), namely the concentration, as given by Eq. (E.10), does not have such a simple dependence on  $r$ , in general. We thus find that the initial set of equations has a problem of coherence. This problem may be relaxed if we recognize that only the azimuthal component of the flow has been included in the equations. Including secondary components adds two unknowns, making the system undetermined. Another option

is to maintain the assumption of purely azimuthal flow, but forcing  $\varphi(r, z)$  to have a power-law dependence on  $r$ . Let us simply suppose:

$$f(\varphi) = C \cdot \varphi^\beta \quad (\text{E.24})$$

where  $C$  is a constant and  $\beta$  a positive exponent. Then:

$$f^{-1}(x) = \left(\frac{x}{C}\right)^{1/\beta} \quad (\text{E.25})$$

Combining Eqs (E.10), (E.11) and (E.25), we obtain:

$$\varphi = (r/r_c)^{\sigma/\beta} \quad \text{for } r < r_c \quad (\text{E.26})$$

Now  $\varphi(r, z)$  goes as  $r^{\sigma/\beta}$ , which should be the same as  $r^{\sigma-2}$ , according to Eq. (E.23). The condition for the coherence of the set of equations therefore reads:

$$\beta(\sigma - 2) = \sigma \quad (\text{E.27})$$

Recall that  $\sigma = (1 + \lambda_2)/\lambda_2$ . Eq. (E.27) is equivalent to:

$$\beta = \frac{1 + \lambda_2}{1 - \lambda_2} \quad \text{or} \quad \lambda_2 = \frac{\beta - 1}{\beta + 1} \quad (\text{E.28})$$

The set of Eqs (E.4) can be made coherent through an appropriate choice of the  $f(\varphi)$  function and of the value of  $\lambda_2$ . We may consider  $\beta = 2$ : in this case Eq. (E.28) imposes  $\lambda_2 = 0.333$ , which is quite different from the widely accepted value,  $\lambda_2 = 0.85$ . Alternatively, taking  $\lambda_2 = 0.85$ , then  $\sigma = (1 + \lambda_2)/\lambda_2 = 2.176$  and the above Eq. (E.28) yields  $\beta = 12.33$ , quite a large value !

Summarizing, it may be adequate to model the viscometric function with a power-law  $f(\varphi, \beta) = C\varphi^\beta$ , resulting in  $\varphi = (r/r_c)^{\sigma-2} = (r/r_c)^{2\beta/(\beta-1)}$ . If the value of  $\lambda_2$  is imposed,  $\beta$  is determined through the condition set by Eq. (E.28).

## E.5: Model and experiments for a density matched suspension

### E.5.a: Power law viscometric functions

In this paragraph, a power law  $f(\varphi, \beta) = C\varphi^\beta$  with an integral power  $\beta$  is considered as a model for the viscometric function  $f$  (Fig. E.4). For a density-matched suspension, the critical radius  $r_c(\bar{\varphi})$  and the radially averaged volume fraction  $\bar{\varphi} = \tilde{\varphi}$  are invariant along  $z$ . As a consequence, the prefactor  $f(\varphi=1) = C$  representative of the amplitude of normal stress differences has no influence upon the radial distribution of particles:  $\varphi(r) = G(r/r_c)$  in the stationary regime, as shown by Eqs. (E.10) and (E.11). The prefactor  $f(\varphi=1) = C$  only influences the migration kinetics towards the equilibrium concentration profile.

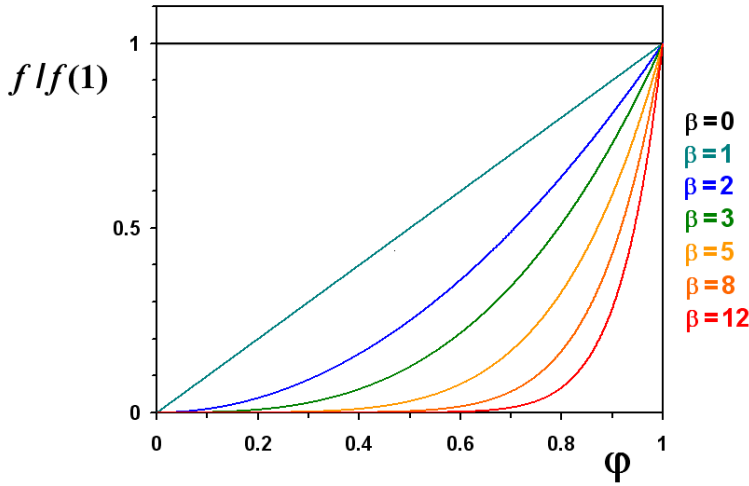


**Fig. E.4** Power law viscometric functions  $f(\varphi, \beta) = f(\varphi=1)\varphi^\beta$  with integral exponent values  $\beta = 0, 1, 2, 3, 5, 8$  or  $12$ .

Equation (E.12) was solved numerically to get the jamming radius  $r_c(\bar{\varphi}, k, \beta)$ , see Fig. E.5. In Fig. E.5.a, we impose  $\lambda_2 = 0.85$ , and consider different values of  $\beta$ . In Fig. E.5.b, we impose that the coherence condition Eq. (E.28) be satisfied for each  $\beta$  value, which amounts to adjusting the  $\lambda_2$  value for each  $\beta$ . Recall that coherence demands  $\beta \approx 12$  for  $\lambda_2 = 0.85$ . We find that  $r_c$  significantly increases with the value of the  $\beta$  exponent, in both cases (a, b). One might ask: what should be the average concentration for shear-banding to be observable? Clearly this concentration increases with  $\beta$ . If  $\beta$  is large, only very concentrated suspensions will show shear-banding.

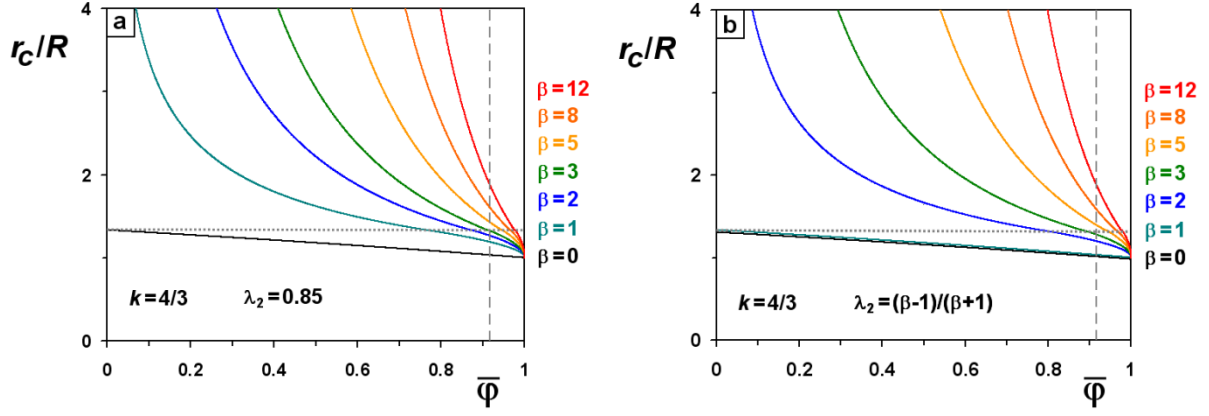


**Fig. E.5** Reduced critical radius  $r_c/R$  versus the radially averaged reduced concentration  $\bar{\varphi}$  for different integral values of the  $\beta$  exponent, with (a)  $\lambda_2 = 0.85$  or (b)  $\lambda_2 = (\beta-1)/(\beta+1)$ , and  $k=4/3$ . Dashed lines indicate the radially averaged reduced concentration  $\bar{\varphi} = 0.55/0.6$  and the dotted lines show the reduced critical radius  $r_c/R = k = 4/3$  for full fluidization of the suspension.

Figures E.6.a and E.6.b show the concentration profiles  $\varphi(r) = G(r/r_c)$  and the velocity profiles  $v(r)/v(R)$  derived from Eqs. (E.13) for  $k=4/3$  and a volume averaged concentration  $\tilde{\varphi}(r) = 0.55/\Phi_m$ , with  $\Phi_m = 0.6$ . The calculation predicts a localized flow (shear-banding) for low values of  $\beta$ , while larger values ( $\beta > 3$ ) lead to full fluidization. In other words, large positive curvature of the  $f(\varphi)$  function in the high concentration regime strongly reduces migration effects (Fig. E.6.a), and then the density matched suspension is fluidized through the full gap (Fig. E.6.b).

Both the experimental concentration profile  $\varphi(r)$  (Chapter D, Fig. D.5) and the experimental dimensionless velocity profile  $v(r,\Omega)/v(R,\Omega)$  for a volume averaged concentration  $\tilde{\Phi} = 0.55$  and a control parameter  $k=4/3$  are fairly well described by considering a large value of  $\beta$ , say  $\beta > 8$  (Figs. E.6 where  $v(R,\Omega)$  is the suspension velocity close to the inner cylinder). Experimental data shown in Fig. E.6 correspond to  $z$  averages of concentration profiles  $\varphi(r)$  and dimensionless angular velocity profiles  $\omega(r,\Omega)/\omega(R,\Omega)$  with  $\omega(r,\Omega) = v(r,\Omega)/r$  for altitudes  $z \geq 10$  mm above the bottom plane of the Couette flow (see Chapter C, Fig. C.27 and Fig. E.7 for more details). The angular velocity  $\omega(r,\Omega) = v(r,\Omega)/r$  decreases almost exponentially close to the inner rotating cylinder and vanishes near the outer cylinder (Chapter C, Fig. C.27).

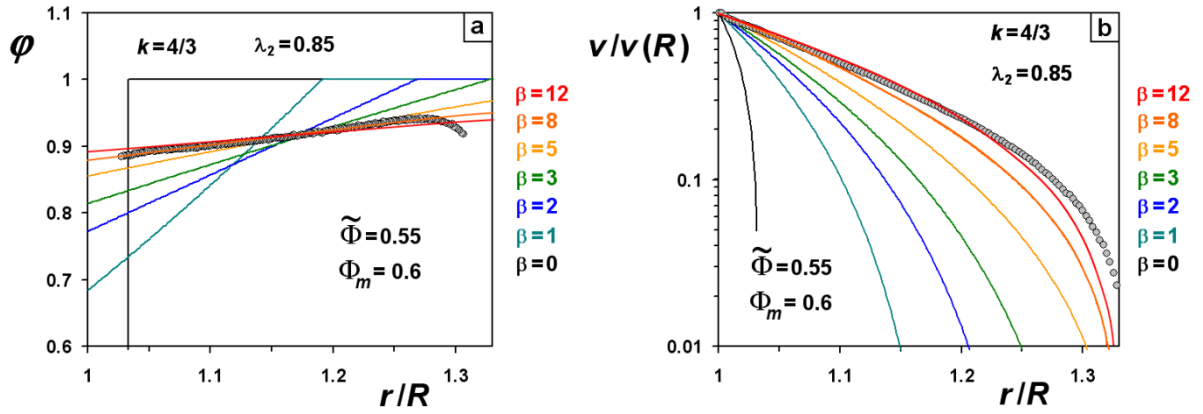


**Fig. E.6** (a) Stationary concentration profile  $\varphi(r)$ ; (b) velocity profile  $v(r)/v(R)$ , versus dimensionless radius  $r/R$  for different integral values of the  $\beta$  exponent, with  $k = 4/3$ ,  $\lambda_2 = 0.85$ ,  $\tilde{\Phi} = 0.55$  and  $\Phi_m = 0.6$ . Grey circles are experimental data (see Fig. E.7 and chapters C and D).

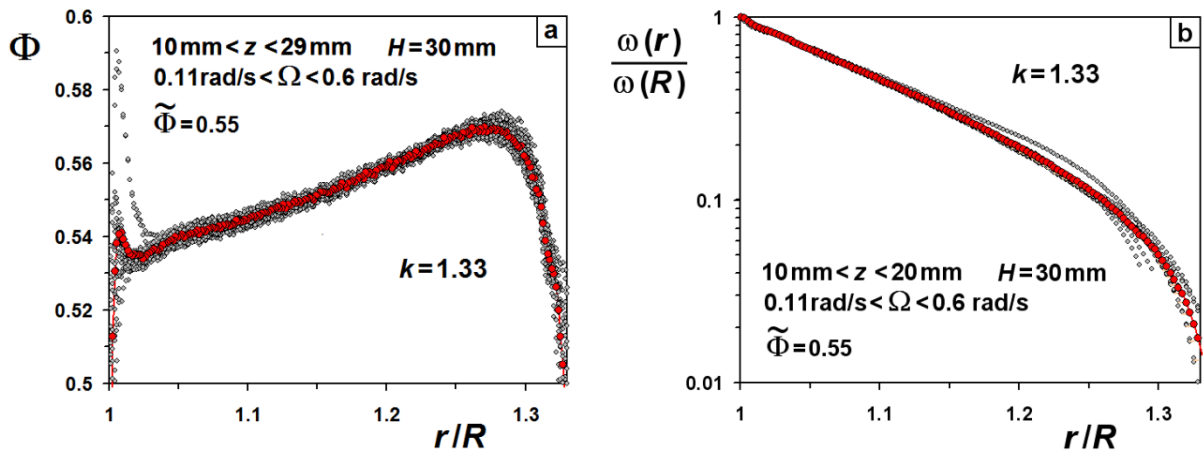


**Fig. E.7** Experimental data, from Chapters D and C. (a): concentration profiles  $\varphi(r)$ ; (b) angular velocity profiles  $\omega(r, \Omega)/\omega(R, \Omega)$  with  $\omega(r, \Omega) = v(r, \Omega)/r$  versus dimensionless radius  $r/R$  for  $0.11 \text{ rad/s} < \Omega < 0.57 \text{ rad/s}$  and altitudes  $z \geq 10 \text{ mm}$  above the bottom plane of the Couette geometry ( $k = 4/3$ ,  $H = 30 \text{ mm}$  and  $\tilde{\Phi} = 0.55$ ). Red circles:  $z$ -averaged concentration profile for  $10 \leq z \leq 29 \text{ mm}$  in (a) and  $z$ -averaged angular velocity profile for  $10 \leq z \leq 20 \text{ mm}$  in (b).

In view of the linear decay of the angular velocity in semi-log plots (Fig. E.7.b), it is interesting to consider an exponential law  $\omega(r, \Omega) = v(r, \Omega) / r \propto e^{-(r-R)/(r^*-R)}$ . Fitting this law to experimental data, we deduce a characteristic length,  $\xi_{\text{exp}} = (r^* - R) / (kR - R)$ , in dimensionless form. A value of  $\xi_{\text{exp}}$  may thus be obtained for each  $z$  in the experiment. Restricting the analysis to  $10\text{ mm} < z < 20\text{ mm}$  (away from wall effects due to the bottom of the Couette cell), we find  $\xi_{\text{exp}}$  values between 0.37 and 0.41 (see Fig. E.8). Thus  $\xi_{\text{exp}}$  is about constant, as we might expect, because of the  $z$ -invariance of the density-matched system. In parallel, we calculated theoretical values,  $\xi_{\text{theory}}$ , by fitting the exponential law to the theoretical velocity profiles of Fig. E.6.b. Results are displayed in Fig. E.9 below. We see that  $\xi_{\text{theory}} \cong \xi_{\text{exp}}$  only if  $\beta > 8$ . The best match is obtained for  $\beta > 8$ , in line with the direct comparison of velocity profiles (Fig. E.6.b).

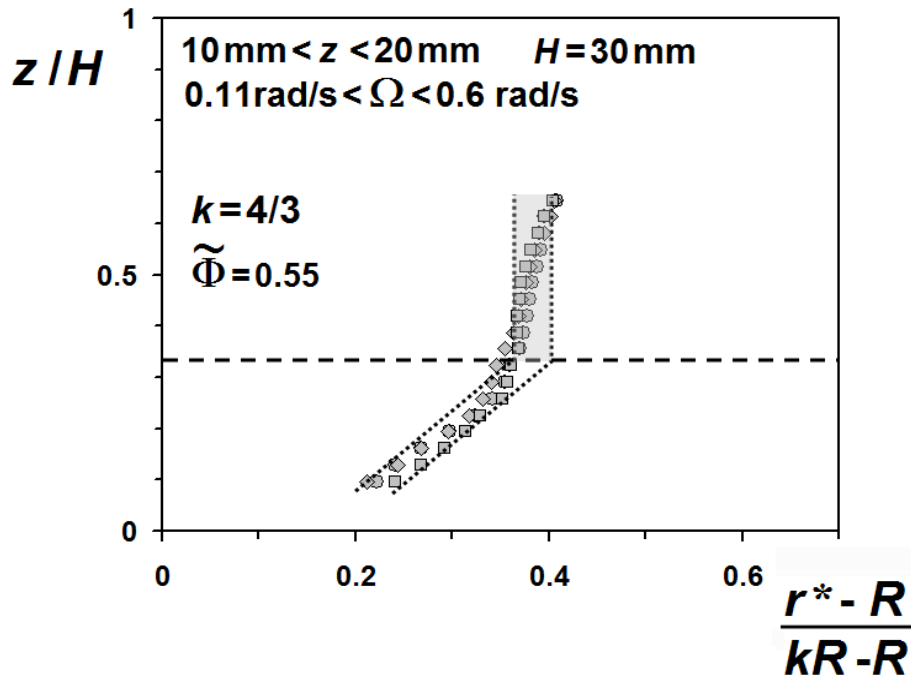


**Fig. E.8** Experimental reduced decay length  $\xi_{\text{exp}} = (r^* - R) / (kR - R)$  of the angular velocity profile  $\omega(r, \Omega)$  versus the dimensionless altitude  $z/H$  for angular velocity  $0.11\text{ rad/s} < \Omega < 0.57\text{ rad/s}$  ( $k = 4/3$ ,  $H = 30\text{ mm}$  and  $\tilde{\Phi} = 0.55$ ). Dotted lines are guides to the eye. The horizontal dashed line is an approximate boundary between the lower zone of the Couette cell, influenced by bottom wall effects, and the upper zone ( $z > 10\text{ mm}$ ).

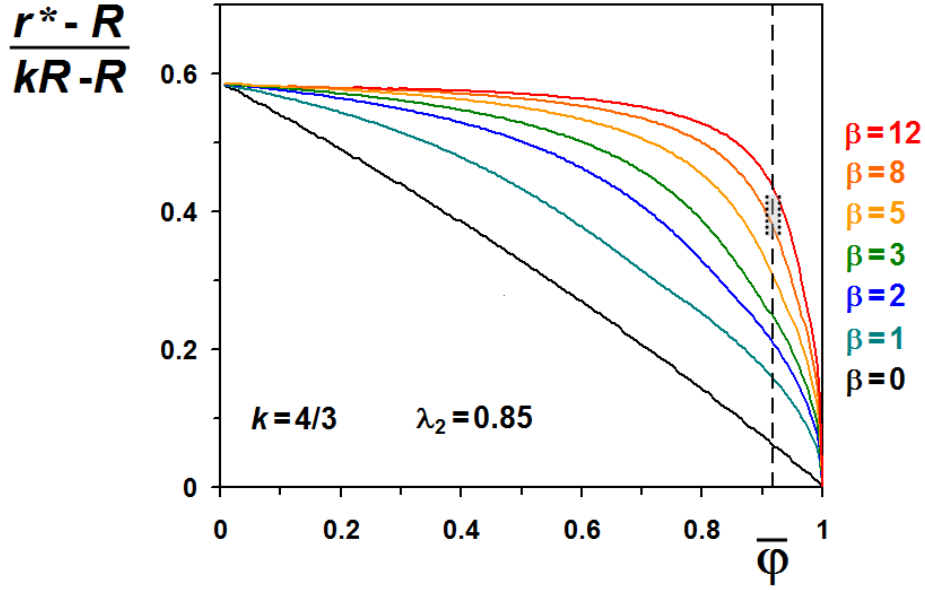


**Fig. E.9** Theoretical reduced decay length  $\xi_{theory} = (r^* - R)/(kR - R)$  of the angular velocity profile  $\omega(r) = v(r)/r$  versus  $\bar{\varphi}$  for different integral values of the  $\beta$  exponent, with  $\lambda_2 = 0.85$  and  $k = 4/3$ . The dashed line indicates the averaged reduced concentration  $\bar{\varphi} = \tilde{\Phi}/\Phi_m$  in the experiment, with  $\tilde{\Phi} = 0.55$  and  $\Phi_m = 0.6$ . Experimental values ( $\xi_{exp}$ ) are indicated in the small grey rectangle with dotted vertical boundaries.

Recall that the above data correspond to  $k = 4/3$ , the ratio between cylinder radii in our experiment (20 and 15 mm). Changing  $k$  obviously changes the concentration and velocity profiles. Interestingly, data at larger  $k$  ( $=5.5$ ) are available from the work by Boyer *et al.*. We now wish to examine these data in the light of the above model.

Boyer *et al.* (2011) studied the flow of a density matched suspension in a rotating rod flow with a very large gap ( $R = 10\text{mm}$ ,  $kR = 55\text{mm}$ ). Among their data, they provide a few points of an experimental concentration profile obtained for a 40% solid average fraction (i.e.  $\bar{\varphi} = 0.67$ , with  $\Phi_m = 0.6$ ). These points (Fig. 8 in Boyer *et al.* 2011) were obtained while the shear cell had been operated for a few hours, similarly to what we did in our experiments to obtain stationary profiles. We will then consider that these data indeed correspond to a stationary regime, in spite of these authors' suspicion that they might rather correspond to transient regime (see paragraph 4.3 in Boyer *et al.* 2011).

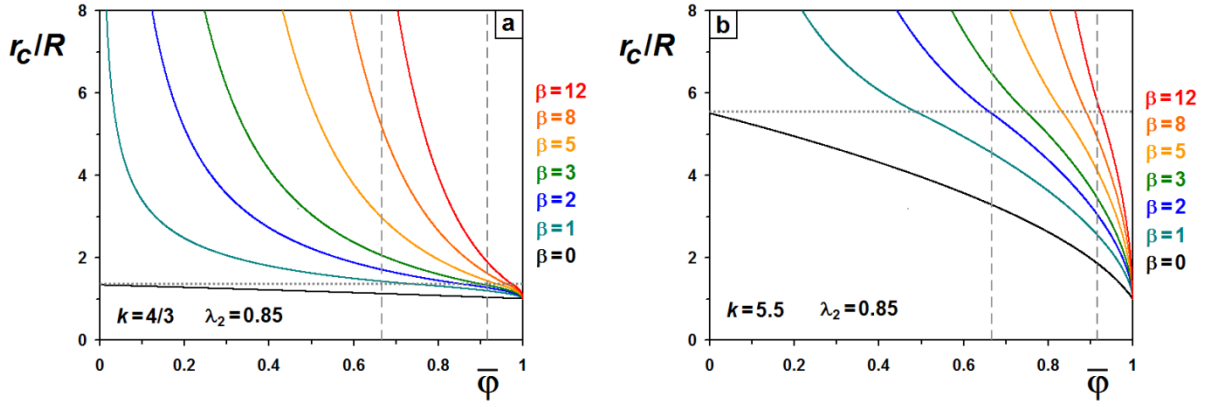


**Fig. E.10** Reduced critical radius  $r_c/R$  versus the radially averaged reduced concentration  $\bar{\varphi}$  for different integral values of the  $\beta$  exponent in the power law viscometric function  $f(\varphi, \beta)$  with  $\lambda_2 = 0.85$  and  $k = 4/3$  (a) or  $k = 5.5$  (b). Dashed lines indicate either the averaged reduced concentration  $\bar{\varphi} = 0.4/0.6$  or  $\bar{\varphi} = 0.55/0.6$ . The dotted lines show the reduced critical radius  $r_c/R = k = 4/3$  (a) or  $r_c/R = k = 5.5$  (b) for full fluidization of the suspension.

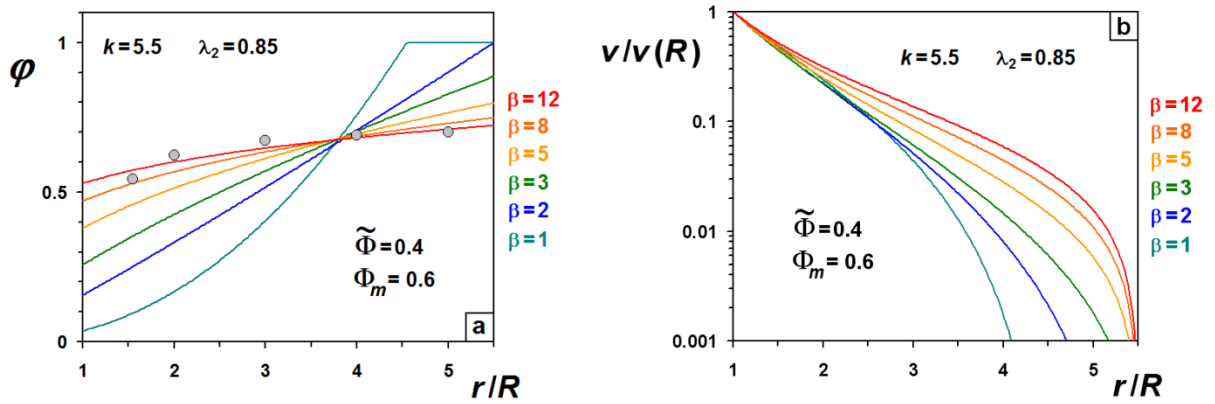


**Fig. E.11** Concentration profile  $\varphi(r)$  (a) and velocity profile  $v(r)/v(R)$  versus dimensionless radius  $r/R$  for different integral values of the exponent  $\beta$  in the power law viscometric function  $f(\varphi)$  with  $k = 5.5$ ,  $\lambda_2 = 0.85$ ,  $\lambda_3 = 0.5$ ,  $\tilde{\Phi} = 0.4$  and  $\Phi_m = 0.6$ . Grey circles show the experimental reduced averaged concentration profile from Boyer et al (2011) for a volume averaged concentration  $\tilde{\Phi} = 0.4$  (assuming  $\Phi_m = 0.6$ ) and  $k = 5.5$  ( $R = 10\text{mm}$ ,  $kR = 55\text{mm}$ ).

Predictions for the jamming radius, depending on  $k$ , are illustrated below in Fig. E.10. Panel (a) is the repetition of Fig. E.5.a, for  $k = 4/3$ , to be compared to  $k = 5.5$  in panel (b). We see that a suspension which completely flows across the gap at  $k = 4/3$  may shear-band at  $k = 5.5$ ; see e.g. the case  $\bar{\varphi} = 0.67$  for  $\beta \leq 2$ . Large aspect ratios therefore favor flow localization.

Fig. E.11 shows calculated profiles, concentration  $\varphi(r)$  (panel a) and dimensionless velocity  $v(r)/v(R)$  (panel b), for the conditions of Boyer et al. experiments. The only source from their experiments is the set of 5 concentrations points, **obtained through pipetting of the suspension with a large syringe**, which are well fitted to with an exponent  $\beta = 12$ . The calculation confirms the absence of flow localization in a large gap Couette geometry, and the result for  $\beta$  is well in line with our findings for the  $k = 4/3$  system.

### E.5.b: Morris and Boulay viscometric functions

In the former paragraph, we tested the hypothesis of a power-law  $f(\varphi, \beta)$  (Eq. (E.24)). We now want to test the alternate propositions represented by Eqs. (E.7.c) and (E.8). Eq. (E.7.c) is the form proposed by Morris and Boulay,  $f_{MB}(\varphi)$ . We adopt a generalized form of the Boyer *et al.* function, which we denote  $f_{BPG}(\varphi, \beta)$  :

$$f_{BPG}(\varphi, \beta) = 3.3 \Phi_m \varphi^{\beta-1} (\varphi - \varphi_c) Y(\varphi - \varphi_c) \quad (\text{E.29})$$

where  $\beta = 1, 2$  or  $3$  and  $\varphi_c = 0.22/\Phi_m$ .  $Y$  is the Heavyside function.  $\beta = 1$  gives the original Boyer et al. function  $f_{BPG}(\varphi)$ , Eq. (E.8). In this model, normal forces are null when  $\varphi < \varphi_c$ . The role of the  $\beta$  exponent is to increase the curvature of the function for high concentrations. This feature is expectably important, in view of what we observed with the power-law function. Graphs of these functions are shown in Fig. E.12. In Fig. E.13 we compare the Morris-Boulay function with the power-law  $f(\varphi, \beta) = f(\varphi = 1) \varphi^\beta$ .

The essential results, obtained with the different types of functions, are shown in Fig. E.14. We again compare computed profiles with those from our experiments. Corresponding parameter values are recalled in the figure caption. We find that  $f_{MB}$  fairly well accounts for the experimental profiles, in a similar way as the power-law function for  $\beta = 12$  (see Fig. E.6 for comparison). A weak particle slip close to the outer cylinder can account for the small

deviation between experimental and predictions of the force balance model at  $r \cong kR$  for the Morris & Boulay viscometric function, (Fig. E.14.b).

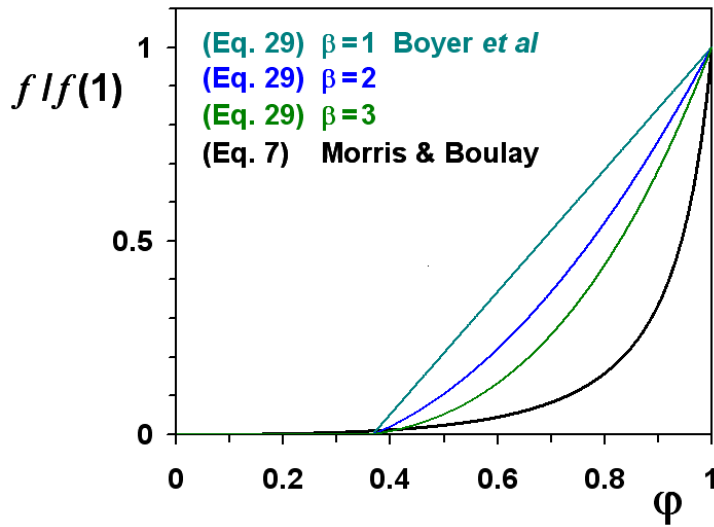


**Fig. E.12** Viscometric functions  $f_{MB}(\varphi)$  and  $f_{BPG}(\varphi, \beta)$  either based on Eq.(E.7) from Morris and Boulay (1999) or Eq. (E29) with  $\beta = 1, 2$  or  $3$ .

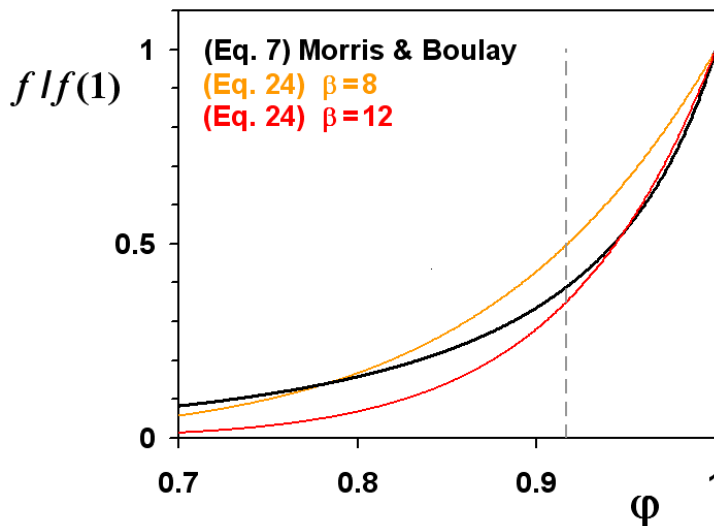


**Fig. E.13** Viscometric functions  $f_{MB}(\varphi)$  and  $f(\varphi, \beta)$  either based on Eq.(E.7) from Morris and Boulay (1999) or a power law with  $\beta = 8$  or  $12$  (Eq. E.24).

Conversely, the basic  $f_{BPG}$  function, for  $\beta = 1$ , leads to profiles very far from the experimental ones. Increasing  $\beta$  up to 3 reduces the mismatch, but only partially. We thus confirm the importance of the curvature of the  $f$  function at high concentration. The linear behaviour of the basic Boyer *et al.* function at high concentration is clearly inefficient in accounting for the measured profiles. Looking at Fig. E.13, we see that the graph of  $f_{MB}$  function is closely fitted with a power-law function for  $\beta = 12$ , at  $\varphi \geq 0.92$ . The fact that  $f_{MB}$  and the power-law for  $\beta = 12$  are equally compatible with experimental profiles (Fig. E.14)

shows that the essential information lies in the high concentration regime, where both types of functions have similar behaviours. Conversely, the behaviour of the function at low and medium concentrations has very little influence on the profiles. Consequently, the experiments (either ours or the concentration measurements in [Boyer et al. 2011](#)) cannot tell much about what should be the shape of  $f(\varphi)$  at low  $\varphi$ . We thus do not rule out the fact that normal forces may be null below a threshold concentration, as put forward by [Boyer et al. \(2011\)](#).

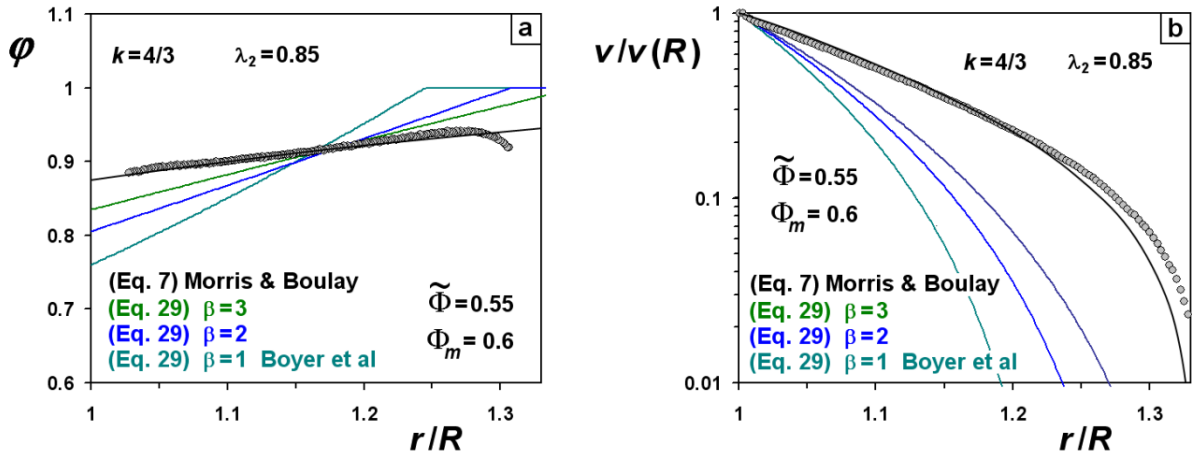


**Fig. E.14** Stationary concentration profile  $\varphi(r)$  (a) and dimensionless velocity profile  $v(r)/v(R)$  (b) versus dimensionless radius  $r/R$  either for a power law viscometric function  $f(\varphi, \beta)$  (Eq.E.29 with  $\varphi_c = 0.22/\Phi_m$  and  $\beta = 1, 2$  or  $3$ ) or the Morris & Boulay expression  $f_{MB}(\varphi)$  (Eq.E.7) with  $\tilde{\Phi} = 0.55$ ,  $\Phi_m = 0.6$ ,  $\lambda_2 = 0.85$  and  $k = 4/3$ . Grey circles show either the  $z$  averaged experimental concentration profile (a) or the  $z$  averaged experimental velocity profile  $v(r)/v(R)$  for  $k = 4/3$ ,  $\tilde{\Phi} = 0.55$  and  $\Phi_m = 0.6$  (see Fig. E.7).

## E.6: Model and experiments for a non density – matched suspension

In the case of a density matched suspension, only the shape of  $f(\varphi)$ , not its amplitude, was important. For non buoyant particles, the vertical equilibrium directly involves the amplitude of  $\hat{\eta}_n$ , and then that of  $f(\varphi)$ , see Eq. (E.15). This amplitude may be represented by  $f(\varphi=1)$ , the maximal value of the viscometric function. Physically, a larger  $f(\varphi=1)$  means a more intense re-suspension. Below we report results of computations performed with either the Morris-Boulay function  $f_{MB}(\varphi)$  or the Boyer et al. function  $f_{BPG}(\varphi)$ , in basic form (Eq.E.8 or i.e. E.29 with  $\beta = 1$ ). We did not test the power-law function  $f(\varphi, \beta)$ , Eq. (E.24),

since  $f_{MB}(\varphi)$  was found to perform similarly to the power-law in the case of neutrally buoyant particles.

Equations (E.17-E.19) were solved numerically to get the dimensionless equilibrium height  $\hat{h} = h(\tilde{\varphi}, \Omega)/H$  of the suspension and the radially averaged concentration profile  $\bar{\varphi}(\tilde{\varphi}, \Omega, \hat{z})$  in the vertical direction ( $0 \leq \hat{z} \leq \hat{h}$ ) with  $\lambda_2 = 0.85$  and  $\lambda_3 = 0.5$ . Next, the radial velocity profile  $v(\bar{\varphi}, \Omega, r, \hat{z})$  and concentration profile  $\varphi(\bar{\varphi}, \Omega, r, \hat{z})$  at altitude  $\hat{z} = z/l$  were computed by introducing the calculated  $\bar{\varphi}(\tilde{\varphi}, \Omega, \hat{z})$  in equations (E.10-E.14). Results are shown in Figs. (15,16, 17).

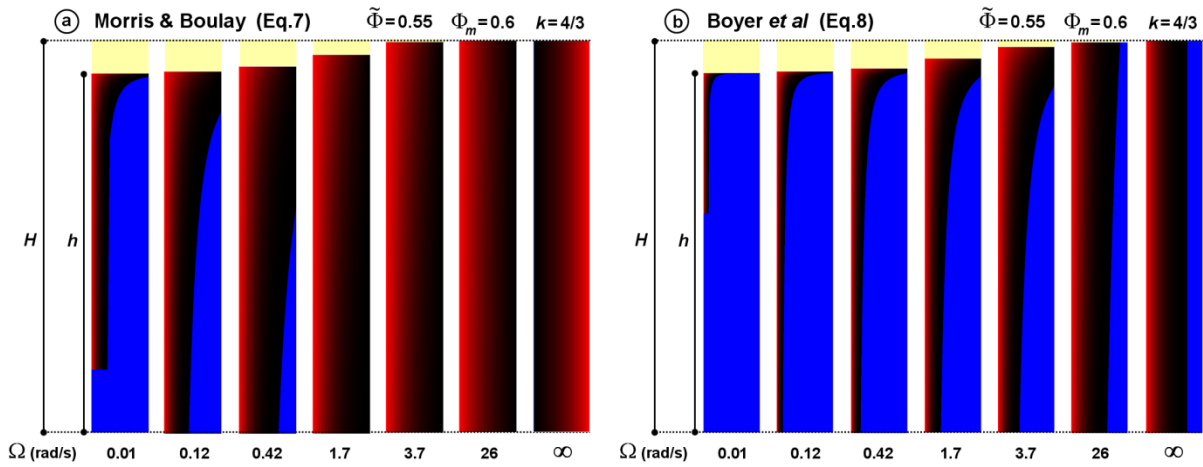


**Fig. E.15** Shear induced re-suspension of non buoyant particles in a viscous fluid ( $\tilde{\Phi} = 0.55$ ,  $\Phi_m = 0.6$ ,  $H = 30\text{mm}$ ,  $\Delta\rho = 0.3\text{g/cm}^3$ ). 2D images of velocity profiles  $v(r,z)/v(R)$  through the gap versus the angular velocity  $\Omega$  of the inner cylinder either for the Morris & Boulay  $f_{MB}(\varphi)$  (a) (Eq.E.7) or the Boyer viscometric function  $f_{BPG}(\varphi)$  (b) (Eq.E.8) with  $\lambda_2 = 0.85$ ,  $\lambda_3 = 0.5$ ,  $\varphi_c = 0.22/\Phi_m$  and  $k = 4/3$ . The red color intensity scales as  $v(r,z)/v(R)$  and decreases from the left sidewall (inner cylinder) to the right sidewall (outer cylinder). The blue color indicates an arrested flow and the yellow color a pure fluid region.

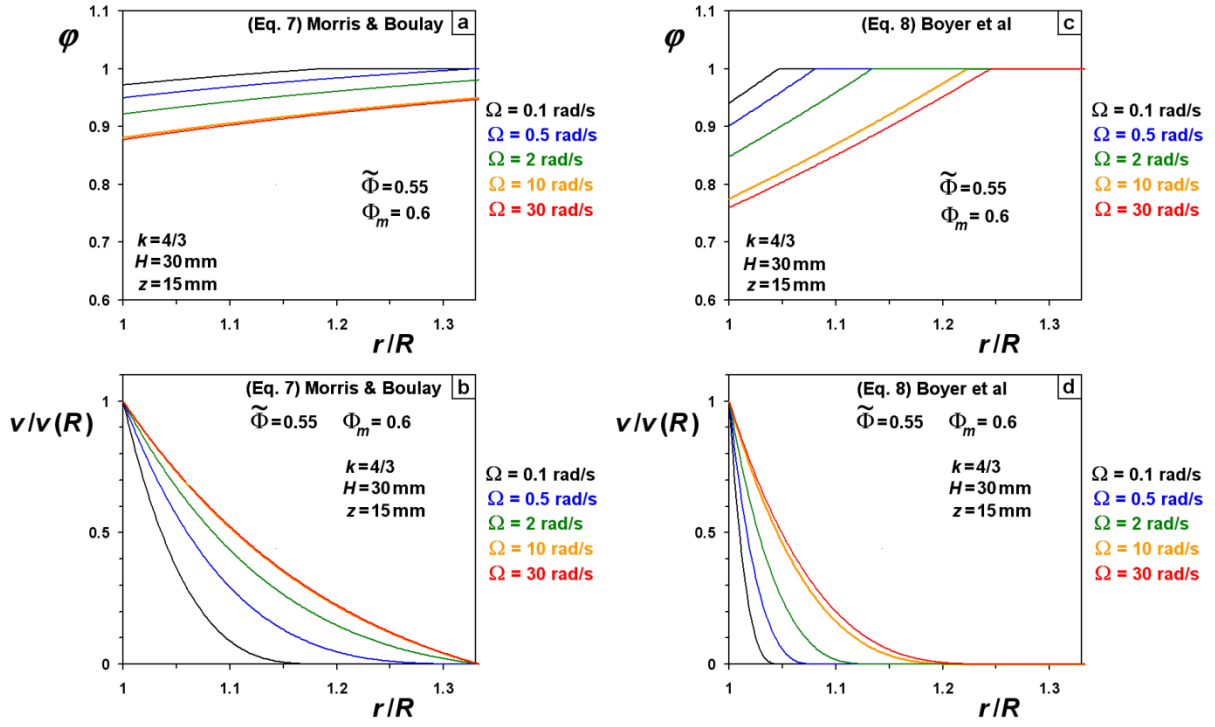


**Fig. E.16** Shear induced re-suspension of non buoyant particles in a viscous fluid ( $\tilde{\Phi}=0.55$ ,  $\Phi_m=0.6$ ,  $H=30$  mm,  $\Delta\rho=0.3$  g/cm<sup>3</sup>). Stationary concentration profile  $\phi(r,\Omega)$  and dimensionless velocity profile  $v(r,\Omega)/v(R,\Omega)$  versus dimensionless radius  $r/R$  either for the Morris & Boulay  $f_{MB}(\phi)$  (a,b) (Eq.7) or the Boyer viscometric function  $f_{BPG}(\phi)$  (c,d) (Eq.8) at altitude  $z=H/2$  with  $\lambda_2=0.85$ ,  $\lambda_3=0.5$  and  $k=4/3$ .

The shear induced resuspension causes an increase of the equilibrium height  $h$  of the suspension from the minimal height  $h_o$  at zero angular velocity ( $\phi=1$ ) up to the maximal height  $H=h_o/\tilde{\phi}$  when particles reach the upper air / liquid interface (Figs. E.15).

Considering the Morris & Boulay viscometric function  $f_{MB}(\phi)$  (Figs. E.15.a, E16.a, b), the suspension becomes fully fluidized through the gap for an angular velocity  $\Omega^* \approx 0.5$  rad/s, in line with experiments (Chapter C, Fig. C.34). One may note that the system is fully fluidized before the upper liquid layer disappears, a feature that is also observed experimentally (Fig. E.17).

On the other hand, shear banding is always present in the case of the Boyer *et al.* (2011) function (Figs. E.15.b and E.16.c, d) and a much higher angular velocity,  $\Omega^* > 30$  rad/s, is necessary to reach a  $z$ -invariant 2-phase flow as with neutrally buoyant particles (Fig. E.16.d). Despite shear banding, the particles reach the upper air/liquid interface ( $h/H=1$ ) at  $\Omega \approx 5$  rad/s, well below  $\Omega^*$  (Fig. E.17).

Below, in Fig. E.17, we show the predictions of the model for the height  $\hat{h} = h(\tilde{\varphi}, \Omega) / H$  of the suspension. In other words, we calculate the amplitude of the shear-induced dilatancy of the granular medium inside the gap of the Couette cell. The figure shows that calculated values of  $\hat{h}$  from both  $f(\varphi)$  functions are not very different. Dilatancy is not a very sensitive parameter in discriminating between both types of functions, contrary to concentration and velocity profiles.

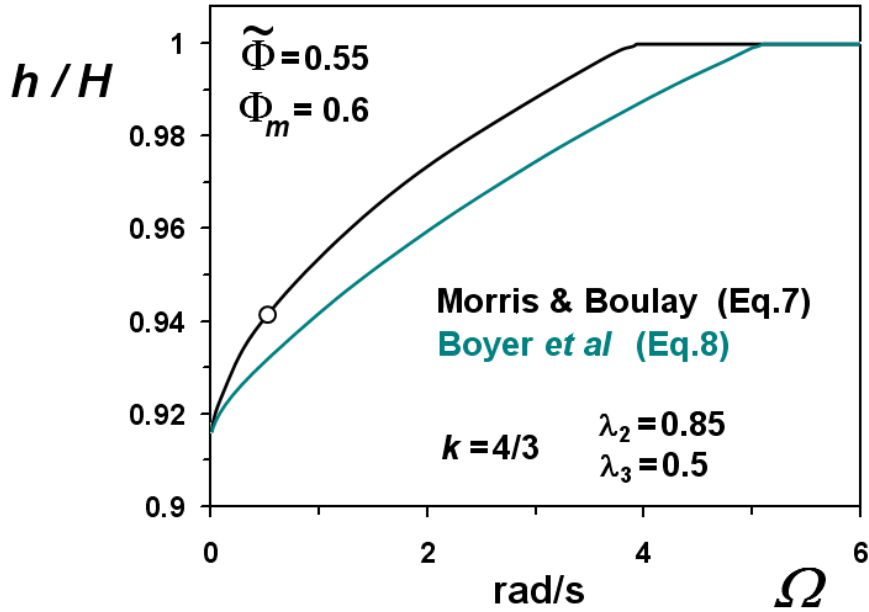


**Fig. E.17** Shear induced re-suspension of non buoyant particles in a viscous fluid ( $\tilde{\Phi} = 0.55$ ,  $\Phi_m = 0.6$ ,  $H = 30\text{mm}$ ,  $\Delta\rho = 0.3\text{g/cm}^3$ ). Reduced height  $h(\Omega) / H$  of the suspension versus angular velocity  $\Omega$  of the inner cylinder for Morris & Boulay  $f_{MB}(\varphi)$  (a) (Eq.E.7) or Boyer viscometric function  $f_{BPG}(\varphi)$  (b) (Eq.E.8) with  $\lambda_2 = 0.85$ ,  $\lambda_3 = 0.5$ ,  $\varphi_c = 0.22 / \Phi_m$  and  $k = 4/3$ . The open symbol indicates the full fluidization of the suspension in the case of Morris & Boulay viscometric function while shear banding is always present for the Boyer et al function.

We now confront the predictions of the model to experimental data obtained with the non-density matched PMMA particles (chapters C, D). The force balance model using  $f_{MB}(\varphi)$  with a prefactor  $f(\varphi = 1) = 7.5$  (as given by Eq. (E.7.c)) reasonably describes the experimental velocity profiles  $v(r, \Omega, z)$ , as we can see from Fig. E.18 (for  $z/H = 1/3$ ), and Fig. E.19 (for  $z/H = 1/2$ ), and the  $z$  variation of the reduced decay length  $\xi = (r^* - R) / (kR - R)$  of the angular velocity for  $0.11\text{rad/s} < \Omega < 0.57\text{rad/s}$  (Fig. E.20). Note

that the curve  $r^*(z)$  faithfully reproduces the observed bell shaped boundary between flowing and nearly *arrested* regions (Chapter C, Fig. C.34).

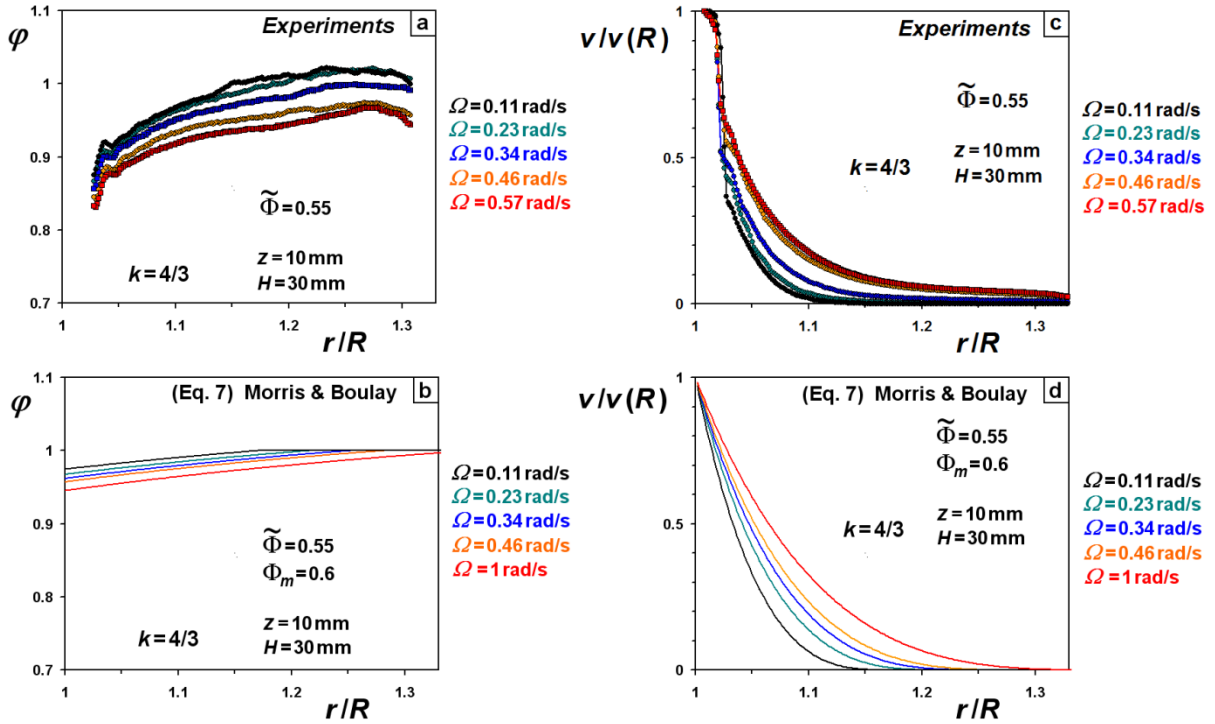


**Fig. E.18** Shear induced re-suspension of non buoyant particles in a viscous fluid ( $\tilde{\Phi} = 0.55$ ,  $\Phi_m = 0.6$ ,  $H = 30 \text{ mm}$ ,  $\Delta\rho = 0.3 \text{ g/cm}^3$ ). Stationary concentration profile  $\varphi(r, \Omega)$  and dimensionless velocity profile  $v(r, \Omega)/v(R, \Omega)$  versus dimensionless radius  $r/R$  for  $z/H = 1/3$  and angular velocity  $0.11 \text{ rad/s} < \Omega < 0.57 \text{ rad/s}$ . Experimental observations at altitude  $z = 10 \text{ mm}$  (a,c) and predictions of the force balance model (b,d) using the Morris & Boulay viscometric function  $f_{MB}(\varphi)$  (Eq.E.7) with  $\lambda_2 = 0.85$ ,  $\lambda_3 = 0.5$ ,  $k = 4/3$ .

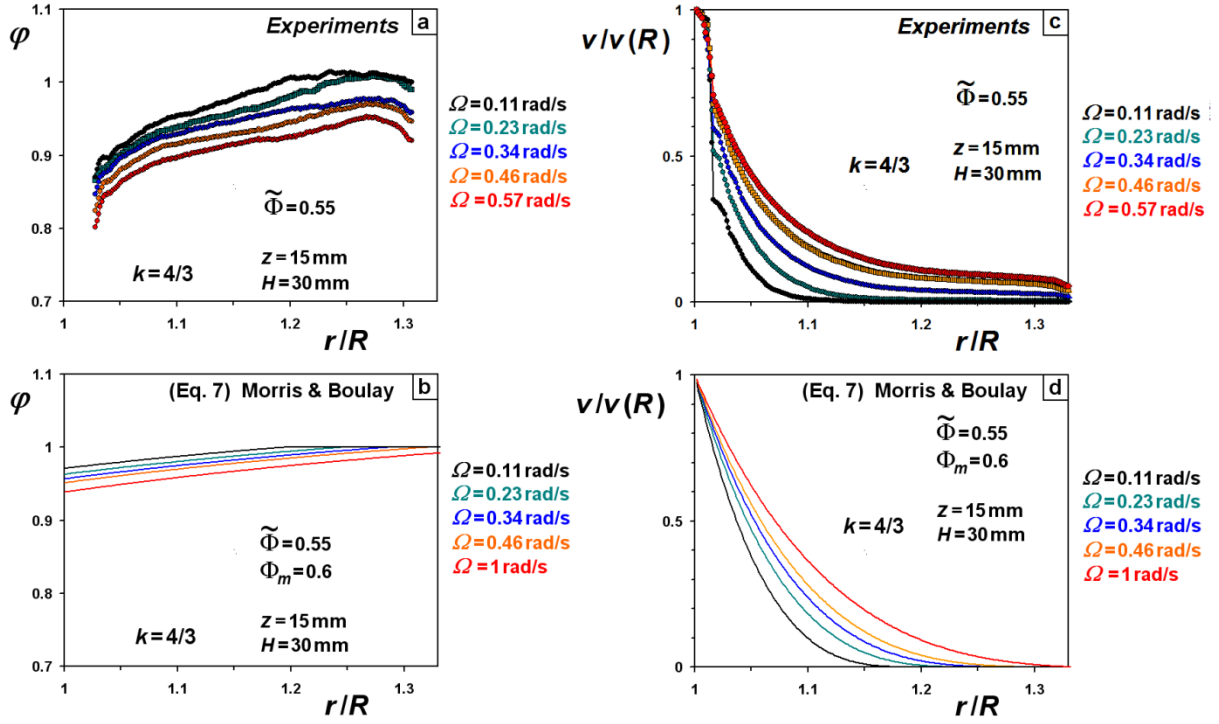


**Fig. E.19** Shear induced re-suspension of non buoyant particles in a viscous fluid ( $\tilde{\Phi} = 0.55$ ,  $\Phi_m = 0.6$ ,  $H = 30$  mm,  $\Delta\rho = 0.3$  g/cm<sup>3</sup>). Stationary concentration profile  $\phi(r, \Omega)$  and dimensionless velocity profile  $v(r, \Omega)/v(R, \Omega)$  versus dimensionless radius  $r/R$  for  $z/H = 1/2$  and angular velocity  $0.11$  rad/s  $< \Omega < 0.57$  rad/s. Experimental measurements at altitude  $z = 15$  mm (a, c) and predictions of the force balance model (b, d) using the Morris & Boulay viscometric function  $f_{MB}(\phi)$  (Eq. E.7) with,  $\lambda_2 = 0.85$ ,  $\lambda_3 = 0.5$ ,  $k = 4/3$ .

The above study was dedicated to a  $\tilde{\varphi} = 0.55$  suspension, the average concentration in almost all our experiments. We made a few complementary tests with larger average concentrations. Practically, we started from the 55% system, and just removed a small volume of the immersion fluid, by pumping out of the fluid layer on top of the system at rest. Rather surprisingly, we noticed that localisation of the flow was about the same as before (at 55%) throughout the gap of the shear cell. Interestingly this trend is reproduced by the force balance model, as we show below. We performed calculations for  $\tilde{\varphi} = 0.58$ . We find that the increased average concentration reduces the critical angular velocity necessary for particles to reach the air / liquid interface (Fig. E.21), but weakly influences concentration and velocity profiles in the high shear regime (compare Fig. E.19. b, d and Fig. E.22). Such an agreement

confirms the adequacy of the Morris and Boulay viscometric function  $f_{MB}(\varphi)$  to describe the flows of concentrated suspensions at volume averaged concentration up to 58%.

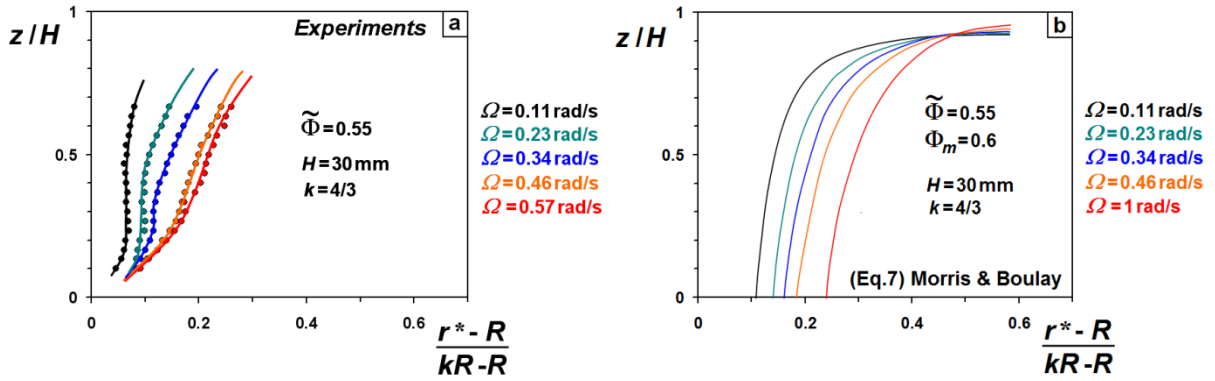


**Fig. E.20** Shear induced re-suspension of non buoyant particles in a viscous fluid ( $\tilde{\Phi} = 0.55$ ,  $\Phi_m = 0.6$ ,  $H = 30$  mm,  $\Delta\rho = 0.3$  g/cm<sup>3</sup>). Reduced decay length  $(r^*-R)/(kR-R)$  of the angular velocity profile  $\omega(r) = v(r)/r$  versus the dimensionless altitude  $z/H$  for angular velocity  $0.11$  rad/s  $< \Omega < 0.57$  rad/s. Experimental measurements (a) and predictions of the force balance model (b) using the Morris & Boulay viscometric function  $f_{MB}(\varphi)$  (Eq.7) with  $\lambda_2 = 0.85$ ,  $\lambda_3 = 0.5$  and  $k = 4/3$ .

Extrapolating to still higher concentrations ( $\tilde{\varphi} > 0.58$ ), the model predicts an almost  $z$ -invariant 2-phase flow. Nevertheless it may be an elusive goal to test this prediction experimentally, due to the difficulty of controlling the value of the concentration so close to maximum packing.

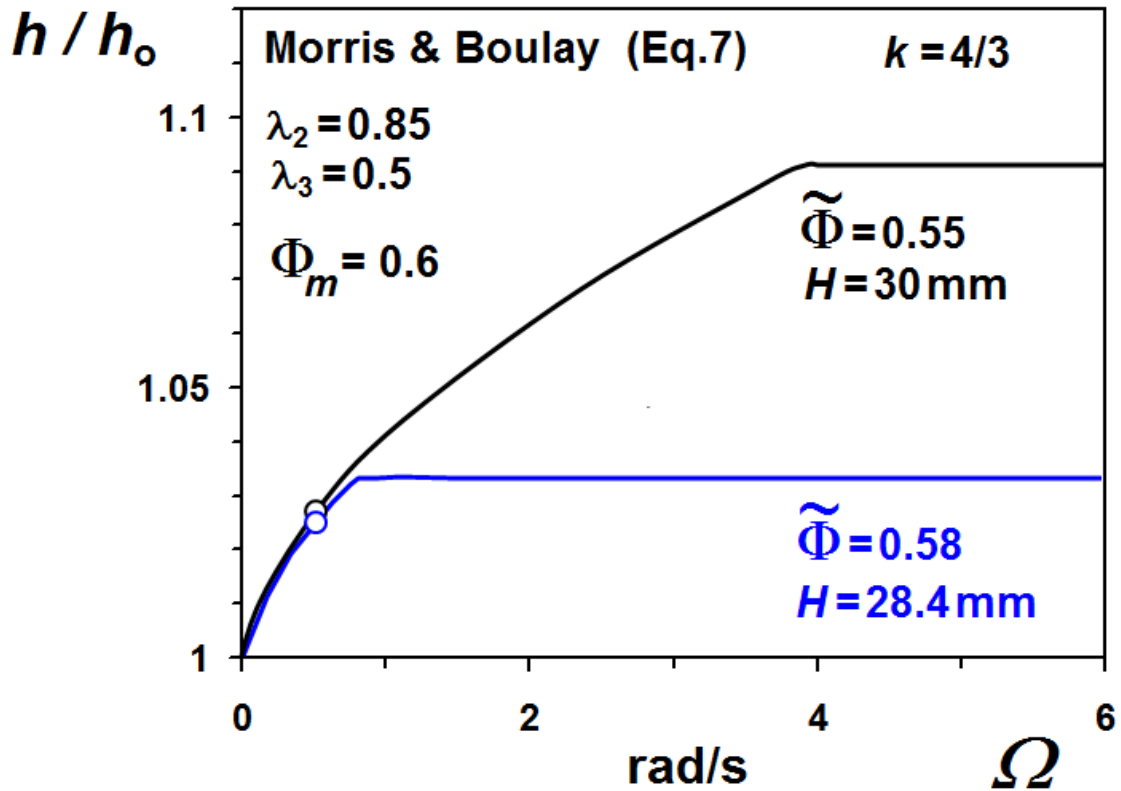


**Fig. E.21** Shear induced re-suspension of non buoyant particles in a viscous fluid ( $\Phi_m = 0.6$ ,  $h_o = 27.5 \text{ mm}$ ,  $\Delta\rho = 0.3 \text{ g/cm}^3$ ). Reduced height  $h(\Omega)/h_o(\Omega=0)$  of the suspension versus angular velocity  $\Omega$  of the inner cylinder for a volume averaged concentration  $\tilde{\Phi} = 0.55$  ( $H = 30 \text{ mm}$ ) or  $\tilde{\Phi} = 0.58$  ( $H = 28.4 \text{ mm}$ ). Morris and Boulay viscometric function  $f_{MB}(\varphi)$  with  $\lambda_2 = 0.85$ ,  $\lambda_3 = 0.5$ ,  $\varphi_c = 0.22/\Phi_m$  and  $k = 4/3$ . The open symbols indicate the full fluidization of the suspension.

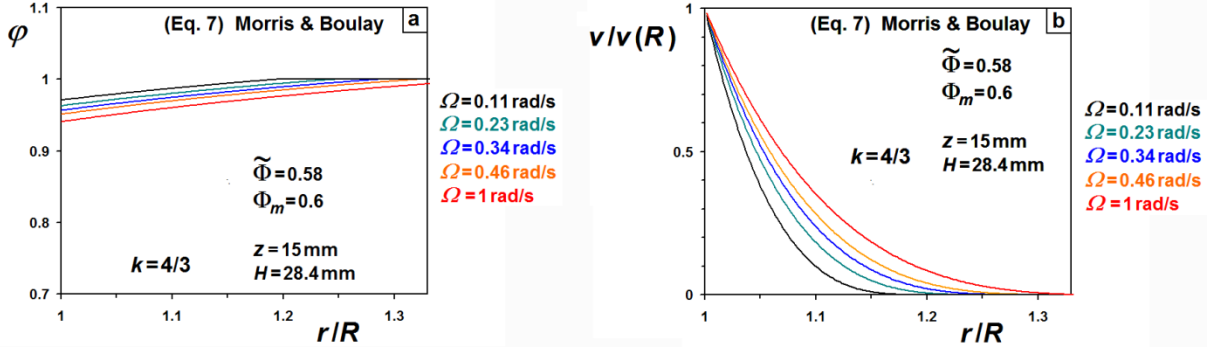


**Fig. E.22** Shear induced re-suspension of non buoyant particles in a viscous fluid ( $\tilde{\Phi} = 0.58$ ,  $\Phi_m = 0.6$ ,  $h_o = 27.5$  mm,  $H = 28.4$  mm,  $\Delta\rho = 0.3$  g/cm<sup>3</sup>). Stationary concentration profile  $\phi(r, \Omega)$  and dimensionless velocity profile  $v(r, \Omega)/v(R, \Omega)$  versus dimensionless radius  $r/R$  for  $z = 15$  mm and angular velocity  $0.11 \text{ rad/s} < \Omega < 0.57 \text{ rad/s}$ . Predictions of the force balance model using the Morris & Boulay viscometric function  $f_{MB}(\phi)$  (Eq.7) with  $\tilde{\Phi}_m = 0.6$ ,  $\lambda_2 = 0.85$ ,  $\lambda_3 = 0.5$  and  $k = 4/3$ .

## E.7: Summary and conclusion

In this chapter, we tested the ability of the so-called force balance model to account for our experimental observations about the flow of density-matched ( $\Delta\rho = 0$ ) and non density-matched ( $\Delta\rho > 0$ ) suspensions in relatively large gap shear cells. Essentially, the model involves shear forces and normal forces which are simply proportional to the local shear rate, with proportionality factors, the viscometric functions  $\hat{\eta}_s$  and  $\hat{\eta}_n$ , that only depend on the local concentration  $\phi$ .

In the case of a *density-matched system*, the gravity plays no role. As a consequence, the flow characteristics, in terms of  $\phi(r)$  and  $v(r)$  profiles, only depend on the ratio  $f(\phi) = \hat{\eta}_n/\hat{\eta}_s$ . We tested different forms of the  $f$  function, and found that experimental results (those of chapters C, D herein and the concentration measurements of [Boyer et al. \(2011\)](#)) were satisfactorily reproduced by the theory with appropriate forms for  $f$ : the basic Morris-Boulay function  $f_{MB}(\phi)$  (Eq. (E.7.c)), or a power-law  $f(\phi, \beta)$  (Eq.(24)) with  $\beta > 8$  were found adequate. Conversely, the function proposed by Boyer et al. was found incompatible with the data. We found that the variation of the  $f$  function in the high- $\phi$  range was the essential feature that determined adequacy. The behaviour of the function at low and medium  $\phi$  only had a small impact on the calculated profiles. Consequently, our study cannot make a

difference between the different functions at low and medium  $\varphi$ . We thus do not exclude that normal force differences may be null below a threshold concentration  $\Phi_c \cong 0.22$ , as put forward by [Boyer \*et al.\* \(2011\)](#) and Dbouk [[Dbouk thesis 2011](#)].

For the non density-matched system, we came out with the same conclusion that  $f_{MB}(\varphi)$  was the good choice to reproduce the main features of the re-suspension experiments. In this case, however, the agreement is not perfect, as some features are not quantitatively reproduced. An obvious source of disagreement may have come from wall slip, which is evident in experimental records, and not taken into account by the model, at current stage. However a deeper limitation of the model stems from the basic principle that the granular system under shear self-organizes into a fluid phase that coexists with a jammed phase, corresponding to  $\varphi=1$  (recall that the jammed phase may be “virtual”, when  $r_c > kR$ ). Analyzing experimental profiles, we identified the jammed phase as the “dead zone” (chapters C, D). Clearly the concentration in this zone ( $\varphi_{dz}$ ) is everywhere less than the maximum concentration, i.e.  $\varphi_{dz} < 1$ , and is even far from uniform, as it decreases from bottom to top (see Fig. D.10). Moreover, the dead zone is not strictly “dead”, and should rather be called “nearly arrested”, since non negligible particle motions are detected therein and contribute to the velocity fluctuation profiles (chapter C). These features had already been noticed by Lenoble, using laser speckle imaging [[Lenoble thesis 2005](#)]. The nearly arrested phase therefore looks closer to a slowly moving vitreous material than to a solid. It would be interesting to reconsider the basic principles of the model, to include the coexistence with a vitreous phase. Experimentally, the nearly arrested phase shows both migration and dilatancy effects, which should be accounted for by the theory. A difficulty that we may anticipate is related to the very high concentrations ( $\varphi \rightarrow 1$ ), meaning that macroscopic contact chains may be very important, and result in non local rheology [[Mansard and Colin 2012](#), [Mills and Snabre 2009](#)], and finite-size effects.

## Chapter F – Single Particle Tracking (SPT)

The works reported in the previous chapters were dedicated to azimuthal motions of a large number of particles and their spatial repartition inside the gap of the Couette cell. Results were stated in terms of statistical data:  $\langle v_\theta(r) \rangle$ ,  $\langle [\delta v_\theta(r)] \rangle^{1/2}$  and  $\langle \Phi(r) \rangle$ . In this chapter we conversely focus on the motion of a single particle. This particle is a fluorescent tracer, similar to those used in the previous experiments, but in principle we only have one such tracer in the whole suspension. We deal with the time( $t$ ) variable vector function  $\mathbf{r}(r, \theta, z, t)$ , which represents the position of the tracer in cylindrical coordinates, inside the Couette flow. Our goal is to show that particle motion does not simply amount to circling around the Couette cell symmetry axis, corresponding to the *primary motion* in Couette flow, but also includes *secondary* components in the form of motions in  $(r, z)$  coordinates. We will start with the “monodisperse” (180-200  $\mu\text{m}$ ) system and look at the motion of one of the constituting particles. As we will see, the experiments indeed evidence large amplitude secondary motions, and considerable position noise along  $r, \theta, z$ . A very important point is the sensitivity of the trajectories to particle sizes, which is the key to understanding the size segregation effect under shear. Stating the problem in terms similar to those of the “Brazil-nut effect” [Rosoto *et al.* 1987, Jullien *et al.* 1990, Jullien *et al.* 1992], we want to know the path followed by either a small ( $\ll 200 \mu\text{m}$ ) or a large ( $\gg 200 \mu\text{m}$ ) “intruder” inside the otherwise monodisperse material. Here the shear flow, instead of vibration in BNE, is the mechanism that drives segregation. As we will see, our experiments indeed reveal considerable differences between trajectories depending on the size of the “intruder”.

The chapter is organized as follows:

- The first Section (F1) is about the experimental techniques. We start (paragraph F1.1) with a primitive version of the experiment, named “passive mode”. In passive mode, we may decide to operate the setup “classically”, i.e. with only the inner cylinder rotating, or reversely with the outer cylinder. The experiment only yields information about the  $(r, z)$  position of the tracer at low time sampling rate (on the order of one per minute, at best). The data thus do not show details of the tracer trajectory, but are sufficient to evidence large scale meridian motions. The second part, F1.2, is about the full 3d single particle tracking (SPT) version, which is based on servo systems and is fully automated. This version is named “active mode”. A paragraph is dedicated to the system performance in terms of responses to quick

displacements of the particle. We also report tests which we carried out with a tracer inside a simple density matched fluid, namely the 3-component Cargille mixture.

- Section F2 reports our observations with a “host-like tracer”, i.e. a tracer of same size as the other particles constituting the –approximately- monodisperse granular system. In principle, tracer trajectories are statistically the same as those of any host (non dyed) particle. Data concern both the density-matched ( $\Delta\rho = 0$ ) and the non density-matched ( $\Delta\rho > 0$ ) systems. In the latter category, comparison is made between data from active and passive SPT. The Section includes a discussion about the influence of the servo systems as a possible cause of perturbation on the particle motion.
- Section F3 is about size effects. We report observations made with tracers that may be either smaller or larger than the host particles. Such tracers are called “intruders”, in reference to the terminology used by researchers who study the Brazil-nuts effect (BNE).
- In Section F4 we discuss the general features of the meridian motions: noise, “loops” and toroidal flow, ergodicity of the trajectories and possible effects related to properties of the tracers.
- The chapter ends with a summary (F5) of the main results, together with prospects for future developments.

## **F.1: Experimental techniques**

Single particle tracking experiments cannot work when there are too many tracers inside the Couette cell. This is easily understandable if we imagine having to track one given particle inside a cloud of many others ones with a variety of complicated motions, just by naked eye. The ideal situation is when there is only one fluorescent particle inside the system. In practice it is about impossible to introduce only one fluorescent particle inside the cell. In our procedure, tracers are picked up with a glass pipette from a diluted suspension of fluorescent particles, and are loaded into the granular suspension inside the Couette cell. In general the number of particles inside the pipette varies between zero and a few. These particles are afterwards dispersed inside the fluid by stirring with a thin spatula. In typical conditions, we

find one isolated fluorescent particle that we can choose to be the tracer to be tracked. The initial position of the tracer is not controlled a priori, but we are able to shift it to a different zone if necessary, still by means of the little spatula. Once the Couette cell is in operation, it may happen that this tracer comes close to a second one after some time, but this is a rare event, not a serious limitation in general.

### F.1.1: “Passive” mode

In this version, the experiment is based on a simple vertical sheet of light that goes through the axis of the Couette cell, very similarly to the concentration field experiments (chapter D). A video camera makes an image of the illuminated zone, on one side, see Fig. F.1 below.

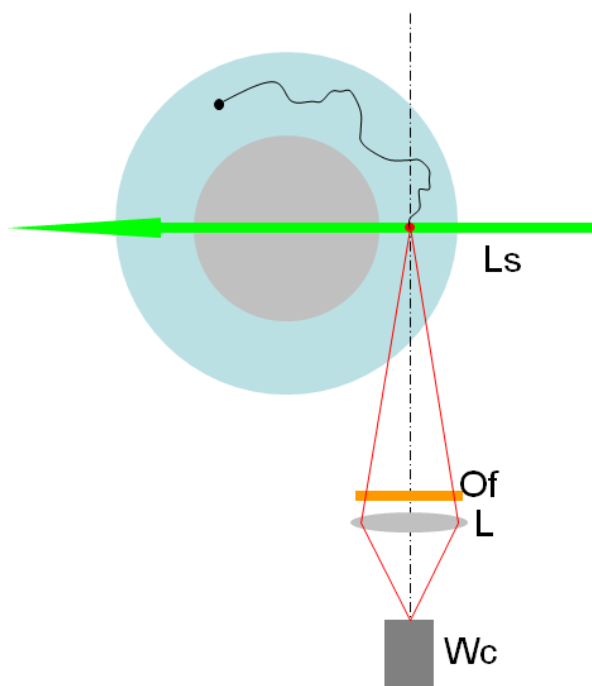


**Fig. F.1** « Passive mode » tracking. The undulated line is an hypothetical path followed by the tracer. At some time  $t_1$ , the tracer comes across the laser sheet. The resulting bright fluorescent spot is detected by the camera. The position of the spot at time  $t_1$ , in  $(r,z)$  coordinates is recorded. Wc: web cam (Philips SPC 900NC); L:  $f=50$  mm objective; Of: orange filter; Ls: laser sheet.

Whenever the tracer comes across the laser sheet, say at time  $t_i$ , it becomes fluorescent. In the flux of images generated by the camera (6 im/s), the intensity suddenly increases. A dedicated software then triggers recording of the image, and a 2d tracking algorithm calculates the  $(r, z)$  coordinates of the bright spot. We thus obtain one point in the particle

meridian position:  $(r_i, z_i)$  at time  $t_i$ . Due to the shear flow, the particle soon gets out of the laser sheet and goes on its way around the Couette axis. Later on, after one more revolution, it comes back across the laser sheet, giving a new position:  $(r_{i+1}, z_{i+1})$  at time  $t_{i+1}$ . The procedure thus yields successive positions of the particle, at very slow sampling rate, on the order of  $\omega$ , at best. This is very limited information, but it may be enough to evidence slow large scale meridian motion of the tracer.

In passive mode, the Couette cell may be operated with different combinations:  $\Omega_{in} = \Omega, \Omega_{out} = 0$  (inner cylinder rotating),  $\Omega_{out} = -\Omega, \Omega_{in} = 0$  (outer cylinder rotating), or with any repartition between contra-rotating cylinders. We may thus study the possible influence of contra-rotation on the particle meridian motion. We even carried out tests with little amounts of fluctuations on either  $\Omega_{in}$  or  $\Omega_{out}$ , to simulate the position noise due to the servos in the active mode (see next paragraph), and to address the question of whether such noise would have an influence on particle trajectories.

### F.1.2: Automated tracking system

Basically, we want to know the trajectory of the tracer in the standard configuration, where only the inner cylinder is rotating, i.e.  $\Omega_{in} = \Omega, \Omega_{out} = 0$ . The 3 coordinates of the tracer are functions of time:  $r(t), \theta(t), z(t)$ . The 3d tracking system exploits the possibility of making the particle about immobile in  $\theta$  using the contra-rotation of the Couette cell cylinders. Recall that the average shear applied to the sample is defined through the difference  $\Omega = \Omega_{in} - \Omega_{out}$ . Increasing both velocities by a same *offset* value ( $\Omega_{in} \rightarrow \Omega_{in} + \Omega_{off}, \Omega_{out} \rightarrow \Omega_{out} + \Omega_{off}$ ) does not change the average shear, and simply amounts to rotating the whole Couette cell in the laboratory frame at angular velocity  $\Omega_{off}$ . The tracer, whatever its position  $(r, z)$  within the gap of the shear cell at time  $t$ , can be made about immobile in azimuth by tuning the offset such that  $\Omega_{off}(t) = -\dot{\theta}(t)$ . In our experiment, we use this property to maintain the tracer always inside a given reference plane  $\Pi_{ref}$ , see Fig. F.2. This job is done automatically, as we explain below. Within  $\Pi_{ref}$  the particle is free to move in  $r$  and  $z$ . This meridian motion is directly observable, even by naked eye, observing the tracer

perpendicularly to  $\Pi_{ref}$ . Instead of the naked eye, we use a camera and the tracer  $(r, z)$  position is obtained in the same way as in the passive mode (Fig. F.1), but now at high sampling rate. The procedure directly yields  $r(t), z(t)$ ; the azimuth  $\theta(t)$  is computed by time integration of  $\Omega_{off}(t)$ .

### F.1.2.a: Experimental setup (active SPT)

Apart from the Couette shear cell, the setup comprises a mobile microscope head (MMH) connected to a computer (PC1), and a fixed side camera, connected to a second computer (PC2). The purpose of the MMH is to permanently provide a focused video image of the tracer. This image is analyzed in real time by a dedicated software to provide the error signals for the servo system.

The cameras, both in the MMH ( $S_a$  in Fig. F.2) and for side observation ( $S_b$  in Fig. F.2) are simple webcams (Philips SPC 900NC). Webcams are interesting for their low cost, also for their small mass, a decisive advantage for the mobile MMH unit. The fluorescence of the tracer is excited by a laser beam, at 532 nm (Quantum Laser Opus). The laser light is fed through an optical multimode fiber<sup>8</sup> whose output is attached to the MMH front lens and directed towards the scene to be observed. A longpass filter (TFI Technologies 540LP) inside the microscope blocks the scattered laser light and allows the orange fluorescence light to pass towards the detector. With this arrangement, a few milliwatts of laser light are sufficient to provide a bright fluorescence image of the tracer. The MMH magnification and resolution are sufficient to resolve the sizes of the tracers currently in use, i.e. between 20 and 600 micrometers.

The MMH can be moved by means of a couple of motorized translation stages (Newport 850G-HS): one vertical ( $z_m$ ) and one horizontal ( $x_m$ ) parallel to the microscope axis. The latter is directed towards the Couette cell axis, thus defining a reference vertical plane  $\Pi_{ref}$  containing the optics and cell axes. A bright focused image of the tracer is obtained when: (i) the tracer is inside  $\Pi_{ref}$ , (ii) the microscope axis goes through the tracer center and (iii) focusing is achieved to the tracer radial position ( $r$ ). In general, the experiment is run at

---

<sup>8</sup> The fiber is of multimode<sup>8</sup> type, with a 0.2 mm core. Multimode fibers are cheap and injection of the laser beam into the input end is easy. However the light from the output of the fiber has a characteristic grainy structure (a speckle), which is not appropriate for uniform illumination. Fortunately, the speckle can be time averaged at high frequency by mechanical vibration of the fiber. In our setup, we vibrate the fiber at 62 Hz. The procedure yields a very uniform illumination, both for naked eye and video.

constant average shear ( $\Omega_{in} - \Omega_{out} = cst$ ). Condition (i) is fulfilled by tuning the offset to the corresponding  $\Omega_{off}(r, z)$  value, as explained above. Condition (ii) and (iii) are fulfilled by moving the  $z_m$  and  $x_m$  translation stages, respectively. In a preliminary version of the experiment, these tunings were operated “by hand” in real time by a single person observing the image of the tracer on a video screen, and transmitting orders through a couple of joysticks [Lenoble thesis 2005]. As the task turned out about impossible beyond a few minutes of tracking, we moved to the fully automated version which we describe here. Now  $\Omega_{off}$  and  $z_m$  degrees of freedom are handled through a 2-d tracking routine, whose role is to keep the tracer image centered in a predefined rectangular zone (ROI, for “region of interest” -  $\pi_{ref}$ ) of the  $S_a$  sensor. Focusing ( $x_m$ ) is achieved by means of an autofocus system, whose principle is inspired from the autofocus function of compact disk/digital versatile disks (CD/DVD) pickup heads (see Hsu *et al.* 2009, and references therein). In short, the imaging optics ( $L_{1,2}$ ) is rendered slightly astigmatic by adding a weakly cylindrical lens (denoted  $A$  in Fig. F.2) between both lenses. This arrangement provides a couple of sharp elongated images of the spherical tracer (Fig. F.3), corresponding to two different focusing positions ( $x_m$ ). The ellipticity of the image is used as the error signal to drive the focusing system. By definition, focusing is achieved in the intermediate position (the middle one in Fig. F.3a): there, the image is slightly blurred, but of zero ellipticity.

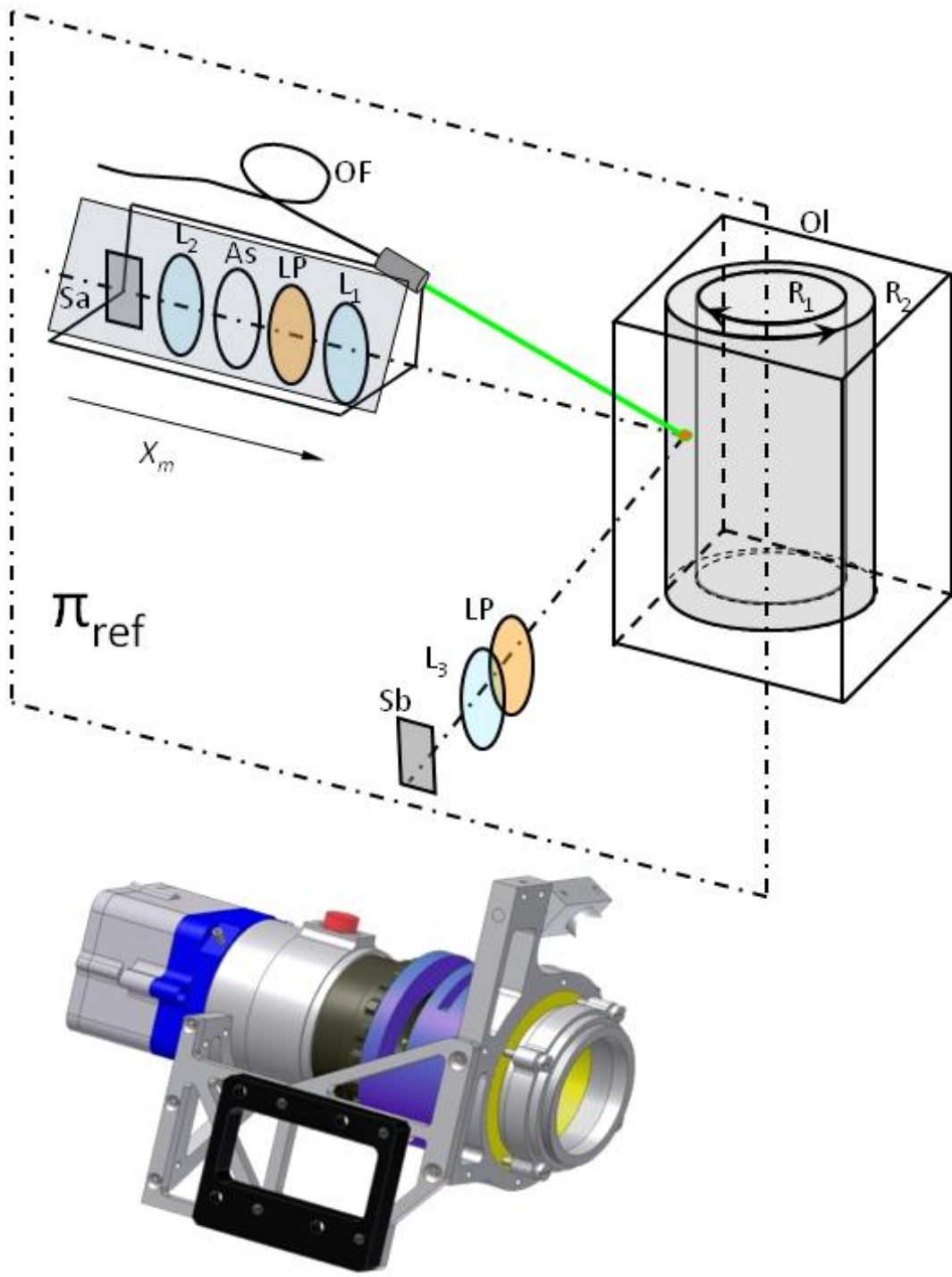


**Fig. F.2** General scheme of the automated SPT setup.  $L_1$ ,  $L_2$ ,  $L_3$ : objectives, and corresponding focal lengths  $f_1= 80$  mm,  $f_2= 50$  mm,  $f_3= 50$  mm.  $S_a$ ,  $S_b$  are CCD sensors. LP: longpass filter. As: astigmatic optics. OF: multimode optical fiber. Sketch of MMH unit

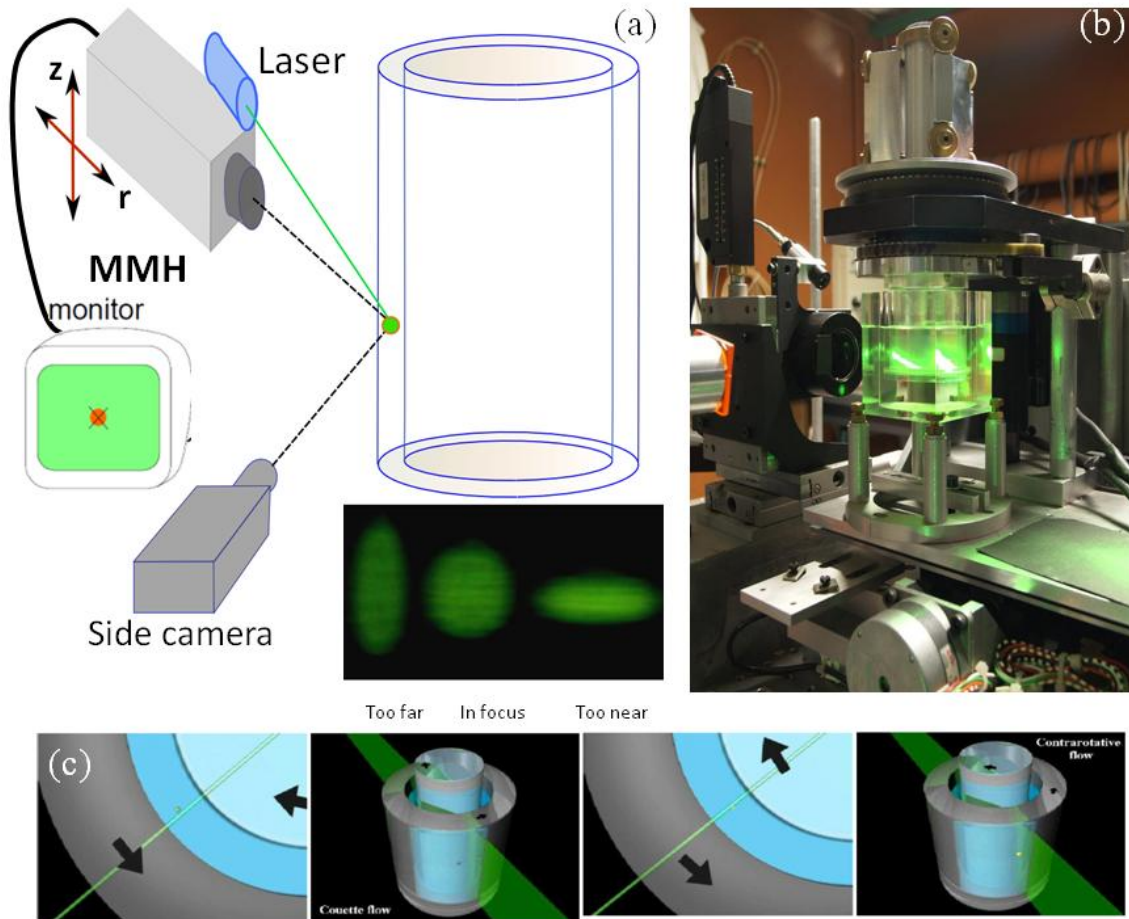


**Fig. F.3** Automated Single Particle Tracking setup. (a) design and photos of astigmatic images of a spherical tracer ( $200\ \mu\text{m}$  in diameter) are shown. (b) photo of SPT used for trajectories recordings and (c) contra rotation principle.

### F.1.2.b: Servo system performance

The functioning of the servo loops is explained in Appendix F-A. The whole system works with  $640 \times 480$  images, at 30 frames per second rate. The system records successive positions  $(x_m, z_m)$  of the imaging optics and calculates the time integral of the applied offset voltage:

$$\theta_m(t) = \int_{t_0}^t \Omega_{\text{off}}(t') dt' \quad (\text{F.1})$$

Here  $t_0$  is the start time of particle tracking. In an ideal system, the particle cylindrical coordinates are simply given by  $r = -x_m + A$ ,  $z = z_m + B$ ,  $\theta = \theta_m + C$ , where  $A, B, C$  are

constants related to the setup. In reality the relation between machine and particle coordinates inevitably differs from the above simple forms due to non instantaneous time responses of the servo system. Examples of such responses are displayed below in Fig. F.4. Note the characteristic delay, overshoots and oscillations in response to a step change in focus or particle altitude (Fig.F.4.a,b). Here a large step change, about 0.6 mm, has been imposed to evidence the non ideal response of the system. We generally observed that responses to steps  $< 0.4$  mm, i.e. about 2 particle diameters, were closer to ideal as they would not show overshoots and oscillations. However the delay, about a second in Fig. F.4.a,b, was not better than 0.6 s for small steps. These features have characteristics that depend on the chosen PID parameter values, but are inevitable as they are caused by finite masses and friction of the moving parts, and delays in video signal processing. However note that, conversely to  $x_m, z_m$  responses, the response in  $\theta_m$  looks about instantaneous within experimental resolution. In Fig. F.4, the sampling rate of machine coordinates is 3 points per second. This low rate is sufficient for the current applications to granular pastes, but could be increased up to the frame rate if necessary.

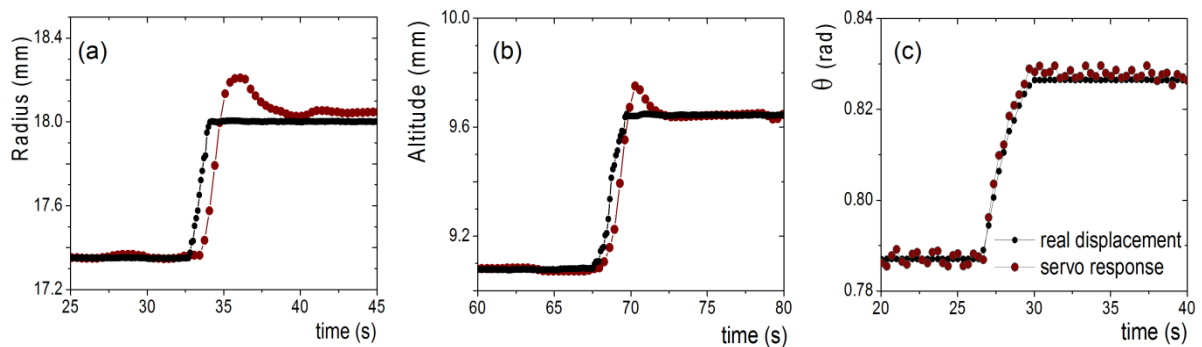


**Fig. F.4** Time responses of the servo system to step-like changes in tracer position coordinates. The test is carried out by suddenly shifting the position of the Couette cell relatively to the imaging optics. Reference curves are obtained from position sensors attached to the cell.

Improvements in  $x_m, z_m$  responses may be envisaged through diminishing masses, friction and processing time. However, considering the technological difficulty of such changes, we moved to the simpler solution which amounts to adding a side camera, as illustrated in Fig. F.1. Doing so, we exploit the fact that the servo system keeps the tracer

within the reference plane. The side camera (also a simple webcam) provides an overall view of the flow region within  $\Pi_{ref}$  showing the tracer as a small spot therein. The tracer  $r, z$  coordinates are obtained from a 2-d particle tracking routine. The spatial resolution is about  $36 \mu\text{m}$ , and the time sampling rate is 30 points per second (it is currently operated at 10 points/s, which we found sufficient). For the angular coordinate, we make the approximation  $\theta = \theta_m$ , justified by the almost instantaneous response in  $\theta_m$ .

In principle, there is no limitation in time of tracking, i.e. a tracer trajectory can be recorded over a period as long as desired. In practice however it turns out difficult to keep track of a particle that comes close to the ends of the Couette region, either at the liquid-air interface on top or inside the parallel-disk region at the bottom. A tracer that goes into this region is lost, and we must add a new one in the Couette cell to start a new experiment. Another limitation is related to the number of tracers inside the fluid, as we already mentioned. It is about impossible to avoid that the tracer under tracking comes close to another fluorescent particle<sup>9</sup> in a several-hour experiment. In such cases, the system may keep focused on the initial tracer, jump to the second one, or merely loose both, with about equal probabilities.

### F.1.2.c: A neutrally buoyant tracer in a Newtonian fluid

Here we report a few tests of the automated SPT technique with a very simple system, namely a neutrally buoyant particle inside a Newtonian fluid, in Couette shear flow. The fluid is the 3-component Cargille liquid mixture (NJ, USA) described in chapter B. We could achieve only approximate neutral buoyancy, as we could check from tracers' sedimentation trajectories. We found that the tracers were slightly heavier than the fluid,  $\Delta\rho \approx 0.0023 \text{ g}\cdot\text{cm}^{-3}$ , where  $\Delta\rho$  is the solid-fluid density difference. The fluid was tested within a 3 to  $700 \text{ s}^{-1}$  shear rate range and found to have a constant shear viscosity  $\eta = 0.25$  Poise.

If the system were of infinite height, i.e. ideal ( $H \rightarrow \infty$ ), one would simply expect the particle to stay on a constant circle. In reality, the Couette cell has a finite height, and the flow is influenced by “end effects” [see Benjamin *et al.* 1978a]. It is therefore of interest to investigate the 3-d trajectory of an isolated tracer in such conditions, as we may expect slight departures from the ideal flow to be revealed. As we already mentioned, inertia forces may be

---

<sup>9</sup> This parasitic particle may well be one that we lost in the parallel-plate zone in a previous experiment.

another source of deviation from pure azimuthal flow. In the standard configuration,  $\Omega_{in} = \Omega$ ,  $\Omega_{out} = 0$ , azimuthal (otherwise called “pure Couette”) flows are observed whenever  $\omega_1$  is not too large [Taylor 1923, Andereck et al. 1985], the upper bound in velocity being set by the inequality  $Ta < Ta_c$ . Here  $Ta = \Omega_{in}^2 R_1 e^3 / \nu^2$  is the Taylor number,  $e$  is the gap width and  $\nu = \eta / \rho$  is the fluid kinematic viscosity, and  $Ta_c = 1712$  is the threshold value corresponding to the onset of the toroidal Couette-Taylor flow. In our conditions, namely  $\Omega \leq 5$  rad/s, we have  $Ta \leq 98$ . The above value of the Taylor number is very thus very far below the onset of the Taylor-Couette instability in the ideal cell ( $H \rightarrow \infty$ ).

Pure Couette flow in stationary regime is predicted to be purely azimuthal and is given by [Guyon, page 136, 2001]:

$$v_\theta(r, \omega_1, \omega_2) = A \cdot r + B/r \quad (\text{F.2a})$$

with

$$A = \frac{\Omega_{out} R_{out}^2 - \Omega_{in} R_{in}^2}{R_{out}^2 - R_{in}^2}, \quad B = \frac{(\Omega_{in} - \Omega_{out}) R_{out}^2 R_{in}^2}{R_{out}^2 - R_{in}^2} \quad (\text{F.2b})$$

If the system were ideal, and if the particles were both infinitely small and perfectly buoyant ( $\Delta\rho = 0$ ), each tracer should stay on a circle with an angular velocity given by Eq. F.2a,b. In reality the trajectories in the finite-size cell are not simply azimuthal. Each tracer is observed to migrate across the gap, from the inner to the outer cylinder, see Fig. F.5. The migration time  $\tau_{mig}$ , on the order of minutes, is found to approximately scale as the inverse of the average shear rate. From the data we estimate  $\tau_{mig} \approx 400/\omega$ , in seconds.

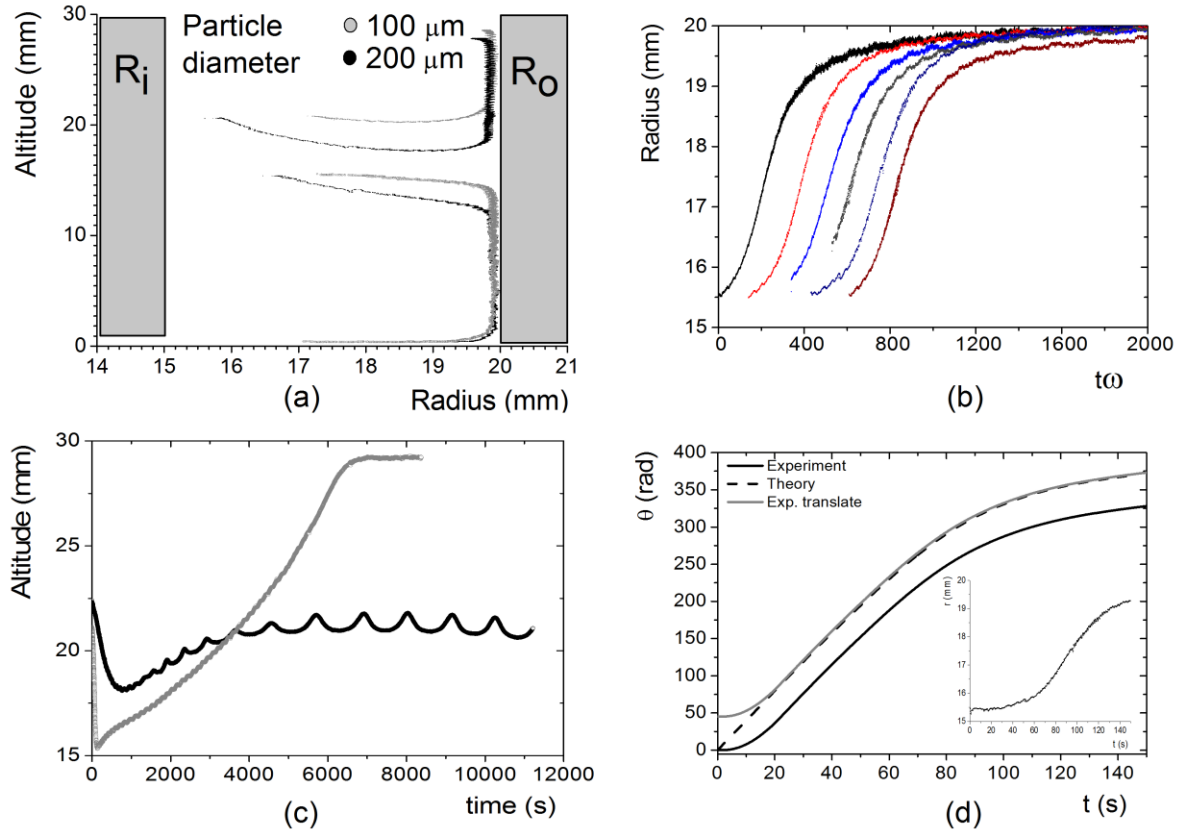


**Fig. F.5** (a) Non-azimuthal trajectories of single tracers in Cargille fluid mixture. Each tracer was initially injected near the inner cylinder wall, at about mid-height.  $\Omega = 4.56$  rad/s. (b) The radial motion (particle migration) is represented versus scaled time  $t \cdot \omega$ . The graphs are artificially separated along the  $t \cdot \omega$  axis to help readability. Tracer diameter ( $\mu\text{m}$ ) and  $\omega$  value (rad/s), from left to right: (100, 0.57), (100, 0.57), (100, 1.99), (100, 4.56), (100, 4.56), (200, 1.99). (c) Vertical motion. Periodic oscillations are caused by a misalignment of the outer cylinder (see text). Grey curve: (100, 4.56); black curve (100, 0.57). (d) Example of an azimuthal trajectory, for  $\Omega = 4.56$  rad/s. The black solid line is the experimentally recorded trajectory  $\theta_m(t)$ ; the dotted line is deduced from the radial particle position, supposing a standard  $v_\theta(r, \Omega, 0)$  profile, given by Eq. (2). The grey curve is the up-shifted copy of the black one, to show coincidence with the ideal trajectory. The inset shows the corresponding  $r(t)$  trajectory.

The radial migration ends close to the outer wall and is taken over by a vertical motion, on a much slower time scale, as can be seen from the graphs in Fig. F.5.c. Whether a given particle moves upwards or downwards depends on the initial position. The data (see Fig. F.5.a) suggest a partitioning of the flow volume into a couple of re-circulation cells of similar extensions and opposite circulations. In the bottom cell, a reverse radial migration is observed along the bottom end of the apparatus, towards the rotation axis. However no closed

$(r, z)$  trajectories of tracers could be recorded: in general particles getting close to the parallel-disk zone at the bottom of the system were lost by the tracker. On the top side the tracers were observed to stay for a long time (hours) at the same position: close to the outer cylinder and at 2-3 mm from air-fluid interface.

The tracer radial migration may be exploited to gain information on the azimuthal flow profile at about mid-height of the Couette cell. Let us define:

$$\theta^{(0)}(t) = \int_{t_0}^t \frac{v_{\theta}^{(0)}[r(t')]}{r(t')} dt', \quad (\text{F.3})$$

with  $v_{\theta}^{(0)}(r) = v_{\theta}(r, \Omega_{in} = \Omega, \Omega_{out} = 0)$ . The initial time  $t_0$  is defined as the time when application of a finite shear starts. In usual conditions, shear is applied progressively along a linear ramp from zero up the prescribed value of  $\omega$ . The ramp duration is about 10s to reach 1 rad/s.

In Eq. F.3 the integrand is simply the (ideal) angular velocity of the tracer, in a Couette cell whose outer cylinder is immobile. Note that this statement only holds under the assumption that the particle at each time in the course of its migration across the gap follows the ideal azimuthal flow. If the latter assumption is correct, then the recorded azimuthal trajectory  $\theta_m(t)$ , given by Eq. F.2, and that given by Eq. F.3 should be the same. As can be seen from the example displayed in Fig.5.d, both trajectories indeed coincide, within a translation parallel to the ordinate axis. The shift in ordinate simply corresponds to the progressive application of shear, which is signaled by the concave part of  $\theta_m(t)$  near the time origin. This part is absent of the ideal curve, since we suppose that the average shear  $= \Omega$  for  $t \geq 0^+$  when calculating  $\theta^{(0)}(t)$ .

In some of the records, a slight systematic mismatch between both curves is evident and mostly shows up as a difference in slopes at large times. The long time limit corresponds to the tracer coming about in contact to the outer wall. The mismatch may simply be caused by a slight error in determining the positions of the boundaries in the video image from the side camera, resulting in a systematic error in  $r$  and  $v_{\theta}^{(0)}(r)$ . Errors of the order of 50  $\mu\text{m}$  are inevitable, due to the poor contrast between fluid and cylinder walls in the video images. Another source of mismatch is fundamental, and may be viewed as a tracer finite-size effect. Indeed, at large times, the particle comes nearly in contact with the wall, i.e.  $r \cong R_{out} - a$ . Due to very large viscous forces between the particle and the wall, the particle velocity is less than the corresponding fluid velocity in absence of the particle, i.e.  $v_{\theta}^{(0)}(R_{out} - a)$ . The difference in velocities, sometimes called “slip” [Feng *et al.* 1994], thus contributes as a

difference between the slopes at large time. Note that  $\dot{\theta}_m(\infty) - \dot{\theta}^{(0)}(\infty) < 0$  in this context. A positive difference can only be caused by an instrumental error.

A practical information is of interest concerning the short scale details of the recorded trajectories, and their sensitivity to small misalignments of cylinders. Fluctuations looking like a noise in particle position are visible along the vertical parts of the trajectories (Fig. F.5.a). These details can be reliably attributed to the roughness of the cylinder walls, which is on the order of 0.1 mm (as we mentioned, to limit wall-slip in experiments with granular materials). In a few examples, the noise is overwhelmed by well visible periodic excursions (as can be seen in Fig. F.5.c). Such modulations are hardly perceptible when the alignment is optimal, i.e. within the  $\pm 50 \mu\text{m}$  tolerance. However some of the experiments were carried out in “non optimal” conditions with a misaligned outer cylinder. As a result, the position of the outer wall in the image was oscillating at circular frequency  $\Omega_{off}$ , causing a modulation in the tracer radial position, also at  $\Omega_{off}$  (Fig. F.5.c). Due to fluid volume conservation, the vertical position is also affected. Note that because the gap is much inferior to the cell height, the modulation in  $z(t)$  is definitely larger than that in  $r(t)$ . Therefore misalignment defects are most sensitively revealed by details in vertical flows.

A question naturally arises as to whether such defects have a macroscopic influence on the tracer trajectory and then, on the overall flow itself. While we are not able to answer the question in general, a rather reassuring outcome of these experiments is that, concerning the azimuthal velocity profile, no such influence has been detected. We base this statement on the comparison between  $\theta^{(0)}(t)$  and  $\theta_m(t)$ , which gave the same results independently of whether alignment was optimal or not.

Summarizing: the goal of this study was to check that the SPT apparatus was able to track the tracer in the simple situation of a Newtonian fluid, whose density was matched to that of the particle. We indeed could follow the particle with about no limitation in time, and we checked that the recorded trajectories were in line with the standard azimuthal flow profile  $v_\theta(r)$  for pure Couette flow (Eq. F.2). Gathering the information about  $v_\theta(r)$  through the gap was made possible by the slow migration of the particle between both cylinders. The cause of this migration is unclear to us, and beyond the scope of this study. We nevertheless include a short discussion on this point in Appendix F-B.

## F.2: (r, z) trajectories of a “host like” tracer

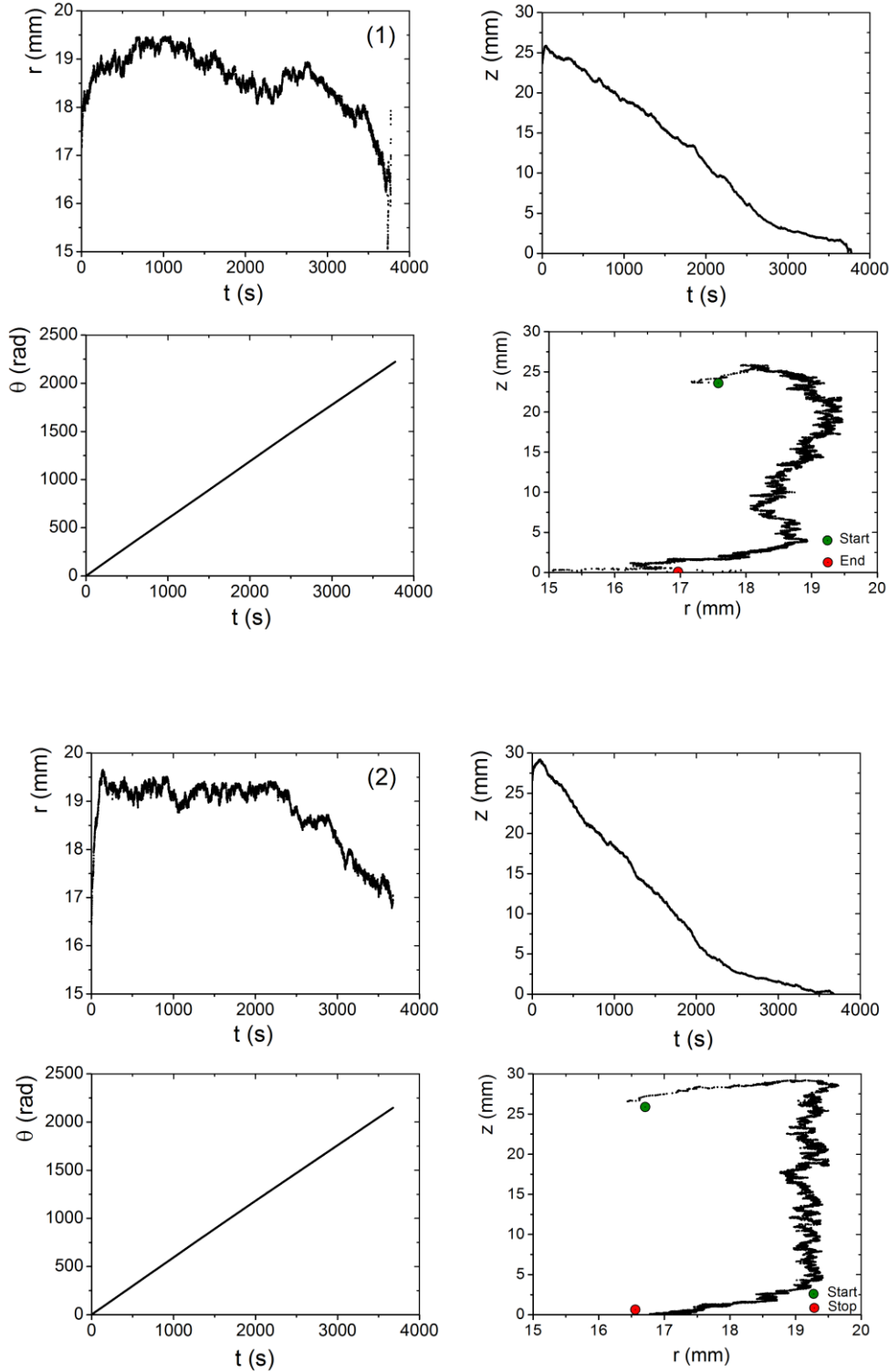
Here we consider the case of a “host-like tracer”, i.e. a tracer of same size (180  $\mu\text{m}$ ) as the other particles constituting the –approximately- monodisperse granular system. Thus the motion of the tracer is supposed to represent the motion of any of the non dyed particles constituting the granular system. The study is limited to a unique average shear ( $\Omega = 0.57$  rad/s) for different  $\Omega_{in,out}$  combinations.

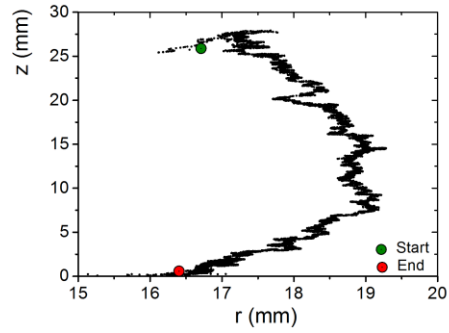
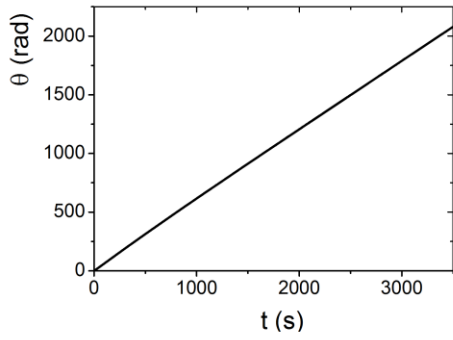
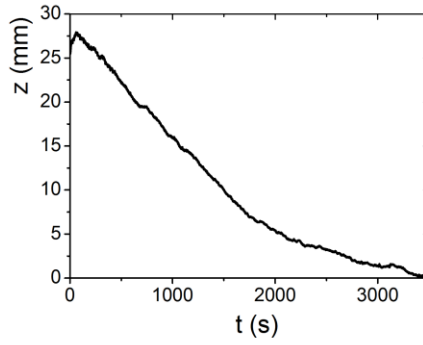
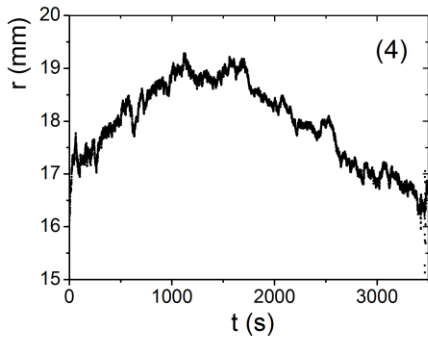
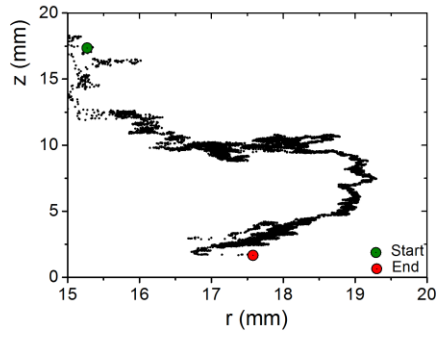
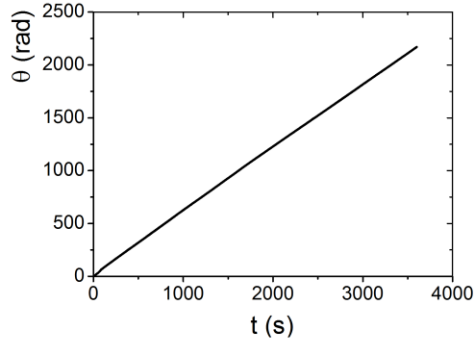
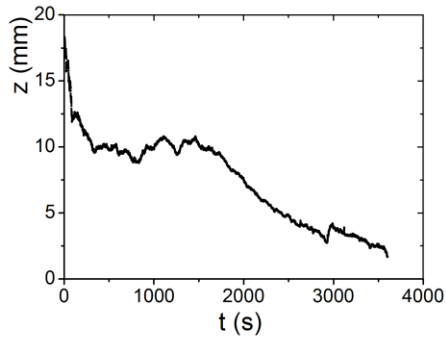
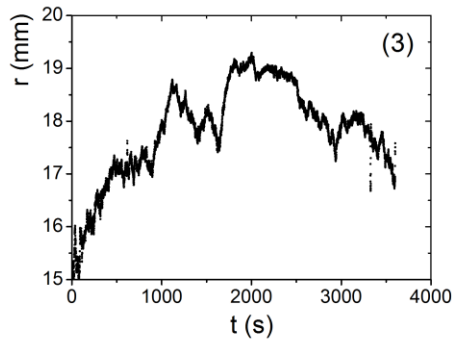
We tried to define operating conditions such that the trajectories pertain to the stationary regime. The procedure is as follows: the shear cell initially is at rest ( $\Omega=0$  rad/s). If a tracking experiment has been carried out before, we most often find the tracer somewhere close to the bottom corner of the inner cylinder. We pick it up there by means of the little spatula; and we bring it up to some desired initial position inside the granular sediment. Then we start shear, at the prescribed value of  $\Omega$  ( $= 0.57$  rad/s, here), and let it run for about 30 mn. Then we shortly stop the shear cell and start the automated tracking. The interruption of the shear does not last more than a few seconds. According to what we learnt about azimuthal velocity and concentration profiles (chapters C, D), half an hour is well enough to reach the stationary regime. We believe that the few-second stop is short enough to avoid any significant relaxation of the system, and, consequently, that the recorded tracer trajectory is completely within stationary regime.

### F.2.1: in the density – matched system (active mode)

We start with the  $\Delta\rho=0$  system (PMMA + Cargille fluid mixture). The figures below (Figs F.6.1 to 6.5) show a few trajectories, obtained in active tracking mode. In each figure, the panels in first row show the particle cylindrical coordinates ( $r, z, \theta$ ) as functions of time ( $t$ ). The meridian motion is shown in the bottom row, at left. The data of Fig. F.6 have been recorded with different initial positions of the tracer, near the top of the suspension and at mid gap (Figs F.6.1, 6.2, 6.4), or close to the inner cylinder (Fig. F.6.3 and 6.5). All figures show a common trend: the tracer first drifts towards the outer cylinder, then dives to the bottom of the shear cell, and drifts back towards the cell axis. Usually, the tracer is lost by the automated tracker when it gets close to the bottom corner of the inner cylinder. The experiment thus cannot evidence an upward motion along the inner cylinder, starting from the bottom, though

the recorded paths strongly suggest that it should be so. The trajectories bear some similarity with those in the pure Cargille fluid (paragraph F.1.4), at least in the bottom half of the shear cell, where the trends compare well. However, there is no clear analogy in the upper half. Note that some of the data (Fig. F.6.3) reveals qualitative differences between top and bottom.





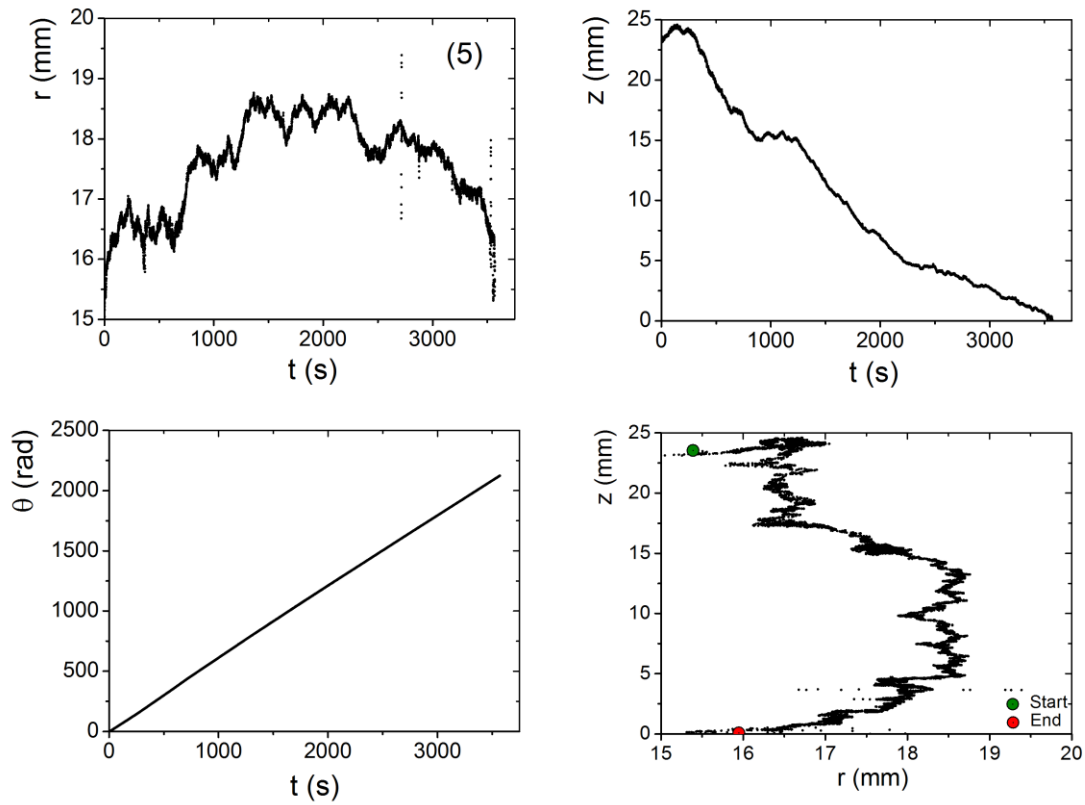


**Fig. F.6** Trajectories of a host-like tracer in the density-matched suspension.  $\Omega = 0.57$  rad/s. Active tracking

## F.2.2: in a non density – matched system

Here we deal with the  $\Delta\rho > 0$  system (PMMA + C16S150).

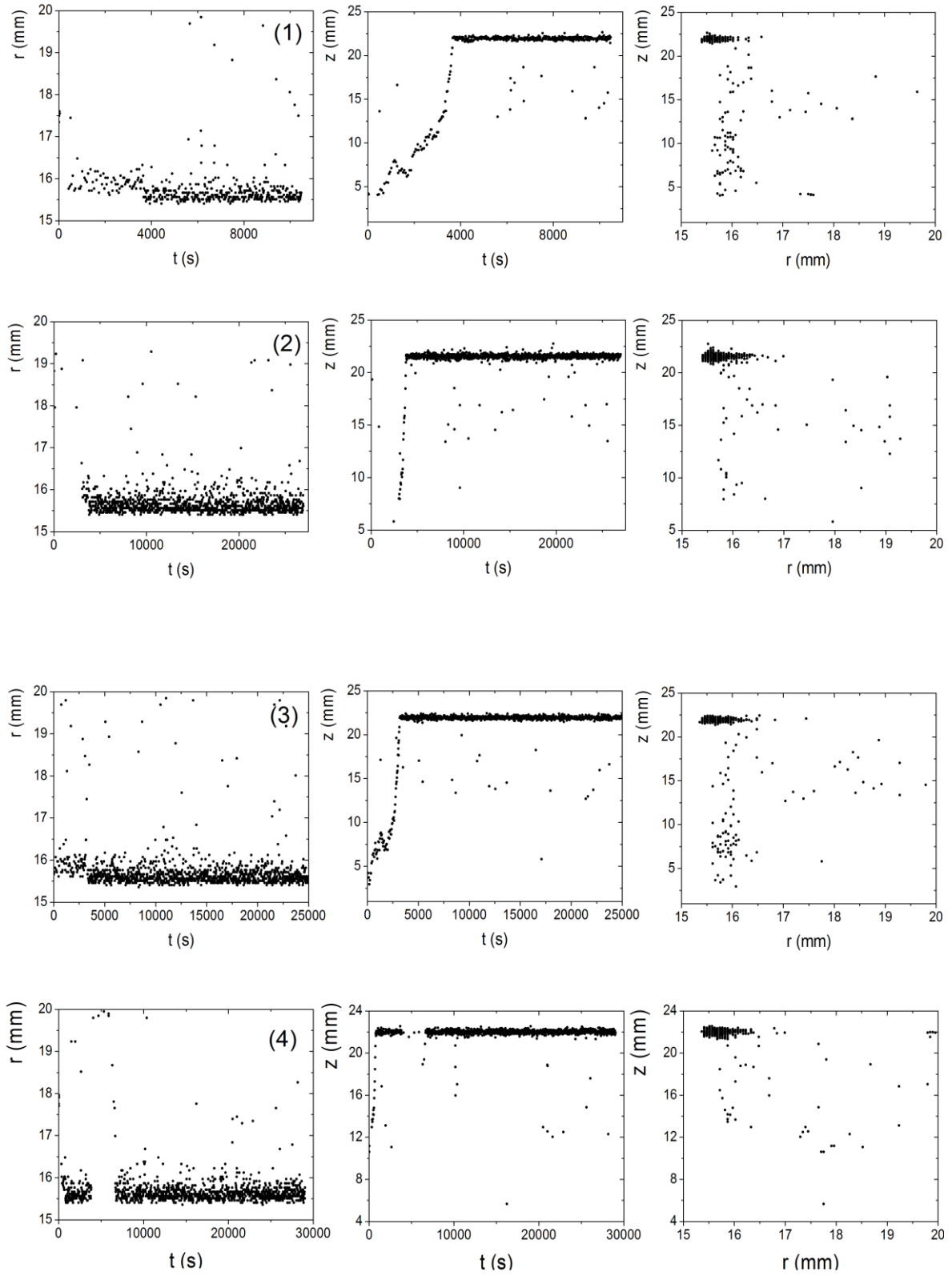
### F.2.2.1: Passive mode

The passive mode yields the  $(r, z)$  coordinates of the tracer each time it comes across the laser sheet, see Fig. F.1. Consequently the particle has made a complete revolution, or “transit” in the terminology of [Lenoble thesis 2005], around the Couette axis between 2 successive points in the  $\{r_i, z_i\}$  data file. Though the time resolution is poor, the experiment is of interest at least to reveal some trends of the secondary flows. We may operate the setup

with either the inner or outer cylinder in rotation, or in contra-rotation ( $\Omega_{off} \neq 0$ ), and thus check whether the assumption of rotation invariance still holds for non azimuthal motion. Results displayed below in Figs. F.7.1 to F.7.4 have been obtained with the non density matched granular suspension (C16-S150 immersion fluid,  $2a \cong 180 \mu\text{m}$ ,  $\Delta\rho > 0$ ), with the inner cylinder rotating, at the same velocity as above ( $\Omega = 0.57 \text{ rad/s}$ ). Trends are not as clear as in the density-matched suspension. We note that the tracer positions tend to accumulate on top of the suspension, close to the inner cylinder.

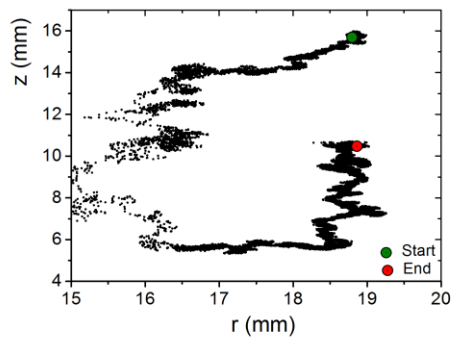
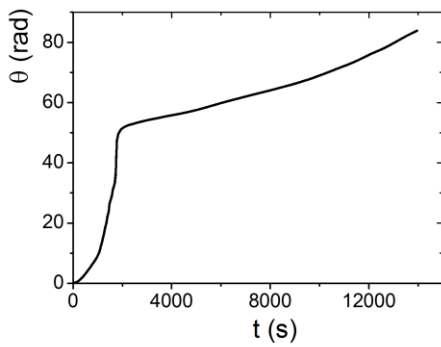
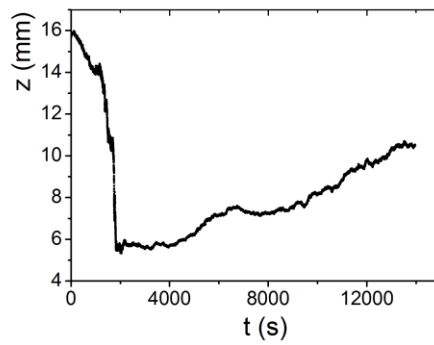
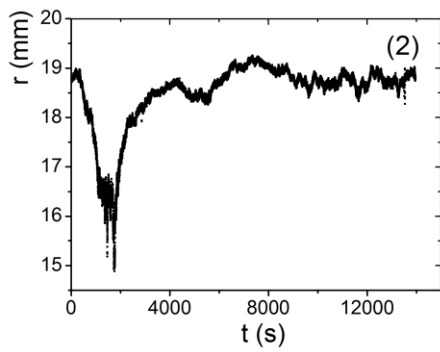
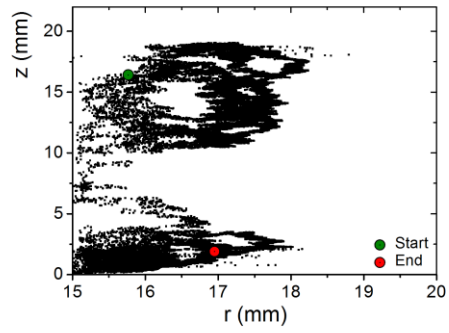
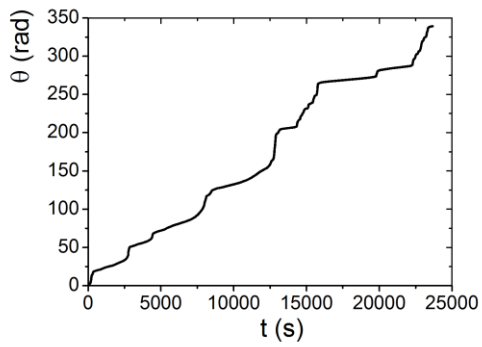
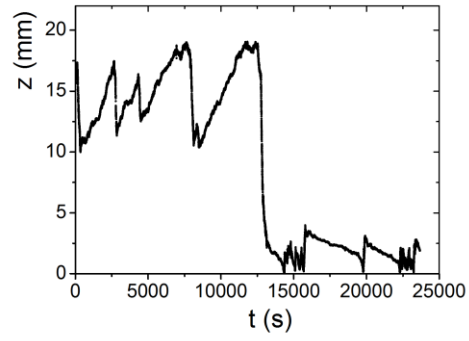
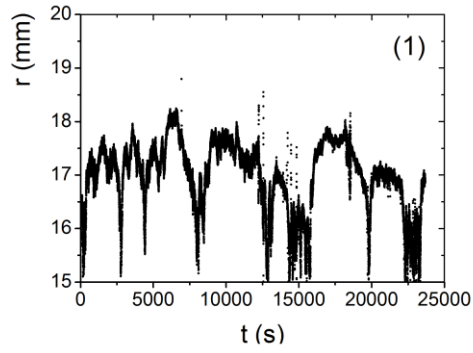
We made a few more experiments, with the outer cylinder rotating, i.e.  $\Omega_{in} = 0, \Omega_{out} = -\Omega$ . Trajectories showed the same trends as above. Similarly to what we observed about azimuthal velocity and concentration profiles, shifting the rotation from the inner to the outer cylinder does not markedly change the meridian motion of the tracer. This statement however only holds “statistically”, as far as we can tell.

We also used the passive mode technique to address a technical question about active SPT. The active mode inevitably makes the cylinders of the Couette cell oscillate, because of to the nature of the servo system. We wanted to detect possible impacts on particle trajectories due to this particularity. We operated the shear cell in passive mode, say with the inner cylinder rotating, and applied a small sinusoidal voltage  $V_{ac}$  on the motor of the outer cylinder. The amplitude of  $V_{ac}$  was tuned so as to reproduce oscillations in  $\theta$  similar to those in Fig. F.4.c ( $V_{ac} \approx 0.02 \text{ Volt}$ , while  $V_{DC} = 1.00 \text{ Volt}$ , corresponding to  $0.57 \text{ rad/s}$ ). In this case too, we found that operating the shear cell in such conditions induced no visible trend in the tracer meridian motion.



**Fig. F.7** Trajectories of a host-like tracer in the non density-matched suspension.  $\omega = 0.57$  rad/s. Passive mode. Inner cylinder rotating ( $\omega_1 = \Omega, \omega_2 = 0$ ).

### F.2.2.2: Active mode



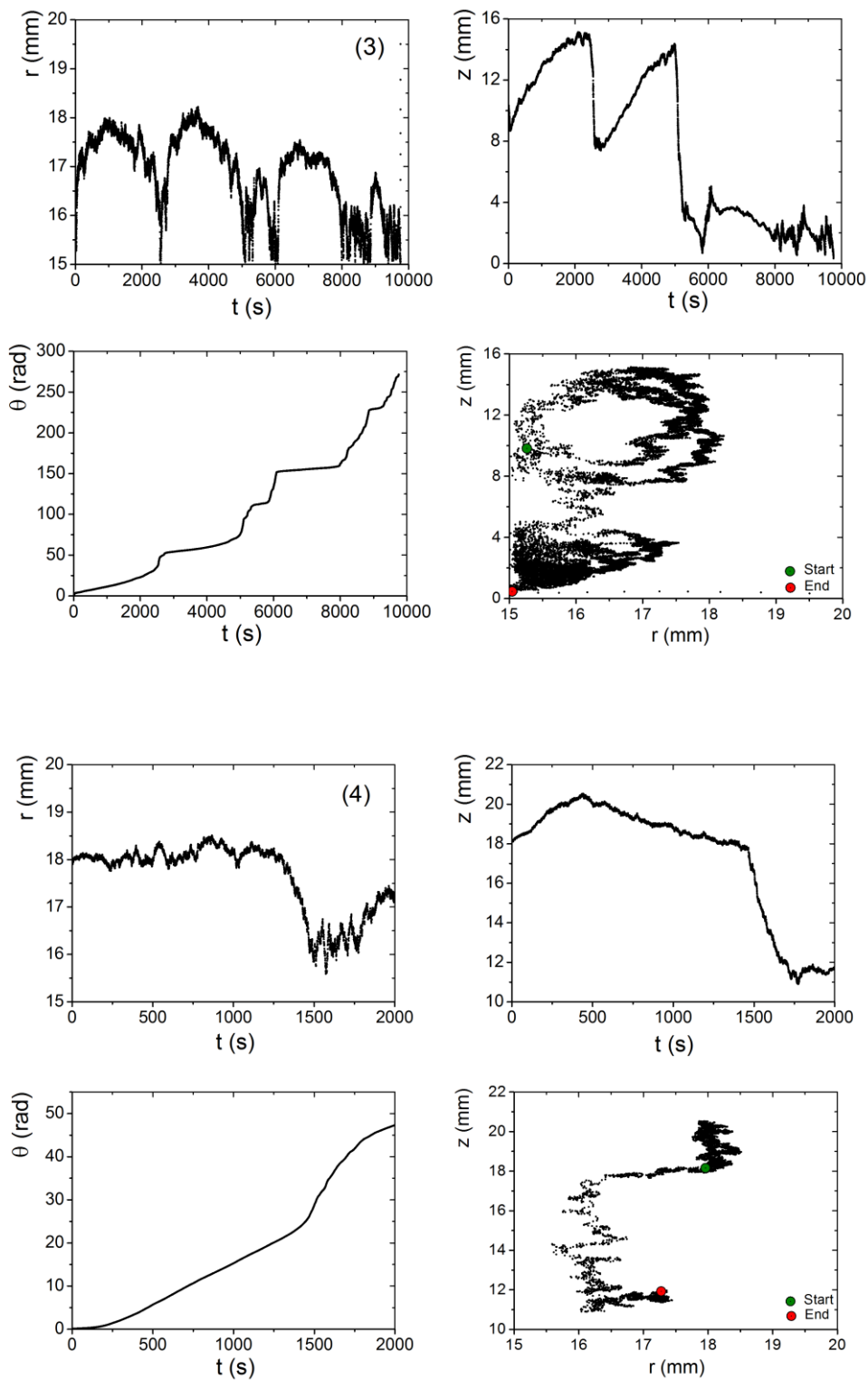


**Fig. F.8** Trajectories of a host-like tracer in the non density-matched suspension.  $\Omega = 0.57$  rad/s. Active mode.

Here we deal with single particle tracking in active mode, still at  $\Omega = 0.57$  rad/s. 4 different realisations are shown in Figs. F.8. A three-dimensional representation of a trajectory is displayed in Fig. F.9.

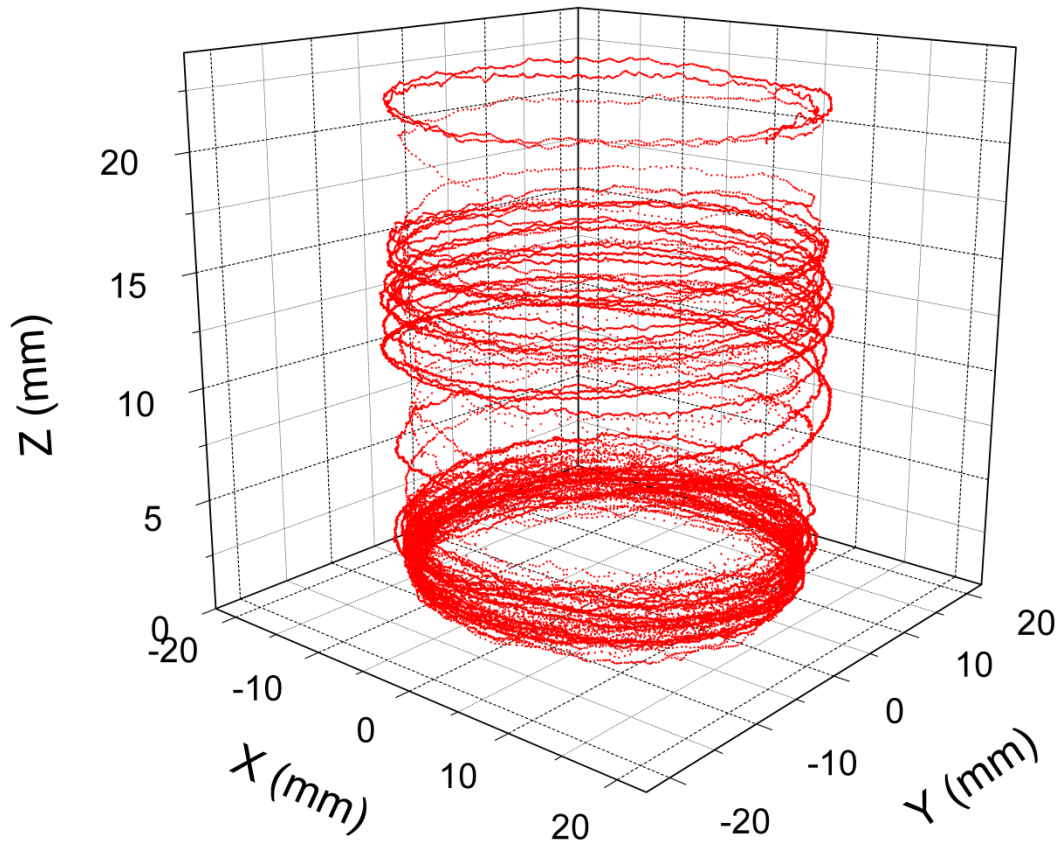


**Fig. F.9** Example of 3D trajectory of a host-like tracer in the non density-matched suspension. Recording time: 28 hours. Average volume fraction: 58% at rest in the sediment.

**Azimuthal motion:** Gathering data from different tracers allows us to build azimuthal flow profiles spanning the whole gap, as shown in Fig. F.10. The procedure is similar to that used in paragraph F.1.2.c. Essentially we select sequences of points of the trajectory inside a domain  $[r, r + \delta r] \times [z, z + \delta z]$  and calculate  $\theta$ -velocities inside each domain. We obtain instantaneous velocities, as in Fig. F.10.b (open circles). The points in Fig. F.10.a (solid triangles) are time averages inside each sequence. Note that the profile is only poorly sampled near the inner cylinder, where the shear rate is highest, because of the vertical and horizontal motion of tracers, which limits the residence time inside a given domain.

The angular velocity profiles are found approximately exponential inside the shear zone, in agreement with recent PIV measurements by S. Wiederseiner [[Wiederseiner thesis](#)]

2010], and with ours (chapter C). The data reveal that tracers are not strictly immobile outside of the shear zone, in agreement with trajectography measurements. The trajectories are indicative of an extremely slow plug flow, confirming that particles inside the so-called “dead zone” in fact are slowly moving.

In principle, the azimuthal velocity profiles obtained by SPT should be the same as those measured by trajectography, within statistical scatter. Indeed a good match is found, as illustrated by the example in Fig. F.10.b.

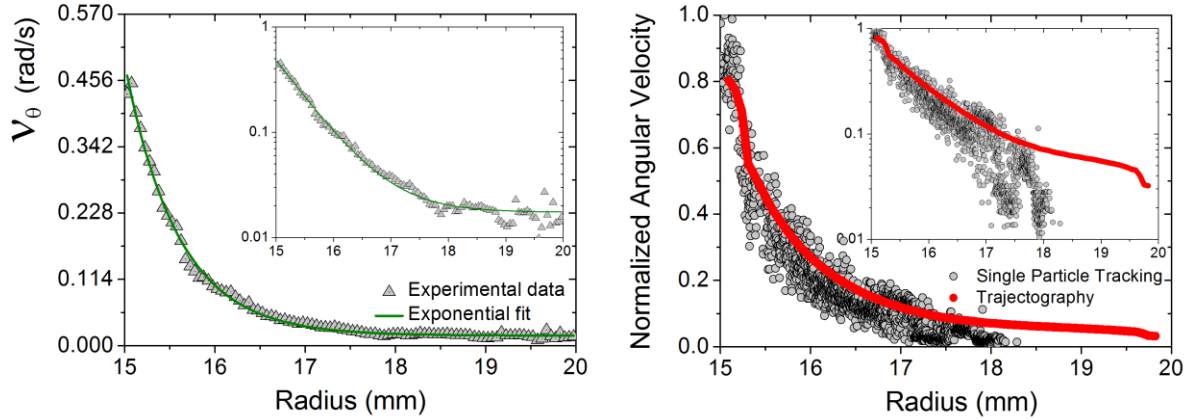


**Fig. F.10** Examples of azimuthal velocity profiles built from tracer trajectories. (a) Averaged velocity values (triangles) and fitted exponential profile (solid line), for  $11\text{mm} \leq z \leq 14\text{mm}$ . The inset is a semi-log plot of the experimental velocity profile. (b) Instantaneous velocity values (open circles), normalized by  $\omega$ . The red solid line is the reduced angular velocity measured by trajectography (chapter C) at  $z = 15$  mm.

**Meridian motion:** Our records reveal that the tracer 3d trajectory does not simply reduce to the superposition of a regular circular motion around the Couette symmetry axis and of a Brownian-like random noise. Complex secondary convection patterns are clearly evidenced in  $(r, z)$  trajectories, see Fig. F.8. These patterns do not reduce to simple features, as we could already notice from the passive mode data (Fig. F.7). Nevertheless the trajectories do not seem completely random: scanning each trajectory in time reveals that it is composed of successive loops, or fractions of loops, spanning the local width of the shear zone. In a few examples (not all!), loops in the upper half of the shear cell are counter clockwise (say +) and change to clockwise (-)<sup>10</sup> in the bottom part, when the particle comes near the bottom corner of the inner cylinder. This kind of behaviour is well visible in Fig. F.8. Another general

<sup>10</sup> Counter-clockwise is in reference to the representation in Figs F.6, 7, 8, with the azimuthal flow velocity pointing forwards.

tendency is that the tracer drifts down to the bottom zone, similarly to what we observed in the density-matched suspension. But, rather unexpectedly, the available examples in active mode do not reproduce the tendency of the tracer to go on top of the suspension, observed in passive mode

### F.3: Size effects (non density – matched system)

We come to the motions of particles whose size is different from those of the host particles, hence the name “intruder”. We already made a few attempts at observing differences between *azimuthal* motions of small particles (100  $\mu\text{m}$  in diameter), as we reported in chapter C. The trajectography measurements did not evidence clear differences in  $v_\theta$  profiles, but there remains the possibility that meridian motions be very sensitive to the particle size. Below we show a few particle meridian trajectories, obtained with large and small intruders, in passive and active modes.

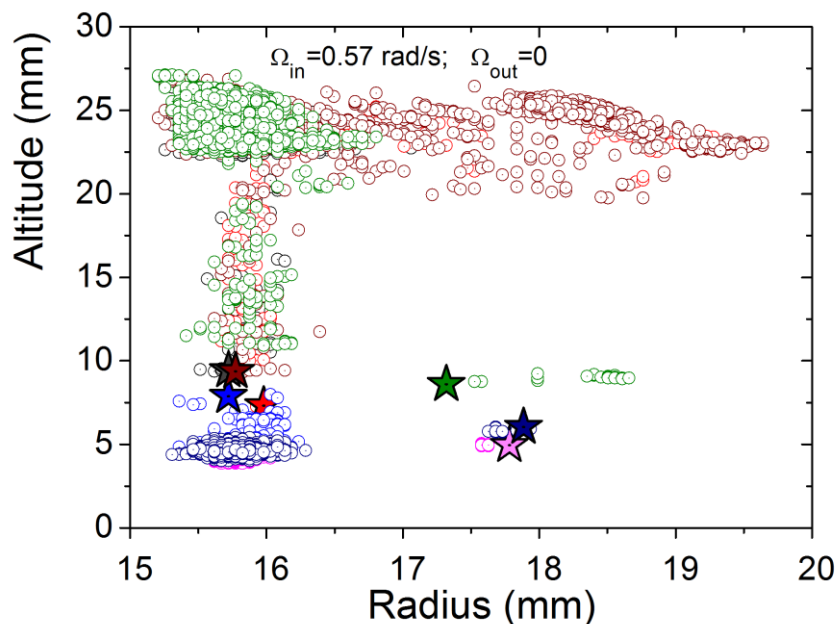


**Fig.F.11**  
*Meridian motions of a 600 $\mu\text{m}$  tracer, recorded in passive SPT mode. Data with different colours come from different experiments. Stars represents initial position in each experiment.*

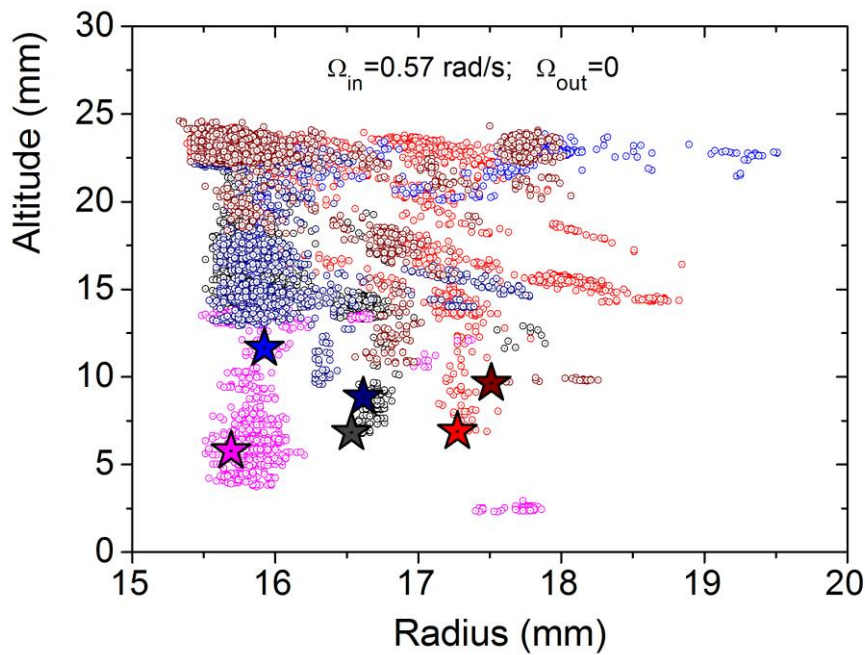


**Fig.F.12**  
*Meridian motions of a 100µm tracer, recorded in passive SPT mode. Data with different colours come from different experiments. Stars represents initial position in each experiment.*

Fig. F.13 below shows a few examples of trajectories obtained by active SPT with both small ( $2a = 100 \mu\text{m}$ ) and large ( $600 \mu\text{m}$ ) intruders, together with those of a “host-like” tracer for comparison. Similarly to the host-like tracers, intruders show definite meridian motions. However, a clear dependence on tracer size is evidenced, as the large tracer was observed to drift down to the bottom in about 1500-2000 s while it took about 5000-7000 s for the small one. The trajectories also differed in numbers of positive loops: zero with the  $600 \mu\text{m}$  tracer, about 6 with the  $200 \mu\text{m}$  tracer, all of them located at the bottom corner.

The active and passive tracking modes show similar trends, such as the propensity of the large intruder to migrate towards the inner cylinder. In some of the records, the large tracer ended on top of the suspension (Fig. F.11), but this was only observed in passive tracking. In active tracking records, the particles always ended close to the bottom corner (Fig. F.13c). Small intruders, conversely to large ones, seem to explore the sheared zone, similarly to host-like tracers. In other words, the effect of shear is to localise large intruders close to the bottom, top and inner cylinder boundaries. Conversely, no clear localisation is observed with small intruders. Note that the down drift of each tracer on the time scale of the experiments is an irreversible event. It is not known whether the particle escapes out of the bottom zone and comes back into the upper part on much longer time scales.

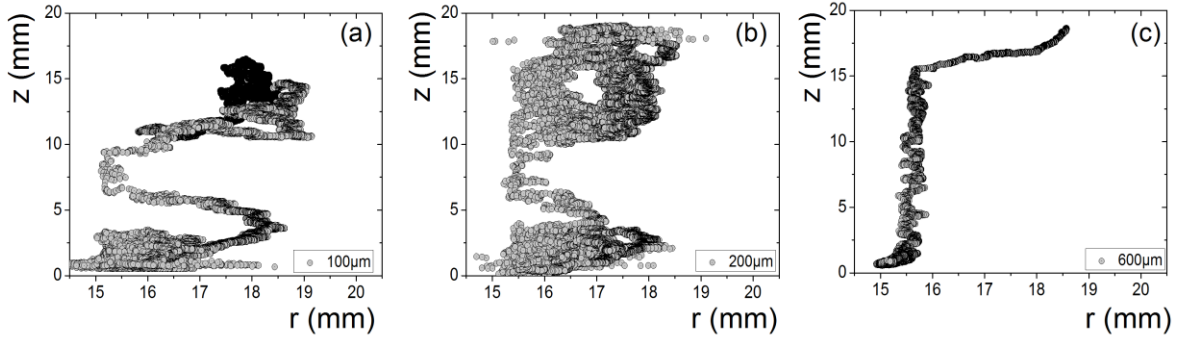


**Fig. F.13**  $r$ - $z$  trajectories obtained with tracers of different sizes, at  $\Omega=0.57$  rad/s. In this series, the tracers were initially loaded in the active zone, near the upper boundary of the system.

## F.4: Discussion

### F.4.1: Shear – induced particles diffusion

As evidenced in Fig. F.9, each component  $(\theta, r, z)$  features characteristic short scale fluctuations looking like noise in particle position. The fact that particle motions in concentrated suspensions include a part of short-scale randomness is well known. The fluctuations have been modelled as similar to successive steps of a random walk, resulting in diffusion of the particle. The source of diffusion is not thermal, as in ordinary Brownian motion, but due to the flow itself through collisions between particles; hence the name “shear-induced diffusion” [Breedveld *et al.* 1998, Tetlow *et al.* 1998, Hajra *et al.* 2004]. In principle, the trajectories of two ideal (smooth) spheres colliding in viscous flow are symmetrical and reversible. However the surfaces of real particles are never ideally smooth. Roughness breaks the symmetry of the interaction [Wilson and Davis 2000, Cunha and Hinch 1996], resulting in a lateral shift ( $\Delta$ ) of the after-collision particle trajectories.  $\Delta$  is null for ideally smooth spheres, and  $>0$  when roughness is present.  $\Delta$  has been measured [Arp and Mason 1977] and calculated [Cunha and Hinch 1996] in the case of particles of same size  $a$  and same amount of roughness  $\varepsilon a$ . In a sheared suspension, a given particle undergoes many such collisions and each shift may be viewed as a step of a random walk. A diffusion results,

quantified by a diffusion coefficient  $D$ , which depends on  $a, \varepsilon$ , the shear rate  $\dot{\gamma}$  and the concentration  $\phi$  [Cunha and Hinch 1996]. Simple scaling suggests:

$$D \propto a^2 \phi^2 \dot{\gamma} \quad (\text{F.4})$$

This relation was successfully tested by Leighton and Acrivos [Leighton and Acrivos 1987b], who exploited fluctuations of the transit time of a tracer (the time between 2 successive crossings through a given meridian plane, as in passive mode experiments) in a Couette device, for suspensions up to 40% in concentration. In principle, our trajectories offer much more information, since we constantly follow the particle. Transit times are just a very small subset of the data. It was thus tempting to exploit the data, to test the above relation at higher concentrations and for very different values of the shear rate. Unfortunately, the counter part of having a variety of  $\phi$  and  $\dot{\gamma}$  values inside the same system is that the tracer never remains in approximately constant  $\phi$  and  $\dot{\gamma}$  for a long time. Our analysis indeed confirmed that we do not have enough statistics to probe eq. (F.4) “locally”. In theory, one might imagine testing the equation in the general conditions of variable  $\phi$  and  $\dot{\gamma}$ , but this would necessitate a dedicated theory, including secondary motions. This condition is far from being satisfied at the current stage.

We end this paragraph with a comment about what is sometimes called “ergodicity” of the trajectories. In principle, if the tracer is exactly equivalent to the host-particles, and if tracking is operated as long as we want, diffusion should make the tracer explore all possible positions inside the suspension, with a probability proportional to the concentration in stationary regime. Thus the cloud of tracer’s positions in  $(r, z)$  plane should merely reproduce the stationary concentration field. This is not so in experimental records, see e.g. Fig. F.13.b, meaning that the recorded trajectories are not ergodic. The fact that the trajectories do not explore the dead zone is obviously not surprising, since particles only have tiny motions in this zone. Consequently, diffusive motion is extremely slow and about inexistent on the scale of experimental record time. In practical conditions, the tracer can only visit the active zone. Qualitatively, active mode trajectories such as in Fig. F.13.b correctly reproduce the hierarchy of concentrations, which are definitely larger at bottom than on top of the shear zone. However, differences are much exaggerated, due to the fact that tracers seemingly get “trapped” when they come close to the corner of the inner cylinder. The reason of this behaviour, and why it was not present in the passive mode records, is not known. We may suspect that surface states of the dyed particles used as tracers make them not exactly equivalent to host particles, and, consequently, is a source of segregation. Indeed segregation is sensitive not only to size, but also to surface roughness, and state, in general [Plantard *et al.*

2006]. However this argument cannot explain the differences between active and passive tracking records.

### F.4.2: Loops

Some of the recorded trajectories show that the tracer sometimes makes loops, which are well discernible in spite of the noise due to diffusion. Such features may indicate that the flow is of toroidal type, a bit like that of a Newtonian fluid beyond the Taylor instability of Couette flow [Andreck *et al.* 1985, Conway *et al.* 2004]. The loops may look either clockwise (- sign, according to the trigonometric convention) or counter-clockwise (+ sign). They are located at different places along the inner cylinder boundary and their signs vary among experiments.

Here we focus on records with host-like tracers, since their trajectories are supposed to evidence secondary flows of the suspension. Loops in the density-matched suspension ( $\Delta\rho = 0$ ) are distinctly negative, very similarly to trajectories of the tracer in the pure fluid. Trajectories in the non density-matched system ( $\Delta\rho > 0$ ) are very complex due to considerable fluctuations. In active mode, they nevertheless feature well recognizable loops, of both signs: large positive loops in the high and medium parts of the shear zone, and small negative ones near the bottom corner of the inner cylinder. In average, the data reveal a kind of 2-cell structure. The existence of the positive circulation at mid height had already been reported by M. Lenoble [Lenoble thesis 2005] at  $\Omega = 0.3$  and 1 rad/sec, based on the early version of the SPT setup. This version was controlled by hand and only provided short parts of the trajectories at each run. Our data now provide solid proofs for this feature. Lenoble also mentioned a negative loop near the top of the sample, which we cannot confirm here, though tendencies in this direction may be found in some of the records. Lenoble also did not notice the negative circulation at bottom, probably because of technical limitations.

The loops identified in active mode, unfortunately, are not recognized in passive mode records. We checked that the loops were still visible when reducing the data of active mode trajectories to the subset of points captured in passive mode ( $\theta = \pi, 3\pi, 5\pi \dots$ ). Consequently, the problem does not simply stems from the fact that sampling is poor in passive mode. We currently do not know what causes the differences between both types of records.

The secondary flows evidenced from the trajectories are very slow compared to the primary azimuthal flow. Because of the large fluctuations and of the multi-scale structure of

the trajectories, the ratio of corresponding velocities,  $v^{(2)}/v_\theta$ , spans a large interval of values, say between  $10^{-4}$  and  $10^{-1}$ . Large values correspond to very rapid steps of the tracer, and lowest ones to near stagnant zones. Lenoble [Lenoble thesis 2005] discussed the potential influence of inertia forces and concluded that these were too weak to explain the observed recirculations, given the small angular velocities in our experiments (the corresponding Taylor number, based on the suspension effective viscosity, is estimated  $\approx 0.01$  in our conditions). Conway *et al.* invoked the role of centrifugal forces in their experiments, but these were operated at much larger velocities (130 cm/s along the rotor!) [Conway *et al.* 2004].

Interestingly, Ramachandran and Leighton (hereafter referred to as RL) [Ramachandran and Leighton 2008] recently addressed the problem of the stability of the laminar flow of a suspension inside a tube. They predicted that the rectilinear Poiseuille flow might not be stable whenever normal forces were anisotropic, as is the case with non colloidal suspensions. Following their reasoning, the flow inside a classical cylindrical tube, of circular cross-section, should be rectilinear, but recirculation cells should be observed inside tubes of non circular cross-section. RL illustrate their predictions with elliptic, square and rectangular tubes. The computed characteristic velocities of secondary flows are very weak, but should be discernible from shear-induced diffusion provided that the cross-section be large enough compared to the particle size. In other words, loops should be recognizable in spite of the diffusion noise. As far as we know, the predictions of RL theory have not been experimentally verified yet. It is very tempting to make a link between this theory and the loops that we observed in Couette flow. Indeed, there are some similarities between the Poiseuille flow inside a rectangular tube and the azimuthal flow inside a finite-size Couette shear cell. However the comparison is purely qualitative at this stage. Going further would imply first computing the primary flow  $v_\theta(r, z)$  inside the *finite-size* Couette cell, meaning that we must take into account the bottom and top boundaries, and, second, to calculate the perturbation to this flow caused by anisotropic normal forces. This rather formidable task is much beyond the scope of our contribution.

### F.4.3: Size effect

In average, trajectories of small tracers (100  $\mu\text{m}$ ) look similar to those of the host-particles (Figs. F.12, 13). Gathering this observation with the data from trajectography (chapter C), we conclude that no definite differential flow is detected between small particles and the rest of the suspension, either in primary or secondary components.

Large intruders behave quite differently, see Figs. F.12 and F.13.c. Here data from active and passive mode records converge and show that the large intruder does not explore the shear zone, except on the very top, but is confined close to the inner cylinder wall. There the tracer drifts down to the bottom corner, along an almost rectilinear path.

The observed radial confinement of the big intruder is well in line with experiments carried out by Lenoble, whose aim was to study segregation between large and small particles in a the same kind of Couette cell. Fig. F.14, an excerpt from Lenoble's work [[Lenoble thesis 2005](#)], shows a segregation pattern induced by shear ( $\Omega = 0.31 \text{ rad/s}$ ) in a mixture composed of a binary mixture of PMMA spherical particles in the C16S150 fluid, containing large (180  $\mu\text{m}$ ) and small (20  $\mu\text{m}$ ) particles. Corresponding mass fractions were  $\Phi_{small} = 16\%$  and  $\Phi_{large} = 84\%$ , respectively. Consequently the mixture contained a few large particles among many small ones (about 1 big particle per 5000 small ones, in average). The figure clearly shows the intense segregation, with the large particles accumulating along the inner cylinder. Based on the data from SPT, we imagine that big particles migrated towards the rotor, drifted down to the bottom as far as they could and piled up along the cylinder wall.

In general, it seems that large particles tend to accumulate in regions where the concentration in small particles is lowest. In the case of interest, large particles are only a few and then may be viewed as a perturbation of the distribution of small particles. In this view, the regions of low  $\Phi_{small}$  are those obtained with monodisperse particles (chapter D), since the absolute value of particle size is not important in determining the shape of the concentration field (chapter E). We indeed observed that  $\Phi$  was lowest near the inner cylinder and on top of the suspension.

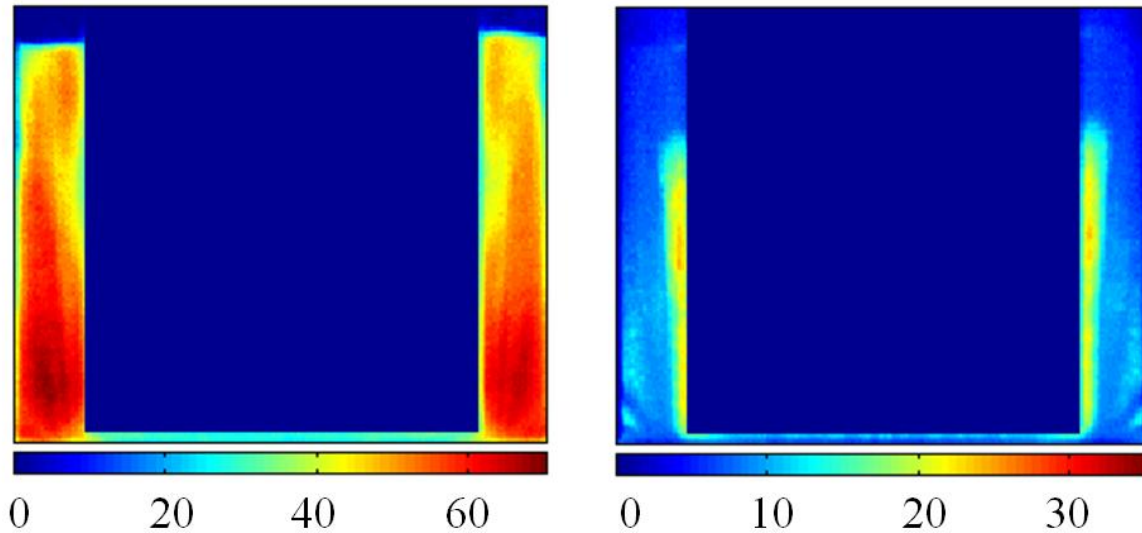


**Fig. F.14** *Shear-induced segregation in Couette cell (courtesy: Marie Lenoble-Eloy). Mixture of large (180  $\mu\text{m}$ ) and small (20  $\mu\text{m}$ ) particles in C16S150 ( $\Delta\rho > 0$ ), in 16/84 % proportion. The figure shows concentrations maps in stationary regime, for  $\Omega = 0.31$  rad/s: small particles at left, and large ones at right. Values of concentration follow the colour codes at bottom. Here concentrations were obtained from colored tracers.*

## F.5: Summary and conclusions

We have described and tested a single particle tracking (SPT) setup based on a Couette cell equipped with contra-rotating cylinders. A direct advantage of the setup is to directly visualize the meridian  $(r, z)$  motion of a given particle inside the shear flow. The system allows us to record trajectories of single fluorescent tracers currently with a 50  $\mu\text{m}$  spatial resolution, at 10 points per second rate and hours of recording time. We tested the procedure in the “simple” case of a Newtonian fluid and verified that the azimuthal flow profile explored by the particle was in agreement with the theoretical one.

Recirculation patterns were observed with all systems, Newtonian fluid, and granular suspensions. However and not surprisingly, the main features of the patterns were not the same: they definitely depend on the particular system. A question about using contra-rotating cylinders is whether the recorded trajectories are equivalent to those in the reference situation where only one cylinder (usually the inner one) is rotating. The measurements clearly yield a positive answer in so far as the azimuthal velocity field is concerned, but no definite

conclusion can be drawn on the sole basis of SPT. Rather reassuringly, the passive mode records do not reveal definite differences when either the inner or outer cylinder is rotated. But the characteristic loops evidenced in active mode are not confirmed in passive mode.

Non azimuthal convections have already been noticed in Couette flows of granular materials [Khosropour *et al.* 1997, Conway *et al.* 2004]. However the reports were concerned with “dry” systems and observations were limited to particles close to the outer wall. To our knowledge, 3-d trajectories of individual particles everywhere inside the bulk of a shear granular suspension have not been reported before. We find that non azimuthal convection is always present within the shear zone, even at very low rotor speed. As we noticed, the trajectories feature definite loops but are not simply toroidal, due to very large fluctuations.

The tests made with tracers of different sizes were aimed at understanding shear-induced segregation, i.e. why mixtures of particles with different properties, be it size [Barentin *et al.* 2004] or surface state [Plantard *et al.* 2006], tend to separate in more or less pure fractions. We suspect that secondary flows may be type selective, and thus play a role in segregation<sup>11</sup>. A few attempts have been made at describing segregation as due to shear-induced diffusion, because the diffusion coefficient depends much on particle size [Shauly *et al.* 1998]. From our observations, re-circulation loops are well discernible from diffusion, meaning that size-selective secondary flows may be more efficient than diffusion in driving segregation. It is tempting, in this context, to make a parallel between shear-induced segregation and the “convection-connection” which was put forward by Knight *et al.* to explain the Brazil-Nut effect [Knight *et al.* 1993].

We end with prospects. Because of the very large fluctuations, as mentioned above, secondary flows within sheared suspensions can only be described statistically. Full characterization of the flows calls for more series of measurements, at variable  $\omega$ ,  $\Delta\rho$  and particle size. Another point is about tracers themselves. As we mentioned, the surface properties of the dyed particles are a matter of concern, because of the sensitivity of segregation to surface properties of the particles. Instead of being impregnated at the surface, it would be most interesting to have the dye confined inside the core of the tracer. Elaborating such “surface-neutral” tracers might be possible using micro-fluidics engineering.

---

<sup>11</sup> Coming back to the above question on equivalence, we may mention that size-segregation patterns are observed to be about the same when either the inner or the outer cylinder is rotating, at given  $\Omega$ . If segregation is driven by secondary flows, the latter observation is an indication that the above mentioned equivalence is met for all aspects of the flow in the granular material.

## Appendix F-A: Servo system

The inner and outer cylinders are driven by two identical direct current motors (Faulhaber 3863H), through belt transmissions. Each motor includes a digital tachometer and is fed by a tension driven servo-amplifier (MATTKE MTRF25...61/5-15) including a power unit (pulse width modulation, PWM in Fig. II.11). One motor ( $\omega_2$ ) is driven to permanently keep the image of the tracer at the center of the ROI, while the other one ( $\omega_1$ ) functions in slave mode so as to maintain  $\omega_2 - \omega_1 = \omega$ , the prescribed average shear. If we define ( $\omega_1 = \omega, \omega_2 = 0$ ) as the reference configuration, the offset is simply  $\Omega = \omega_2$ .

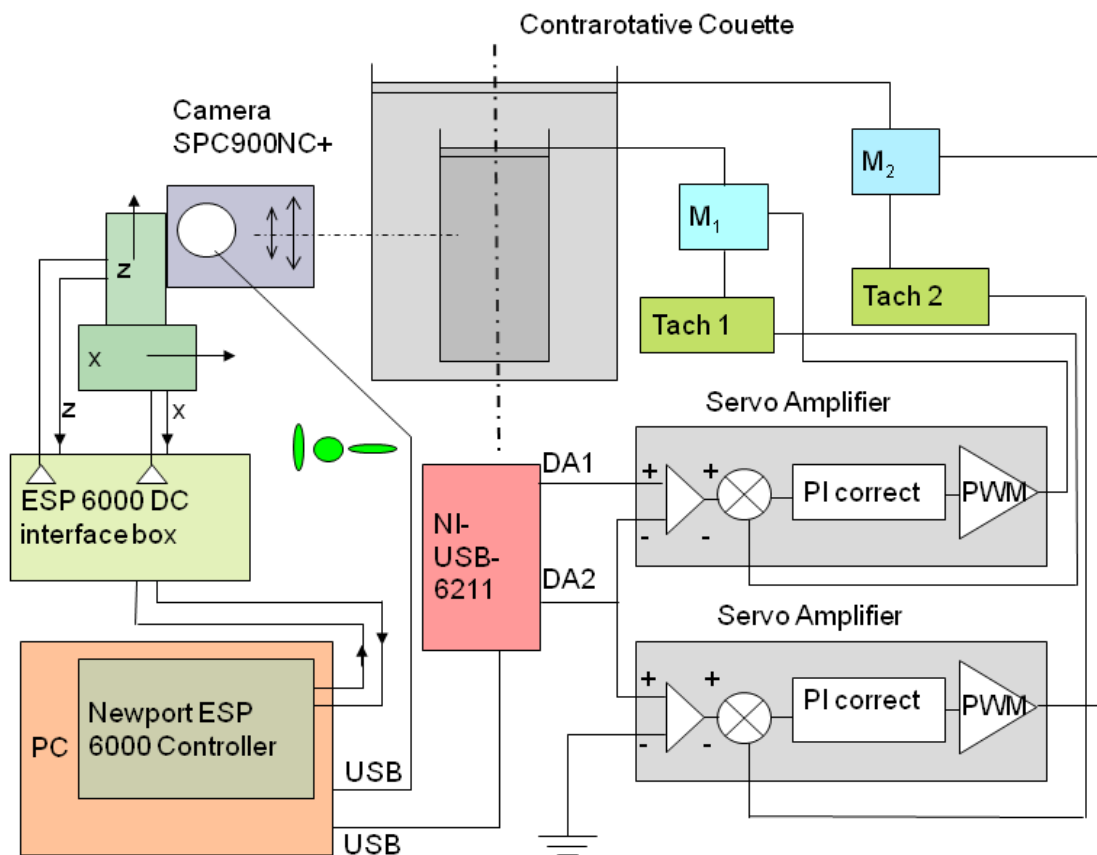


**Fig. F-A1** Overview diagram of the servo system.

The system software has been developed in CVI Labwindows environment, to provide an ergonomic interface to the user. The main modules are:

- An image acquisition module, based on a native Windows library (vfw.h, AviCap32.lib, MsVfw32.lib)
- An image processing module whose goal is to locate the particle image barycentre and calculate the image ellipticity. The corresponding error signals (in  $x_m, z_m, \Omega$ ) are obtained through a single-pass screening of the image. In typical conditions, the particle appears as a well resolved bright spot and a basic thresholding is sufficient to obtain a sharp contour. A rectangular ROI, about twice the particle image spot in surface area, is drawn and centred onto the particle at the beginning of the tracking experiment. For instance, a 180X180 square ROI is adequate for a 200  $\mu\text{m}$  tracer. The ellipticity  $e$  is simply deduced from the numbers of illuminated lines ( $n_l$ ) and columns ( $n_c$ ) inside the ROI:  $e = (n_l - n_c) / (n_l + n_c)$ . At each step, the software determines the particle position and ellipticity inside the ROI, whose position is incremented at the following step to maintain centring of the ROI.

The corrections signal in  $\Omega$  is sent to the motor power units through a multifunction module (NI-USB-6211). Corrections in  $x_m, z_m$  are sent to the translation stages that support the imaging optics through a dedicated Newport ESP6000 system: similarly to the Couette cell motors, the system comprises a servo-amplifier (a PCI card) and a power unit. Classical proportional-integral-differential-feed-forward (PID-FF) schemes are applied to control the positions of the stages, and the cell motors velocities.

## Appendix F-B: Tracer migration in Newtonian fluid

Though the neutrally buoyant particle in the Newtonian fluid was simply used for an instrumental test, we may shortly tackle the question concerning the non azimuthal motion of the tracer. What is the nature of this motion?

A first remark is about the so-called “inertial particle migration”, an effect by which a spherical particle of finite size in a simple Couette shear flow drifts perpendicularly to the flow (horizontally in our experimental scheme) and settles at an equilibrium position between the flow boundaries (Halow and Wills 1970, Ho and Leal 1974, Feng *et al.* 1994). Where the equilibrium position is located is a complicated problem, as predictions are very sensitive to  $\Delta\rho$ , in other words to whether neutral buoyancy is perfectly achieved or not (Feng *et al.* 1994). Interestingly the analysis by Ho and Leal leads to a characteristic time for particle migration:  $\tau_{mig} = \nu \cdot (L/a)^3 \cdot U^{-2}$ , which we may take as a basis for comparison. Taking  $L = d = 0.5$  cm as the shear flow characteristic length,  $a = 0.01$  cm and  $U \approx 1$  cm/s, we find  $\tau_{mig} \approx 3 \times 10^4$  s, about a hundred times more than what we experimentally observe (Fig. F.4.b). This argument leads us to ruling out inertial particle migration as the cause of the observed tracer drifting across the gap.

An alternate scheme is suggested by the works dedicated to end effects in finite size Couette cells. Indeed the presence of top and bottom boundaries, as is obviously the case in real experimental setups, causes non azimuthal flows in the form of re-circulation patterns, even at very small Reynolds (or Taylor) numbers (Benjamin 1978a, Benjamin 1978b, Czarny *et al.* 2003). Otherwise stated, a purely azimuthal flow is not possible in a finite height Couette cell; re-circulation flows are always present, with characteristics that depend on whether the inner or outer cylinder is rotating, and on the nature of the shear cell ends (Czarny *et al.* 2003). However the available information, to our knowledge, only concerns stationary flows. In principle, stationarity of the azimuthal flow in our experiment is achieved, since the characteristic time  $\tau_\theta = d^2/\nu \approx 1$  s is short compared to the particle drift time ( $\tau_{mig} \geq 100$  s). Conversely, the vorticity diffusion time along the vertical,  $\tau_\theta = H^2/\nu$ , is of order 100 s, indicating that the non azimuthal components of the flow within the particle migration time may have not reached stationarity. Consequently the nature of the non azimuthal flow (suggested by the graphs in Fig. F.5.a) is not the same as the stationary flows reported in the above cited studies. This may essentially be a transient flow, whose genesis is not known yet. This point calls for future theoretical work.

## Chapter G- Conclusion and prospects

We have studied various aspects of the flow of concentrated non colloidal suspensions inside a Couette shear cell. All reported experiments used transparent suspensions, made of PMMA spherical particles inside a viscous fluid. The fluid was either density-matched ( $\Delta\rho = 0$ ) or non density-matched ( $\Delta\rho > 0$ ) with the particles.

Essentially, we studied characteristics of the primary and secondary components of the flows, as well as position fluctuations in the velocity direction. To achieve this goal, we set up and used three novel experimental techniques: multiparticle video-trajectorygraphy (MPVT), concentration photometry and automated single particle tracking (SPT).

Primary (orthoradial) velocities were measured by PVT in both types of suspension, from the spatiotemporal displacements of fluorescent tracers or of the small volumes of fluorescent immersion liquid between particles. Photometry measurements were performed in parallel to velocimetry, to obtain concentration profiles within the whole shear cell.

In the case of the  $\Delta\rho = 0$  suspension, we found a very good agreement between experimental data and predictions of the force balance model. In the frame of this model, the essential information derived from experimental data is the ratio  $f(\varphi) = \hat{\eta}_n / \hat{\eta}_s$ , where  $\hat{\eta}_s$  and  $\hat{\eta}_n$  are the viscometric functions corresponding to shear and normal forces, respectively. From the measured concentration and velocity profiles, we could delineate the shape of this function in the high concentration range. Note worthily, this shape differs from that recently inferred by Boyer *et al.* based on the reverse Weissenberg effect (the dip of the free surface caused by shear near the inner cylinder).

The non density matched suspension behaved very differently, as we saw: the effect of gravity is very intense, as can be seen from the localization of the primary flow. Localization is a case of shear-banding, whereby a sheared zone, near the inner cylinder, coexists with a nearly “dead” phase near the outer cylinder. We observed that the dead phase in fact was not a jammed phase, as it was of spatially variable concentration and a zone of very slow fluctuations. In this context, we concluded that the force balance model, in the current version, was valid in the fluid zone, not in the dead phase. Fortunately, we came out with the same shape for the function  $f(\varphi)$  as above, using the data corresponding to the fluid zone.

The force balance model pertains to effective fluid theories. Still using MPVT, we performed a few measurements to test the validity of the effective fluid picture in our system. We measured orthoradial velocities of “intruders”, namely tracers that were either smaller or bigger than the suspension host-particles. We found small velocity differences, which were in line with the picture of small particles dodging among bigger ones. This behaviour was that

expected in view of the generally large wall slip revealed by velocity profiles of the host particles.

The analysis with MPVT of particle displacements made possible the measurement of the diffusion coefficient in the flow direction. Interestingly, the diffusion coefficient  $D_{\theta\theta}$  keeps an almost constant value ( $D_{\theta\theta}/a^2|\dot{\gamma}| \approx 0.4 \div 0.5$  for density matched suspensions in line with data from Breedveld *et al* ) and decays above a crossover volume fraction  $\Phi \approx 0.55 - 0.56$  around the so-called “random-loose packing” concentration. In non density-matched suspensions, gravity effects increase the diffusion coefficient  $D_{\theta\theta}/a^2|\dot{\gamma}| \approx 1.5 \div 2.5$  and further shift the transition toward higher concentrations ( $\Phi \approx 0.57 - 0.58$ ). The high concentration regime corresponds to the occurrence of transient clusters and to fluctuations over longer time scales.

The SPT technique allowed us to reconstitute 3-dimensionnal trajectories of individual tracers, over many hours of recording time. We thus could study characteristics of secondary flows in our systems. The records revealed the existence of vortices that were readily discernible from the background noise due to shear-induced diffusion. As we saw, the main features of the meridian motions depended on whether the suspension was density-matched or not, and, most importantly, the motions were very sensitive to particle size. Meridian trajectories of small and big intruders were qualitatively different. Overall, the SPT experiments confirm the existence of secondary flows, and the data support the view that these flows may overwhelm diffusion as a cause of shear-induced migration and size-segregation, especially in the highly sheared regions.

A general comment is in order about the technique of contra-rotating cylinders that we used throughout this work. This technical feature is at the very basis of the automated SPT setup. Contra-rotation also intervenes in the concentration measurements, not as a basic principle, but as a necessary step to spatially average data from different diametric cuts. Our reasoning to exploit experimental data is based on the assumption that the structure and the flow within the suspension is only determined by the difference of angular velocities of the cylinders. This statement is certainly not correct in general, but it tends to hold true in the limit of vanishing velocities. Fortunately enough, we could check that the approximation was valid within experimental uncertainty, in so far as we dealt with primary flows and concentration profiles. Tests concerning secondary motions were few and not decisive. At the current stage, we do not know whether rapid changes in offset velocity due to the servo

system in automated mode have an influence on meridian trajectories. Though no clear reason comes up why it should have a large influence, the question remains open.

We end with a few prospects:

- We solved the equations of the force balance model within the assumption that a fluid phase coexists with a jammed phase ( $\varphi=1$  in equations). Since the measurements indicate a variable concentration in the almost arrested region, we believe that the current assumptions should be revisited and that more general solutions not involving a jammed zone should be looked for. Recall that large scale fluctuations occur inside the nearly arrested zone, indicating collective motions due to contact chains. This observation calls for a non local version of the model.
- Particle position fluctuations, of much larger amplitude in the flow direction compared to transverse directions, could in fact control the dynamics of concentrated suspensions and migration phenomena near the jamming transition. As a suggestion for future studies, one may use counter-rotation of the cylinders to keep particles at given  $r$  within the spatio-temporal window. This would help analyzing particle fluctuations over an extended range of time scales.
- We noticed that secondary trajectories were highly fluctuating, most strikingly in the case of the  $\Delta\rho > 0$  system. We definitely need a lot more records to elaborate statistical laws about the trajectories. The currently available data show that fluctuations occur at all scales, from particle diameter up to the shear cell size. Forthcoming studies should then be based on a multiscale statistical analysis tool.
- We currently have no clear view about the origin of secondary motions. It is tempting to invoke the anisotropy of normal forces, as is done in Ramachandran-Leighton theory, but we must keep in mind that re-circulation already occurs in the pure Newtonian fluid. As we explained, these motions are most probably end effects (due to horizontal boundaries of the shear cell). It is then highly desirable to reduce end effects in future design. The setup may be improved with a layer of heavy fluid at bottom.
- As we explained, the current procedure to elaborate fluorescent tracers is not ideal, because of the surface modifications following dye impregnation. It would be much better to fabricate special PMMA particles with a fluorescent core, thus preserving

surface neutrality. We believe that this goal may be achieved using techniques from microfluidics. If they are made available, such tracers would be of much help to researchers in the field of suspensions hydrodynamics.

## Chapitre G- Conclusion et perspectives

Nous avons présenté une série d'études sur l'écoulement d'une suspension non colloïdale concentrée dans une cellule de Couette. Toutes nos expériences sont faites avec des suspensions modèles transparentes, constituées de sphères de PMMA dans un fluide newtonien, dans les versions isodense et non-isodense.

Essentiellement, notre travail a consisté à mesurer les composantes primaire et secondaire des écoulements, ainsi que les fluctuations de position des particules dans le direction de la vitesse. Pour effectuer ces mesures, nous avons mis en œuvre trois techniques innovantes : video-trajectographie de particules (PVT), photométrie de concentration, et poursuite de particule (SPT).

Les écoulements primaires dans les deux types de suspension ont été caractérisés par PVT, en suivant les déplacements orthoradiaux de traceurs fluorescents ou directement des petits volumes de liquide séparant les particules hôtes. En parallèle, les mesures photométriques nous ont permis de construire les profils de concentration dans tout le volume de la cellule de Couette.

Dans le cas de la suspension isodense, nous avons montré que l'ensemble des caractéristiques de l'écoulement primaire est en très bon accord avec le modèle d'équilibre des forces normales. L'information essentielle tirée de la comparaison expérience-théorie est le rapport  $f(\varphi) = \hat{\eta}_n / \hat{\eta}_s$  des fonctions viscométriques normale et tangentielle. Nos mesures permettent de préciser la forme de cette fonction à haute concentration. On notera que la forme trouvée diffère sensiblement de celle proposée récemment par Boyer *et al.* à partir de l'effet Weissenberg inverse (le creusement de la surface libre de la suspension sous l'effet du cisaillement). Nous avons étendu cette étude au cas de la suspension non isodense, pour lequel l'effet de la gravité est très intense et provoque une localisation de l'écoulement, variable entre le bas et le haut du système. La localisation se traduit par une coexistence entre une zone relativement fluide, et une zone « morte », en fait quasiment à l'arrêt et siège de fluctuations très lentes. Dans ce cas, le modèle d'équilibre de force, dans la forme que nous avons adoptée, reste valide, mais seulement dans la zone cisailée. L'analyse des données dans cette zone aboutit à la même forme de la fonction  $f(\varphi)$  que celle obtenue avec la suspension isodense. La zone « morte » n'est pas décrite correctement par le modèle.

Nous avons par ailleurs examiné les limites de la description en terme de fluide effectif en mesurant les vitesses orthoradiales de traceurs (ou « intrus ») plus petits ou plus grands que les particules hôtes. Les petits écarts trouvés entre les vitesses des différentes espèces sont

faibles, mais on vérifie que les plus petites particules ont tendance à se faufiler entre les grandes ; ce qui est le comportement attendu.

Les analyses des déplacements par vidéo-trajectographie ont permis la mesure des coefficients de diffusion dans la direction de l'écoulement. De manière remarquable, le coefficient de diffusion  $D_{\theta\theta}$  conserve une valeur relativement constante ( $D_{\theta\theta} / a^2 |\dot{\gamma}| \approx 0.4 \div 0.5$  pour une suspension adaptée en densité, en accord avec les données expérimentales de Beedveld *et al.*) and chute de manière spectaculaire pour une concentration  $\Phi \approx 0.55 - 0.56$  voisine de la concentration d'empilement aléatoire de sphères dures monodisperses. Dans les suspensions non adaptées en densité, les effets gravitaires contribuent à augmenter le coefficient de diffusion  $D_{\theta\theta} / a^2 |\dot{\gamma}| \approx 1.5 \div 2.5$  et déplacer vers de plus fortes concentrations  $\Phi \approx 0.57 - 0.58$  la transition associée à la formation d'amas. Dans ce régime, les fluctuations n'interviennent qu'à plus grande échelle de temps.

Nous avons utilisé la technique SPT pour enregistrer les trajectoires de traceurs individuels, en 3 dimensions ; ce qui nous a permis d'étudier les caractéristiques des écoulements secondaires dans la cellule de Couette. Cette étude a montré l'existence de rouleaux nettement discernables du « bruit » provoqué par la diffusion induite par cisaillement, et dont les aspects dépendent des caractéristiques de la suspension, avec de nettes différences entre les suspensions isodense et non isodense. Un résultat important de cette étude est la très grande sensibilité des trajectoires secondaires à la taille de particule : les mouvements méridiens des gros et petit intrus sont qualitatives et spectaculaires. On confirme ainsi l'existence des composantes secondaires des écoulements, dont l'importance peut être supérieure à celle de la diffusion dans l'établissement des profils de migration et de ségrégation, en particulier dans les régions fortement cisillées.

Techniquement, nous avons abondamment utilisé la fonction à deux cylindres contra-rotatifs de nos cellules de Couette. Cette fonction entre dans le principe même de la technique de poursuite de particule. Elle intervient aussi, non pas dans le principe, mais comme un outil de moyennisation incontournable dans les mesures de concentration. Théoriquement, nos raisonnements sont construits en supposant que la structure et les écoulements dans la suspension ne sont sensibles qu'à la différence de vitesses angulaires entre les deux cylindres, ce qui n'est certainement pas correct en général, mais tend à devenir exact à la limite des faibles vitesses. Nous avons vérifié par des tests expérimentaux la validité de cette approximation pour ce qui concerne les écoulements primaires et les profils de concentration.

Des tests pour les écoulements secondaires ont été faits, mais sont moins nombreux et convaincants. Des doutes subsistent quant aux conséquences des changements rapides de répartition des vitesses entre les deux cylindres, inhérents au principe du montage de SPT.

Plusieurs pistes se dessinent à l'issue de ce travail, pour une suite possible :

- Nous avons résolu les équations du modèle d'équilibre de forces dans l'hypothèse générale où une phase fluide coexiste avec une phase bloquée, c'est-à-dire « morte strictement » ( $\varphi = 1$  dans les équations). Nos mesures indiquant toutefois une concentration variable dans la région presque statique, il faut reconsidérer les hypothèses adoptées et rechercher des solutions plus larges impliquant des phases non bloquées. Cette question rejoint celle des fluctuations dans la zone fortement concentrée, qui indiquent la présence de mouvements par blocs. Une description adéquate pourrait être fournie par une version non locale du modèle de Morris-Boulay.

- Les fluctuations de position des particules, bien plus importantes dans la direction de l'écoulement par rapport aux directions transverses, pourraient en fait contrôler la dynamique des suspensions concentrées et les phénomènes de migration près de la limite de blocage. Une suggestion pour de futures études consiste à utiliser le système contra-rotatif pour garder plus longtemps les particules dans le champ d'observation. Cela permettrait une analyse du déplacement statistique des particules dans une suspension très concentrée sur de plus grandes échelles de temps.

- Nous avons constaté le caractère très fluctuant des trajectoires secondaires, surtout avec le système non isodense. Il faudrait multiplier les mesures de SPT, pour mieux cerner les propriétés statistiques de ces trajectoires. Les données dont nous disposons indiquent clairement que les fluctuations interviennent sur des tailles variables. Les études à venir devraient donc s'appuyer sur une méthode statistique d'analyse multi-échelle, depuis la taille de particule jusqu'à celle de la cellule de cisaillement.

- La question reste ouverte concernant l'origine des mouvements secondaires. On peut naturellement invoquer l'effet d'anisotropie de forces normales dans les suspensions, suivant l'analyse de Ramachandran-Leighton, mais les re-circulations constatées dans le fluide simple posent le problème de l'influence des parois horizontales de la cellule. Nous avons le projet de remplacer le fond de la cellule par

une couche de fluide lourd, pour tester cette hypothèse. Cette amélioration n'a pas été faite, faute de temps ; elle apparaît nécessaire pour résoudre la question des effets de bords.

- Comme nous l'avons indiqué, les traceurs fluorescents que nous utilisons sont non idéaux, du fait des modifications de surface inhérentes au procédé d'incorporation des colorants. Il serait très utile pour l'ensemble de la communauté des chercheurs travaillant sur les suspensions concentrées, de disposer de traceurs véritablement neutres, c'est-à-dire dont les surfaces et les densités moyennes soient identiques à celles des particules hôte. Nous imaginons que la synthèse de particules de PMMA avec un cœur fluorescent est possible en utilisant des techniques de micro-fluidique.

## Bibliography

- Abbott J., Tetlow N., Graham A., Altobelli S., Fukushima E., Mondy L. and Sephens T., “*Experimental observations of particle migration in concentrated suspensions : Couette flow*,” *Journal of Rheology* **35**, pp. 773–795, (1991).
- Acrivos A., Batchelor G. K., Hinch E. J., Koch D. L. and Mauri R., “*Longitudinal Diffusion of Spheres in a Dilute Suspension*”, *Journal of Fluid Mechanics* **240**, pp. 651-657, (1992).
- Adelson E. H. and Bergen J. R., “*Spatiotemporal energy models for the perception of vision*”, *Journal of Optical Society of America A*, **2**, pp. 284-299, (1985).
- Adelson E. H., “*Mechanisms for motion perception*”, *Optics and Photonics new*, pp. 24-30, (1991).
- Adrian R., “*Particle imaging techniques for experimental fluid mechanics*”, *Annual Review of Fluid Mechanics* **23**, pp. 261-304, (1991).
- Alvarez L., Weickert J. and Sanchez J., “*Reliable estimation of dense optical flow fields with large displacements*”, *Int. J. Computer vision*, **39**, 1, pp. 41-56, (2000).
- Andereck C., Liu S. and Swinney H., “*Flow regimes in a circular Couette system with independently rotating cylinders*”, *Journal of Fluid Mechanics* **164** : 155, (1985).
- Anderson S. J. and Burr D. C., “*Spatial and temporal selectivity of the human motion detection system*”, *Vision Research*, **25**, pp. 1147-1154, (1985).
- Arp P. A. and Mason S. G., “*The kinetics of flowing dispersions*” , *Journal of Colloid and Interface Science* **61**(1), pp. 21- 43, (1977).
- Averbakh A. A., Shauly A., Nir A., and Semiat R., “*Slow viscous flows of highly concentration suspensions—Part I: Laser Doppler velocimetry in rectangular ducts*”, *International Journal of Multiphase Flow* **23**, pp. 409–424, (1997).
- Barentin C., Azanza E., and Pouligny B., “*Flow and segregation in sheared granular slurries*”, *Europhysics Letters* **66** : 139, (2004).
- Barron J. L., Fleet D. J., and Beauchemin S. S., “*Performance of optical flow techniques*”, *International Journal of Computer Vision*, **12**, 1, pp. 43-77, (1994).
- Benjamin T. B. , “*Bifurcation phenomena in steady flows of a viscous liquid I. Theory*”, *Proceedings of the Royal Society A* **359**, London , pp. 1 – 26, (1987a).
- Benjamin T. B. , “*Bifurcation phenomena in steady flows of a viscous liquid II. Experiments*”, *Proceedings of the Royal Society A* **359**, London , pp. 27 – 43, (1987b).
- Blanc F., Peters F., and Lemaire E., “*Experimental Signature of the Pair-Trajectories of Rough Spheres in the Shear-Induced Microstructure in Non-Colloidal Suspensions*”, *Physical Review Letters E*, **107**, 208302, (2011).
- Bocquet L., Lorset W., Schalk D., Lubensky T.C. and Gollub J.P., “*Granular shear flow dynamics and forces: Experiments and continuum theory*”, *Physical Review Letters E* **65** : 011307 , (2001).
- Bonn D., Rodts S., Groenink M., Rafai S., Shahidzadeh-Bonn N. and Coussot P., “*Some applications of magnetic resonance imaging in fluid mechanics: Complex flows and complex fluids*”, *Annual Review of Fluid Mechanics* **40**, 209–233, 0066-4189, (2008).
- Boyer F., Pouliquen O. and Guazzelli E., “*Dense suspensions in rotating-rod flows: normal stresses and particle migration*”, *Journal of Fluid Mechanics* **686**, pp. 5 – 25, (2011).
- Bracewell R. N., “*The Fast Hartley Transform*”, *Oxford University Press, Inc., New York*. **11**, (1986).
- Bracewell R. N., Buneman O., Hao H. and Villasenor J., “*Fast Two-Dimensional Hartley Transform*”, *Proceeding of IEEE* **74**, 9, (1986).

- Breedveld V., Van den Ende D., Tripathi A. and Acrivos A., “*The measurement of the shear-induced particle and fluid tracer diffusivities by a novel method*”, *Journal of Fluid Mechanics* **375**, pp. 297–318, (1998).
- Breedveld V., “*Shear-induced self-diffusion in concentrated suspensions*”, PhD thesis, University of Twente, (2000).
- Breedveld V., Van den Ende D., Bosscher M., Jongschaap R. J. J. and Mellema J., “*Measuring shear-induced self-diffusion in a counter-rotating geometry*”, *Physical Review Letters* **E 63**, pp. 1403–1412, (2001).
- Breedveld V., van den Ende D., Bosscher M., Jongschaap R. J. J., and Mellema J., “*Measurement of the full shear - induced self - diffusion tensor of non colloidal suspensions*” *Journal of Chemical Physics* **116**, 23, pp. 10529-10535, (2002).
- Chow A. W., Sinton S. W., Iwamiya J. H., and Stephens T. S., “*Shear-induced particle migration in Couette and parallel-plate viscometers: NMR imaging and stress measurement*”, *Physics of Fluids* **6**, pp. 2561–2576, (1994).
- Conway S. L., Shinbrot T. and Benjamin J. G., “*A Taylor vortex analogy in granular flows*”, *Nature* **431**, pp. 433 – 437, (2004).
- Corpetti T., Mémin E. and Perez P., “*Dense estimation of fluid flows*”, *IEEE Transaction on pattern analysis and machine intelligence*, **24**, 3, pp. 365-380, (2002).
- Cunha R. F. and Hinch E. J., “*Shear-induced dispersion in a diluted suspension of rough spheres*”, *Journal of Fluid Mechanics* **309**, pp. 211 – 223, (1996).
- Dbouk T., “*Rheology of concentrated suspensions and shear-induced migration*”, PhD thesis, Université de Nice-Sophia Antipolis, (2011).
- Feng D. J., Hu H. H. and Joseph D. D., “*Direct simulation of initial value problems for the motion of solid bodies in a Newtonian Fluid: Part 2. Couette and Poiseuille flows*”, *Journal of Fluid Mechanics* **227**, pp. 271 – 301, (1994).
- Frankel N. A. and Acrivos A., “*On the Viscosity of a Concentrated Suspension of Solid Spheres*”, *Chemical Engineering Science* **22**, pp. 847–853, (1967).
- Gadala –Maria F. and Acrivos A., “*Shear-induced structure in a concentrated suspension of solid spheres*”, *Journal of Rheology* **24**, pp 799 -811, (1980).
- Gibson J. J., “*The perception of the visual world*”, Boston: Houghton Mifflin (1950).
- Govindarajan R., Nott P. R. and Ramaswamy S., “*Theory of suspension segregation in partially filled horizontal rotating cylinders*”, *Physics of Fluids* **13(12)**, pp. 3517 – 3520, (2001).
- Graham A. L., Altobelli S. A., Fukushima E., Mondy L. A. and Stephens T. S., “*NMR imaging of shear induced diffusion and structure in concentrated suspensions undergoing. Couette flow*”, *Journal of Rheology* **35**, pp. 191–201, (1991).
- Gray M. N. T., “*Granular flow in partially filled slowly rotating drums*”, *Journal of Fluid Mechanics* **441**, pp. 1-29, (2001).
- Guyon E., “*Physical hydrodynamics*”, Oxford University Press, page **136**, (2001).
- Hajra S. K. and Khakhar D. V., “*Sensitivity of granular segregation of mixtures in quasi-two-dimensional fluidized layers*”, *Physical Review Letters* **E 69**, 031304, (2004).
- Halow J. S. and Wills G. B., “*Experimental observations of sphere migration in Couette systems*”, *Industrial Engineering Chemistry Fundamentals* **9**:603, (1970).
- Heitz D., Mémin E., Schnörr C., “*Variational fluid flow measurements from image sequences: synopsis and perspectives*”, *Journal Experiments in Fluids*, DOI 10.1007/s00348-009-0778-3, (2009).
- Hesselink L., “*Digital image processing in flow visualization*”, *Annual Review of Fluid Mechanics* **20**, pp. 421–485, (1988).
- Ho B. P. and Lead L. G., “*Inertial migration of rigid spheres in twodimensional unidirectional flows*”, *Journal of Fluid Mechanics* **65** : 365, (1974).

- Horn B. and Schunck B., “*Determining optical flow*”, *Artificial Intelligence*, **17**, pp. 185-204, (1981).
- Hsu W-Y., Lee C-S, Chen P-J, Chen N-T, Chen F-Z, Kuo C-H and Hwang C-H, “*Development of the fast astigmatic auto-focus microscope system*”, *Measurement Science and Technology* **20**, 045902, (2009).
- Huang H. T., Fiedler H. E., and Wang J. J., “*Limitation and improvement of PIV. part I: Limitation of conventional techniques due to deformation of particle image patterns*”, *Journal Experiments in Fluids*, **15**, pp. 168-174, (1993).
- Huang N., Ovarlez G., Bertrand F., Rodts S., Coussot P. and Bonn D., “*Flow of wet granular materials*”, *Physical Review Letters* **94**, 028301 (2005).
- Hubel D. H. and Wiesel T. N., “*Receptive fields, binocular interaction and functional architecture in the cat's visual cortex*”, *Journal of Physiology* **160**, pp. 106-154, (1962).
- Jackson R., “*The Dynamics of Fluidized Particles*”, Cambridge University Press, Cambridge, (2000).
- Jarry S., Roussel N., Rodts S., Bertrand F., Le Roy R. and Coussot P., “*Rheological behavior of cement pastes from mri velocimetry*”, *Cement and Concrete Research* **35**, pp. 1873–1881, (2005).
- Jin B. and Acrivos A., “*Theory of particle segregation in rimming flows of suspensions containing neutrally buoyant particles*”, *Physics of Fluids* **16(3)**, pp.641 – 651, (2004).
- Jullien R. and Meakin P., “*A Mechanism for Particle Size Segregation in Three Dimensions*”, *Nature* **344**, pp. 425-427, (1990).
- Jullien R. and Meakin P. , “*Three-Dimensional Model for Particle-Size Segregation by Shaking*”, *Physical Review Letters* **E 69**, pp. 640 – 643, (1992).
- Khosropour R., Zirinsky J. , Pak H.K. and Behringer R.P., “*Convection and size segregation in a Couette flow of granular material*”, *Physical Review Letters* **E 56**, pp. 4467–4473, (1997).
- Knight J. B., Jaeger H. M. and Nagel S. R., “*Vibration induced size-separation in granular media: the convection connexion*”, *Physical Review Letter* **E 74**, pp. 3728 – 3731, (1993).
- Koh C. J., Hookham P., and Leal L. G., “*An experimental investigation of concentrated suspension flows in a rectangular channel*”, *Journal of Fluid Mechanics* **266**, pp. 1–32, (1994).
- Krieger M. I. and Dougherty T. J. , “*A mechanism for non-Newtonian flow in suspension of rigid spheres*”, *Transactions of the Society of Rheology* **3**, pp. 137–152 (1959).
- Krishnan G. P., Beimfohr S., and Leighton D. T., “*Shear-induced radial segregation in bidisperse suspensions*”, *Journal of Fluid Mechanics* **321**, pp. 371 – 393, (1996).
- Lee S. and Song J.-B., “*Mobile robot localization using optical flow sensors*”, *International Journal of Control, Automation, and systems*, **2**, 4, pp. 485-493, (2004).
- Leighton D. T., and Acrivos A., “*The shear-induced migration of particles in concentrated suspensions*”, *Journal of Fluid Mechanics* **181**, pp. 415–439, (1987a).
- Leighton D. T. and Acrivos A., “*Measurement of Shear-Induced Self-Diffusion in Concentrated Suspensions of Spheres*”, *Journal of Fluid Mechanics* **177**, pp. 109-131 (1987b).
- Leighton D. T., and Rampall I., “*Measurement of the shear-induced microstructure of concentrated suspensions of non-colloidal spheres, in Particulate Two-Phase Flow*”, edited by M. C. Roco-Butterworth-Heinemann, Boston, pp. 190–208, (1993).
- Lemaitre A., Roux J. N. and Chevoir F., “*What do dry granular flows tell us about dense non-Brownian suspension rheology?*”, *Rheological Acta* **48**, pp. 925 – 942, (2009).
- Lenoble M., “*Écoulement et segregation dans des pâtes granulaires modèle*”, PhD Thesis, Université Bordeaux1, (2005).
- Lenoble M., Snabre P. and Poulligny B., “*The flow of a very concentrated slurry in a parallel-plate device: influence of gravity-driven threshold*”, *Physics of Fluids* **17** : 073303, (2005).

- Lhuillier D., “Two-fluid model for suspension and migration phenomena”, Communication to GISEC33 meeting, see <http://www.crpp-bordeaux.cnrs.fr/IMG/pdf/D-LHUILIER.pdf>
- Lipson S. G. and Seiden G., “Particle banding in rotating fluids : a new pattern forming system”, *Physica A* **314**, pp. 272 – 277, (2002).
- Lorincz K. A., and Schall P., “Visualization of displacement fields in a sheared granular system”, *Soft Matter* **6**, pp. 3044-3049, (2010).
- Lyon M. K., and Leal L. G., “An experimental study of the motion of concentrated suspensions in twodimensional channel flow. Part I. Monodisperse systems”, *Journal of Fluid Mechanics* **363**, pp. 25–56, (1998).
- Mansard V. and Colin A., “Local and non local rheology of concentrated particles”, *Soft Matter* **8**, pp. 4025 – 4043, (2012).
- Martinot-Lagarde G., “Effets mécaniques de la lumière sur des sphères de polystyrène dans l'eau: mesure et applications physico-chimiques”, PhD thesysis nr. **1330**, Université Bordeaux1, (1995).
- McKenna S. P. and McGillis W. R., “Performance of digital image velocimetry processing techniques”, *Journal Experiments in Fluids* **32**, pp. 106-115, (2002).
- Mehri D., “Migration et ségrégation des particules dans les suspensions concentrées : étude expérimentale et modélisation”, PhD Thesysis, Université de Nice Sophia-Antipolis, (2001).
- Merzkirch W. and Gui L. C., “A method of tracking ensembles of particle images”, *Journal Experiments in Fluids*, **21**, pp. 465-468, (1996).
- Meunier A. and Bossis G., “The influence of surface forces on shear-induced tracer diffusion in mono and bidisperse suspensions”, *European Physical Journal E* **25**, pp.187 – 199, (2008).
- Mills P. and Snabre P., “Rheology and structure of concentrated suspensions of hard spheres. Shear induced particle migration”, *Journal de Physique II*, **5**, pp. 1597-1608, (1995).
- Mills P. and Snabre P., “Apparent viscosity and particle pressure of a concentrated suspension of non-Brownian hard spheres near the jamming transition”, *European Physical Journal* **E30**, pp. 309–316, (2009).
- Morris J. F. and Boulay F., “Curvilinear flows of non colloidal suspensions: the role of normal stresses”, *Journal of Rheology* **43**, pp. 1213 – 1237, (1999).
- Moucheront P., Bertrand F., Koval G., Tocquer L., Rodts S., Roux J. N. and Chevoir F., “MRI investigation of granular interface rheology using a new cylinder shear apparatus”, *Magnetic Resonance Imaging*, **28**, 6, pp. 910-918, (2010).
- Mueth D. M., Debregeas G. F., Karczmar G. S., Eng P. J., Nagel S. R. and Jaeger H. M., “Signatures of granular microstructure in dense shear flows”, *Nature*, **406**, pp. 385-389, (2000).
- Nott P. R. and Brady J. F., “Pressure-driven suspension flow: simulation and theory”, *Journal of Fluid Mechanics* **275**, 157, (1994).
- Onoda G. Y. and Liniger E. G., “Random loose packings of uniform spheres and the dilatancy onset”, *Physical Review Letters* **E 64**, pp. 2727–2730, (1990).
- Orpe A. V., and Kudrolli A., “Velocity correlations in dense granular flows observed with internal imaging”, *Physical Review Letters* **E 98**, 238001, (2007).
- Ouriemi M., Aussillous P. and Guazzelli E., “Sediment dynamics. Part 1: bed-load transport by laminar shearing flows”, *Journal of Fluid Mechanics* **636**, pp.295 – 319, (2009).
- Ovarlez G., Bertrand F. and Rodts S., “Local determination of the constitutive law of a dense suspension of noncolloidal particles through magnetic resonance imaging”, *Journal of Rheology* **50**, pp. 259–292, (2006).
- Phillips J., Armstrong R. C., Brown R. A., Graham A. L., et Abott J. R., “A constitutive equation for concentrated suspensions that accounts for shear-induced particle migration”, *Physics of Fluids*, **A v.4 (1)**, pp. 30-40, (1992).

- Pine D. J., Gollub J. P., Brady J. F., and Lehansky A. M., “*Chaos and threshold for irreversibility in sheared suspensions*”, *Nature* **438**, 15, pp. 997-1000, (2005).
- Plantard G., Saadaoui H., Snabre P. and Pouligny B., “*Surface-roughness-driven segregation in a granular slurry under shear*”, *Europhysical Letters* **75(2)** : 335, (2006).
- Prasad A. K., “*Particle image velocimetry*”, *Current Science* **79**, 1, (2000).
- Raffel M., Willert C. and Kompenhans J., “*Particle image velocimetry*”, Springer, Berlin Heidelberg New York, (2000).
- Ramachandran A. and Leighton D.T., “*The influence of secondary flows induced by normal stress differences on the shear-induced migration of particles in concentrated suspensions*”, *Journal of Fluid Mechanics* **603**, pp. 207-243 (2008).
- Reynolds O., “*Experiments showing dilatancy, a property of granular material, possibly connected with gravitation*”, *Proceeding of Royal Institution of Great Britain*, (1886).
- Rosato A., Strandburg K. J., Prinz F. and Swendsen R. H., “*Why the Brazil Nuts are On Top: Size Segregation of Particulate Matter by Shaking*”, *Physical Review Letters E* **58**, pp. 1038-1040, (1987).
- Saleh B. E. A. and Carl T. M., “*Fundamentals of Photonics*”, Chapter 3, “*Beam Optics*,” pp. 80–107 New York: John Wiley & Sons, (1991).
- Scarano F. and Riethmuller M. L., “*Advances in iterative multigrid PIV image processing*”, *Journal Experiments in Fluids*, **S51-S60**, (2000).
- Schneider C. A., Rasband W. S. and Eliceiri K.W., “*NIH Image to ImageJ: 25 years of image analysis*”, *Nature Methods* **9**, pp. 671-675, (2012).
- Shapley N. C., Armstrong R. C., and Brown R. A., “*Laser Doppler velocimetry measurements of particle velocity fluctuations in a concentrated suspension*”, *Journal of Rheology*, **46**, 1, pp. 241-272, (2002).
- Shauly A., Wachs A. and Nir A., “*Shear-induced particle migration in a polydisperse concentrated suspension*”, *Journal of Rheology* **42**, pp. 1329 – 1348, (1998).
- Sieden G. and Thomas P. J., “*Complexity, segregation, and pattern formation in rotating-drum flows*”, *Reviews of Modern Physics* **83**, pp. 1323-1365, (2011).
- Sierou A. A. and Brady J. F., “*Shear - induced self - diffusion in non - colloidal suspensions*”, *Journal of Fluid Mechanics* **506**, pp. 285-314, (2004).
- Snabre P. and Pouligny B., “*Size segregation in a fluid-like or a gel-like suspension settling under gravity or in a centrifuge*”, *Langmuir* **24**, pp. 13338–13347, (2008).
- Snabre P., Pouligny B., Metayer C. and Nadal F., “*Size segregation and particle velocity fluctuations in settling concentrated suspensions*”, *Rheological Acta* **48**, pp. 855-870, (2009).
- Snabre P., Blaj O., Pouligny B., “*An optical flow method to analyze fluctuating particles in flowing concentrated granular systems*”, *GISEC 33*, Bordeaux, (2011).
- Taberlet N., Richard P. and John Hinch E., “*S shape of a granular pile in a rotating drum*”, *Physical Review Letters E* **73**, 050301(R), (2006).
- Taylor G. I., “*Stability of a viscous liquid contained between two rotating cylinders*” , *Philosophical Transactions of the Royal Society* **A223**, London , pp. 289 – 343, (1923).
- Taylor G. I., “*Dispersion of soluble matter in solvent flowing slowly through a tube*”, *Proceeding of the Royal Society London, Ser. A*, **219**, 186, (1953).
- Tetlow N., Graham A. L., Ingber M.S., Subia S. R., Mondy L.A. and Altobelli S. A., “*Particle migration in a Couette apparatus: Experiment and modeling*”, *Journal of Rheology* **42(2)**, pp. 307- 327, (1998).
- Timberlake B. D. and Morris J. F., “*Concentration band dynamics in free-surface Couette flow of a suspension*”, *Physics of Fluids* **14(5)**, pp.1580 – 1589, (2002).

- Wahl D. D. and Simpson J. J., “*Physical processes affecting the objective determination of near surface velocity from satellite data*”, Journal of Geophysical Research Atmosphere **95**, pp. 511-528, (1990).
- Weber J. and Malik J., “*Robust computation of optical flow in a multiscale differential framework*”, International Journal of Computer Vision **14**, 1, pp. 67-81, (1995).
- Wiederseiner S., “*Rheophysics of concentrated particle suspensions in a Couette cell using a refractive index matching technique*”, Thèse de l'Ecole Polytechnique Fédérale de Lausanne. n°**4627** (2010).
- Weiderseiner S., Andreini N., Epely-Chauvin G. and Ancey C., “*Refractive – index and density matching in concentrated particle suspension: a review*”, Journal of Experiments in Fluids **50**, pp. 1183 – 1206, (2011).
- Willert C. E. and Gharib M., “*Digital particle image velocimetry*”, Journal Experiments in Fluids, **10**, pp. 181-193, (1991).
- Wilson H. J. and Davis R. H., “*The viscosity of a diluted suspension of rough particles*”, Journal of Fluid Mechanics **421**, pp. 339- 367, (2000).
- Zarraga I. E., Hill D. A. and Leighton D. T., “*The characterization of the total stress of concentrated suspensions of non colloidal spheres in Newtonian fluids*”, Journal of Rheology **44**, pp. 185 – 220, (2000).